ADVANCES IN SEPARATION AND DETECTION IN OPEN TUBULAR CHROMATOGRAPHY

by

BRIAN NICHOLAS STAMOS

Presented to the Faculty of the Graduate School of

The University of Texas at Arlington in Partial Fulfillment

of the Requirements

for the Degree of

DOCTOR OF PHILOSOPHY

THE UNIVERSITY OF TEXAS AT ARLINGTON

MAY 2017

Supervising Committee:

Purnendu K. Dasgupta, Supervising Professor
Peter Kroll
Hyejin Moon

Acknowledgments

In the long journey that has been my time in graduate school there have been many that have helped me along the path. My deepest gratitude to my supervising professor Dr. Purnendu K. Dasgupta, for whom which I would have never made it through this time. His wealth of knowledge is absolutely staggering. Thank you again for your continued support and help.

I would also like to thank my committee members, Dr. Peter Kroll, Dr. Richard Timmons and Dr. Hyejin Moon for their continued support and advice during this time.

Finally I would like to thank my amazing coworkers that have been invaluable during my time here. Many many thanks to Phillip Shelor for his unending support and help.

Abstract
ADVANCES IN SEPARATION AND DETECTION IN OPEN TUBULAR CHROMATOGRAPHY

Brian Nicholas Stamos, PhD

The University of Texas at Arlington, 2017

Supervising Professor: Purnendu K. Dasgupta

Ion chromatography is an important method of analysis in the field of analytical chemistry with applications in a wide variety of applications from pharmaceutical analysis to purity assurance in semiconductor raw materials. The initial motivator for this research, however, was an extraterrestrial one; to perform ionic analysis of Martian soil extracts.

The research reported in this dissertation had two major goals. The primary goal was to create a method of conductivity detection that was applicable to small inner diameter open tubular capillaries. An auxiliary goal was to apply this method of detection in ways that were previously not possible. I, did, however, take part in other research, that were not related to these central themes. These are included as appendices.

To accomplish the primary goal, a detection method, commonly referred to as Capacitively Coupled Contactless Conductivity Detection (C^4D) was adopted and improved. Previous technology allowed measurement of ions in the low-mid mM range in capillary bores down to 20 µm. Smaller capillaries are advantageous for open tubular chromatographic separations. They permit greater efficiencies and decrease sample

and eluent consumption. In characterizing our detector, we also realized taht these detectors do not really measure conductance, rather, they measure the admittance between the electrodes. We refer to such detectors throughout hereinbelow as admittance detectors. The detector developed this work permits sensitive detection (low to mid μM levels) in capillaries as small as 5 μm in bore.

This detector developed in this research was then applied to Whole Column Detection (WCD). In the present WCD application, the entire column admittance is imaged. The column is scanned by moving the detector across it. This provides many advantages over stationary detection, including faster analysis, decreased method development time, and column health monitoring, among others.

Table of Contents

List of Figures

List of Tables

1.1 Introduction

Solution conductivity arises from the transport of charge carried by ions through their electrical field-induced movement. Electrical conductance is a universal and unique property of ions in solution and is dependent on the nature and concentration of ions in a solution. Ion exchange chromatography necessarily uses ionic eluents. In its early days, ion exchange chromatography was conducted with high capacity columns with high ionic strength eluents; minor changes in effluent conductance accompanying replacement of the eluent ion in the effluent by the analyte ion as the latter eluted, rendered conductivity detection of limited value. In 1975, Small et al.[1] removed this barrier by installing a unique post-separation device (which they initially termed a *stripper*, and later a *suppressor*) that removed the conductivity due to the eluent ions. For example, in anion exchange chromatography, with NaOH as the eluent and the post column device is a cation exchanger that exchanges all influent cations for H^+, the suppressor effluent was pure water. The membrane device suppresses the conductivity of the eluent, hence the name. Analytes like chloride, nitrate, sulfate, etc. elute from the column at different times and exit the suppressor as HCl, HNO_3, H_2SO_4, etc., which ionize fully into conducting ions, and are thus sensitively detected by their conductivity on a background of nearly nonconducting water. Since its introduction, this technique, called ion chromatography (IC), it has become the primary method of ion analysis and conductivity detection has remained the mainstay.[2]

Conductivity measurements are typically performed via galvanic contact of the electrodes with the solution. To prevent electrolysis occurring at the electrodes, an AC voltage is applied, with a typical frequency of 1-15 kHz. The current passing through the solution is directly related to the conductivity of the solution. This current is then converted to voltage, amplified as necessary, rectified and sent to a readout/data acquisition system. While galvanic detection is easily used with cell volumes of 1 -10 µL, adapting this to smaller volumes becomes increasingly difficult. While packed capillary ion chromatography, recently commercialized with 0.4 mm bore packed columns, still use galvanic contact conductivity detection, in open tubular chromatography or capillary electrophoresis (CE) systems it is difficult to use any separately connected cell because of the large dispersion caused by the connection as well as the detection cell. Direct on-column measurements with electrodes in galvanic contact (e.g., through holes drilled in the wall)[3] or bifilar wire disposed in the flow path[4] or end column detection[5] have been reported but have not generally been adopted because of practical difficulties. If the detector requires the column to be modified, the entire assembly will need to be discarded if either the column or the detection system has a problem. Although the measurement of conductivity of a solution at high frequencies without galvanic contact (through a dielectric, e.g., glass) had been known for a long time[6], this had not been practiced in microscale systems until 1998 when two separate groups independently introduced non-galvanic measurement of solution conductivity in small bore tubes. Although a new term, capacitively coupled contactless conductivity detection or C^4D[7,8] was coined, the principle was the same as that known earlier as *Oscillometry*. The C^4D technique, originally applied to CE, has also been used in IC.[9] A typical configuration

involves two ring-shaped electrodes placed directly on the capillary, separated typically < 1 mm apart. An AC excitation voltage is applied, typically in the range of 15-350 kHz.[10] The field capacitively couples through the capillary wall (behaving as a dielectric) to the solution within. The current passes through the solution and then is picked up by the second electrode, again passing through the wall by capacitive coupling. Generally, the overall behavior is similar to that of a galvanic contact conductivity detector in that the lower the resistance of the solution, the higher the measured current. However, this is not *always* true, as will be seen later. Since its introduction, the only major change in C^4D design has been the addition of a ground shielding plane between the electrodes, designed to reduce the capacitive coupling of the electrodes through the air. Performance improvements have resulted from closer electrode spacing, material choice, and the exact nature of their amplification circuitry.[11,12] In this laboratory, we are interested in small bore (5-30 µm bore) open tubular capillaries for chromatography because small diameter tubes lead to more efficient chromatograms. They also reduce size, weight, and sample/eluent/power consumption, making them suitable for portable applications as well as space based exploration. In addition, unlike packed columns, an open tubular column can survive drying and then freezing. If conductometric open tubular ion chromatography is to be conducted in the suppressed mode, a small enough suppressor that will ion exchange the eluent counterion completely for H^+ (or OH^- for cation chromatography) with minimal dispersion is still a challenge.

Towards the effort of detection at these small scales many different designs were considered. In particular different methods of amplification and rectification of the signal were tested. While many previous designs employ diode rectified signals, we used an

integrated circuit chip (Analog Devices AD536A) that converts the root mean square (RMS) value of an alternating waveform to an equivalent positive (DC) voltage. This device is a true RMS to DC converter, which has the ability to measure complex AC or AC plus DC input signals. This measurement is more useful than just rectification because it relates directly to the power of the signal allowing small changes to be detected more easily.

A second key difference is the transimpedance amplifier (current to voltage converter) gain. In previous designs this was typically 4-5 x 10^5 V/A. We instead used gain values up to 10^9 V/A. Further, if the frequency is chosen properly, the phase shift can be adjusted. With these changes, we have created a more sensitive C^4D, which we have now appropriately labeled an admittance detector that can perform sensitive detection in very small capillaries down to 2 µm.

Chapters 2 through 4 describe the creation of a low frequency admittance detector and its application as part of an open tubular ion chromatograph. Chapters 5 and 6 expand the applications of this detector to drive a new method of whole column detection based on scanning as well as the miniaturization of the aforementioned open tubular ion chromatograph. A more detailed description is given below.

Chapter 2 describes the creation of a better model to help explain why low frequencies work better when cell resistances are very high. A key finding in this was that what are typically called capacitively coupled contactless *conductivity detectors* are not in fact conductivity detectors at all, but admittance detectors. Admittance being the reciprocal of impedance. From this work it is easier to explain why the optimum frequency range decreases with decreasing conductivity, capillary bore and increasing electrode gap.

Author contributions:

Min Zhang: Primary author and writer of the manuscript.

Brian Stamos: Preliminary experiments, including helping to construct the admittance detector, high voltage experiments to 100 V p-p, humidity and heat baseline experiments.

Natchanon Amornthammarong: Initial low frequency admittance detector experiments. First to show that it could in fact be done at lower frequencies.

Chapter 3 involves the design and applications of admittance detectors for high impedance systems. A more thorough description of the design for the low frequency admittance detector is given. It is tested over a range of frequencies wherein linearity and sensitivity are explored, with measurements made in capillaries as small as 2 μm i.d. It is also applied to capillary electrophoresis where such detectors are particularly beneficial.

Author contributions:

Min Zhang: Primary author and writer of the manuscript.

Brian Stamos: Constructed the admittance detector, including all testing leading up to the final electronics configuration. Initial signal to noise, LOD and frequency optimization experiments and separations.

Chapter 4 introduces a new open tubular ion chromatograph for which there are many advantages. One of the primary goals of this work involves the analysis of ions in soil found on the planet Mars. In addition to requiring a system that can survive the rigors of

space travel, including limited heating for columns and eluents, other factors are equally important. These include low eluent consumption, low power consumption, and the elimination of the need of high pressure pumps, which contribute greatly to weight.

Author contributions:

Bingcheng Yang: Worked on separations for open tubular columns and modification techniques.

Min Zhang: Manuscript author and performer of final experiments and applications.

Tinakorn Kanyanee: Worked on separations and the injection system, and alternate methods of detection.

Brian Stamos: Constructed the admittance detector and helped in the building of the injection system for this work.

Chapter 5 describes a new method of whole column detection. While the few available methods of whole column detection are traditionally performed by imaging an entire column at once, a linear stage was instead employed to sweep the detector across the column for increased fidelity. This method was enabled by a new detector that could acquire data at high sampling rates.

Author contributions:

Brian Stamos: Manuscript author and performer of experiments.

Shin-Ichi Ohira: Initial design of the quadrupole detector layout, which was adapted for packed capillary scale scanning work.

Chapter 6 describes the construction of a field-portable ion chromatograph. This is a further miniaturization of the instrument described in chapter 4. Through the use of application specific electronics and a 3 solenoid arrangement to replace a six port injection valve, weight has been reduced dramatically to 1 kg without batteries, or 3 kg with the ability to run for 24 hours on battery power alone.

Author contributions:

Brian Stamos: Manuscript author and performer of all experiments.

Weixiong Huang: Constructed initial design of the portable ion chromatograph.

In all, these chapters represent the creation of a new and more sensitive admittance detector, as well as a novel application.

Chapter 2 Capillary Scale Admittance Detection

Min Zhang, Brian N. Stamos, Natchanon Amornthammarong, and Purnendu K. Dasgupta*

Department of Chemistry and Biochemistry, The University of Texas at Arlington, Arlington, Texas 76019-0065, United States

2.1 Abstract

Techniques that have been variously termed oscillometric detection or (capacitively coupled) contactless conductivity detection (C^4D) are known actually to respond to the admittance. It is not often appreciated that the frequency range (*f*) over which such systems respond (quasi)linearly with the cell conductance decreases acutely with increasing cell resistance. Guidance on optimum operating conditions for high cell resistance, such as for very small capillaries/channels and/or solutions of low specific conductance (σ), is scant. It is specially necessary in this case to take the capacitance of the solution into account. At high frequencies and low σ values, much of the current passes through the solution behaving as a capacitor and the capacitance is not very dependent on the exact solution specific conductance, resulting in poor, zero, or even negative response. We investigated, both theoretically and experimentally, capillaries with inner radii of 5–160 μm and σ ≈ 1–1400 μS/cm, resulting in cell resistances of 51 GΩ to 176 kΩ. A 400-element discrete model was used to simulate the behavior. As model inputs, both the wall capacitance and the stray capacitance were measured. The solution and leakage capacitances were estimated from extant models. The model output was compared to the measured response of the detection system over broad ranges of *f* and σ. Other parameters studied include capillary material and wall thickness, electrode spacing and length, Faraday shield thickness, excitation wave forms, and amplitude. The simulations show good qualitative agreement with experimental results and correctly predict the negative response behavior observed under certain conditions. We provide optimum frequencies for different operating conditions.

2.2 Introduction

Electrical properties of a medium have long been probed through an insulating wall using alternating excitation; the term “oscillometry” has been in use since before 1950. The benchmark instrument, the Sargent Model V Oscillometer, operated at a frequency (*f*) of 5 MHz and could detect a dielectric constant change of 0.003 units.[13] A major application was monitoring conductometric titrations.[14] The 1980s witnessed the first such detectors for capillary scale isotachophoresis, using four wire–electrode arrangements,[15,16] and an oscillometric flow-through detector that measured permittivity or conductivity.[17] Spurred by increasing needs in capillary electrophoresis (CE), Zemann et al..[18] and da Silva and do Lago[19] independently introduced such a detector for CE with two tubular/ring electrodes placed/painted on the capillary a small distance apart. They respectively used *f* = 20–40 kHz and 600 kHz. Zemann et al.. first coined the term capacitively coupled contactless conductivity detection (originally abbreviated as CCCD and later, more commonly, as C^4D). Many C^4D improvements have been proposed;[20-25] there are several recent reviews;[26-28] Kubáň and Hauser in particular have made sustained contributions through both original work and reviews.[29-32]

C^4D simulations assume either (a) the simple model, which involves just one or two capacitors (wall capacitance) in series with the solution resistance and a capacitor in parallel (interelectrode/stray capacitance)[17] or (b) the discrete element model (DEM), wherein the first two elements above are divided into a multitude of RC elements in a network,[19] with an additional leakage capacitance from the coupling of a Faraday shield, if used between the electrodes, to the solution. The effect of the shield has been

theoretically and experimentally examined.[23] Others investigated the effects of electrode width, spacing, and excitation frequency on detector performance[33] and the effect of wall thickness at constant inner diameter (ID).[34] The apparent superiority of thinner walls has been noted; this disappears at higher specific conductances (σ). The DEM correctly predicted the overshooting artifact with abrupt conductivity transitions.[24] The effects of frequency, voltage, cell geometry, and electronic components, simulated with the simple model, was compared with experimental data.[35, 36] Another two companion papers expansively covered C^4D behavior using both models.[37, 38] A high-resolution DEM (but not the simple model) corresponded well with experimental data; merits of lock-in detection were also demonstrated.[39] Although many have shown that the simple model fails in many details, it continues to be used.[40-42]

Given such extensive extant knowledge, it may seem superfluous to add more to this. Actually, available guidance for optimum operating conditions is scant. Operating frequencies, for example, range from 250 Hz[43] to 1.25 MHz[34] (available commercial detectors permit operations in the 38–612 and 50–1200 kHz range). We have been interested in (suppressed) open tubular ion chromatography (OTIC),[44-46] preferably in columns of <20 μm ID.[47] In suppressed conductometric chromatography or CE,[48] the background σ is very low. Even in nonsuppressed systems, good limits of detection (LODs) require low to modest background σ. With rare exceptions,[49] the focus has been on σ ≥ 200 μS/cm) and/or capillary ID ≥ 25 μm (majority ≥ 50 μm). Small diameters and low σ or both have never been discussed. Importantly, we found that a commercial C^4D can produce completely anomalous response in this domain or over large spans of σ.

(See Figure A-S1 in the Supporting Information.) Others have also observed that, while the response may be linear at a higher concentration, the response slope can become zero[34] or even negative.[21, 24] Rather than a full exploration of this behavior, the reaction of some has been to define the LOD “as the concentration at which the injected analyte peak does not decrease any more”.[21]

The solution interrogated represents not only a resistor, it is also a dielectric with a finite capacitance (C_{aq}) that is in parallel with the resistor. This has largely been ignored. However, two recent papers have made important contributions. One took into account C_{aq} and provided measured data from model fits. However, the lowest concentration studied was 1 mM.[50] A second recent paper[51] not only recognized the presence of C_{aq} and devised conditions to measure the admittance when it is dominated by capacitance (in hydroorganic solvents). Unfortunately, when the objective was to measure conductance, they chose to neglect C_{aq}. As the conductance of the resistive component and the admittance of the capacitive component in parallel scales in the same fashion with the capillary radius (r) or the interelectrode gap (l_g), as a first approximation, the ratio of the current that flows through the capacitive component versus the resistive component is not dependent on r or l_g but solely on σ and the excitation frequency (f). As σ decreases and f increases, more of the current flows through the capacitive component, making the system insensitive to σ. Moreover, the dielectric constant actually decreases as the electrolyte concentration increases,[52] resulting in a decrease in C_{aq}. In many cases, especially at low σ and higher f, the current through the cell can decrease with increasing σ.

Present day suppressed ion chromatographs (ICs) reach a background conductivity (σ) of ~0.1 μS/cm. Conductivity detectors with typical background noise levels of 1–2 nS/cm respond to strong electrolytes from this pure water background to ~1–2 mM concentrations linearly. The concentration−σ relationships at higher concentrations are nonlinear, but this is not because of detector nonlinearity. In contrast, under optimized conditions, a C^4D signal (i) is linear with σ over a span of less than ~2 orders of magnitude, (ii) approaches finite cell currents as σ approaches 0 or ∞, and (iii) is dependent on measurement frequency, regardless of the specific value of σ. This behavior is hardly unexpected for the configuration; any other expectation stems from the inappropriate nomenclature; it measures the admittance. Others have also recognized this and have decided to refer to such a general class of detectors as *contactless impedance sensors*.[51] We prefer *admittance* over impedance, since the primary measured variable is current; in much the same way, *conductivity detector* is preferred over *resistivity detector*. In addition, the admittance signal does include effects of the wall with which the electrodes are very much in contact. The term *contactless* admittance or impedance thus seems inappropriate. While the name may be too catchy or perhaps now too entrenched to be replaced, a C^4D is not. Whatever the name, in many instances, its virtues cannot be matched by a standard conductivity detector.

Capillaries of small radius (*r*) are essential in OTIC. In CE, a small *r* permits better heat dissipation and greater efficiencies. The ohmic resistance increases with $1/r^2$. Here, we report experimental and theoretical parametric studies, with special attention to

situations where the cell has a high ohmic resistance, whether because of small r, σ, or both. The lessons learned are then used to fabricate a simple detector capable of efficient detection, even in very small capillaries; we show successful use down to r = 1 μm.[53]

2.3 Model

Since a simple model failed to explain the pattern of the experimental data at high cell resistance (R_{cell}) values, we adopted the DEM model, as schematically depicted in Figure 2-1b. It is similar to that proposed by Gaš et al..,[24] but differs as detailed below. We increased the number of RC elements per electrode in the simulation until, at 200 elements per electrode, the output was numerically stable. The model has four resistors in the center that, together, add up to R_{cell}, which is given by

$$R_{cell} = \frac{10^4}{\sigma}\left(\frac{l_g}{\pi r^2}\right) \quad (1)$$

where σ is the specific conductivity in expressed in units of μS/cm. The value of each resistor in the RC elements on each electrode (R_e) is given by $R_{cell}l_e/(nl_g)$ (see the Supporting Information), where l_e is the electrode length (l_e = 10 mm in this study) and n is the number of elements per electrode (here, n = 200).

A leakage capacitance (C_l)[24, 39] arises from the coupling of the Faraday shield and the inner solution. Most DEM simulations (e.g., ref 24) just assume a value for C_l. Johnston et al..[39] put an insulator on each electrode sleeve and then enclosed these with a grounding sleeve. The leakage capacitance in this case is an annular capacitor consisting of serial annuli of air and the silica wall of thickness equal to l_g. The manner

of shielding used in the present work would appear to be more common, based on the literature. In our detector, although a concentric geometry with an air gap may be esthetically ideal and perhaps realized by some; in practice, in our case, the shield inevitably touches the capillary wall over some fraction F_t of its perimeter. The leakage capacitance is that due to the wall (which we separate into the coating and the bulk silica) over the contacted fraction from eq 2:

$$C_l = \frac{2\pi F_t D_c D_w t_e}{D_w \ln\left(\frac{r_o}{r_o - t_c}\right) + D_c \ln\left(\frac{r_o - t_c}{r}\right)} \quad (2)$$

A more-accurate form of eq 2 where C_l does not reduce to zero, even when F_t is zero (leakage capacitance through the air remains), is given in the Supporting Information; however, for most purposes, eq 2 suffices. Here, F_t is the fraction of the outer perimeter of the capillary touched by the shield (this can vary from 0 to 0.5; F_t is taken to have a value of 0.4 in our model, except as stated), D_w and D_c are the absolute permittivities of the wall material and the coating, respectively (3.38×10^{-11} and 3.0×10^{-11} F/m, respectively), r_o is the outer radius of the capillary, and t_c and t_e are the respective thicknesses of the coating and the shield, respectively. While R_{cell} is distributed across l_g, C_l addresses only the length corresponding to t_e (0.13 mm in this study). To get approximately the same length resolution as that on the electrodes (200 elements/10 mm), we divided the leakage capacitance in three elements. With l_g = 0.4 mm, R_{cell} was distributed into four components, being, respectively, 1/3, 1/6, 1/6, and 1/3 of the total, as shown in Figure 2-1b.

The resistive component of the sample solution, whether enclosed by the electrodes or that defined by R_{cell}, is in parallel with the solution capacitance (C_{aq}). At low σ values

and high frequencies, this has a significant effect on the results. C_{aq} was computed from eq 3:

$$C_{aq} = \frac{D_{aq}\pi r^2}{l_g} \quad (3)$$

where the solution dielectric constant (D_{aq}) is given by

$$D_{aq} = \varepsilon_0(80.72 - 3.796 \times 10^{-5}\sigma - 5.452 \times 10^{-6}\sigma^2) \quad (4)$$

Based on the data in ref 52 (also see Figure A-S2 in the Supporting Information), $\varepsilon_0 = 8.854 \times 10^{-12}$ F/m.

The field couples to the solution by the wall capacitance (C_w total in series, thence 2 C_w per electrode; each individual capacitor in the 200 elements was, therefore, 0.01 C_w); this was measured by reducing the stray capacitance (C_s) to ~0 by using a large l_g value (5 mm), and reducing R_{cell} to ~0 by filling the capillary with molten Wood's metal, allowing it to solidify, and measuring the current at different frequencies at a constant known applied voltage (V_{app}). The double layer capacitance (~25 μF/cm^2)[54] is in series with C_w but is 10^6 to 10^9 times larger; its reactance and, thence, influence on the results is negligible.

The stray capacitance (C_s) leads to crosstalk across the electrodes, independent of R_{cell}. We measured C_s by setting R_{cell} to approximately infinity (∞); the closest approximation was a dry-gas-filled capillary.

Measured values of C_w, C_s, and σ were used. A homogeneous solution was assumed. Matrix solution to the necessary set of Kirchhoff equations were solved using LabVIEW (see Supporting Information); the output of interest being the root mean square (RMS) current.

2.4 Experimental Section

Construction of the Detection Cell

The detector is schematically illustrated in Figure 2-1a. The detection cell is enclosed by a grounded metal box. Detection electrodes (10 mm long, unless otherwise stated) were made by casting Woods metal alloy (with a melting point (mp) of 70 °C) for each individual capillary to obtain conformal contact.

A 0.4-mm-diameter hole was drilled through a sheet of mu-metal (magnetic permeability ~5 mH/m, thickness 0.13 mm, except as stated), flanked by insulating adhesive tape on each side (total thickness of 0.36 mm). The capillary was passed through the hole and the sleeve electrodes were pressed to have intimate contact with either side of the central sheet. The mu-metal was grounded to function as a Faraday shield and minimize the stray capacitance.

2.4.1 Measurement Setup

A Tektronix Model FG504 function generator (www.tek.com) provided excitation in fixed or swept-frequency mode; a sine wave (27 V p-p) was used, except as stated. Applied

voltage effects were investigated by amplifying the Model FG504 output, using a high-voltage operational amplifier (Model PA15A, www.apexanalog.com) powered by an adjustable ±250 V supply (Model LQD-425, www.lambda.com). The pickup electrode was connected directly to a low noise current preamplifier (Model SR570, Stanford Research Systems, www.thinksrs.com) with the shortest possible double-male-ended BNC connector. To keep within the gain-bandwidth product (GBW) of the SR570, very high amplification was not used; rather, secondary amplification was provided by a Tektronix Model AM502 amplifier. The overall gain ranged from 10^6 V/A to 10^9 V/A. The RMS value of the amplified ac signal was processed by a RMS-to-DC converter (Analog Devices, Model AD536A, www.analog.com). The overall output was calibrated by a metrology-certified oscilloscope (Agilent, Model 54621A, www.agilent.com). The AD536A output, as well as the Model FG504 frequency-indicating output in the swept frequency mode, were acquired using a 16-bit Model USB-1608FS DAQ card (www.mccdaq.com). Data acquisition and processing software were written in LabVIEW (http://www.ni.com/). Shielded cables with BNC termini were used for signal transmission.

2.4.2 Capillaries

Polyimide-coated fused silica (PFS, www.polymicro.com), poly(methyl methacrylate) (PMMA, ~16 μm ID, ~350 μm outer diameter (OD), custom-extruded; www.paradigmoptics.com), polyether ether ketone (PEEK, 25–150 μm ID, 360 μm OD; www.westernanalytical.com), polytetrafluoroethylene (PTFE, ~50 μm ID, ~350 μm OD;

www.zeusinc.com) capillaries were obtained as indicated. Unless stated otherwise, the data pertain to PFS capillaries (PFSCs).

2.4.3 Electrolyte

KCl was the model electrolyte. Measurement solutions were prepared by mixing 1 or 10 mM KCl solution with deionized water online. Feed solutions were protected by a N_2 blanket. Two peristaltic pumps (Dynamax RP-1, www.rainin.com) delivered the KCl and water, respectively; the flow ratio (total 0.9 mL/min) was varied to get different concentrations/conductivities (see the Supporting Information), the mixture proceed through a Visco-Jet Micro-Mixer (TCMA0120113T, www.theleeco.com), a conductivity detector (Dionex, Model CDM-I, www.dionex.com) and a flow splitter prior to the admittance detector. The frequency dependence of the response was studied with different size capillaries filled with 0–10 mM KCl. Acquisition of the frequency-dependent data were started only after the feed specific conductance was stable to <0.2 or <2 μS/cm for <1 mM KCl or >1 mM KCl, respectively, as measured by the precalibrated CDM-I. All measurements were made under flow conditions.

2.5 Results and Discussion

2.5.1 Frequency Dependence of Stray Capacitance and Wall Capacitance Values

Relative permittivity is generally not frequency dependent below 1 MHz (shown for a reference capacitor in Figure A-S3 in the Supporting Information). Accordingly, the measured wall and stray capacitances increased only slightly from 0.1 kHz to 500 kHz

(see Figures A-S4 and A-S5 in the Supporting Information). Hence, no frequency dependence was assumed in the models.

The wall capacitance measurements can be classified in four groups: (i) vary r_o at constant r (~50 μm); (ii) vary r at constant r_o (~180 μm); (iii) vary both r and r_o at constant $r_o - r$ (~50 μm); and (iv) for r = 12.5 μm and r_o = 180 μm, change l_e.

Theoretically, the wall capacitance at each electrode (2 C_w) is expressed as

$$C_w = \frac{\pi D_c D_w l_e}{D_w \ln\left(\frac{r_o}{r_o - t_c}\right) + D_c \ln\left(\frac{r_o - t_c}{r}\right)} \quad (5)$$

The data are shown in Figure 2-2. It will be seen that all measured results correspond closely to the solid line computed by eq 5 (because the polyimide coating is thin and D_c and D_w are similar, only marginally higher results are calculated if the entire capillary is assumed to be silica. These agreements also indicate excellent contact of the conformally cast electrodes; commonly used tubular sleeve electrodes provide much worse contact, as evidenced from much lower C_w values under otherwise identical conditions (see Figure A-S6 in the Supporting Information).[38]

2.5.2 Stray Capacitance and the Faraday Shield

In the absence of a shield, the measured stray capacitance generally agreed well with

$$C_s = \frac{\pi \varepsilon_0 (r_o^e - r_o)^2}{l_g} \quad (6)$$

where r_o^e is the outer radius of each electrode; for all practical purposes, the permittivity of dry air can be taken as ε_0. With l_g = 0.12 mm (electrodes as close as possible without

making contact), C_s was measured to be 54.4 ± 5.7 fF (the computed value was 50.2 fF, but the error in microscopically measuring l_g in this range can be significant). With a C_s value this high, the background current was so high that the signal-to-noise (S/N) ratio at any sample concentration was greatly compromised. At l_g = 2 or 5 mm, C_s decreased to 2.67 ± 0.57 and 0.72 ± 0.18 fF, respectively, decreasing the crosstalk current proportionally. In cases where the placement of a grounded shield is impossible or inconvenient (e.g., with microfluidic chips or integrated admittance and optical detectors,[55] increasing l_g will be beneficial; an increase in overall R_{cell} will move the preferred operating frequency to a lower value (see below), further reducing crosstalk.

C_s was reduced dramatically with the shield, but not to zero, because of the capillary passage aperture. With the electrodes touching the shield insulation tape ($l_g \approx 0.4$ mm), C_s did not show a monotonic change with r; it ranged from 0.26 fF to 0.44 fF (see Table S1 in the Supporting Information, r_o = 182 μm, r = 2.5–125 μm), probably because of the impossibility of locating the capillary reproducibly within the shield aperture. There was no discernible change in C_s upon replacing the paper insulation of the shield with PTFE (PTFE tape, 0.43 ± 0.07 fF; paper tape, 0.44 ± 0.07 fF; r_o = 182, r = 12.5 μm). If the electrode gap was increased with the shield present, C_s decreased dramatically; at l_g = 2 mm, the C_s value was 6.8 ± 0.2 aF; at l_g = 5 mm, C_s was not measurable.

Most users of admittance detectors are aware of drifting baselines at high sensitivities if either the humidity or temperature changes markedly. Temperature effects are well-known. The permittivity of air increases greatly with the water vapor content;[56] C_s thence

increases markedly as the humidity changes. We verified that changing the humidity of the N_2 in a N_2-filled capillary has no effect on C_s, and so this effect must be entirely due to changing the humidity of the space between the electrodes. Figure A-S7 in the Supporting Information shows the temporal change in the baseline of a dry gas-filled capillary in a commercial detector as a flow of N_2 of specified relative humidity (RH) is established around the detector head over a time span of 15 min. Filling the electrode gap with a low dielectric constant material like polyethylene does not substantially eliminate humidity dependence. To avoid humidity effects where maximum sensitivity is needed, we suggest using a desiccant in small regenerable bags within the detector head enclosure.

2.5.3 Faraday Shield Thickness

The Faraday shield serves to reduce C_s and the crosstalk. Even the thinnest mu-metal shield used was very effective, as described above, with little room for improvement with a thicker shield. Moreover, an increase in t_e also connotes an increase in C_l that reduces response slope, especially at higher frequencies. Increasing the capillary passage aperture will reduce C_l but at the expense of increasing C_s. An increase in t_e also necessitates an obligatory increase in l_g. Therefore, a thin high magnetic permeability metal sheet and a small aperture are ideal. Accordingly, with l_g = 2 mm, increasing t_e from 0.13 mm to 0.6 mm to 1.2 mm, resulted in a decrease in the optimum frequency (f_{opt}) and the net signal: for 100 µM KCl flowing through (r_o = 180, r = 12.5 µm) reduced f_{opt} from 1.8 kHz to 1.4 kHz to 1.0 kHz; the relative response decreased from 1 to 0.87 ± 0.03 to 0.69 ± 0.03 (see Figure A-S8 in the Supporting Information).

Operation with High R_{cell}: Behavior of a Small Bore (r = 7.5 μm) Capillary

Some early modeling[37, 57] showed that f_{opt} decreases as σ decreases but provided no quantitative guidance. In applying admittance detection to a low σ situation, Kubáň et al..[58] found that a better S/N ratio was obtained at f = 25 kHz, compared to higher frequencies, but lower frequencies were not explored.

Experimental data and model calculations are shown respectively in the top and bottom rows in Figure 2-3 (r, r_o = 7.5, 180 μm). The leftmost panels (Figures 2-3a and 2-3d) show the current vs frequency behavior at low KCl concentrations (C, from 0 to 0.4 mM) up to 50 kHz. At $f \geq 50$ kHz and $C \leq 0.4$ mM (σ ≤ 75 μS/cm), the current becomes insensitive to concentration, as the sum of the capacitive currents begins to dominate. Both theory and model, as shown in Figures 2-3a and 2-3d, depict this behavior and indicate the failure of an admittance detector to behave as a conductance detector at high R_{cell} and high f. Data over the complete range of concentrations and frequencies for different capillary radii are given in the Supporting Information (Figures A-S9–S16).

Figures 2-3b and 2-3e shows response behavior (i vs σ) in the same low concentration range at different frequencies. Although apparent linearity in log–log plots do not ensure a linear relationship of the original variables, the coefficients of determination (r^2) for the linear relationship between r and σ at the two lowest frequencies are reasonable (r^2 = 0.994) over this 1.6 orders of magnitude range of concentration, although the linear correlation between log i and log σ is decidedly better. Table S2 in the Supporting

Information provides the regression equation details for both *i* vs σ and log *i* vs log σ. The linearity gets poorer as the frequency increases. At 10 kHz the lowest concentration datum is not part of a linear plot. At frequencies >10 kHz, at least the two lowest concentration points clearly do not conform to linearity. The model shows the same pattern as the experimental data; however, the quantitative details differ.

Arguably, the most important performance criterion is the relative change of the signal with conductance, $(1/i)(di/d\sigma)$; since noise is typically proportional to the absolute value of the background current, a plot of this term versus σ represents how the S/N ratio changes with concentration (Figure 2-3c). The corresponding model results appear in Figure 2-3f. At frequencies between 0.5 kHz and 4 kHz, the relative sensitivity decreases monotonically with σ, both in the model and the experiment; the 10 kHz results fall in the same group at higher σ values. Both modeled and experimental 25 kHz and 40 kHz results indicate much lower sensitivities at low σ values than those at lower frequencies. The pronounced maxima seen in the models in the lower-frequency data are less prominent in the experimental results, and these are shifted to higher σ values in the experiment. In general, qualitatively similar events occur in both the model and the experiment, but model predictions are shifted to lower σ and higher *f* values, relative to those experimentally observed. Table S3 in the Supporting Information contains detailed numerical data.

Analogous to a $(1/i)(di/d\sigma)$ plot is $(di/i)/(d\sigma/\sigma)$ (the slope of a log i–log σ plot) vs σ: this provides an indication of the relative response (see Figure A-S17 in the Supporting Information); a relatively flat portion indicates uniform sensitivity (linear response zone).

2.5.4 Optimum Frequency for Detection of 100 µM KCl in a Water Background Capillary Bore and Interelectrode Spacing

For the same value of σ, R_{cell} is affected by changes in either the capillary radius r or the interelectrode gap l_g. Therefore, the effects of r and l_g are considered together in this section. Our ultimate interest is in the applicability of these detectors in suppressed IC. The choice of an electrolyte of suitable σ was based on the typical midrange peak conductance in a typical IC analysis. In our experience, the median peak height is ~15 µS/cm; based on this observation, we chose 100 µM KCl (σ = 14.7 µS/cm) as the illustrative analyte whose response, injected into a flowing water stream, was determined. Figures 2-4a and 2-4b show the experimental and modeled results for variations in r and l_g. Note that the model only shows qualitative agreement with the observed results; as such, if both are plotted in the same scale, the similarity is not seen. In both cases, an increase in R_{cell} moves the optimum range of f downward. The model correctly predicts the general pattern observed experimentally from variations in r (Figure 2-4a) but predict a higher current than that actually observed; the departure is greater at higher f and lower R_{cell} values, suggesting that one or more of the capacitive parameters are overestimated in the model. During the progress of this work, we became aware of the recent elegant work of Shen et al..[50, 59] which shows that the wall coupling capacitance (C_w) is affected by σ and is generally much lower than that given

by eq 5. Presently, this dependence cannot be explicitly expressed in a corrective equation; a future further refinement of the model will be needed to address this. However, it is clear that such a correction will result in a better agreement between the model and the experiment, since reducing C_w will result in a decrease of the current. Variations in l_g lead to similar results (see Figure 2-4b); the model predicts greater currents and higher frequencies for current maxima than those experimentally observed.

At very low σ and r values, l_g must be minimized and f therefore must be low. In other situations, there may be a choice of higher l_g and lower f versus lower l_g and higher f. We tested a situation where only l_g was varied. Experimental and model results are shown in Figures A-S18a and A-S18b in the Supporting Information. While this may not be true in all situations (e.g., if i is so small that it becomes the primary source of noise), in this range of parameters, higher l_g–lower f choice consistently exhibits a greater value of $(1/i)(di/d\sigma)$, suggesting that greater l_g may be better for higher S/N ratios. However, inasmuchas the major use of such detectors is in separations, l_g must be kept smaller than the narrowest analyte zone in these cases.

Numerical data for the behavior of an r = 12.5 μm, r_o = 182 μm capillary over a wide range of σ are listed in Table S4 in the Supporting Information for l_g values of 0.4, 2, and 5 mm.

2.5.5 Optimum Frequency as a Function of Background Conductance and Capillary Size

It would be apparent that the optimum frequency for detection will be dependent both on the background conductance itself and r. We report experimental data for a variety of situations in Tables S5 and S6 in the Supporting Information. Figure A-S19 in the Supporting Information provides a graphical summary: the optimum response frequency range is plotted for various values of R_{cell} and compared with what is observed experimentally.

2.5.6 Electrode Length

Since C_w increases directly with l_e, the capacitive coupling and the overall current is expected to increase with l_e. However, this will not be observed if the length of the sample zone is the limiting factor; narrow sample zones are typical in capillary separations. In such situations, increasing l_e will not be beneficial, because the detector background (and, concomitantly, the noise if the background σ is significant) will increase without any proportionate gain in the sample signal. Therefore, the effect of electrode length was evaluated by actually injecting sample plugs. We injected 0.17 nL of 0.2 mM KCl into a r = 5 μm capillary, corresponding to an sample length of 2.2 mm, which is greater than l_g (0.4 mm) but smaller than l_e (5–15 mm). Figure A-S20 in the Supporting Information shows the results. The peak heights for l_e = 10 mm (0.462 ± 0.008 nA) and 15 mm (0.464 ± 0.008 nA) were statistically indistinguishable and that for l_e = 5 mm (0.496 ± 0.007 nA) was marginally greater; however, this degree of difference could possibly arise from limitations in the reproducibility of electrode placement.

Similarly, the differences in peak half widths in the three respective cases of l_e = 5, 10, and 15 mm ($0.7_1 \pm 0.0_1$, $0.7_8 \pm 0.0_1$, and $0.6_8 \pm 0.0_4$ s) were below the resolution of 10 Hz data acquisition rate used. Neither peak height nor half width exhibited statistically discernible variation as a function of l_e. The minimum convenient electrode length will seem appropriate.

2.5.7 Capillary Wall Thickness

A reduction in capillary wall thickness increases C_w. Similar to an increase in l_e, this also increases the background but unlike changing l_e, the sample signal is also enhanced, regardless of the width of the sample zone. However, the overall situation is complicated by a simultaneous increase in C_l. Tůma et al..[34] previously compared r = 38 μm for r_o values of 180 and 75 μm but at a single frequency of 1.25 MHz. We examined the background current and response slope at different background σ values for r = 50 μm for r_o values of 100 and 182 μm at frequencies of 100–500 kHz at l_g = 2 mm. The results in Table S7 in the Supporting Information show the expected simultaneous increase in both the response and the background; however, the response to background ratio, $(1/i)(di/d\sigma)$, generally showed no marked increase and often deteriorated. This suggests that going to thinner wall capillaries may not always be beneficial if all other operating conditions are held constant. The major exception is the common situation: the absolute current levels near the LOD are very low and inadequate current levels constitute the principal noise source.

2.5.8 Capillary Material

PMMA, PTFE, and PEEK capillaries were compared with similarly sized PFSCs. The relative permittivities of the four materials are, respectively, 2.6–4 (decreasing with increasing frequency), 2.1, 3.2, and 3.82. Detailed data are given in Table S8 in the Supporting Information. From the measured C_w for the PMMA capillary used, based on a simplified version of eq 5 (no coating), the relative permittivity is calculated to be 2.7 ± 0.2. The responses of the PMMA and PFS capillaries were very comparable, but PMMA capillaries consistently provided a lower background. The background current of PTFE capillaries did not vary in a consistent fashion with σ. The response was greater than comparable PFSCs at low σ but gradually became lower at high σ. True conformal contact with PTFE may be an issue. PEEK capillaries consistently provided greater response than PFSCs but the background was also higher than, or comparable to, PFSC counterparts. Overall, no material stood out in performance. Except for PMMA vs PFSCs, differences in permittivity alone could not explain the observed differences, albeit minor.

2.5.9 Excitation Voltage and Waveform

Tanyanyiwa et al..[22] have previously shown signal improvements by increasing V_{app}. In their operational domain, however, the optimum frequency was ≥100 kHz and the signal was very low at low kHz levels. The study focused on signal only, rather than S/N. The present HV amplifier permitted operations to 400 V p-p, but its lower GBW limited operation to $f \leq 40$ kHz (see Figure A-S21a in the Supporting Information). Within this frequency range, the output current linearly scaled with V_{app} (see Figure A-S21b in the

Supporting Information). Actual performance was tested by injecting 100 μM KCl into a water carrier; the results are shown in Figure 2-5. While the signal increased monotonically up to maximum V_{app}, S/N did not actually increase past V_{app} = 150 V and actually decreased above 300 V because the background increased faster with V_{app} than did the signal; however, this may be different for other conditions.

The output currents from sine, triangle, and square wave resulting from the same $V_{app,rms}$ were compared. Especially at higher frequencies, the square wave was severely distorted through this particular set of amplifiers and produced a much lower signal. With suitable amplifiers, this is not observed.[53] No distortion was observed for the sine and triangular waves and the output currents were essentially the same.

2.5.10 Anomalous Response

A mismatch of probe frequency and R_{cell} results in anomalous response that largely stems from *i* not being a single valued function of σ at the operating frequency. Although, in our model or these specific experiments, we did not see the negative response in Figure A-S1a in the Supporting Information, we have seen this not only with commercial detectors but also with our electronics with different cell designs. It can be readily shown that minor changes in the parameters assumed can profoundly affect the results. While we incorporated the change in the solution permittivity with σ, the real part of permittivity of aqueous solutions decreases steeply with *f* (not considered here). If, in fact, C_{aq} becomes so small that it can be ignored at higher *f*, or C_I is, in fact, greater than what is being assumed (for example, if the “insulators” on the shield play a role in determining C_I, it will be higher than that computed from eq 2), there will be a

pronounced negative dip in a current (i)−σ plot. Figure 2-6a shows such behavior computed for C_l values equaling 1, 3, or 10 times that from eq 2 or for C_{aq} = 0. The location of such dips is frequency-dependent and moves to higher σ with increasing f. The obverse anomalous behavior, denoted by a peak in the current−σ relationship at very high conductance (r = 50 μm and σ >1400 μS/cm) at high frequencies (f = 1.1 MHz) has also been observed;[60] increased leakage to the shield was suggested. This behavior, namely the current response producing a peak as a function of σ, is also actually observed at very low frequencies. Probe frequencies in this region have hardly been explored previously, because the resulting currents are so low. Figure 2-6b shows how the response can change from negative to a split peak in a cell with very small l_g and no shield. Since a plot of i versus σ exhibits a maximum in the σ domain of interest, i_{max} occurs before the peak maximum, resulting in a skewed inverted W-shaped response at 50−100 Hz, to a more conventional positive response by 500 Hz. The real component of permittivity decreases as f increases;[61] this is also true for electrolytes.[62] Therefore, the dependence of the permittivity on both σ and f makes the interpretation of behavior across broad frequency ranges difficult.

2.6 Conclusions

It may be overly optimistic to hope that capacitively coupled contactless conductivity detection (abbreviated as C^{4}D) devices will henceforth be called admittance detectors. Were this so, however, the realization that it is *not* a conductivity detector would make its behavior more explicable to the user. The term will also cover other efforts where the intent of a similar arrangement is to measure capacitance;[63] however, in the presence of a significant parallel conductor, it really does not.[64] An admittance detector of the

general design discussed here produces a signal that is linearly related to σ only over a limited range of excitation frequencies and over a limited range of σ. The optimum frequency range decreases with decreasing background σ, capillary bore and increasing electrode gap; these are factors that contribute to a greater cell resistance (R_{cell}). As the optimum frequency decreases, so does the response slope ($di/d\sigma$); however, as the background current also decreases, it is still possible to achieve sensitive detection if external noise can be minimized and an adequate degree of amplification is possible. The capacitance of the solution becomes important at low σ values. The ratio of the current that is capacitively vs resistively carried *through the solution* is independent of the cell dimensions, because the conductance and capacitance scale identically. However, a change in σ or *f* can affect this ratio, because the solution permittivity is dependent on both. Generally, behavior very different from that of a conductivity detector is to be expected when σ is low and *f* is high.

Since these detectors are mostly used in separations involving sharp bands, increasing the electrode length has no advantage as long as electrode contact is good, and cast electrodes can provide this without sacrificing mobility. Long electrodes can be advantageous in measuring the bulk conductivity of low σ fluids. With regard to electrode spacing, for very low σ solutions, there is little choice but to have them as close as possible (with a shield); for higher σ solutions, reasonably close electrode spacing with a shield and high *f* operation is already justifiably the most popular mode, since greater electrode spacing may deteriorate the observed separation efficiency. In systems where a shield is not possible, low-*f* operation with the electrodes placed to

operate in the appropriate R_{cell} domain may be attractive, provided that the detection volume remains below the band volume.

The grounding shield should be thin; additional thickness has little effect on further reducing C_s but increases C_l. Capillary conduits of many other polyimide-coated fused silica (PFS) materials are commonly available today and are often less fragile and less expensive. There is only a marginal difference in performance for similar dimensions.

Perhaps the most important lesson is that a frequency which results in the greatest current from a background solution of given σ may not be the best frequency to detect small changes in σ against that background; despite a high current *i* (which also increases background noise), d*i*/dσ may be too small to be useful.

2.7 Acknowledgements

This chapter has been reprinted with permission for Min Zhang, B. N. Stamos, N. Amornthammarong, and P. K. Dasgupta. Min Zhang, Brian N. Stamos, Natchanon Amornthammarong, and Purnendu K. Dasgupta “Capillary Scale Admittance Detection.” Anal. Chem., 2014, 86 (23), pp 11538–11546.

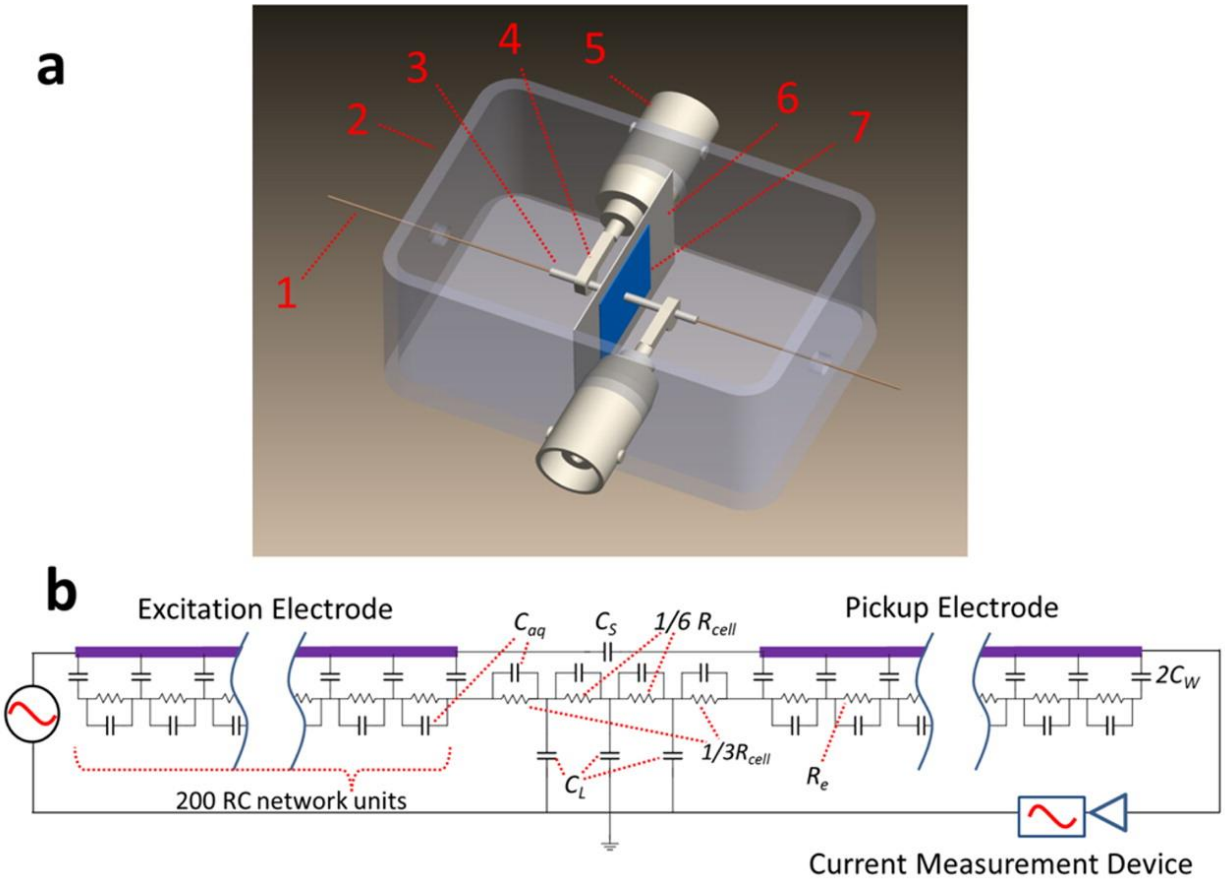

Figure 2-1. Detection cell representation and diagram.
(a) Detection cell configuration [legend: 1, capillary; 2, grounded metal box; 3, electrode cast by Woods metal alloy; 4, crimp-snap connectors; 5, BNC connector; 6, grounded Faraday shield; and 7, adhesive paper tape for insulation]. (b) Equivalent circuit [legend: R_e, segmented solution resistance; R_{cell}, interelectrode resistance; C_W, wall capacitance; C_S, stray capacitance; C_L, leakage capacitance; and C_{aq}, aqueous solution capacitance]. In panel b, only 12 units of R_e and C_W were shown to simplify the drawing; 400 segments were used in the model.

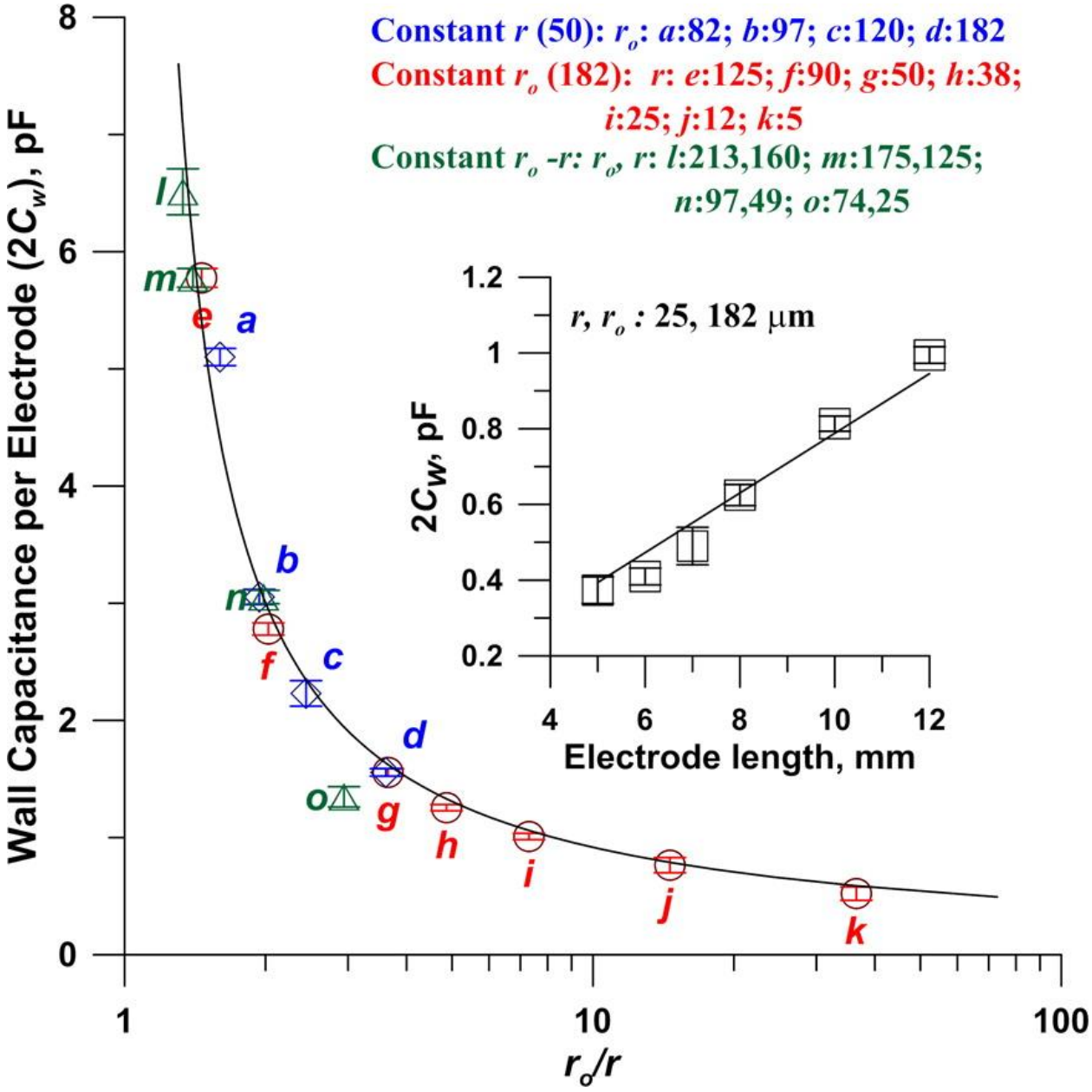

Figure 2-2. Wall Capacitance versus electrode length.
Calculated (solid line) and measured (point) wall capacitance versus r_0/r and electrode length (inset). Legend: (○) r_0 = 182 μm; (◇) r = 50 μm; (△) $r_0 - r$ = 50 μm. Capillary filled

with Woods metal; sine wave, 27 V p-p; f = 1–50 kHz; l_g = 5 mm; l_e = 10 mm; t_e = 0.13 mm.

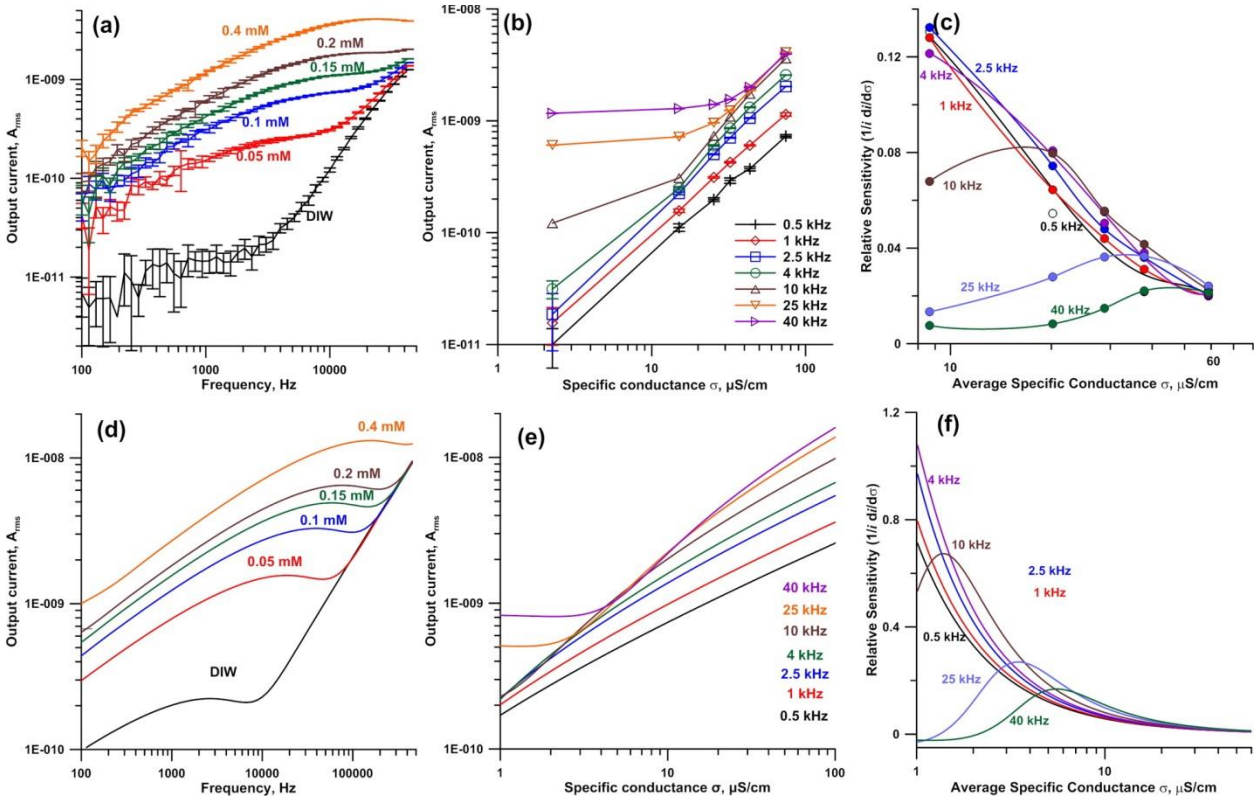

Figure 2-3. (a) Current–frequency plot, (b) calibration plot, (c) slope of the calibration curve, and (d–f) corresponding modeling data
r_o = 182 μm, r = 7.5 μm. Note logarithmic axes for all panels except panels (c) and (f).

Sample, KCl solution; sine wave 27 V p-p; l_g = 0.4 mm; l_e = 10 mm; t_e = 0.13 mm; for deionized water (DIW) in model, σ = 1 μS/cm.

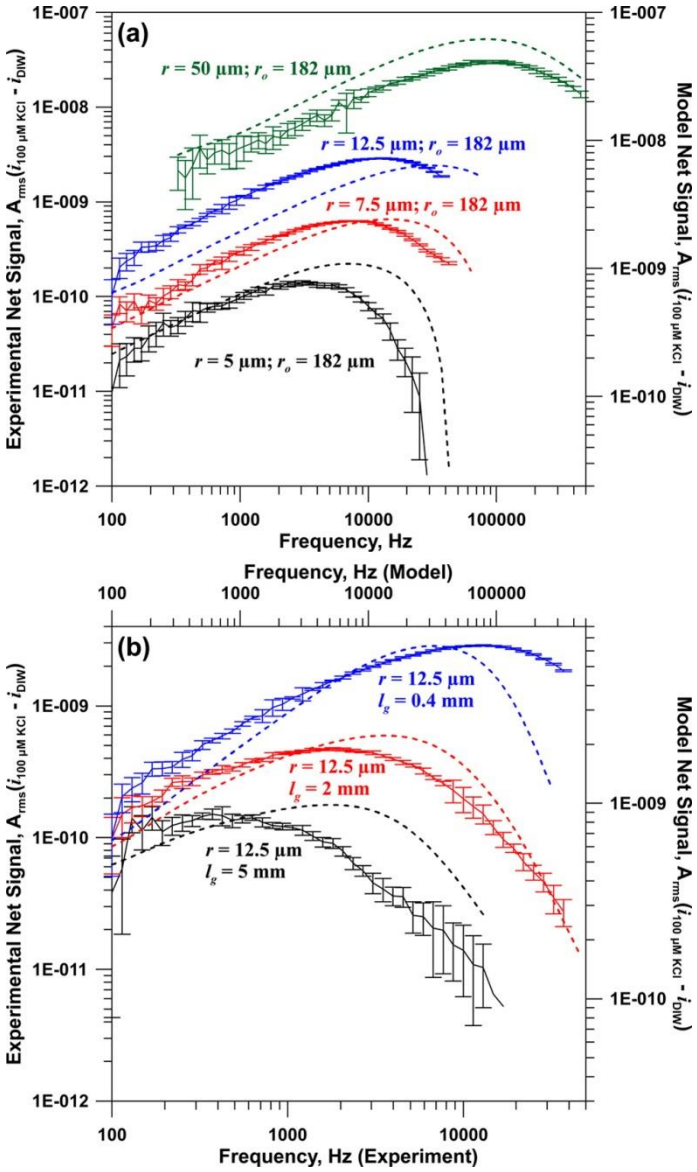
(a)
r = 50 µm; r_o = 182 µm
r = 12.5 µm; r_o = 182 µm
r = 7.5 µm; r_o = 182 µm
r = 5 µm; r_o = 182 µm
Experimental Net Signal, A_rms(i_100 µM KCl - i_DIW)
Model Net Signal, A_rms(i_100 µM KCl - i_DIW)
Frequency, Hz
Frequency, Hz (Model)
(b)
r = 12.5 µm
l_g = 0.4 mm
r = 12.5 µm
l_g = 2 mm
r = 12.5 µm
l_g = 5 mm
Frequency, Hz (Experiment)

Figure 2-4. Experimental and modeled net response to 100 μM KCl with variations in (a) r (l_g = 0.4 mm) and (b) l_g; for both plots, r_o = 182 μm.
Other conditions are as described for Figure 3.

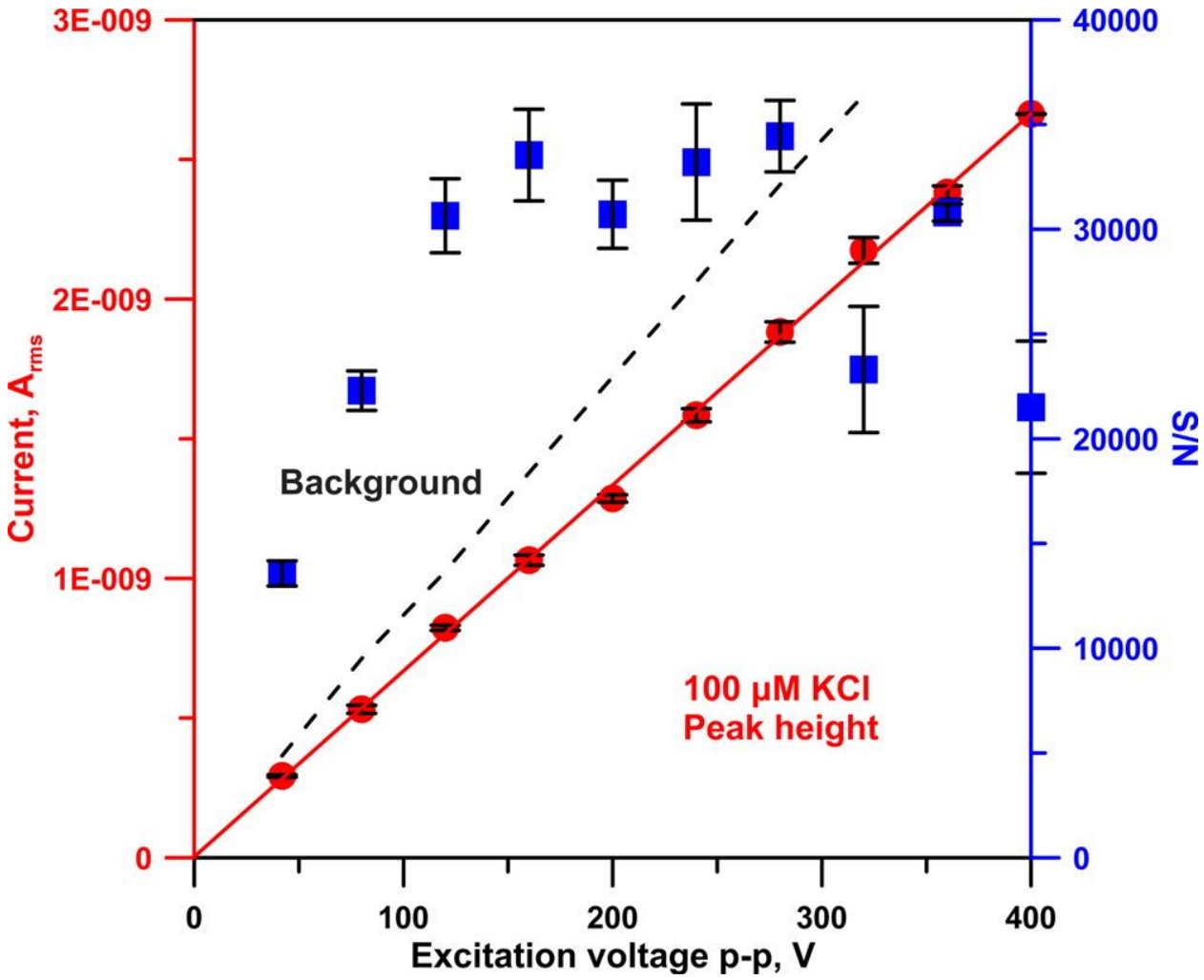

Figure 2-5. Effect of V_{app} on the peak height (circles, best linear fit shown as the solid red line), background (dashed line), and S/N (squares).
[Conditions: r = 7.5 μm, r_o = 170 μm, PMMA; triplicate injection of 0.11 nL 100 μM KCl;

injector to detector distance, 37 cm; carrier: DIW, 32 nL/min. f = 500 Hz. Noise is taken

to be the standard deviation of a 30-s baseline signal acquired at 10 Hz.

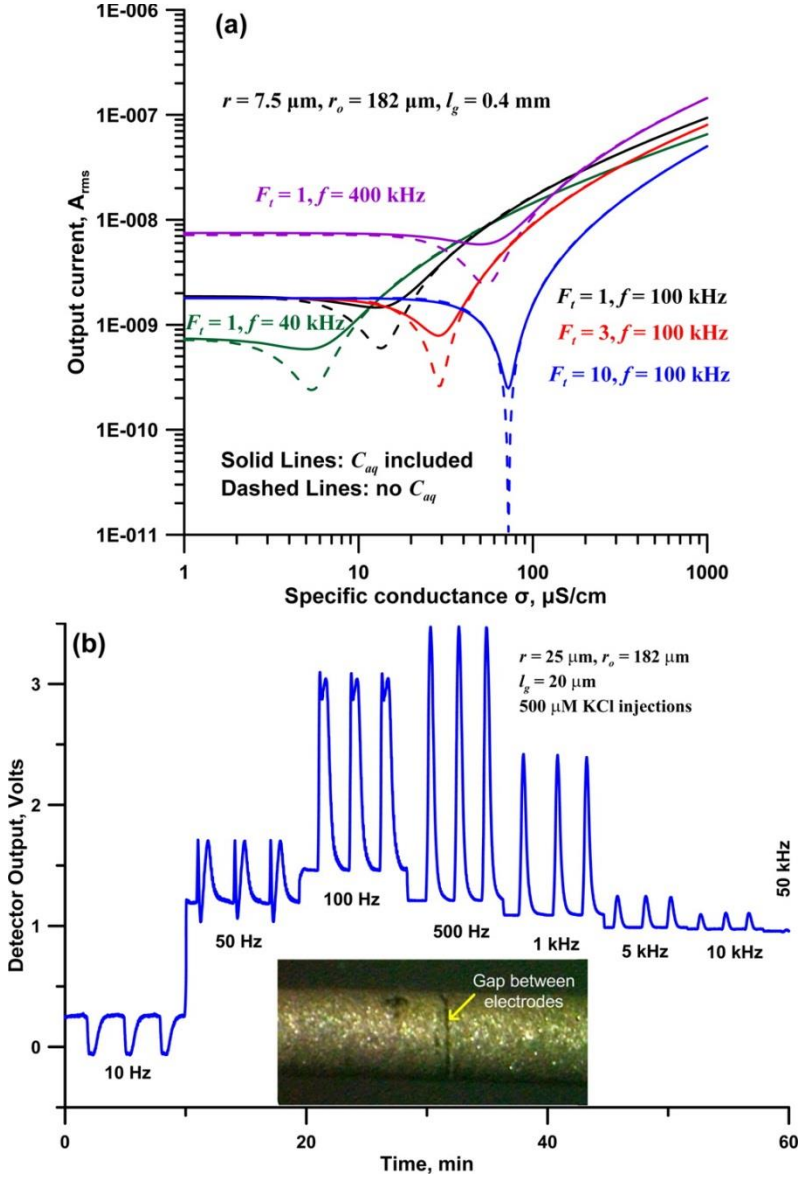

Figure 2-6. (a) Anomalous behavior, as depicted by simulations. (b) Anomalous behavior is also observed for cells with very small l_g values.
Solid lines represent the base case (F_t = 1), f = 40, 100, 400 kHz, and 3 and 10 times the base value of C_l, f = 100 kHz. Dashed lines represent data for C_{aq} = 0. Other conditions are as described for Figure 1-3. (b) Anomalous behavior is also observed for cells with very small l_g values. The cell was constructed by painting a 5-cm length of the

capillary with conductive silver ink. After drying, the coating was scored with a scalpel under a microscope. No shield was used. The response passes through zero somewhere between 10 Hz and 50 Hz.

Chapter 3 Admittance Detector for High Impedance Systems. Design and Applications.

Min Zhang†, Brian N. Stamos†, Purnendu K. Dasgupta†*

†Department of Chemistry and Biochemistry, The University of Texas at Arlington, Arlington, TX 76019-0065

3.1 Abstract

We describe an admittance detector for high impedance systems (small capillary bore and/or low solution specific conductance). Operation in the low frequency range (≤1 kHz, much lower than most relevant publications) provides optimum response to conductance changes in capillaries ≤20 μm in bore. The detector design was based on studies described in a preceding companion paper (Zhang, M.; Stamos, B. N.; Amornthammarong, N.; Dasgupta, P. K., preceding paper in this issue). The highest S/N for detecting 100 μM KCl (5.5 μM peak concentration, ~0.8 μS/cm) injected into water flowing through a capillary of 7.5 μm inner radius (*r*) was observed at 500-750 Hz. A low bias current operational amplifier in the transimpedance configuration permitted high gain (1 V/nA) to measure pA-nA level currents in the detection cell. Aside from an oscillator, an offset-capable RMS-DC converter formed the complete detection circuitry. Limits of detection (LODs) of KCl scaled inversely with the capillary cross section and were 2.1 and 0.32 μM injected KCl for *r* = 1 and 2.5 μm capillaries, respectively. Used as a detector on an *r* = 8 μm bore polymethylmethacrylate capillary in a split effluent stream from a suppressed ion chromatograph, the LOD was 27 nM bromide (V_{ex} 22 V p-p), compared to 14 nM observed with a commercial bipolar pulse macroscale conductivity detector with an actively thermostated cell. We also show applications of the detector in electrophoresis in capillaries with *r* = 1 and 2.5 μm. Efficient heat dissipation permits high concentrations of the background electrolyte and sensitive detection because of efficient electrostacking.

3.2 Introduction

Separations in the capillary scale have many advantages.[65] The median hydraulic diameter for such operations is continually decreasing. In capillary electrophoresis (CE), tubes of inner radius (r) <12.5 μm are very rarely used,[66] even though it has long been known that deleterious effects of Joule heating effectively decreases with decreasing i.d.[67] and higher separation efficiencies are attained.[2] Reducing column i.d. in liquid chromatography is also beneficial.[68] In particular, open tubular chromatography (OTC) must be conducted in small i.d. capillaries.[69] In a following companion paper, we describe the merits of ion chromatography using latex-coated polymethylmethacrylate (PMMA) OTC ion exchange columns[70] with r = 5-10 μm using a detector similar to that described herein.[71]. Using labeled analytes and a confocal laser induced fluorescence detector, separations of proteins[72] and DNA[73] in r = 1 μm bore columns were demonstrated. Such specialized detection is not attractive for routine analysis. From the beginning, the vast majority of other reports on separations in sub-25 μm bore capillaries have relied on electrochemical detection;[74-7576] this too is not generally applicable. UV-Visible optical absorption detection, commonly performed on-column in the capillary scale using the radial path, rapidly loses its charm with decreasing capillary bore, particularly as the effective light path length tends to be even shorter than the capillary diameter.[2] In dealing with increasingly smaller bore capillaries, arguably the biggest challenge is sensitive detection.

On-column admittance measurement through two exterior electrodes, separated along the column axially, commonly called capacitively coupled contactless conductivity detection (C^4D), has gained in popularity since its introduction in the late 90's.[77,78]

Typically mid-high frequency AC (~10-1000 kHz) is applied to one electrode, and is picked up by the second electrode after being capacitively coupled through the wall to the solution inside, amplified and rectified. As may be expected, an increase in the excitation voltage, without any attendant increase in the noise, can improve the S/N.[79,80] Two commercially available detectors, for example, permits selectable variable frequency operations in the respective ranges of 38-612 and 50-1200 kHz and applied voltages (V_{app}, p-p) of 3-80 and 2-100 V. Recognized advantages of a C^4D, beyond being simple and inexpensive, include facile placement, noninvasive monitoring without galvanic contact and hence no possibility of electrode deterioration.[81,82]

However, no presently described C^4D works meaningfully when the cell impedance is high (whether because r, or the specific conductance of the solution, σ, is small; especially when both are small). The impetus behind this work is that we are interested in extending OT ion chromatography to the suppressed domain and an appropriate detector is needed; Several efforts have already been made in making microscale suppressors;[83-86]

Theoretical simulations and experimental studies described in the preceding companion paper[87] clearly established that for high values of the cell resistance (R_{cell}), for an admittance detector to significantly respond to changes in the solution conductance, the probe frequency must be relatively low. We describe here the design and performance of an admittance detector designed to respond to changes in conductance at high impedance levels and apply this to capillaries of r = 1-10 μm.

3.3 Experimental Section

3.3.1 Detector

The detector is schematically shown in Fig. 1. The basic scheme is the same as that described,[23] except that the single chip fixed gain transimpedance amplifier (TIA, OPA128LM, www.ti.com) was located within the metal box immediately next to the electrodes on its own circuit board with appropriately guarded inputs as recommended by the manufacturer. Shielded cables and SMB or BNC connectors were used throughout. As the current represents a very high impedance source, a high gain TIA arrangement is possible provided the amplifier has a very low bias current (<0.1 pA for this device; manufacturer suggested circuits routinely use transimpedance gains of 1-100 V/nA, feedback resistor, $R_f = 10^9$-10^{11} Ω) for this device. For a dedicated system one stage amplification is sufficient; however, using R_f = 10-1000 MΩ and secondary amplification may provide more flexibility. Resistors ≥1 GΩ were of the glass-sealed type. With a high source impedance, the TIA configuration permits a square wave to be used without distortion across the entire frequency range of present interest (≤ 2 kHz, except as stated), unlike the previous arrangement where a much broader frequency range was studied.[23] At the same amplitude, compared to sine or triangular waves, a square wave provides the largest rms voltage and hence the largest output current. As this was also experimentally observed, only square wave excitation was used in this work.

The excitation source was either (a) a bench top function generator (4011, www.bkprecision.com), boosted in some experiments to higher voltages,[23] or (b)a 555

timer (NE555N, www.st.com) based oscillator, powered by two 9 V batteries to test for portable operation. Even though cast metal electrodes[23] was previously observed to provide superior results compared to tubular stainless steel electrodes, we used the latter (0.4/0.64/7 mm i.d./o.d./length) to conform to common practice. For r_o = 75 μm capillaries, a fused slica sleeve (r =90 μm r_o = 180 μm) was first put in the capillary and the same steel electrodes were used. A paper insulated mu-metal (0.13 mm thick) Faraday shield with a 0.4 mm aperture for the capillary passage separated the electrodes (0.4 mm apart).[23] All easily movable objects within the metal enclosure were affixed with hot-melt adhesive.

Secondary amplification (10-1000x) was provided by another operational amplifier (TL082N, www.ti.com). Unless otherwise stated, overall gain was 1-10 V/nA. The ac signal was integrated by a RMS-DC converter (AD536A, www.analog.com), and the data acquired after low pass filtration (time constant 0.1 s) by a nominally 22 bit low-cost data acquisition card (EMANT300, www.emant.com) at 10 Hz. Effectively the noise level of the card was 2 μV and in the absence of secondary amplification was often the limiting factor in observed noise. The capillary detection cell and the TIA were kept in one metal enclosure, all other components in a second one. Total average parts cost to build a complete detector including power supply ranges from US $100-$200.

3.3.2 Capillary and Chemicals

See preceding paper [23] for vendors. All chemicals were of reagent grade and used without purification. Anion standards were prepared in sodium or potassium form. All solutions were filtered (0.2 μm) before use.

3.3.4 Open Tubular and Macroscale Ion Chromatography

The nonsuppressed OTIC system and arrangement are described in detail in the following paper.[7] Flow injection also utilized the same injection technique. Suppressed IC was conducted on a ICS2000 (www.dionex.com), equipped with a 10 µL injector, 2x50-2x250 mm AG21-AS21 columns, an ASRS 300 suppressor, a CRD200 CO_2 removal device, an actively thermostated DS3-1 detector cell and a CD25 conductivity detector. Electrogenerated KOH (3 mM) was used as the eluent at 0.3 mL/min. A micro-tee was placed prior to the conductivity detector for diverting a small part of the flow through a 16 µm i.d x 340 µm o.d x 26 cm length PMMA capillary that was monitored with the present detector. As the detection limits were very low, we only checked the behavior of a single analyte ion, bromide, not prone to contamination errors. Except in the IC comparison experiment where the admittance detector was housed within the thermally insulated column enclosure, all other experiments were carried on the open benchtop.

3.3.5 Capillary Electrophoresis

A 0-30 kV power supply (CZE2000, www.spellmanhv.com) was used in the –HV mode. The capillary was preconditioned by with 1 M NaOH for 30 min, deionized water for 30 min prior to flushing with the BGE, prepared from histidine (His) and sodium acetate (NaOAc)/acetic acid (HOAc). Time-controlled hydrostatic pressure-based injection was used.

3.4 Results and Discussion

3.4.1 Optimum Frequency

To confirm that lower frequencies than commonly used will also be preferred in the present detector, we tested 110 pL 100 μM KCl injections into a r= 7.5 μm (outer radius r_o = 170 μm) poly(methylmethacrylate) (PMMA) with a deionized water (DIW, σ = 0.5 μS/cm) carrier. The dispersed peak concentration was 5 μM (~0.75 μS/cm). Peak height ($i_{peak} - i_{bgnd}$), background current (i) signal, background noise (taken as the standard deviation of the baseline over a 30 s period) were measured in the range 0.1-100 kHz (n=3). The TIA conversion gain was tested at 10^7, 10^8, 10^9, and 10^{10} V/A while secondary amplification varied from 10^3, 10^2, 10 and 1 (no secondary amplifier), to maintain an overall transimpedance amplification in the range of 1-10 V/nA. Noise did vary some with different resistors and overall gain, but under all conditions, the best S/N was observed at frequencies < 1 kHz. We observed that higher TIA gain was better; no secondary amplification and a TIA gain of 1 V/nA provided the lowest noise and the best S/N. However, the degradation of performance with secondary amplification was modest. At f = 250 Hz, $V_{app,p\text{-}p}$= 22 V, with a TIA gain of 1 nA/V, the noise and S/N of were 432±79 μV and 2270±415, respectively, while with a TIA gain of 10 V/μA and 100x secondary amplification, the corresponding values were ~4x worse, 1740±21 μV and 632±79. The data for the latter case are shown in Fig. 2. The background signal increased monotonically with increasing frequency and dropped abruptly at ~>10 kHz when the gain bandwidth product (GBW) of the overall setup was exceeded. Noise was the highest at 100 Hz (3.3 mV) thereafter remained almost constant at ~2 mV up to ~1 kHz, dropping below 1 mV at higher f, reaching 0.7 mV by 15 kHz. Maximum peak

heights were reached within the range of 250 to 750 Hz. The response actually became negative at frequencies between 5-15 kHz.

3.4.2 Flow Injection and Chromatography in r = 1-2.5 μm Capillaries

Figure 3-3 shows responses to various concentrations of 20 pL of KCl sample injected into DIW flowing through a polyimide-coated fused silica (PFS) capillary (r = 2.5, r_o= 182 μm) with the detector located 18 cm from the injection point. Interestingly, initial injections on the first several samples produced a split peak response (see inset). In such small r capillaries, mass transfer to the wall is efficient and part of the K^+ is exchanged for H^+ in the silanol groups on the wall, until the wall is fully converted to the K^+-form, when "normal" peaks appeared. Based on the observed S/N ratio at 50 μM, the calculated S/N=3 LOD is 0.32 μM but we made no efforts to inject sample concentrations closer to the putative LOD. In addition to the difficulty of reliably preparing standards at that level, it will be apparent from Figure 3-3 that baseline drift, in the absence of any thermostating, will be the limiting factor. The signal was linearly proportional to the concentration (Signal, mV = -(2.51±1.84) + (0.195±0.011) C, □M; r^2 = 0.9907) in the 0-0.3 mM range. The linearity did deteriorate at higher concentrations.

Surprisingly, short-term drift in even smaller capillaries (r = 1 μm, r_o = 75 μm) was relatively lower. Had we put the detection electrodes directly on the smaller r_o capillaries without using sleeves, the S/N may have been even better. Even though only 0.6 pL was injected, we conservatively estimate that the S/N=3 LOD was 2.1 μM. Linear correlation was observed in the 0-200 μM range:

Detector output, mV = (0.048±0.049) + (8.13±0.43)C, mM, r^2=0.9945 …(1)

The linearity deteriorated to r^2~<0.97 by C = 300 μM.

Wall functionalization to carry out chromatography in capillaries of r= 1 μm is difficult. We noted however (as with split peaks from initial KCl injections) that silanol groups on the wall may provide sufficient capacity to do cation exchange chromatography. Figure 3-4 shows two examples of rudimentary chromatographic separations using r= 1 μm capillaries. Figure 3-4a shows an injection of 200 μeq/L each Li^+, Cs^+ and Ca^{2+} using 50 μM tartaric acid. The Li^+ response is hidden within the larger system peak (two system peaks are present, one from a pH mismatch and the second from the large excess of total cation equivalents). Figure 3-4b shows the use of LiOAc as eluent for eluting Na^+ and K^+; both respond with positive peaks with K^+ responding more than Na^+, due to the much greater mobility difference with Li^+. The peaks were broader than we expected – several factors likely play a role: (i) dispersion at the injector interface at these dimensions, (ii) inadequate eluent capacity, at least in Fig. 4a, and perhaps most importantly, (iii) even 1.25 pL, cell volume is 4x larger than the injection volume in Fig. 4a.

Nevertheless, encouraged by these results into territory thus far unexplored by admittance detectors, we attempted even smaller conduits. The manufacturer provided experimental samples of capillaries stated to be r =0.5 ± 0.5 μm; scanning electron micrography of portions we studied showed average radius of these segments to be around 150 nm. Unfortunately we were not able to establish flow though these capillaries at pressures compatible with our injection system.[7]

3.4.3 Open Tubular Nonsuppressed Ion Chromatography

Admittance detection was used in an OTIC system to which a separate article is devoted. Here we therefore provide only one example. 1 mM sodium benzoate ($\sigma \cong 83$ μS/cm) was used as eluent in a PMMA capillary (r = 8 μm; r_o = 170 μm). Optimum S/N in this case should be at somewhat higher f than cases discussed above; this was observed. For all the peaks, the S/N maximizes or reaches a plateau at 1000 Hz (Figure 3-5); frequencies >1500 Hz were therefore not studied.

3.4.4 Admittance Detection for Suppressed IC

Applying admittance detection to macroscale suppressed IC requires operating with a highly resistive medium ($\sigma \leq 1$ μS/cm). Detection limits in suppressed IC is often below the 100 nM range – at this level there are many impurities in standards made under non-cleanroom conditions, chloride and carbonate being the most common. We chose bromide as the test analyte to determine the LOD. The admittance detector response ($V_{app,p\text{-}p}$ = 22 V, f = 500 Hz) is shown in Figure 3-6. The right panel indicates blank subtracted magnification of the bromide peak. The LOD is estimated to be 27 nM, relative to 14 nM estimated for the macroscale commercial detector. Because the LOD was controlled more by fluctuations in the baseline than detector noise, increasing $V_{app,p\text{-}p}$ to 160 V did not significantly improve the LOD (22 nM). It is important to note that these are injected concentrations; the actual peak concentration is likely approximately an order of magnitude lower. Also noteworthy is the detection volume of the admittance detector, including the electrode length (as band volume is greater than this), was ~2.6 nL, some 400x smaller than the comparison benchmark. The admittance detector output exhibited excellent linear correspondence with the IC system

conductance detector output in the 0-6300 nS/cm range ($r^2 \geq 0.9999$) and the data are directly reported in nS/cm on this basis. The calibration equation (n=8) was:

Detector output, nS/cm = (62.12±0.33) *C*, μM + (5.7±13.5), (r^2=0.9998) …(2)

for $C \leq 100$ μM. The response slope distinctly decreased at injected concentrations greater than 0.1 mM along with r^2 (respectively deteriorating to 0.9933, 0.9827, 0.9784 and 0.9726 by *C* = 250, 500, 750, and 1000 μM) revealing the Achilles heel of the technique, limited linearity. Linearity extended to higher concentrations with a higher probe frequency but at the expense of increasing the limit of detection. Autoranging detection where probe frequency will automatically and seamlessly switch at desired conductance crossover points is readily envisioned and will greatly enhance the linear dynamic range.

3.4.5 Capillary Electrophoresis

Admittance detection has been widely used in CE but not in capillaries with $r \leq 2.5$ μm; so we limited our studies to these. Typical output of anion separation is shown in Fig. 7. Given the injection volumes, the responses in the *r* = 2.5 μm capillary should have been significantly greater compared to the *r* = 1 μm capillary but the probe frequency was maintained the same; the optimum *f* would have been higher than for the larger capillary. The use of a less than optimum probe frequency for the larger capillary also results in a minor amount of peak overshooting[88] (note the dips before and after the sulfate peak in Fig. 7a). The noise was also higher than that in the smaller capillary. Interestingly, while the migration sequence in the larger capillary was the same as

others have reported for even larger capillaries,[89] for the *r* = 1 μm capillary, the migration sequence of nitrite and sulfate was changed. These results strongly suggest that the separation mechanism is not controlled by electrophoresis alone but some wall (chromatographic) interaction is also involved. Composition and pH dependence and the nature of the electroosmotic flow suggest that protonated histidine is sorbed on the wall. Divalent sulfate has an opportunity to interact with the wall more easily in a smaller capillary.

Increasing the BGE concentration permits efficient sample stacking and also permits the analysis of high ionic strength samples, e.g., seawater.[2,90] The main drawback of a high BGE concentration is temperature rise from Joule heating; heat dissipation is much more efficient in smaller capillaries. Electropherograms resulting from the addition of 0.5% and 1% (w/v) NaOAc (respectively 61 and 122 mM) to the His-based BGE are shown in Fig. 8; these were obtained at 12.3 kHz. It is interesting that the migration time increased with increasing sample volume. An anonymous reviewer has pointed out that filling a significant portion of the capillary with increasing volumes of sample also will result in reducing the overall current (or strictly, the field strength in the principal migration length); the migration time will increase. In addition, increased retention of an ion pair at increasing electrolyte concentrations is known in many systems, e.g., with zwitterionic phases.[91]Other observations (e.g., if the BGE His concentration is increased to 60 mM or the sample concentration is increased to >1 mM, all anion migration times increase) are also consistent with this explanation.

For operation with highly conductive electrolytes as in Figure 3-8, the operating frequency was increased to 12.3 kHz. This necessitated reducing the gain on the TIA to

keep within its GBW and applying secondary amplification. As previously indicated, such arrangements decrease the S/N noise some, a TIA with a higher GBW may improve this situation.

3.4.6 Battery Powered Operation

It was of interest to determine how well the system will work if it used in a portable configuration that is battery powered. The test system used a 555 oscillator at 255 Hz, a PMMA capillary (r, r_o = 7.5, 170 μm), 0.11 nL 100 μM KCl injection, injector to detector distance 37 cm, DIW carrier flow 42 nL/min, TIA gain 10 V/μA, Secondary amplification 1000 x. The noise being taken as standard deviation of the baseline over 30 s, S/N values for the following conditions were: (a) base case: all are powered by benchtop DC supplies: 562; (b) powered by two 9 V batteries, one being shared by the 555: 337; (c) two 9V batteries powering the circuit and the 555: 767; (d) two independent pairs of 9 V batteries respectively serving the 555 and the rest of the circuit: 760; and (e) AC powered function generator, circuit powered by two 9 V batteries: 658. We conclude that no performance is lost in battery operation. We expect to describe implementation on an actual portable platform in the near future.

In summary, we have described an admittance detector that is capable of sensitive operation in very small capillaries and/or highly resistive solutions, a region that has not previously been accessible to such detectors. The circuitry is simpler than the majority of extant descriptions of such instruments. Relative to the steel tubular electrodes that were used in this paper, custom-fit cast metal sleeve electrodes described in the preceding companion paper[23] provide results even better than those described here and are recommended.

3.5 Author Information

Corresponding Author:

*Email: Dasgupta@uta.edu Fax: 817-272-3808.

Notes

The authors declare no competing financial interest.

3.6 Acknowledgement

This work was supported by NASA Grant NNX11AO66G. We thank Phillip Shelor for his assistance throughout this work. This chapter has been reprinted with permission from M. Zhang, B. N. Stamos and P. K. Dasgupta. Min Zhang, Brian N. Stamos, and Purnendu K. Dasgupta “Admittance Detector for High Impedance Systems: Design and Applications.” Anal. Chem., 2014, 86 (23), pp 11547–11553.

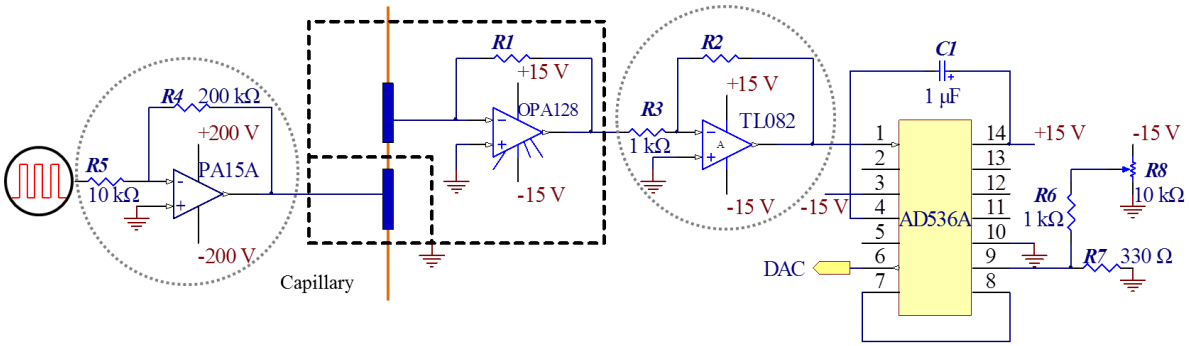

Figure 3-1. Schematic diagram of the admittance detector.

Components enclosed by light dashes are optional; those enclosed by heavy dark dashes indicate a grounded enclosure. R1: 10^6-10^{11} Ω; R2: 10^4-10^6 Ω.

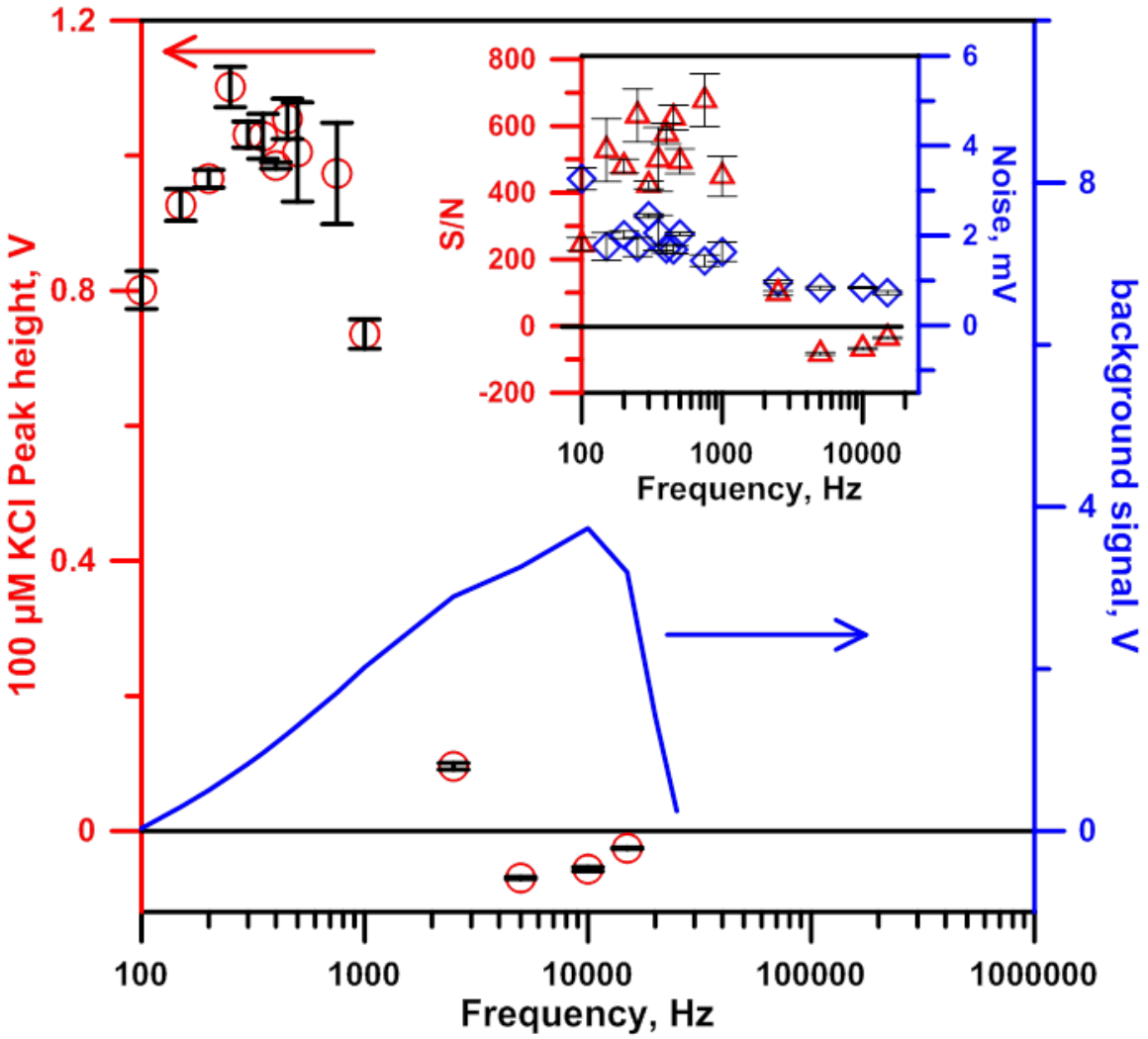

Figure 3-2. Effect of frequency to peak height (circles), baseline (solid line), noise (diamonds, insert) and signal-to-noise (triangles, insert) of KCl sample. Capillary, bare PMMA (r = 8 μm, r_o = 170 μm); injector to detector distance 37 cm; sample, 100 µM KCl; carrier, DIW; injection volume, 0.11 nL; flow rate, 42 nL/min; triplicate injection; $V_{app,p\text{-}p}$ 22 V; TIA, 10 V/μA; secondary amplification: 1000x.

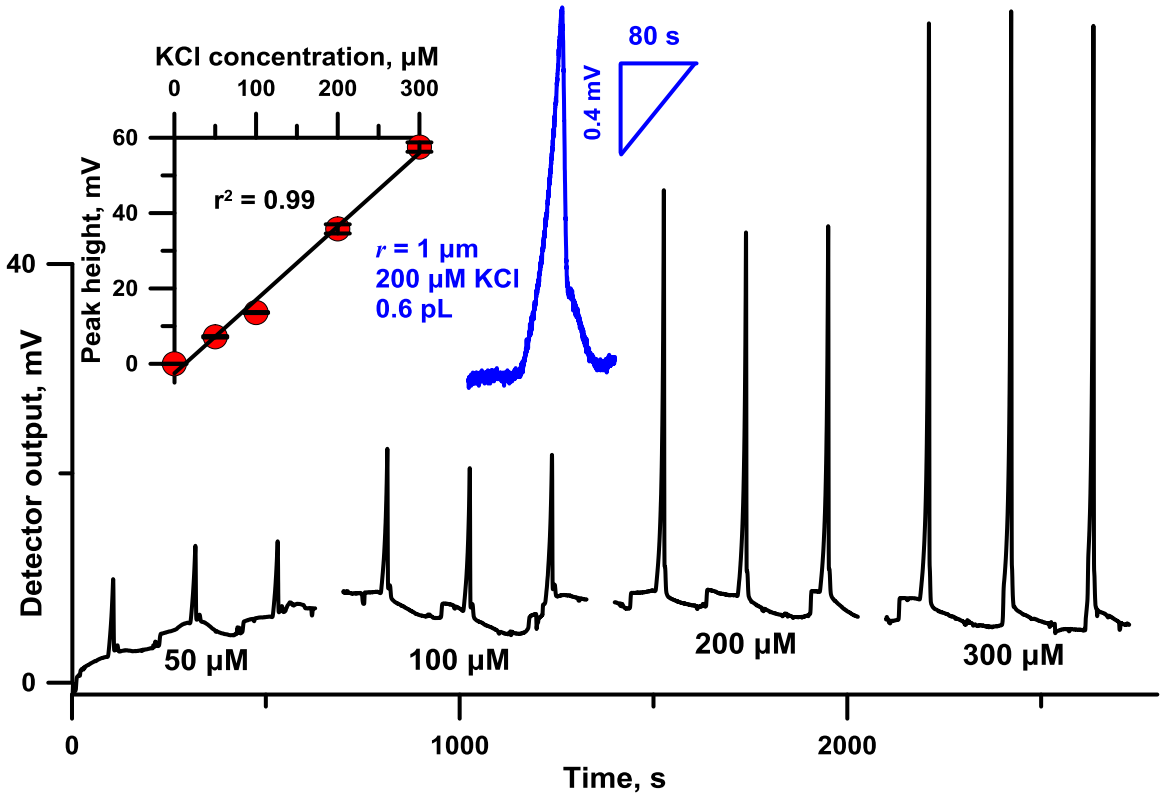

Figure 3-3. Flow Injection response in small bore capillaries (r =2.5 µm, r_o = 182 µm) capillary.

Injector-detector distance 20 cm; 20 pL KCl injection; DIW carrier, flow rate, 2.3 nL/min; $V_{app,p\text{-}p}$ 22 V, 500 Hz; TIA gain 1 V/nA, no secondary amplification. Left inset shows calibration plot; ± 1 SD shown for triplicate injection. Middle inset shows response to 0.6 pL injection of 50 µM KCl in an even smaller capillary (r =1 µm, r_o = 75 µm), injector to detector distance 7 cm, flow rate 44 pL/min. For both capillaries, the concentration at the peak apex relative to the indicated injected concentration is diluted by ~20 x

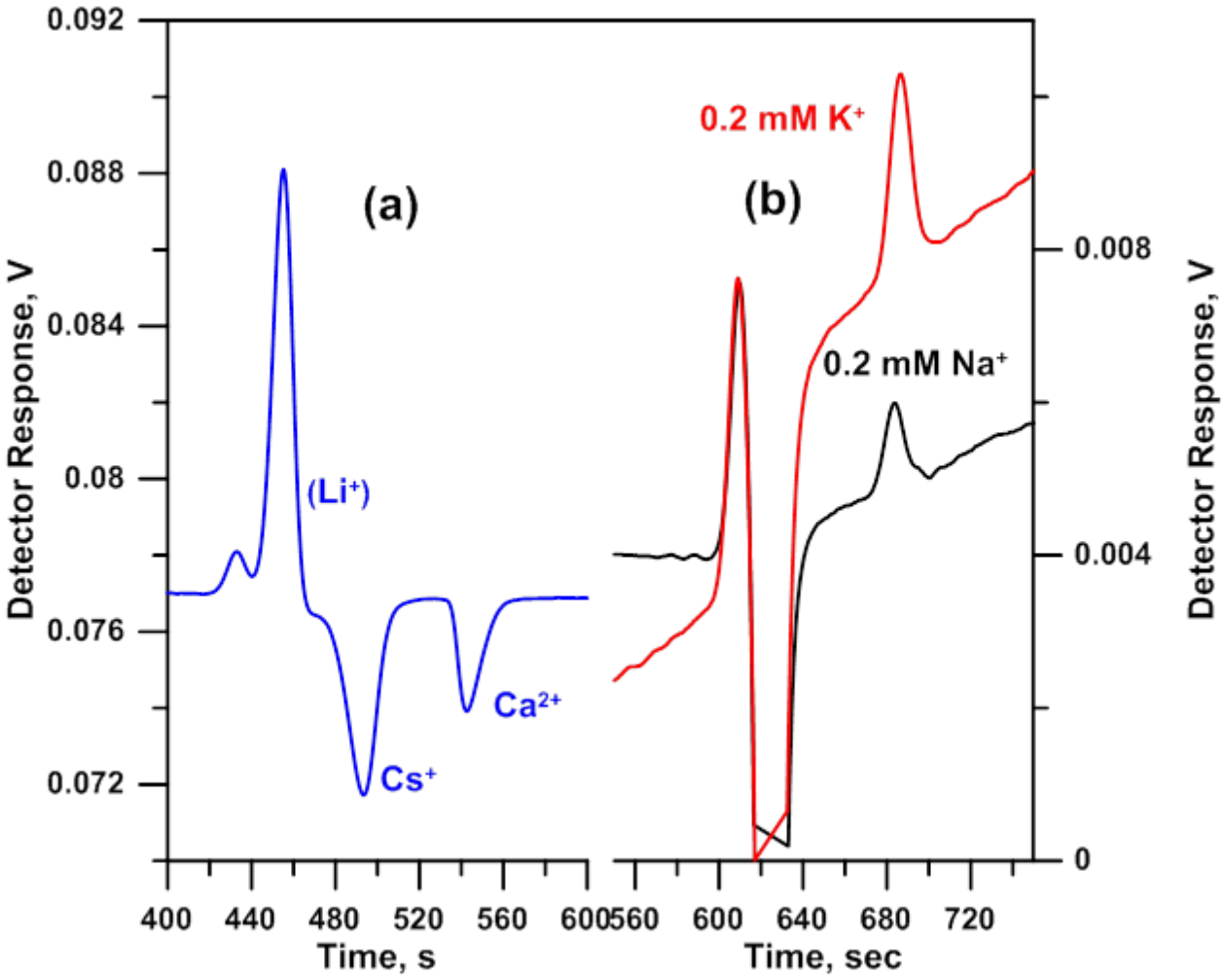

Figure 3-4. Chromatography on r = 1 μm, r_o = 75 μm unmodified polyimide coated fused silica columns.

(a) 50 μM tartaric acid eluent. 200 μM of each cation, 300 fL injected. Injector to detector distance 12 cm, 40 psi pneumatic pressure (~51 pL/min). Li^+ is barely retained and the response is hidden in the larger system peak; f = 500 Hz, $V_{app,p\text{-}p}$ =240 V. TIA gain 1 V/nA; no secondary amplification. (b) 1 mM LiOAc eluent 0.2 mM K^+ and Na^+ are separately injected. 6.9 pL injected. Injector to detector distance 26 cm, 150 psi pneumatic pressure (~83 pL/min), f = 500 Hz, $V_{app,p\text{-}p}$ =22 V. TIA gain 1 V/nA; no secondary amplification Note the much larger response from K^+ due to much greater difference in equivalent conductance, despite longer retention time. Note also the comparability in response between a and b, despite the 20x different injection volume; driven by the high mobility of H^+ and the larger V_{app} used in a. The analysis system was not thermostated, the temperature induced drift is particularly

noticeable because of the significant temperature dependence of $K_{HOAc.}$[28]

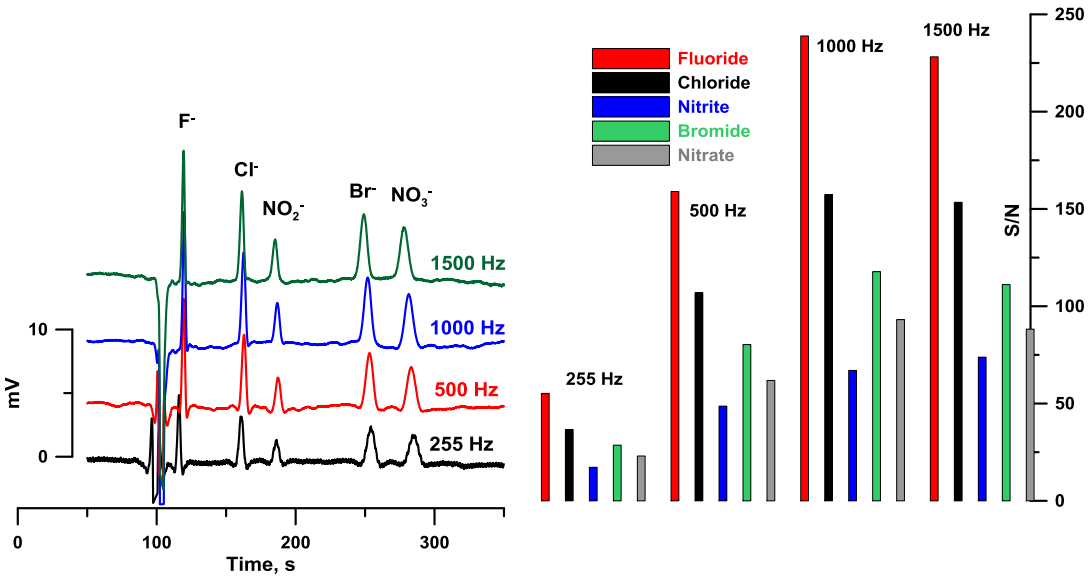

Figure 3-5. Open tubular capillary nonsuppressed ion chromatogram

r = 8 µm, r_o = 170 µm; 45 cm long, AS18 latex coated PMMA capillary; effective length 40 cm; sample, 200 µM each anion, 0.41 nL; eluent, 1 mM sodium benzoate; flow rate, 45 nL/min; $V_{app,p\text{-}p}$ 22 V; TIA 1 V/nA, no secondary amplification.

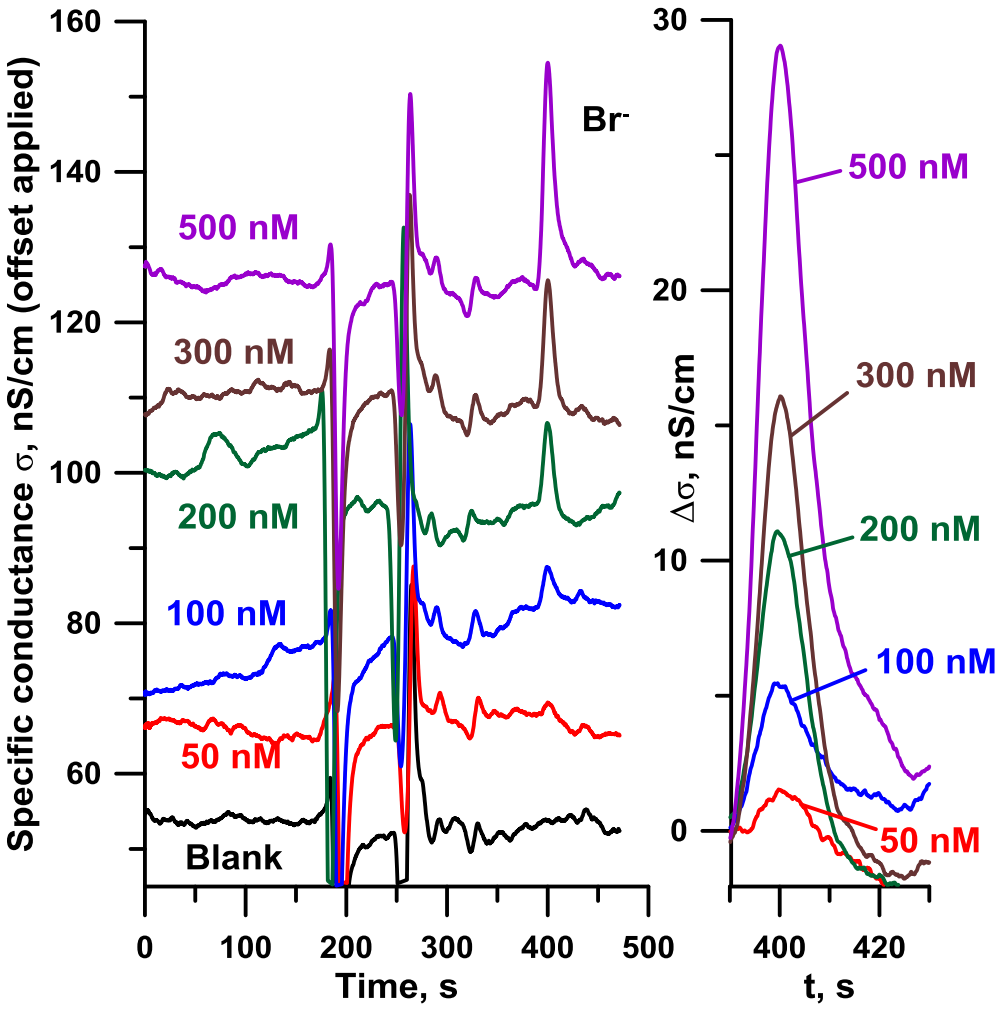

Figure 3-6. Suppressed ion chromatogram of bromide standards
Br^- elutes at ~400 s. Right magnified portion shows the blank subtracted view of the standard in the region of interest. $V_{app,p\text{-}p}$ = 22 V, f =500 Hz. TIA gain 1 V/nA; no secondary amplification.

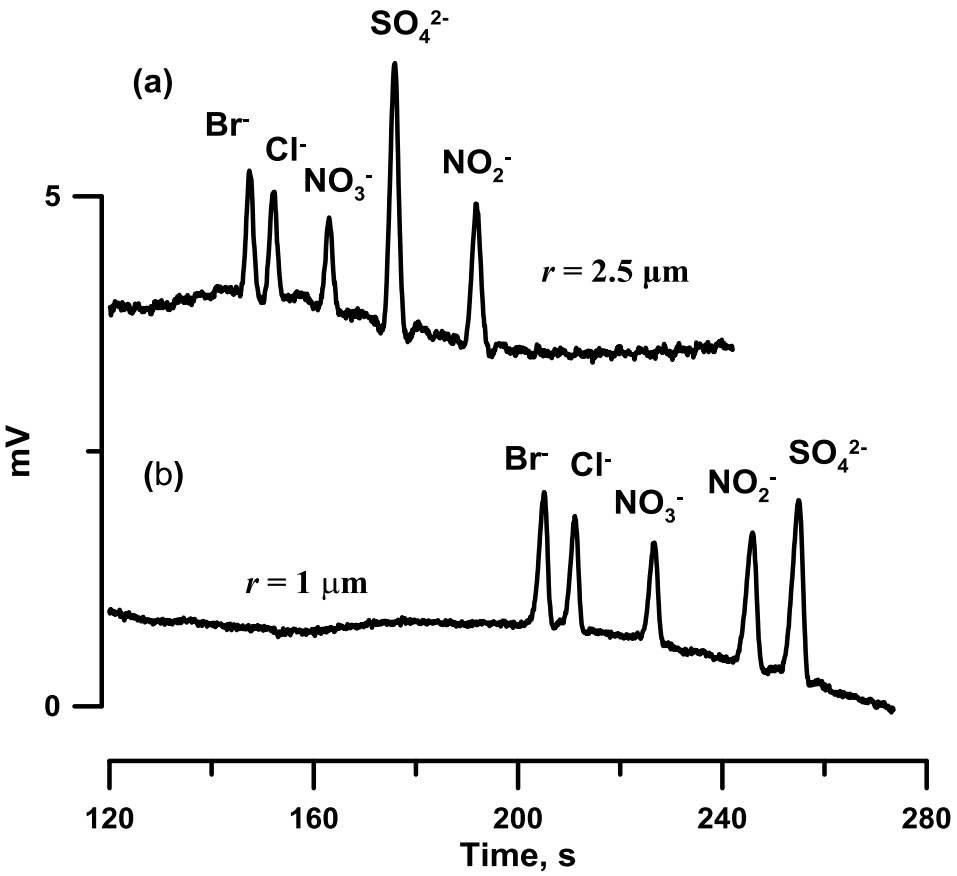

Figure 3-7. Anion electropherogram with admittance detection.
Capillary, (a) *r, r_o* = 2.5 μm, 182 μm, (b) *r, r_o* = 1 μm, 75 μm, each 50 cm length, 42 cm separation length. Sample, 100 μM NO_2^-, 50 μM Cl^-, Br^-, NO_3^- and SO_4^{2-}; BGE, 12 mM His adjusted to pH 4 with HOAc; injection: (a) 10 cm for 30 s; injection volume(length), 0.9 pL(46 μm) (b) 46 fL(7.4 μm) for 2 μm I.D.; Separation voltage: (a) -20 kV, (b) -15 kV. $V_{app,p\text{-}p}$ = 22 V; *f* = 1 kHz. TIA gain 1 V/nA; no secondary amplification.

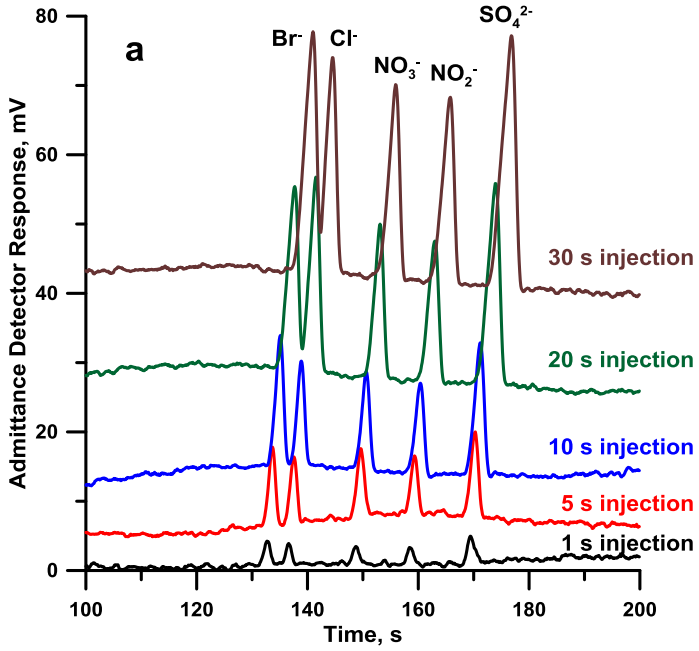
a
Br-
Cl-
NO3-
NO2-
SO4 2-
30 s injection
20 s injection
10 s injection
5 s injection
1 s injection
Admittance Detector Response, mV
Time, s
0
20
40
60
80
100
120
140
160
180
200

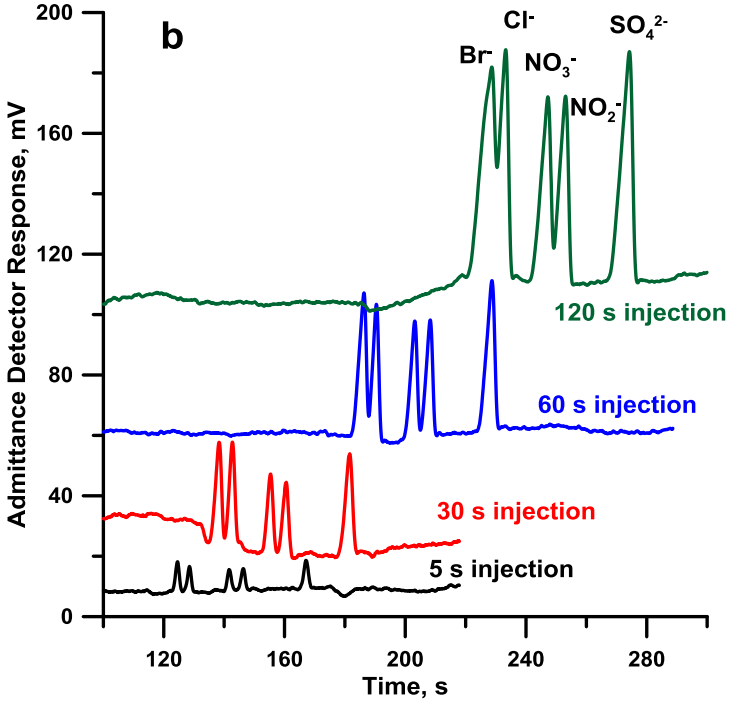
b
Cl-
Br-
NO3-
NO2-
SO4 2-
120 s injection
60 s injection
30 s injection
5 s injection
Admittance Detector Response, mV
Time, s
0
40
80
120
160
200
120
160
200
240
280

Figure 3-8. Electropherogram of anions with BGE of (a) 0.5% NaOAc + 12 mM His, (b) 1.0% NaOAc + 12 mM His, each adjusted to pH 4 with HOAc.
Capillary: r, r_o = 2.5, 182 µm; 35 cm separation length; sample, 200 µM for all anions; hydrodynamic Injection at 50 psi; injection volume(length): 11 pL(0.55 mm), 55 pL(2.75 mm), 110 pL(5.5 mm), 215 pL(11 mm), 325 pL(16.5 mm), 650 pL(33 mm) and 1300 pL(66 mm) for 1,5, 10, 20 30, 60 and 120 s injections, respectively; separation voltage, -20 kV; $V_{app,p-p}$22 V, f 12.3 kHz, TIA 1 V/µA, secondary amplification: 100x.

Chapter 4 An Open Tubular Ion Chromatograph

Bingcheng Yang,[a,b⊥] Min Zhang,[a⊥] Tinakorn Kanyanee,[a,c⊥] Brian N Stamos, and Purnendu K. Dasgupta[a*]

[a] Department of Chemistry and Biochemistry, The University of Texas at Arlington, Arlington, Texas 76019-0065; [b]School of Pharmacy, East China University of Science and Technology, Shanghai 200237, China; [c]Department of Chemistry, Chiangmai University, Chiangmai 50200, Thailand

4.1 Abstract

We describe an open tubular ion chromatograph (OTIC) that uses anion exchange latex coated 5 μm radius silica and 9.8 μm radius polymethylmethacrylate tubes and automated time/pressure based hydrodynamic injection for pL-nL scale injections. It is routinely possible to generate 50,000 plates or more (up to 150,000 plates/m, columns between 0.3-0.8 m have been used) and as such fast separations are possible, comparable to or in some cases better than the current practice of IC. With an optimized admittance detector, nonsuppressed detection permits LODs of sub to double digit μM for a variety of analytes. However, large volume injections are possible and can significantly improve on this. A variety of eluents, the use of organic modifiers and variations of eluent pH can be used to tailor a given separation. The approach is discussed in context of extraterrestrial exploration, especially Mars, where the existence of large amounts of perchlorate in the soil needs to be confirmed. These columns can survive drying and freezing and small footprint, low power consumption and simplicity makes OTIC a good candidate for such a mission.

[⊥]These individuals had equal contributions to this work

4.2 Introduction

The need for low power, small footprint, light weight, low consumable/sample usage analytical instruments is arguably nowhere more important than in planetary explorations. Wet analysis have generally been absent in lunar or Mars rovers/landers, with the exception of the ion selective electrode (ISE) based "Wet Chemistry Laboratory" (WCL) deployed on the Phoenix Mars lander.[92] While gas chromatography in some form has been repeatedly used in such missions, liquid chromatography has been notably absent. There are some unique constraints for extraterrestrial instruments that stem from limited availability of power. Curiosity, the present Mars rover, for example, has a large suite of instruments but total power of ~125 W from a thermonuclear battery. The rover has limited speed both because of power and difficult terrain. As there is limited utility of analyzing soil/samples in one location, most instruments will sit idle most of the time. With the Martian ambient temperature between -100 to -15 °C, liquid chromatography presents some obvious problems if at least the column needs to be heated even when it is not in operation.

Nevertheless, the only one set of wet analysis data generated by in-situ wet analysis of Martian soil extracts has been singularly provocative as the findings suggest that perchlorate constitutes as much as 0.4-0.6% by weight of the soil.[93,94] This has many important ramifications. One driving force behind space exploration is the quintessential curiosity if there is extraterrestrial life. For Mars, perhaps it has now reduced to the question if conditions conducive to life existed, if at the present time there is any evidence of organics being present. The experimental approach to answering this has been to heat the sample and measured the evolved gases by gas chromatography-mass spectrometry but each time the only species detected have been CO_2, H_2O and traces of chlorinated hydrocarbons.[95,96] Since the putative discovery of perchlorate, however, experiments with sand mixed with benzenehexacarboxylic acid (a presumed contributor to Mars surface from meteorites) and $Mg(ClO_4)_2$ have shown essentially identical pyrolysis behavior[97] and

it is being argued that such chlorinated hydrocarbons from pyrolysis are actually indicative of the presence of organics.[98,99]

If such a large amount of perchlorate is not just a local occurrence at the Phoenix study site, it represents both an easily accessible source of O_2 and energy, of great potential importance to any future manned station while at the same time one must also be conscious of the adverse effects of perchlorate exposure.[100] Confirming the presence of perchlorate and mapping its occurrence on Mars with both qualitative and quantitative certainty is essential. Particularly in view of the fact that the "perchlorate ISE" in the WCL was originally designated a "nitrate ISE"[1] and renamed only after the amount of nitrate indicated by the sensor was found to be physically impossible, one needs the most reliable method, within the constraints of a spacefaring instrument.

This laboratory has had an unrelated and independent interest in terrestrial perchlorate over the last decade, both in regards to its environmental significance[101-114]and analysis of perchlorate; regarding the latter, the choice has always been ion chromatography (IC), with or without mass spectrometry.[115- 120] The incompatibility with freeze-thaw cycles makes conventional IC incompatible, however with the present needs. Either open tubular IC (OTIC) or capillary electrophoresis (CE) can presumably meet the present requirements, we are admittedly biased towards the former. Although laudable attempts continue towards CE-based ion analysis systems,[121] a number of commercial CE-based systems were available in the 90's and were expected to replace IC; none are sold for that purpose today. We ourselves attempted to combine what we thought will be the best of both worlds, suppressed conductometric detection with CE,[122-125] but like many others, ultimately decided that a robust separation is difficult to maintain, if ionic strength and/or sample composition varies considerably. Indeed, with the most successful CE background electrolytes for anion analysis,[30] ion-pairing and adsorption on the wall plays a role in the separation.[126]

We therefore chose to pursue OTIC. The topic was reviewed a decade ago,[127] which also covered the theory and early work towards OTIC. Of two more recent reviews, one is devoted to capillary IC;[128] the other[129] primarily describes open tubular column development but covers OTIC as well. The reader is referred to these reviews; these together cover the literature on this topic published during the last decade. These will also confirm that what has been achieved up to now in OTIC is not competitive relative to the current practice of IC. In part, OTIC columns have been too large in inner diameter for time-efficient separations. Capillaries in which ion exchange latex particles are electrostatically attached to the inner wall have been used for separation since the 90's[130-132] and more recently capacities of such columns (even very narrow bore ones) have been measured.[133134] But without suitably sensitive detectors, their potential could not be realized. With this limitation removed,[35,135] we show here attractive performance of nonsuppressed conductometric OTIC.

4.3 Experimental Section

4.3.1 Reagents and Materials

All vendors not stated herein have already been specified in the companion papers. As the polymethylmethacrylate (PMMA capillaries) varied some in their inner radius (outer radius, r_o was constant at 170 μm), actual r for all capillaries were computed using the Hagen-Poiseuille equation[136] by pumping a known flow rate of water through a known length of the capillary and measuring the pressure drop.

Tap water samples were diluted 5x before analysis. Juice samples, bought locally, were passed through C18 cartridges and diluted 50x. The final step before injection for all samples was 0.2 μm pore membrane filtration.

4.3.2 Chromatographic System

Figure 4-1 illustrates the general arrangement. Briefly, the eluent is pumped by N_2 or He pressure via a digital pressure regulator (DPR, 10-100 psi, P/N 990-005123-100, http://ph.parker.com/us/12051/en/oem-ep-miniature-pressure-controller) from a Plexiglas vial (V) of ~25 mL capacity. Sample injection and chromatography is controlled by an electrically actuated 6-port injection valve (IV, vici.com) with a macro size loop (several μL) and two 2-way normally closed solenoid valves (SV1,2, 100 psi, P/N HPBPP011, nresearch.com) and a "zero dead volume" 10-32 tee (vici.com). SV2 is used for rapidly releasing the pressure in the vial. The principal flow output port of IV was connected to the perpendicular arm of the tee and would normally flow to waste via SV1 when the latter is open. Relatively large bore (r = 0.25 mm) PEEK tubing was used for all connections; as such flow through the far larger pressure drop OT column would be largely negligible whenever SV1 was open. The separation capillary was connected to the tee arm opposite to the SV1 connection via a FEP Teflon sleeve for sealing. Note that the capillary terminus was inserted several mm inside the tubing from SV1. Detection was carried out by an admittance detector @1KHz with the detector configuration in the previous paper;[35] specifically refer to Figure 4-5 therein. For all fused silica columns and some early work with PMMA columns we did use a commercial detector ((TraceDec, http://www.istech.at) operated at the lowest available frequency (~38 kHz).

In a typical injection and chromatographic sequence (programmed in LabView), V was pressurized to clean out the column and then SV1 opened momentarily to clean out the line to waste. In a typical case, injection pressure (P_{inj}) was lower than the pressure used for chromatography. After loading the sample loop in IV, IV was switched to the inject position and SV1 was simultaneously opened just long enough for the undiluted sample to be present within the tee. SV1 was now closed for a duration t_{inj} and the total amount introduced into the capillary (for a given length and radius of capillary) was directly related to the product $P_{inj}\ t_{inj}$. Following injection, SV1 was turned on again to clear the tee and the line of all remaining sample and then

closed again to begin chromatography. A sample timing diagram is shown in Supporting Information as Table S1. A portable, miniaturized version of the system which uses miniature high pressure 2-way solenoids to accomplish the same ends and field applications will be described in a forthcoming paper.

4.3.3 Column

Only AS18 latex (courtesy Christopher A Pohl, Thermo Fisher Dionex Corp.) coated capillaries, as previously described and characterized as to their ion exchange capacities[39] were used in this work. PMMA was chosen over silica capillaries has also been previously discussed: relative to silanol groups, -COOH groups on a hydrolyzed PMMA surface provides for stronger binding of the oppositely charged latex particles.[39] PMMA capillaries used ranged in *r* from 8 to 9.75 μm; *r* = 5 μm silica capillaries were also used before PMMA columns were available. It has not been possible as yet to extrude PMMA capillaries in the same dimensions.

For temperature effect experiments, the column was put inside a column heater (Eppendorf CH-30, equipped with a TC-45 temperature controller, www.sial.com). The temperature was independently monitored with a calibrated type J/K thermocouple. Other than as explicitly stated all other experiments were conducted at room temperature 22±2 °C. Because conductivity is highly temperature dependent, room temperature variation causes baseline drift that is particularly visible at high eluent concentrations. Correction for baseline drift (assuming a linear drift with time, see Supporting Information) was made in some chromatograms presented below.

4.4 Results and Discussion

4.4.1 Automated time-pressure based hydrodynamic injection

As the separation capillary itself is the primary resistance to sample introduction, the injected volume, V_{inj}, can be given by the time dependent form of the Hagen-Poiseuille equation:

$$V_{inj} = \frac{P_{inj} t_{inj} \pi r^4}{8 \eta L} \quad \ldots(1)$$

where η is the viscosity of the fluid in the capillary of length L, other parameters having been defined before. Although it may seem at first sight that this will make the V_{inj} very dependent on the sample viscosity, η in eq 1 represents the viscosity of the entire liquid column in the capillary. The injected sample rarely represents >1% of the capillary length while 99+% is the eluent whose viscosity does not change. Sample viscosity thus does not have a major influence on V_{inj}. This is shown in the lower inset of Figure 4-1 where the viscosity of a KNO_3 standard was deliberately modified by adding 0, 1, 2, 5 and 10% glycerol. The viscosity of a 10% glycerol solution is 29% higher than that of water but the observed change in peak area is minimal. However, for dilute aqueous solutions, η varies 2%/°C and this will be reflected in any experiment conducted without thermostating, as in the present case (our laboratory temperature varies ±2°C). The one caveat to strict applications of eq 1, especially at very low values of V_{inj} is that it takes into account neither the diffusion of the sample into the capillary, nor, less importantly, the finite sample flow into the capillary even when SV is open. Except for necessary scaling by *r*, this autoinjected volume (V_{aut}) is essentially independent of the other parameters that appear in eq 1 and will thus appear as a positive intercept if V_{inj} is plotted against t_{inj} all other parameters remaining the same.

After verification that the detector response is linear in the range of interest and operating at large V_{inj} values (so that V_{aut} will be negligible and eq 1 can be used without significant error), we can calculate the response factor, peak area (arbitrary units)/nL injected (computed from eq 1). Based on the observed peak areas at different values of t_{inj}, we can then compute $V_{inj.}$ A plot of V_{inj} vs t_{inj} thus obtained appears in Fig 2.

For the tested column (L= 58 cm), extrapolation of the plot at the lower end (inset, Fig. 2) produces V_{aut} = 40 pL as the intercept (corresponding to ~0.14 mm column length or t_{inj} = 7 ms under these conditions). Relative standard deviation for 270 pL replicate injections of 100 μM KCl (n=10) was 3.9%, a reasonable value given lack of temperature control. Under other conditions remaining comparable, V_{inj} scales with r^4. For r = 1 μm, we have reproducibly injected subpicoliter volumes using this setup.

Note that V_{aut} depends on r and the time the sample remains at the mouth of the capillary (without pressurization) and the specific injector configuration (see Figure C-S1). Figure C-S2 provides additional evidence that the autoinjected amount linearly scales with the sample concentration used.

4.4.2 Temperature Effects on Pneumatic Sample Introduction and Flow Rates

Pneumatic pumping has the advantage of simplicity but temperature variations will induce corresponding changes not only in the injected volume but also the chromatographic flow rate and hence affect retention times (See Figure C-S3 in Supporting Information). Because the temperature dependence of the viscosity of water (that of dilute aqueous solutions is essentially the same) is well characterized, it is possible to correct the applied pressure as temperature varies and maintain a constant flow. We show how well such correction works in Figure C-S4; while these data were obtained by setting the pressure calculated based on the known viscosity (η) of water at a given temperature and holding p/η constant. While this was presently done manually, it is obviously possible to do this on an automated basis. Of course, the system can be thermostated as well. Minor changes in flow rate due to temperature or other reasons can also be corrected for by noting the exact position of the unretained dip/system peak corresponding to the void volume and results in that case can also be reported in terms of retention volume.

4.4.3 Van Deemter Plot and H_{min}

For OT columns, the eddy diffusion term becomes zero; the Van Deemter equation simplifies to

$$H = \frac{2D_m}{u} + Cu \qquad (2)$$

where H is the plate height, D_m is the analyte diffusion coefficient in the mobile phase, u is the linear velocity of the eluent (cm/s) and C is a measure of the rate of interphase analyte mass transfer. We computed H from

$$H = 0.18\frac{Lw_{1/2}^2}{t_R^2} \quad \ldots(3)$$

Van Deemter plots for two identical columns (except for 34 vs 68 cm length) are shown in Figure 4-3 for Cl^- is an analyte. The experimental data are shown as the circles and the solid line is the fit to eq 2, obtained with Microsoft Excel™ Solver[137,138]. Uncertainties in the fit parameters D_m and C were calculated using the jackknife procedure[139] with a macro written in-house. Compared to the best fit values of D_m for Cl^-, (2.16±0.07) and (1.92±0.05) x 10^{-5} cm^2/s, D_m calculated from its known ionic mobility and the Nernst-Einstein equation[41] is 2.02 x 10^{-5} cm^2/s. H_{min} was 6.6 and 7.8 μm, respectively, for the longer and the shorter columns corresponding to 150,000 and 130,000 plates/m. The higher plate height for the shorter column is at least in part due to autoinjection limited V_{inj} being too large for this short column.

4.4.4 Phase Ratio, Eluent Concentration and Composition

It is important to note that the phase ratio (in the case of an ion exchange column this is readily quantitatively defined as the ratio of the stationary ion exchange equivalents to the ionic equivalents present in the mobile phase) is considerably lower for most OTIC columns than a packed column. As has been previously discussed,[39] compared to a packed column, a much lower eluent concentration therefore provides the same phase ratio and elution power. The resulting low background facilitates single column operation. The caveat is that when the analyte concentration exceeds the eluent concentration, the eluent still must supply sufficient

counterions to accompany the eluting analyte ions; as a result, peaks will broaden. However, sufficient separation is still possible if the column has a large enough plate count. As the column diameter decreases, the phase ratio increases, as such a higher eluent concentration or the choice of a stronger eluent ion, or both, are necessary. Most common inorganic anions are of relatively high mobility compared to large organic eluent ions, as such, benzoate, salicylate, phthalate etc., typically provide uniformly positive conductivity response for inorganic analytes, with the retention power being stronger in the order cited. The eluting power of phthalate can be further adjusted by pH as the balance between a monovalent and divalent eluent ion can be controlled. However, a large disturbance in pH by the sample can cause redistribution and two system peaks can result. Low or intermediate mobility inorganic ions such as bicarbonate can also be used as eluent and while majority of inorganic ions will produce positive peaks, majority of organic ions will produce negative peaks. The very low eluting power of HCO_3^- allows the use of higher eluent concentrations and an increase in the upper dynamic range of the analyte concentration it can also provide a transitional path to suppressed chromatography. If only low mobility weak organic acids are to be determined, a high mobility strong acid ion like sulfate can be used and the analytes then show up as negative conductance peaks

4.4.5 Illustrative Separations

A separation of five common anions is shown in Figure 4-4a on a PMMA column. While the separation takes just over 4 min the actual separation window is just over a minute. The separation is carried out at a flow rate significantly higher than the Van Deemter optimum but the plates/m for F^-, Cl^-, NO_2^-, Br^- and NO_3^- were still respectable at 121,000, 116,000, 87,000, 67,000 and 59,000, respectively; the elution order of course being the same as a conventional AS18 column. Figure 4-4b shows a separation in a smaller bore column at a 50% higher linear velocity, despite doubling of the eluent concentration and the higher linear velocity, the retention factors increase significantly due to the increased phase ratio. The apparent plate

heights in chromatogram 4b are actually higher than those in 4a; this is largely a result of the very large injection amounts (~100x the absolute amount of each ion used in 4a), without such large injections the commercial detector was unable to see the analytes well. Apparent plate heights always increase when the amount of sample is too large, OTIC is no exception. Figure C-S5 provides an example how plate heights increase with increasing amounts injected. As latex coating on silica is not very stable over an extended period (especially under alkaline conditions), we have not repeated experiments on silica tubes with lower amounts and the new detector except as already described in the foregoing paper.[35] The caveat here is that all performance data for the silica columns shown here were limited by the detector then used.

Figure 4-5a shows the use of different concentrations of $NaHCO_3$ eluent for the elution of relatively weakly held anions in a smaller capillary, while Fig. 3-5b shows how more strongly retained anions behave with different concentrations of sodium salicylate (NaSal) as eluent. Figure 4-5c shows how adjustment of pH of a phthalate eluent (in this region the eluent ion itself is changing from the monovalent hydrogen phthalate to the divalent phthalate anion) profoundly affects the separation of some very strongly retained anions (with a phthalate eluent, at most pH, analytes 1-6 will elute essentially in the void volume). Note in particular how the separation of iodide, thiosulfate and thiocyanate, (peaks 8-10, only thiosulfate is a divalent ion) and also the appearance of the system peak changes with pH. An optimized separation of such strongly retained ions where perchlorate elutes under ~3.5 min is given in Figure C-S6.

Organic acids in fruit juice samples were separated using a sulfate eluent, results for illustrative samples are shown in Figure C-S7 and Table C-S2. Table C-S3 provides performance parameters for several ions.

4.4.6 Hydrorganic Eluents, Pressure Gradients

Small amounts of organic modifiers, e.g., methanol or acetonitrile can markedly reduce both retention and peak asymmetry. Peak 6a shows the effect of

incorporating 10% methanol in a phthalate eluent. As there is a significant viscosity difference, the flow rate varies at the same applied pressure. The results are therefore best compared in terms of retention volume. The change in retention is obvious; the change in asymmetry is more analyte specific, e.g., the asymmetry (at 10% height) for SCN- exhibits only marginal improvement (2.1→2.0), while that for ClO_4^- decreases from 8.6 to 3.4. At the same volume fraction, acetonitrile has an even more profound effect (Figure C-S8). But acetonitrile affects PMMA capillaries in an interesting fashion. Up to 30%v/v acetonitrile can be used on a continuous basis. By 50% acetonitrile, the polymer swells to block off the bore altogether but even at lower concentrations the swelling causes a clear reduction in diameter (Figure C-S9); this is highly reproducible. Of note is that diffusion of acetonitrile into the polymer and its egress both take time, as such the capillary dimension can be reduced and more than one typical chromatogram easily run in that form before the diameter changes sufficiently. Results on variations in acetonitrile and phthalate concentration, and pH for a acetonitrile containing phthalate eluent are given in Figures C-S10-S12.

Isoconductive gradients between a potassium salt and a higher concentration of lithium salt has previously proposed in nonsuppressed IC.[49] We attempted a gradient between 1.5 mM sodium benzoate and 1.7 mM lithium salicylate (the pair is isoconductive) but there were severe baseline disturbances. On the other hand, because of the generally low pressure requirements, pressure/flow gradients proved attractive. Figure 4-6b shows the separation of 6 anions at three different pressures and Fig. 6c shows the same separation under a pressure gradient.

4.4.7 Repeatability and Dry-Freeze-Thaw-Wet Survival

We tested prolonged operation of the system by running it continuously overnight and making a new injection every two minutes. Within limits of its non-thermostated operation, the system showed excellent performance and stability. Figure 4-7a shows an overview, 7b shows overlay of 20 chromatograms from a portion of these runs and 7c shows variations in plate heights in some 124 consecutive

chromatograms. There was no systematic loss in capacity or efficiency. Peak area RSD ranged between 4.3% and 7.2% for the hundreds of runs overnight. A week-long test for 200 μM ea. Cl^-, NO_2^-, Br^- and NO_3^- showed RSDs of 7.0 to 10.3%, and the retention factor exhibited less than 6.0% RSD for all anions: for a non thermostated system, we deem this very good.

The key test for this approach for Mars exploration is the ability of the column to survive drying and freezing conditions. After three drying and wetting cycles, no loss in performance was discernible. Finally a dried column was stored at -20°C for 24 h, then thawed, rewetted and reused, no changes in performance was observed (Figure 4-8a).

4.4.8 Large Volume Injection and Tolerance of Larger Amounts of Another Ion

The large number of plates in the system allows an unusually large range of sample volume to be injected on column. Baseline separation of the five test ions on a 58 cm PMMA column is maintained over an injection volume of 40 pL- 4 nL; even at 15 nL the five peaks are clearly discernible. The same characteristics allow the measurement of a small concentration of one ion in the presence of a large excess of another. This is demonstrated in Figure 4-9 for the closely eluting pair chloride and nitrite; the latter is quantitated well in the presence of 100 times as much as chloride. A less challenging example is when there is a larger separation between the ions. However, as identification by ISEs is not unequivocal, it may just be possible that there is also a large amount of nitrate in Martian soil. Figure C-S14 demonstrates that perchlorate is easily quantitated in presence of large amounts of nitrate.

In summary, we have described a simple, fast and efficient open tubular anion chromatography system. A portable, miniaturized version of the system which uses miniature high pressure 2-way solenoids to accomplish the same ends and field applications will be described in a future paper. While there is no doubt that incorporation of a suppressor is needed to take this technique to the next stage (an approach we are ardently pursuing), the methodology may already have merit in niche applications. Although not a substitute for gradient operation, the scale and

cost of operation permits simultaneous isocratic operation with multiple eluents, partially achieving the same goals. It is not our intent to suggest that this instrument as described is ready for extraterrestrial explorations. What actual materials are to be used remain to be further studied – PMMA may be too brittle at very low temperatures, for example. We primarily wish to show here the capability of the platform.

4.5 Associated Content

Supporting Information

The program sequence; comparison of autoinjected volumes; peak area vs injection time; flow rate vs temperature; maintaining flow rate by varying temperature and pressure; injected amount vs plate height; strongly retained anions separation; chromatograms of organic acid in juice; analytical parameters for separation anions; effect of added solvent in eluent; effect of acetonitrile to PMMA tubing; effects of acetonitrile, pH and phthalate; fast separation; chromatograms of the separation of nitrate and perchlorate. This material is available free of charge via the Internet at http://pubs.acs.org.

4.6 Author Information

Corresponding Author:

*Email: Dasgupta@uta.edu Fax: 817-272-3808.

Notes

The authors declare no competing financial interest.

4.7 Acknowledgement

This work was supported by NASA Grant NNX11AO66G. BCY acknowledges NSFC grant 21322502; KT acknowledges support from IPST. We thank Phillip Shelor for his assistance throughout this work. This chapter has been reprinted with permission from B. Yang, M. Zhang, T. Kanyanee, B. N. Stamos and P. K. Dasgupta. Bingcheng Yang, Min Zhang, Tinakorn Kanyanee, Brian N. Stamos, and Purnendu

K. Dasgupta “An Open Tubular Ion Chromatograph.” Anal. Chem., 2014, 86 (23), pp 11554–11561.

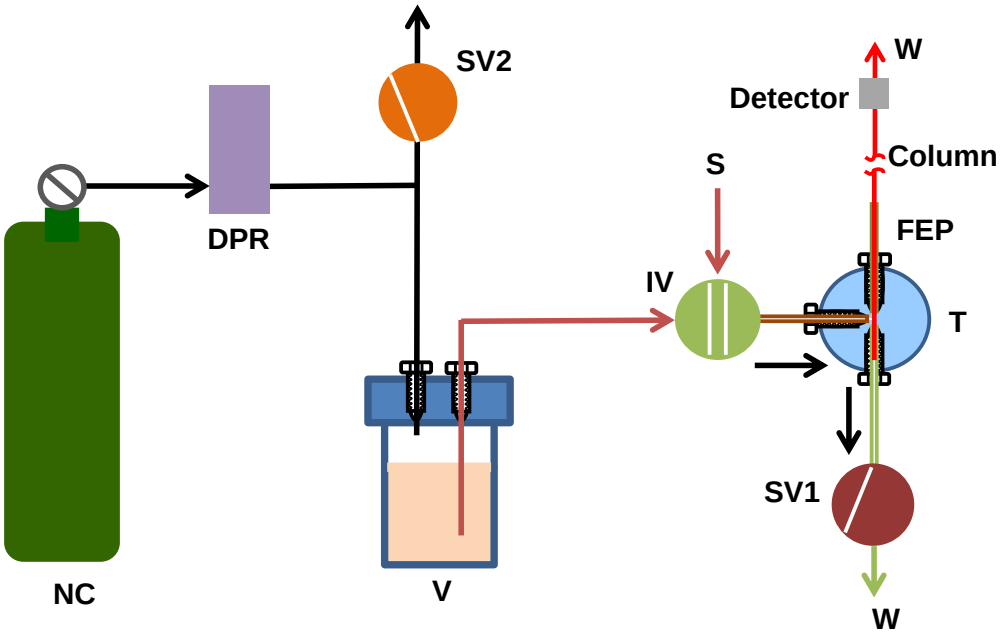

Figure 4-1. Schematic diagram of chromatographic setup.
N_2, nitrogen cylinder; DPR, digital pressure regulator; IV, injection valve; SV, solenoid valve; OTC, open tubular capillary; C^4D, capacitively–coupled contactless conductivity detector; W, waste

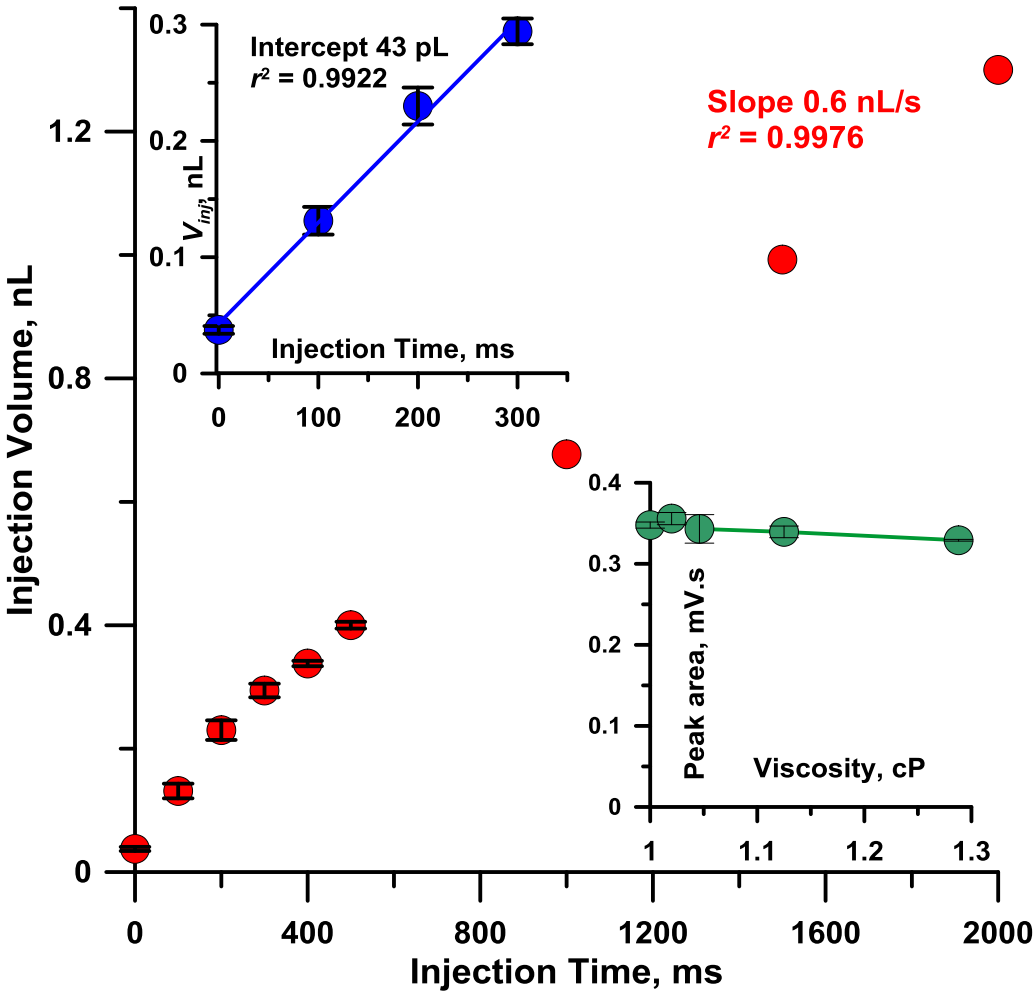

Figure 4-2. Injection volume as a function of injection time.

R = 9.8 µm, L = 58 cm; P_{inj}, P_{elut} = 14 psi; analyte, 100 µM KCl, Error bars (±1 sd, n=3) are shown for injections up to t_{inj} = 500 ms. Eluent :1 mM sodium benzoate (NaBz).

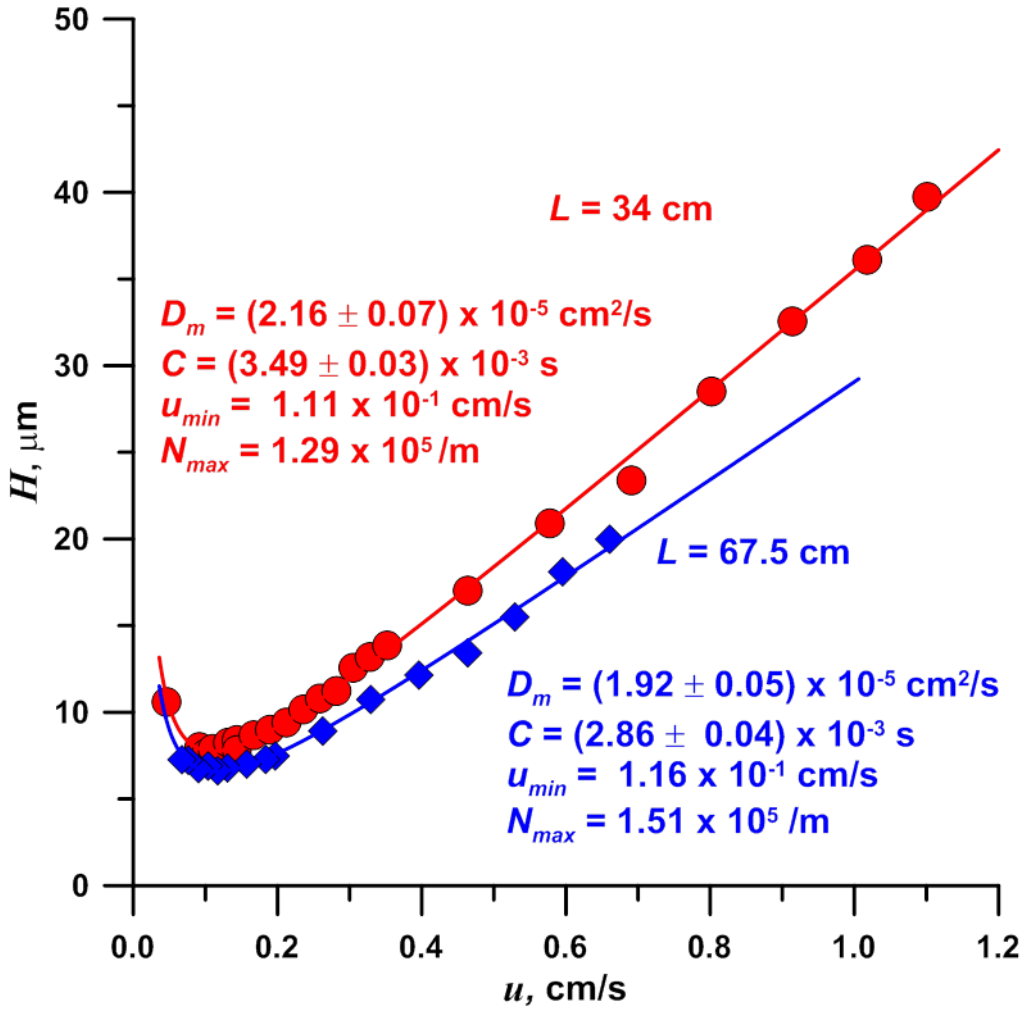

Figure 4-3. Van Deemter plots of OTCs Conditions

analyte, 500 μM Cl^-; injection volume: ~43 pL for 34 cm OTC, 90 pL for 67.5 cm OTC; other conditions as in Figure 4-2.

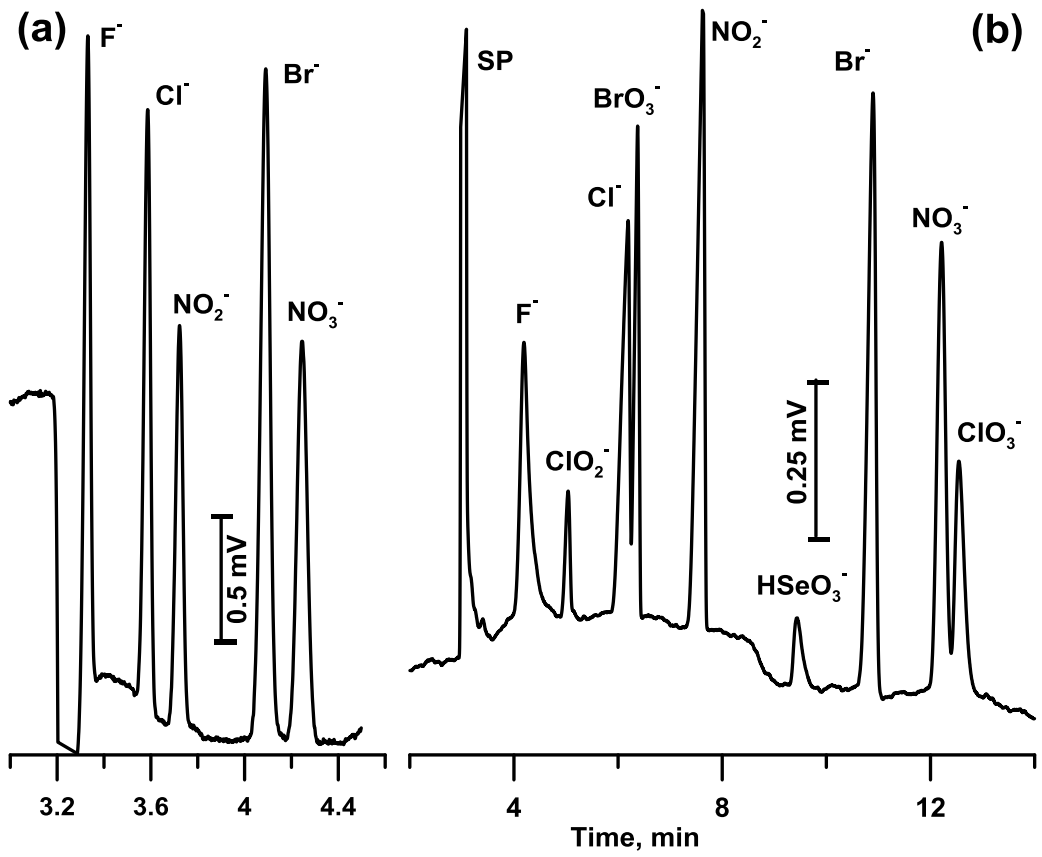

Figure 4-4. (a) Typical chromatogram of anion on 70 cm PMMA column (b) 44 cm fused silica column

(r =9.8 µm): Sample: 90 pL injection; 1 mM NaBz eluent, 30 psi, linear velocity, 0.35 cm/s (63 nL/min); (b) 44 cm fused silica column (*r* = 5 µm), sample: 500 µM each (F^-, ClO_2^-, Cl^-, BrO_3^-, NO_2^-, $HSeO_3^-$, Br^-, NO_3^-, ClO_3^-) as originally prepared the chlorite oxidizes some of the selenite forming chloride and selenate, the latter elutes much later under these conditions, 0.8 nL injection; 2 mM NaBz eluent, 50 psi, linear velocity 0.245 cm/s (11.5 nL/min).

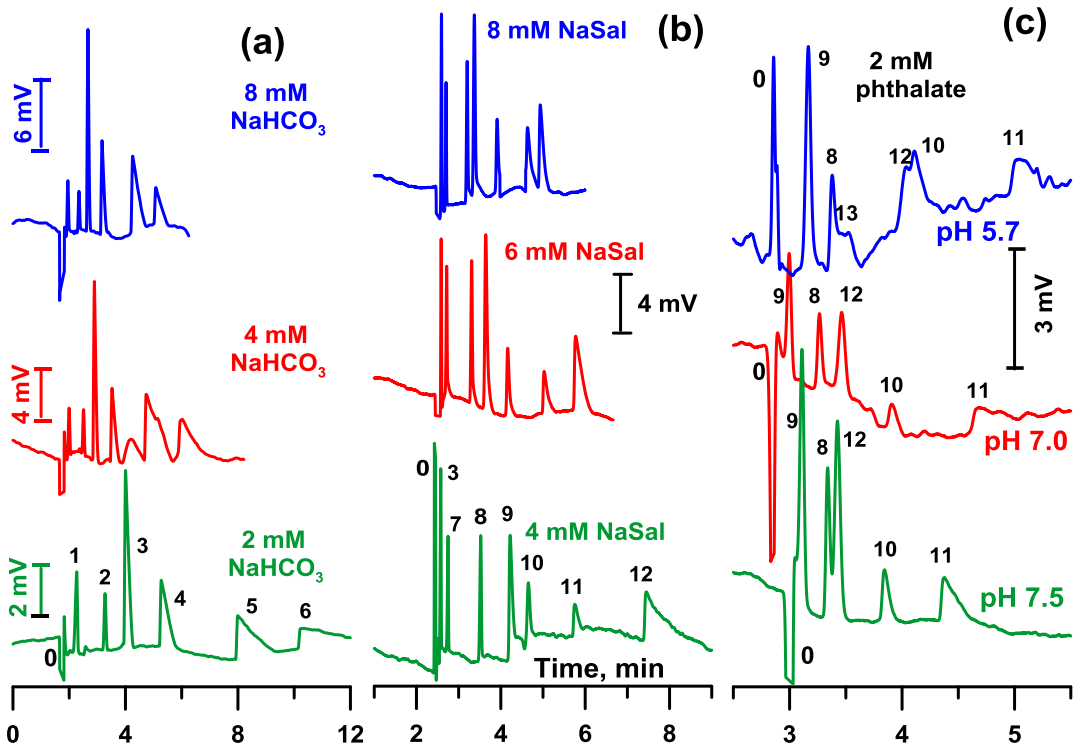

Figure 4-5. Illustrative chromatograms.

(a) various concentrations of $NaHCO_3$ as eluent, 80 psi (19.2 nL/min): (0) system peak, (1) F^-, (2) ClO_2^-, (3) Cl^-, (4) NO_2^-, (5) Br^-, (6) NO_3^-, 1.9 nL ; **(b)** various concentrations of Na-Salicylate as eluent, 50 psi (16.8 nL/min): (7) ClO_3^-, (8) I^-, (9) SO_4^{2-}, (10) SCN^-, (11) ClO_4^-, (12) $S_2O_3^{2-}$ 60 pL ; **(c)** r = 9.8 μm, L = 47 cm PMMA column, 2 mM potassium hydrogen phthalate pH adjusted with LiOH, 14 psi (45 nL/min) : all anions 0.5 mM except ClO_4^- (1 mM), 75 pL injection for pH 5.7 and 7.5 eluents ; a smaller volume was injected for the pH 7 eluent. Peak 13 is from CO_2; note that it only appears with the lowest pH eluent when the sample contains more CO_2 than the eluent.

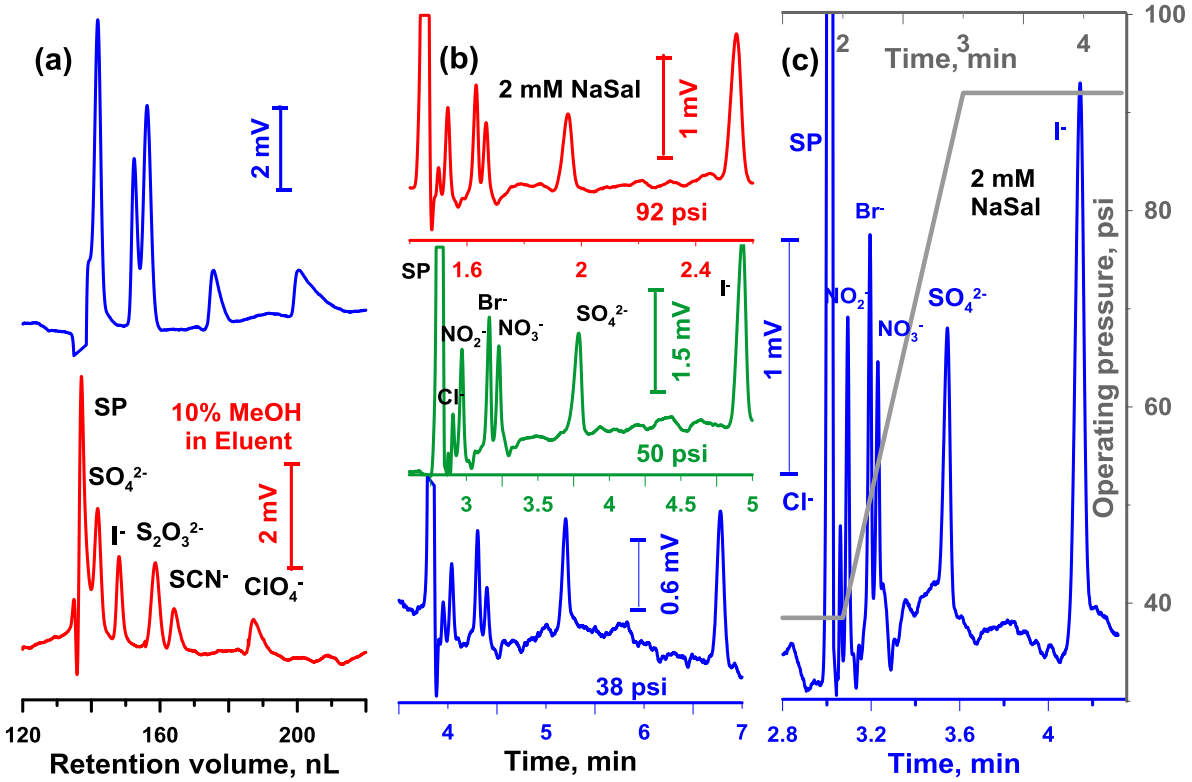

Figure 4-6. (a) Effect of methanol addition on the behavior of strongly retained anions

2 mM K-phthalate pH 7.5 as eluent with and without 10% v/v methanol added in the eluent; other conditions as in Fig. 5c; **(b)** Chromatogram of 6 anions, 2 mM Na Salicylate eluent, at three different pressures, 60 pL injection, r = 5 μm, L = 44 cm, silica column, 0.5 mM each anion, 0.12 nL injection, **(c)** Pressure gradient run, other conditions same as Fig. 6b.

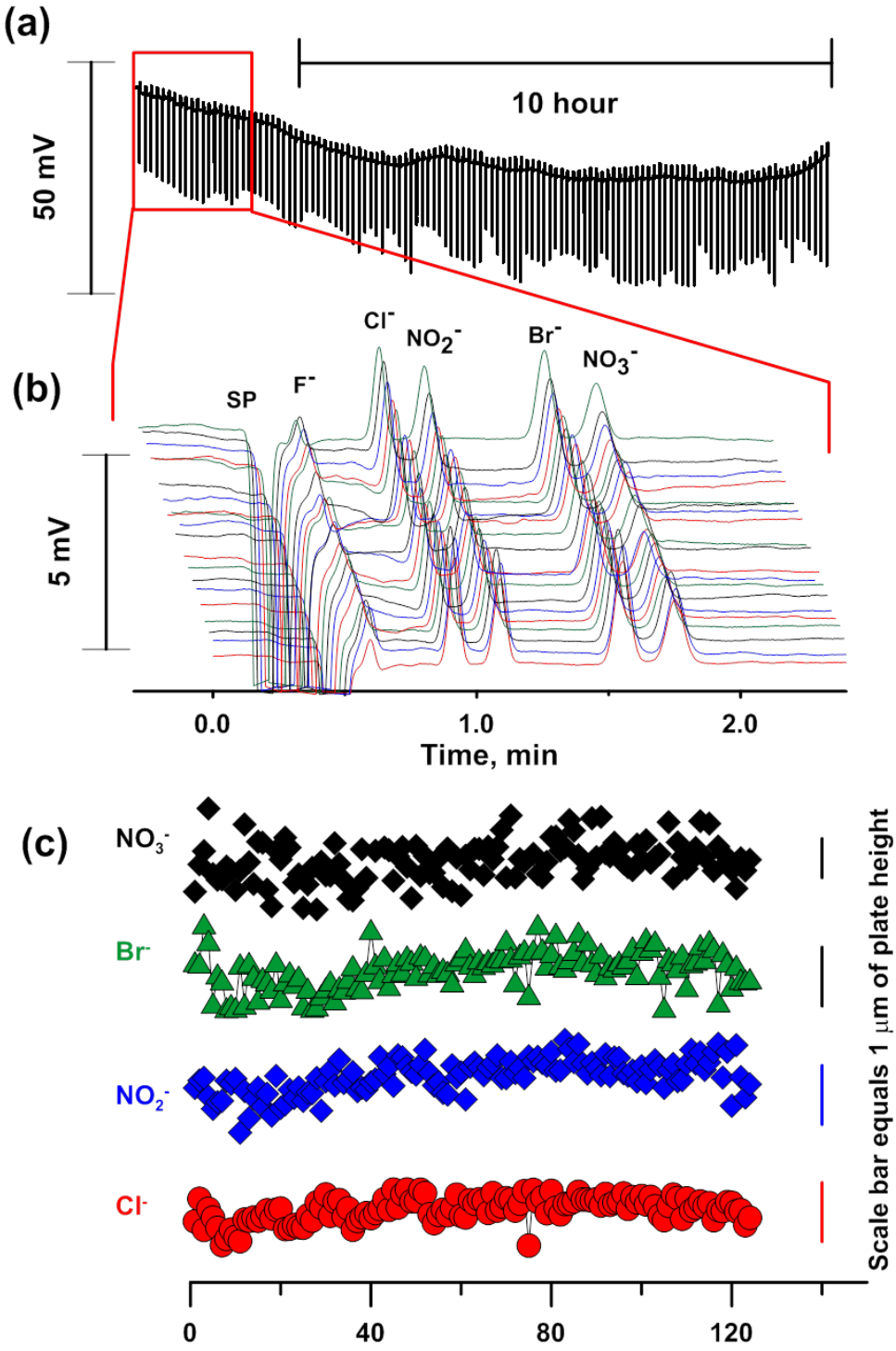

Figure 4-7. (a) Chromatogram for 124 consecutive injections using PMMA based OTC.

The general downward trend of the baseline comes from the temperature decreasing at night. (b) Chromatograms of first 20 injections. (C) Heights of plate of 124 consecutive injections. Conditions: OTC length, 58 cm; injection volume, ~0.13 nL;

injection pressure, 14 psi; sample, 100 µM F^-, Cl^-, NO_2^-, Br^- and NO_3^-; eluent, 1 mM sodium benzoate; linear velocity, 0.21 cm/s (36 nL/min).

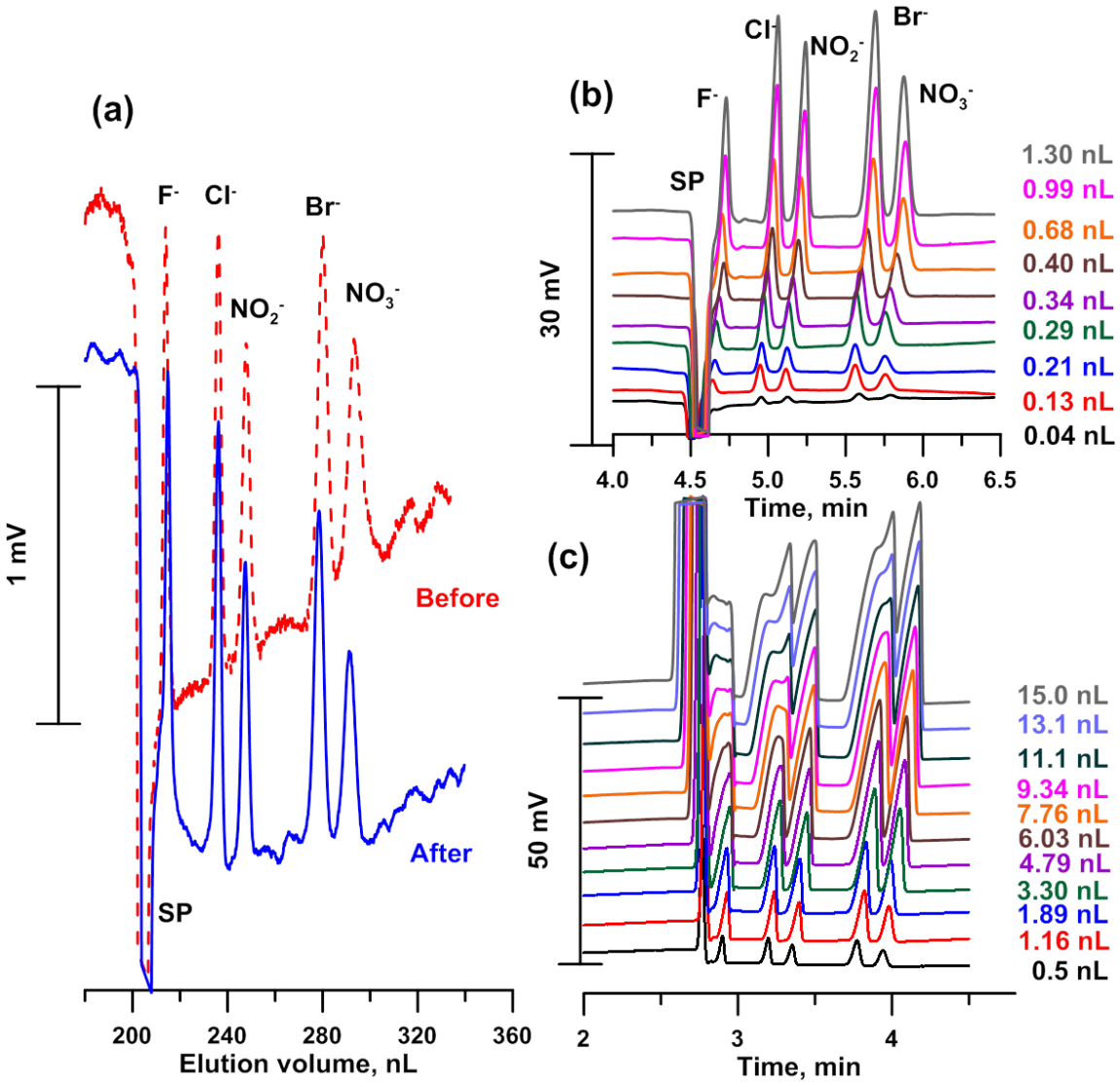

Figure 4-8. (a) Chromatograms before (red dashed line) and after (blue solid line) drying (b) Tolerance to large sample volumes (c) Tolerance to large sample volumes low temperature storage and thawing and reuse. r = 9.8 µm, L = 70 cm, PMMA, Eluent 1 mM NaBz, P_{Elu} 30 psi, sample 200 µM ea F^-; 100 µM, Cl^-, NO_2^-, Br^-, NO_3^-, 0.29 nL injected (b) Tolerance to large sample volumes (<1 nL, low concentration sample). r = 9.8 µm, L = 58 cm, PMMA, Eluent 1 mM NaBz, sample 100 µM ea. F^-, Cl^-, NO_2^-, Br^- and NO_3^-; P_{Elu} 14 psi, linear velocity, 0.21 cm/s (36 nL/min), injection volumes as indicated.(c) Tolerance to large sample volumes (>0.5 nL, high concentration sample). r = 9.0 µm, L = 53 cm, PMMA, Eluent 1 mM NaBz, sample

400 μM F^-; 200 μM Cl^-, NO_2^- , Br^-, NO_3^-; P_{Elu} 25 psi, linear velocity, 0.34 cm/s (51 nL/min), injection volumes as indicated.

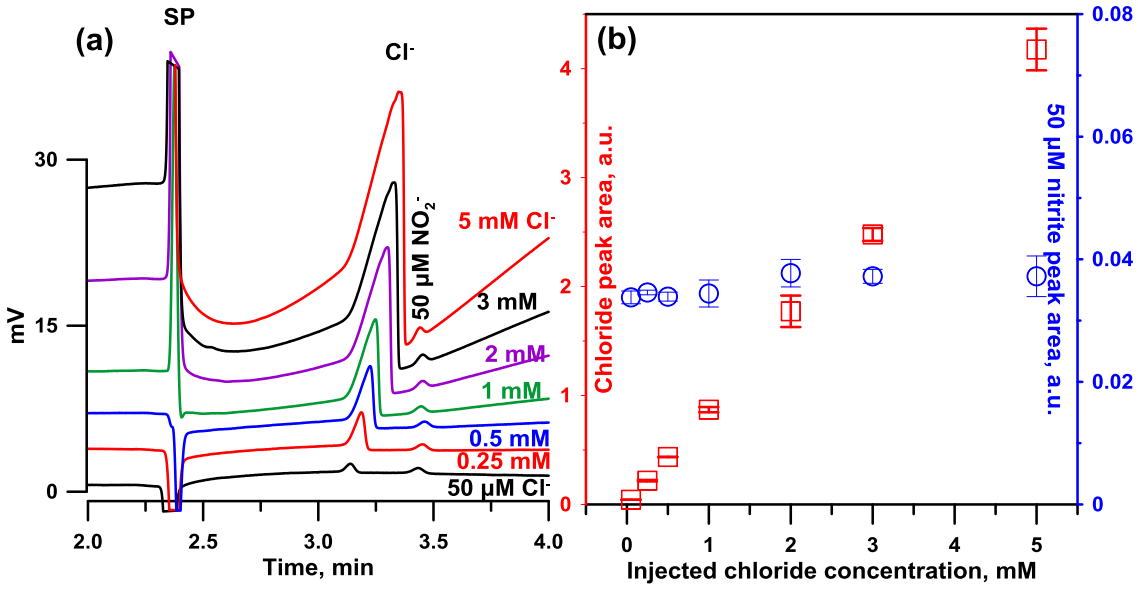

Figure 4-9. Separation and quantitation of nitrite in presence of up to 100 times as much chloride.

The left panel shows the chromatograms, the right panel demonstrates the constancy of the nitrite peak area. ±1 SD error bars are shown (n=3 ea.) r = 9.8 μm, L = 59 cm, PMMA, 50 μMNO_2^- in presence of 50 -5,000 μM Cl^-; 1 mM sodium benzoate; injection volume, 1.84 nL; P_{Elu} 25 psi, linear velocity, 0.35 cm/s (64 nL/min).

Chapter 5 Admittance Scanning for Whole Column Detection

Brian N. Stamos, Purnendu K, Dasgupta*, Shin-Ichi Ohira

Department of Chemistry and Biochemistry, University of Texas, Arlington, TX 76019

Department of Chemistry, Kumamoto University, 2-39-1 Kurokami, Kumamoto, Japan 860-8555

5.1 Abstract

Whole column detection (WCD) implies simultaneous measurement of analytes across the length of a separation column. Tswett's original chromatography experiment, visually following separation of colored plant pigments on a chalk-packed glass column, utilized WCD, albeit qualitative. In more recent times, WCD has exclusively utilized optical detection. One practical application involves capillary isoelectric focusing; a relatively short focusing zone is uniformly illuminated and the entire column is imaged at once in the transmission mode. Other than such instantaneous imaging, scanned imaging also has merits. We have adapted this technique to chromatography. Instead of imaging the entire column at once, the detector scans across the column. The length resolution depends on the scanning velocity and the data acquisition frequency. Columns of significant length (>1 m) can be readily scanned. Open tubular (OT) ion chromatography is particularly amenable to this methodology, as admittance detection can be readily carried out without galvanic contact. We demonstrate its potential with both OT and commercial packed columns. A paired quadrupole electrode geometry is introduced for admittance detection; this arrangement maintains essentially constant and reproducible contact with the column regardless of minor variations in outer diameter and is therefore well-suited for the present application.

5.2 Introduction

In Tswett's first experiment on chromatography of plant pigments, he necessarily carried out visual whole column detection (WCD). Although his ability for quantitation may have been limited by his visual prowess, he saw not only what eluted from the column but *what did not*, not feasible in modern HPLC. Indeed, with such X-ray vision, premature column deaths from recalcitrant components in the injected samples could well have been prevented. In principle, if the bands could be seen qualitatively as Tswett did and further, quantitate them, an end-column detector will be superfluous.

Focusing on the last fifty years, the first WCD-like attempt involved moving a section of the column through a spectrophotometer with the objective of computing partition constants.[140] Birks et al.. studied WCD first theoretically[141] and later experimentally with a single long illuminator and 14 stationary photodiodes.[142] Virtually all other WCD studies originated from Pawliszyn et al.. in capillary electrophoresis (CE) or more commonly, capillary isoelectric focusing (CIEF) systems; a review is available.[143] In CIEF, only a short length (5 cm) is imaged. Other WCD studies have relied on laser induced fluorescence with the attendant advantages and limitations. The only commercial WCD instrument[144] measures absorbance at 280 nm over a 5 cm long imaging zone using a fiber optic array for illumination. Related pioneering work has involved axial optical detection through the entire column where differentiation yields a conventional chromatogram;[145] the presence of any late-eluting strong absorbers can, however, lead to poor S/N.

In simulating chromatography,[146] one invariably notes that the desired separation of the analytes of interest is often complete on-column long before they elute and are seen by end-column detectors. In such cases, time is wasted and post-separation broadening deteriorate the LOD. In gradient elution, a gradient that is too steep or early can cause a pair of weakly retained species, just separated on-column, to re-merge before reaching the detector, a phenomenon that goes unnoticed. Lin et al.. demonstrated with an optical scanner based CCD and a transparent column how precisely one analyte can go past another during gradient elution.[147] Few practicing chromatographers truly trust models to formulate a gradient, more often it is a matter of optimization by trials: it is not *a priori* known how precisely retention factors will vary with eluent composition. In contrast, if one can see the separation develop, conditions can be altered in near real time to tailor the separation. Presently the only intrinsically chromatographic analyte identifier is the “retention factor”. In gradient elution, the analyte temporally moves at different speeds. WCD can provide a 3-D space-time-speed map that can uniquely identify an analyte.

Optical WCD with instantaneous imaging for is more manageable for small imaged regions; the light has to be distributed along the entire region. If the light comes from a point source and the illuminated zone is long, a penalty is paid in S/N because the light intensity at each point proportionally decreases. In contrast, the entire light can be used at one point in a scanned detector so the length of the region scanned depends only on the ability of the scanning mechanism. Although mechanical scanning may seem inferior, we took reassurance from the fact that

Carlson's original photocopying invention (*Electrophotography*) that imaged a whole document at once,[148] has now succumbed to mechanically scanned imaging. A 4800 dots per inch (dpi) optical scanner implies a resolution of ~5 μm and is available for less than US$70. A scanner joins the resulting spatially separated serial images together to create a two dimensional image. If one similarly joins similar spatiotemporally separated serial column scans, we will be looking at a chromatogram developing, a motion picture as it were.

To make a scanning detection paradigm possible, one obviously needs a compact, easily movable sensing head. For an optical detector, either fluorescence and/or absorbance can be interrogated in a transparent column with a translatable sensing head containing two or more optical fibers. Our interest has more been in ion chromatography (IC). Recently admittance (incorrectly, but more commonly, termed contactless conductance) detection has been developed to work with very small capillaries as well as low specific conductance levels.[149-151] Small capillaries and low specific conductance sum up to a high impedance system with very low current levels. Nevertheless, with high gain ultralow bias-current transimpedance amplifiers to immediately amplify the signal, a compact translatable sensing head is possible. While optical detection requires a transparent column, an admittance detector (AD) obviously requires an electrically nonconducting column. This is generally true for IC columns anyway, whether in packed or OT formats. The admittance signal is largely due to the ions in solution as the mobilities are much higher than those in the stationary phase.[152]

5.2.1 Movable Admittance Detection

In their present form, ADs were first conceived in 1998.[153-154] It was quickly realized that they can be moved along a column; this ability was first exploited by Unterholzner et al.[155] for the simultaneous separation of inorganic anions and cations in capillary electrophoresis (CE). In situations with non-uniform electric fields (this would be akin to gradient elution) they noted the *apparent selectivity* between analytes can change depending on the precise column location. Additionally this allows an adjustable effective column length to locate the detector where the resolution is maximum between the desired analyte pair. Macka et al.[156] miniaturized the AD and was able to probe more of the column. They thus reported a plot of *apparent selectivity* for various ions at 11 separate detector locations. Gillespie et al.[157] then adapted this technique to evaluate the progress of coating as a surfactant solution flowed over a hydrophobic monolithic column, and to examine response as a function of the counter ion. Gillespie et al.[158] also first described moving an AD during a chromatographic separation from one stationary location to another to optimally capture separations of both early- and late-eluters. Herein we describe repetitively mechanically scanned AD-based WCD for both OT and packed capillary columns and its potential.

5.3 Experimental Section

5.3.1 Chemicals

Sodium salicylate (as eluent) and chloride, chlorate, perchlorate, iodide, thiocyanate, sulfate and thiosulfate, as sodium or potassium salts as test anions were all reagent grade and used as received (www.fishersci.com). House distilled water, passed through an ARIES water purification system (www.ariesfilterworks.com) provided 18.2 MΩ*cm^{-1} water. All solutions were filtered with (0.2 μm) before use.

5.3.2 Linear Stage Setup

Referring to Figure 5-1, a CRK Series linear stage with 1360 mm of stage travel was used to sweep the detector across the capillary column (www.boschrexroth.com). One revolution of the screw equates to 16 mm of linear travel. We used a TraceDec® (www.istech.at) or Analytical Foundry (AF) (www.analyticalfoundry.com) admittance detector (AD) sensor head mounted to the linear stage platform via individual 3D-printed ABS plastic block holders. For the TraceDec®, the high sensitivity sensor head (HS3059) was used with parameters set as follows: voltage output: -12 dB, gain: 200%. The AF AD design was similar to that published[149] except for exact chip details. The linear stage has a lower and upper T-rail that runs along each side; aluminum (6061) blocks were custom machined to fit in these rails to attach a platform that is adjustable for height. Glued to the platform at the head of the capillary column is a PEEK Tee that serves as part of the injection system.[151] At the capillary exit end, a PEEK union is affixed to the platform, the capillary passes through it. The adjustable platforms allow any column length (within limits of stage travel) and once the platforms are fixed in place, the capillary is held taut and

ferruled male nuts at each end fix the capillary so that it does not change its position by the drag of the sweeping AD sensor head. The linear stage is moved by a 425 oz-in. NEMA 24 stepper motor (1/4 in. shaft) controlled by a QJ8060 stepper motor driver (both from www.buildyourcnc.com) powered by a 24 V DC 6.5 A supply (RS-150-24, www.meanwellusa.com) deliberately limited to a maximum current of 4.13 A.

5.3.3 Capillary Column Setup

With the TraceDec®, the internal ADC was used at the maximum possible sampling rate of 34.14 Hz. The AF AD uses an onboard 20-bit ΔΣ ADC of a programmable system on chip (PSoC) (www.cypress.com) that could acquire 18-bit data at 3.6 kHz. The minimum scan distance is dictated by the physical width of the detection head as well as the part of the column head inside the fitting/PEEK T (~30 mm).

5.3.4 Commercial Packed Column Chromatography and Detector Setup

A GP40 pump (www.dionex.com) with a split flow arrangement provided a column flow rate of 10 μL/min. Sample injection (1.5 μL) was manual using a six port injector (MXP9900-000, www.idex-hs.com) connected to a Dionex 0.4x250 mm AS11-HC capillary column. Unlike silica capillary columns with built in frits, these PEEK columns use external frits held with fittings and a union. Removing the end fitting(s) usually results in expulsion of some of the column packing. On the other hand, snug-fitting sleeve type electrodes commonly used with capillaries cannot obviously be slipped over the end-fittings, much larger than the column. To overcome this, a quadrupole electrode design was developed (Figure 5-2). The

design of this detector head allows it to be assembled on the column without sleeve electrodes to be inserted through the end(s). Four short stainless steel rods (9 mm long, 1.59 mm ϕ) form a set of quadrupole electrodes that surround the capillary, silver epoxy on top and bottom on each side make electrical contact and secure them to a subminiature version B (SMB) coaxial connector. A 100 μm thick sheet of MuMETAL® (www.magneticsheild.com), folded into a U-shape is used as the ground shield between the quadrupole, the shield is insulated on the exterior with 25 μm thick polyimide tape (www.kaptontape.com) to prevent contact with electrodes. Springs apply tension to one side of the assembly to ensure contact at all times. It will be appreciated that unlike sleeve electrodes, differences in outer diameter along the length of the scanned column does not cause loss of contact.

Standard packed column IC is carried out with suppression followed by conductivity detection. Obviously WCD can only be carried out in the non-suppressed mode which has a relatively high background conductance. The Analytical Foundry AD used a high gain-bandwidth product (12.5 MHz) transimpedance amplifier and a modest gain of 0.5 V/μA was chosen.

5.3.5 Open Tubular Column and Injection System

360 μm o.d. fused silica (11-21 μm i.d.) and cyclic olefin capillary (COP, 19 μm i.d.) capillaries were used. In some experiments, the unmodified fused silica tubes were used. In others, capillaries were coated with AS18 latex (COP capillaries after sulfonation) before use; details of COP column preparation appears elsewhere.[159]

The injection system used for the capillary columns has been previously described.[151] Figure 5-1 inset indicates how this injection system is built around the capillary holding tee. The volume injected can be controlled with both pressure and injection time. Except as stated, the columns terminated in a 92 cm long 11 μm ϕ silica restriction capillary. Injections, controlled through a LabVIEW program were performed at 80 psi with a range of 2-7.5 s (injected volumes of 0.17 - 0.65 nL).

5.3.6 Linear Stage Control and Detector Synchronization

All stepper motor movements were controlled by a CY8CKIT-059 prototyping kit (www.cypress.com) containing a programmable system on chip (PSoC 5LP). In this work, ½ stepping was used, this equates to 0.9° increments, translating to 40 μm of linear movement for each such microstep. The PSoC keeps track of the number of microsteps the stage has moved from "Home" (usually the injection end, or any other desired position). The velocity V_s is the product of the microstep length and the stepping rate f_s (Hz) namely, 0.04 f_s mm/s.

For the TraceDec and the AF AD, f was respectively 34 and 1000 Hz, except as stated. The data resolution in terms of column length is equal to V_s/f where f is the data acquisition rate (Hz).The length resolution can be improved (with penalties) by: (a) reducing V_s (increases scan time) or (b) increasing f (increases noise). The PSoC synchronizes the movement of the stage with the data acquisition, allowing each detection point to be taken at precisely the same location on the column through a

LabVIEW routine that allows V_s, number of steps to travel, wait time (if any, between successive scans), total number of scans to be made, and *f,* as input parameters.

Presently scans were unidirectional, meaning the stage returned home to begin the next scan. In addition, at each terminal end, the stage stopped for 2 s to avoid inertial glitches. In this work, V_s ranged from 0.4 to 4.0 cm/s and was 2.8 cm/s unless otherwise stated ($V_{s,max}$ was 10 cm/s; return speed could be higher for unidirectional scans). It is possible in principle to use bidirectional scanning. But beyond generating two semi-independent sets of oppositely directional data, a combined interpretation of both sets is a complex task and was not presently attempted. Also, detector output feedback was not presently used to limit the scanned zone. The minimum/maximum rate of movement of the analytes in the group is essentially immediately learned: this information can be used to limit the span of the next scan to improve temporal efficiency.

5.4 Results and Discussion

5.4.1 Detector Suitability. A Tale of Two Detectors.

The behavior of the detector, especially in regard to its response time (controlled by imbedded signal processing) is obviously critical to the moving detector scheme. Although the number of published papers utilizing admittance detectors now exceed 1000, the number of commercially available detectors are limited, possibly because it is simple to build one. We began experiments with the leading commercial detector

(TraceDec) and of necessity (see following section) used another newly introduced commercial detector. We were aware that the latter followed our own design,[149] facilitating minor modifications. In many of the tests described below, the differences in detector characteristics are compared.

5.4.2 Effect of Scanning Speed on Signal Fidelity

The response of the TraceDec in following a 0.95 nL injection of 500 μM KCl into water was determined at 4 scan speeds ranging from 0.4 to 4 cm/s in a 21 μm ϕ silica capillary with a mobile phase velocity of 0.82 mm/s. If scans at different speeds are started at the same fixed time after injection, it will reach the peak apex at different locations along the tube with different degrees of dispersion, negating a fair comparison. So for different scan speeds. the scans were started at suitably different intervals after injection to reach the peak apex at the same ~5.3 cm of column length as shown in Figure D-S1. The perceived signal height from starting baseline decreased with increasing scanning speed as 1:0.85:0.62:0.42 with no significant change in the peak area. At the two higher scanning speeds the peak is also obviously misshapen. This is caused by some embedded signal post-processing, even at the fastest scanning speed 8 data points are acquired per cm. We have discussed elsewhere the unanticipated effects of signal filtration[160] When no details are available on the nature of the processing algorithm, this can pose a major problem.

The AF detector uses a RMS to DC converter (AD637a, www.analogdevices.com) to rectify the AC signal after initial amplification. The time constant (τ) of the detector output in controlled by an external capacitor (τ = 25 ms/μF). Using τ = 250 ms, the detector response behavior is similar to that of the Tracedec (Figure D-S2) in that the peak height decreases and the tailing increases with scanning speed. With a τ of 25 ms, however, the dependence of the signal on scanning speed is vastly reduced (although it is still perceptible at the highest scan speed, Figure D-S3); there is far less tailing at all speeds relative to Figure D-S2, a direct comparison is shown in Figure D-S4. Figures D-S2-S4 used *f* = 1 kHz. As shown in Figure D-S5, not much is gained in going beyond *f* = 500 Hz. The TraceDec was designed for stationary applications; the highest available *f* (34 Hz) was already demonstrably insufficient, even lower *f* (16.6 and 5.6 Hz) predictably made things worse (Figure D-S6).

5.4.3 Positional and Interval Reproducibility

These parameters were measured by applying three ~3 mm wide marks with a metallic paint pen ~ 5 cm apart on the outside of a silica capillary. Both detectors registered large spikes when passing over the metallic ink marks. Multiple scans were performed at 1.6 cm/s for both detectors; for the AF AD a slower V_s of 0.4 cm/s was also used. For the TraceDec, the reproducibility in locating the marks in all cases (four scans, three marks) were within one data point (Figure D-S7, at 1.6 cm/s and 34 Hz, this resolution is 470 μm); the detector did not separately see the two edges of each mark (Figure D-S8). For the AF AD, with *f* = 1 kHz and V_s = 1.6 cm/s, the theoretical spatial resolution is 16 μm; the real resolution is step resolution of 40

μm; a given location is oversampled. The detector saw each edges of the mark (Figure D-S9). In 5 scans over the three marks, the standard deviation of the location of each edge (6 edges) varied from 40 to 190 μm (average±sd: 100±60 μm). However, the electrodes on this detector are rather tight on the capillary and each pass rubs off some of the paint (at an even higher scanning speed of 2.8 cm/s, the first pass is enough to remove all paint) resulting in diminishing registration of the marks with successive scans and causing concerns on how the smearing of the paint might affect the edge location reproducibility. For this reason, a fresh capillary was re-marked and scanned at 0.4 cm/s (Figure 5-3). With the exclusion of two statistical outliers, both on the same scan, the location of each edge exhibited a standard deviation (SD) of 15-37 μm. The precision (as SD) in measuring the width of each of the 3 marks was 26-67 μm compared to 100-180 μm at V_S = 1.6 cm/s. The SD of the two intervals between the three marks was ≤ 0.47 mm (limited by data resolution) for the TraceDec; the corresponding values for the AF AD was 115-140 and 120-150 μm, at Vs = 0.4 and 1.6 cm/s, respectively. To put in perspective: the typical initial length occupied by the sample in the column is 1500 μm.

A noteworthy aspect of Figure 5-3, is that unlike Figure D-S1, the baseline not only displays structural features, these features are not random detector noise. The minor imperfections in the column coating or silica tubing bore and wall thickness are reproducibly registered by the detector. For this reason, a background subtraction process was always adopted for real chromatographic scans: Four unidirectional

scans were initially made before any sample injection and averaged and stored as the background; this was subtracted from all post-injection scans.

Snug-fit tubular electrodes work well with fused silica tubes but the COP capillaries have greater OD variations. At high scanning speeds, friction becomes large enough to pull the capillary from the end moorings. Silicone lubricants sprayed on the capillary greatly ameliorate this problem without affecting the detector response.

5.4.4 Column Imaging

In a thin layer chromatography (TLC) system, the separation of colored analytes may be imaged by a set of time-lapse photographs. The images may be analyzed off-line with image processing software for quantitation. Here, the observed peak areas more readily provides quantitation. A 20 cm portion of the column was repeatedly scanned (V_S = 2.4 cm/s, *f = 1000* Hz*,* resolution 0.04 mm) using successive unidirectional scans 22.3 s apart. The results are shown in Figure 5-4. With each scan, the analytes further progress down the length of the column. As we are looking at the column with injection/exit ends respectively at left/right, appearance of the bands are mirror images of that displayed by an end column detector. In scan 35, the void dip has just moved into our view window. By scan 43, all analytes are visible, although two pairs (1,2 and 5,6) are unresolved. By scan 51, the void is about ready to move out of our view while 1 and 2 are now resolved. The present column is 60 cm long. It would be apparent that separation was complete by the end of our window at 20 cm; with an end-column detector we will only see greatly

broadened bands, at least under isocratic conditions. With a programmable-position detector and the knowledge as to when the desired separation is complete allows one to save time by performing quantitation on the first occasion the band(s) of interest have been completely separated from the others and then flushing the column out. An example is shown in Figure D-S10. With slow responding detectors, the sensitivity difference between stationary and moving operation is substantial and the likelihood of peak distortion is very significant (Figure D-S11). For quantitative analysis, it will be advantageous to move such a detector in programmed punctuated stationary positions to intercept a peak that has just been separated.

In the present application conductance is the major contributor to the admittance signal. An ion displays much greater mobility in solution than in stationary phase-bound form.[152] As such, OT ion chromatography where the phase ratio (defined in the present case as the ratio of the ion exchange equivalents in the mobile phase to that in the stationary phase[159]) is usually much larger than for a packed column, is more compatible with admittance detection. Although the sensitivity is distinctly poorer for a packed column, it is still possible to follow a separation. Figure D-S12 shows serial scans on a commercial 0.4 mm i.d. anion exchange column depicting the separation of chloride and bromate. Interestingly, Figure 5-4 or Figure D-S12 gives the impression is that the bands are too broad relative to what will be seen in a reasonable efficient chromatogram. This is an illusion. The AS11 capillary 11 for example has a specified plate count of 22000 plates/m, at 20 cm it should thus have 4400 plates. If we were to express the plate

count as $16*(20/w_b)^2$ where w_b is the base-width of the peak *on the column* in cm, w_b will be 1.2 cm.

5.4.5 Formats of Presenting a Dynamic Separation

Chromatographic data in the present system are generated in a new format, we are not as yet sure of the best mode(s) of presentation. Obviously, successive images can be stitched together to make a movie (the SI contains two files: illustrative scan.avi and Figure 5-4.avi; the first comprises of more than 150 scans) and can reveal features on a dynamic basis that is not possible to depict, at least as clearly, in a temporally static fashion. For example, one often observes "active" spots on the column - where analytes "slow down", and that this is more pronounced for some analytes than others. Another static mode of temporal presentation of the chromatographic process is simply the visualization of the raw numerical data in Microsoft Excel™ using *conditional formatting* which allows one to highlight cells in color schemes that rely on their numerical values. One example, shown as the TOC graphic, is reproduced as Figure D-S13; another color scheme is shown in Figure D-S14.

5.4.6 Retention factor

Imaging in the present system being similar to that in TLC, the retardation factor R_f can be defined similarly:

$$R_f = \frac{d_{m,t}}{d_{a,t}} \quad \ldots(1)$$

where $d_{m,t}$ is the distance the mobile phase front has reached in time *t* as indicated by the location of the void dip/peak and $d_{a,t}$ is the location of the analyte peak of interest at time *t*. It will be recognized that the retention factor *k* in current HPLC nomenclature is simply $R_f - 1$. While we can estimate *k* by simply taking the positions of the injection void and the analyte peak obtained during a scan, the imaging is not instantaneous: if the analyte peak location $d_{a,t}$ is imaged at time *t*, the mobile phase front is not imaged until a little later time *t'* (i.e., what is measured is $d_{m,t'}$); the difference *t'* - *t* being the interval for the sensor head to travel from the analyte peak to the void. The error committed by taking $d_{m,t'}$ as $d_{m,t}$ and the resulting error in *k* can be significant if the mobile phase velocity (V_m) cannot be neglected relative to V_s. In such a case, the appropriate expression for *k* is given by (See SI for derivation):

$$k = \frac{(V_s - V_m)(d_{m,t'} - d_{a,t})}{V_s d_{a,t}} \quad ...(2)$$

Figure 5-5 shows the plots of *k* values for a mixture of 7 anions dissolved in water injected into a Na-Salicylate eluent. Similar data except for the analytes dissolved in the eluent appear in Figure D-S15 and comparisons for selected anions are shown in Figure D-S16. Predictably, the *k* values begin at a higher level when the sample is in water but eventually converge to the same values. In both situations, however, the analytes initially display much higher retention. In an open tube, retention is dependent on mass transfer to the wall. Steady state flow in such small capillaries are highly laminar. However, laminar flow is the least efficient vector for transport to the wall. The injection of the sample in the present system is followed by a period to

flush out excess sample. During this interval there is no flow through the column. When chromatography begins, flow in the column starts from near zero. Mass transfer to the wall during the finite time and length needed to establish laminar flow is more efficient than at steady state and leads to the observed higher *k* values.

When the injected sample is dissolved in water, the change in chromatographic characteristics from the inlet region to the steady state has another contributor: the eluent strength initially experienced is much less than that further down the column because of the dilution of the eluent by the sample matrix. At the beginning of the column, *k*'s are much higher and reach a stable value as the steady state eluent concentration is reached (Figure 5-5); the inlet region essentially experience gradient elution. This "inlet effect" is smaller when injected analytes are dissolved in the eluent (see Figures D-S15, D-S16): the equilibration is more rapid (see, e.g., by 8 cm from home, k_{chlorate} is stable when the sample matrix is the eluent but continues to fall when the sample is in water, eventually reaching the same value). In a larger bore column, the inlet effect zone is even longer (compare Figure D-S17 with Figure 5-5).

The order of elution of divalent-monovalent analyte pairs often change in the inlet zone from the time they are first seen by the detector. Both thiosulfate and sulfate bands are initially seen ahead of perchlorate and iodide respectively. As they progress, the monovalent anions catch up, merge and then move ahead (Figures D-S16a,c, D-S18, this is dynamically seen in Figure 5-4.avi). It is well known that ions of different charge are differently affected by a change in the eluent ion concentration. The observed *k* for strongly retained analyte ions like perchlorate is

also strongly affected by the injected concentration due to self-elution, especially initially (Figure D-S19).

5.4.7 Improving Signal to Noise Ratio (SNR) through Stopped-Flow Multiple Scans and Signal Averaging

Being able to use the column as a separation canvas permits stopped-flow signal averaging to improve detection and quantification for analyte peaks with poor S/N, thanks to very slow liquid phase diffusion. Generally only a limited number of peaks requires such treatment and the whole column need not be scanned. Figure D-S20 shows that signal averaging a 2.5 cm zone centered on a low concentration thiosulfate peak (*n*=10, taking 51 s) improved the SNR by a factor of 3.14 almost exactly the theoretical gain of 3.16. Further averaging and SNR increase is possible because the signal is oversampled (see SI for details).

5.4.8 Other Applications. Imaging Column Packing Homogeneity

Admittance scanning is well suited for ascertaining the uniformity of the bed structure of a packed column. Figure 5-6 shows the data for two commercial packed capillary columns, a 5 µm C18 silica filled with 0.75-1.5 mM KCl solution for visualization and a larger bore anion exchange column filled with 4 mM Na-Benzoate. Ions in the interstitial mobile phase as previously noted have greater mobility and contribute more to the admittance signal than do adsorbed/bound ions, the scanned image across the column provides a picture of the homogeneity of the packing, with a greater signal indicating a greater void fraction. While this concept is not new [161] automated scanning makes this far more practical. The spatial features are highly

reproducible, as demonstrated in Figure D-S21 and D-S22. In numerous column scans, we are yet to encounter the ideal perfectly packed column. In general, most columns appear to be better packed in the bottom half than the top half. The present system allows probing nonuniformity even for an OT column (Figure D-S23).

5.5 Conclusions

An admittance detector was adapted to a motorized linear stage able to provide imaging admittance detection for both open tubular and packed capillary columns and permitting visualization of IC separations in real time. The detector can also be operated in punctuated stationary mode, positioning it to quantitate an analyte after it has just separated from others, combining the merits of both stationary and scanning detection. For an analysis that may be legally important, a scanned column can be archived. Desired regions of a column can be repeatedly scanned to improve S/N.

Tallarek, Guiochon and others used NMR imaging to look into how an analyte distributes three-dimensionally in the entrance region of a packed column,[162-164] for an ionic analyte, similar insights, but in a 2-D manner can be obtained presently, in arguably a much simpler manner. Similarly, it allows one to check the uniformity of a packed or open tubular column, even the presence of active sites or “hotspots”. As with any new technique, the full potential of admittance imaging or other scanned imaging approaches will only be known in time. However, the following are already apparent: An end-column detector only sees what elutes while the present approach can also see what is perhaps not moving from the column head and take appropriate action. The admittance image of a column over time is its ongoing column health

status report: a shift in the packing structure or irreversible binding is likely to change the image, of potential significance to quality control.

Absorbance or fluorescence detection based on a fiber optic based scanning detector and a transparent column should be straightforward. Because scanning WCD generates serially evolving images of a column adding each time to the available data, repetitive analysis situations (e.g., in quality control) where known analytes with known retention/migration behavior are involved, rapid, mathematically deconvoluted quantitative analysis[165,166,] should be possible on the fly, long before full physical separation has been attained.

5.6 Associated Content

Supporting Information

Response characteristics and spatial resolution/reproducibility of two admittance detectors, images of dispersion along a column, stationary vs. moving detection, serial scanned images of separations in different formats, derivation of eq 2, retention factors at various column locations, improvement of SNR by repeat scanning, Uniformity of packed and OT columns along their length.

5.7 Author Information

Corresponding Author

* E-mail: Dasgupta@uta.edu. Fax: 817-272-3808.

5.8 Acknowledgement

This work was supported by National Science Foundation (CHE-1506572), NASA (Grant No. NNX11AO66G and 15AM76G) and Thermo Fisher Scientific. We

acknowledge the gift of packed capillary columns from Column Scientific (Xiamen, China).

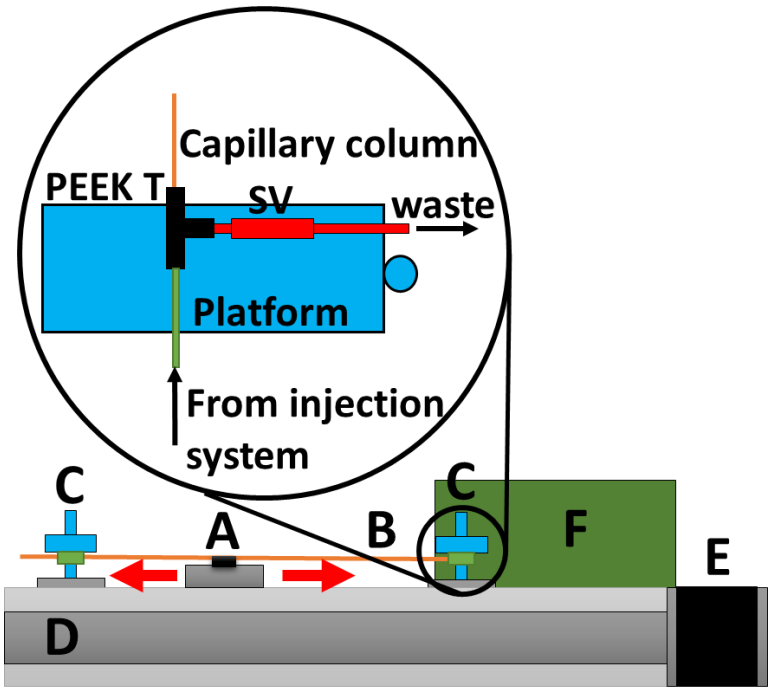

Figure 5-1. Scanning instrument setup

A) A moveable pass-through detector mounted on the moving platform of the linear stage with the capillary column passing through it. B) The capillary column to be scanned. C) Capillary column holders machined from 6061 aluminum. The bottom part attaches to the rails of the linear stage and can be easily moved and then anchored based on the length of the column. Platforms hang over the linear stage with adjustable height to allow different detectors to be used. A PEEK Tee is used at the head of the column to perform injections, while a drilled out union allows the capillary to be fixed in place using a simple nut and ferrule fitting arrangement. D) The linear stage, 1.36 m in length. E) A NEMA24 stepper motor. F) Injection system.

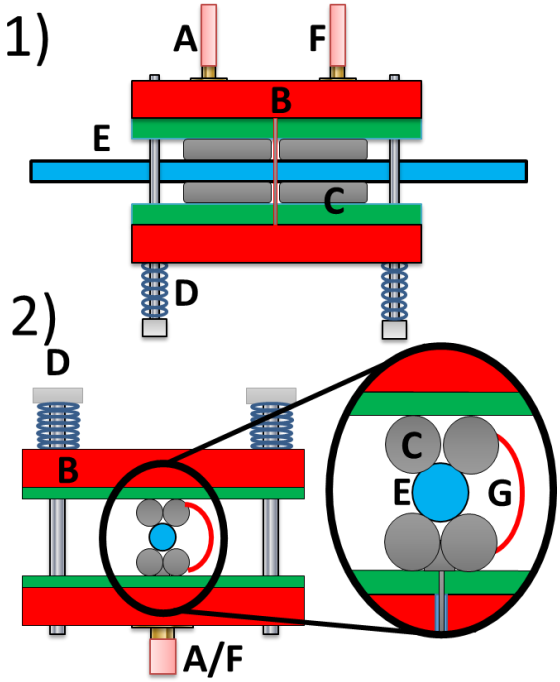

Figure 5-2.1) View of the quadrupole admittance detector (qAD) as seen from above and side

A) Coaxial shielded excitation input (30 V_{pp} excitation voltage) B) qAD stainless steel shielding (red) and insulator (green). C) 1/16” stainless steel Quadrupole electrodes that provide smooth contact with the inserted capillary column. D) Spring tensioners ensure that the quadrupole electrodes stay in close contact with the capillary column. E) The inserted 1/16” PEEK capillary column. F) The pickup electrode that returns to the amplification and rectification circuits. G) Flexible conductor to attach lower and upper electrodes to each other. **2)** View of the qAD along the axis of the PEEK column.

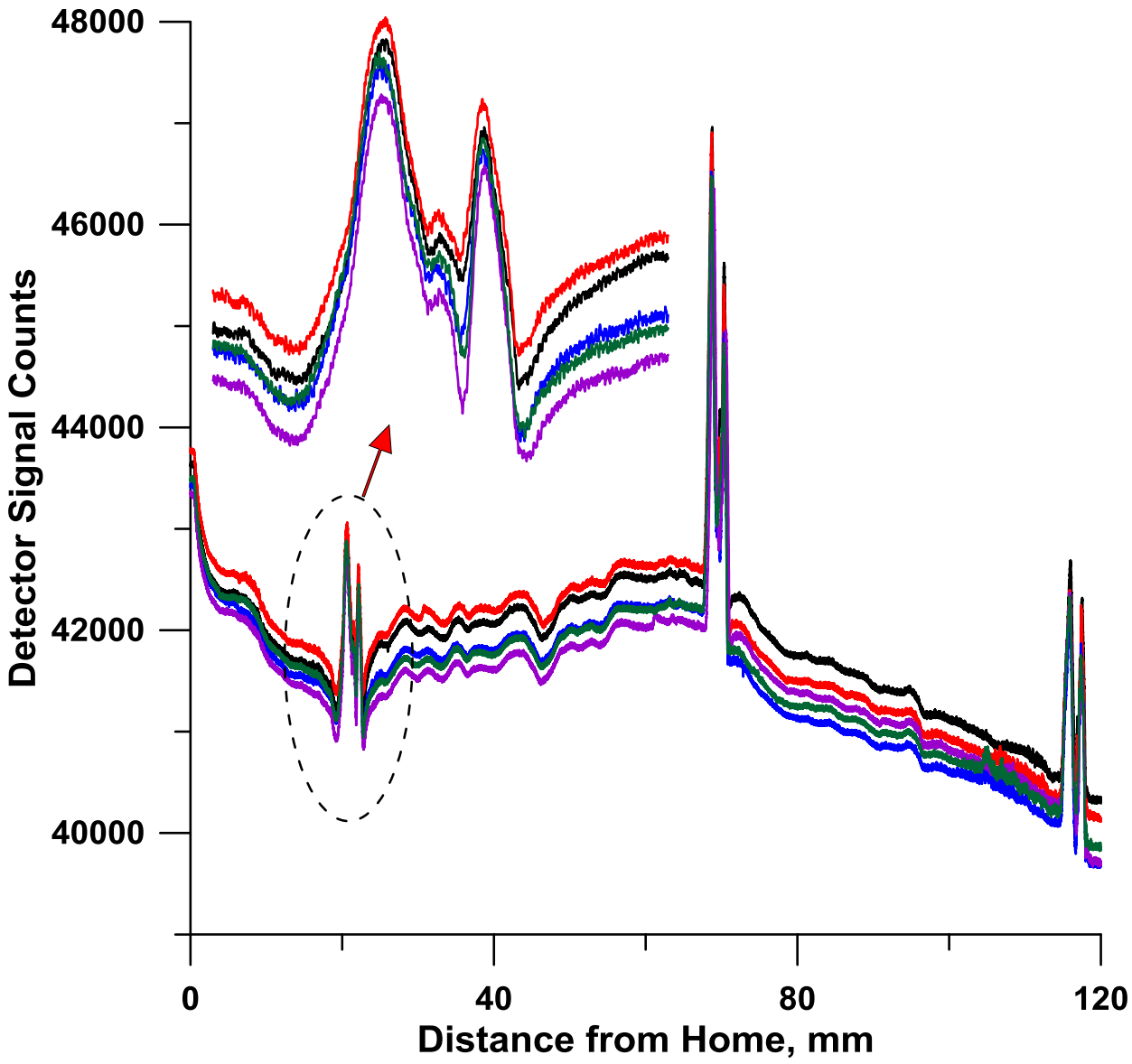

Figure 5-3. Three ~ 2 mm metallic ink marks made on a silica capillary ~5 cm apart and scanned five times
with the AF AD at 4 mm/s, data acquired at 1 kHz. The top left inset shows a magnified view of the responses to the first mark. Note the reproducibility of the baseline trace.

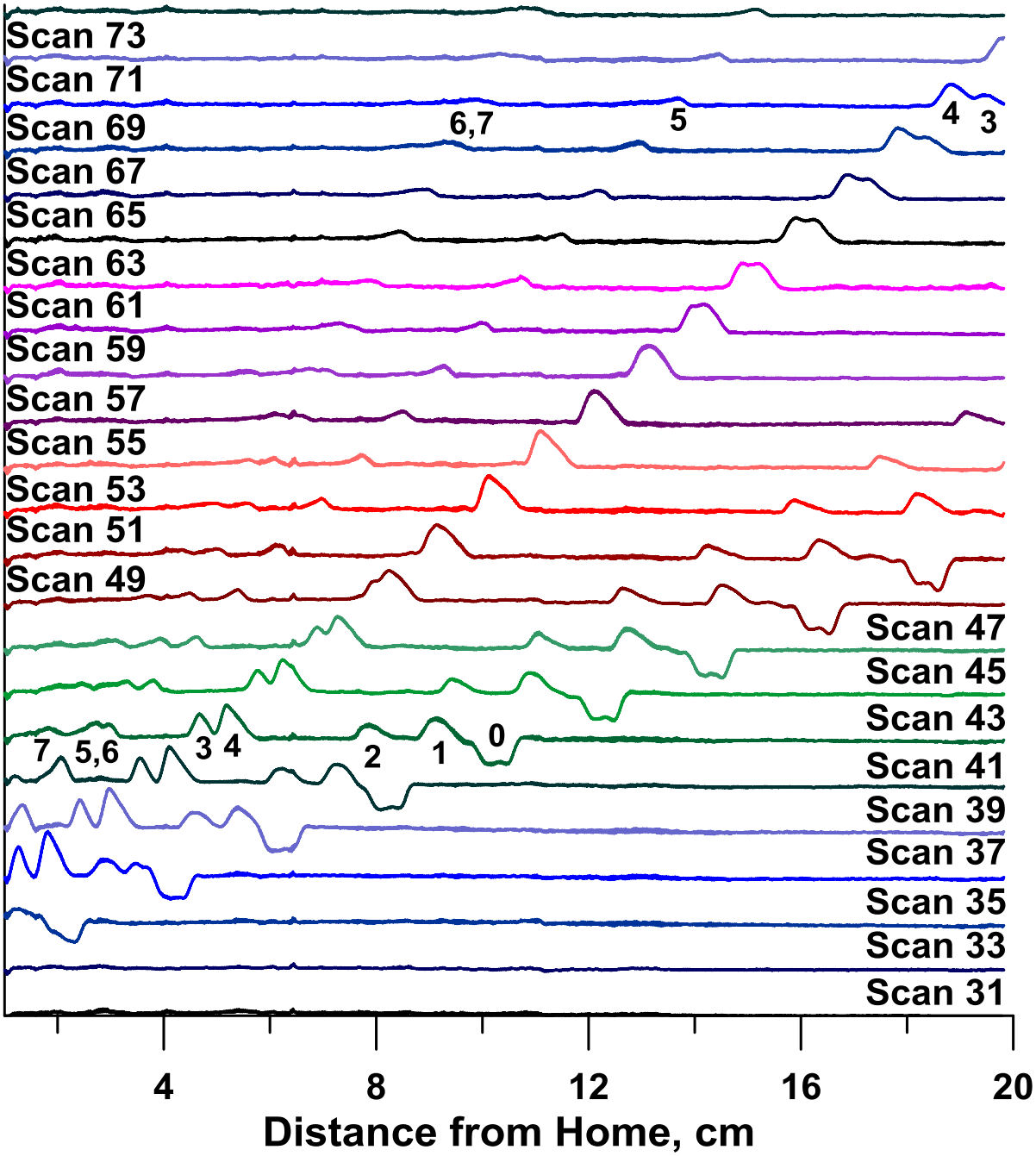

Figure 5-4. Repeated scans on 20 cm length of a 11 μm id, 360 μm od AS18 latex coated silica capillary of total separation column length 60 cm

Injection: 430 pL of 500 μM each of Cl^-, ClO_3^-, I, SO_4^{2-}, SCN^-, ClO_4^-, $S_2O_3^{2-}$ (numbered analytes 1-7 in that order). Eluent, 6 mM sodium salicylate; flow rate, 5.2 nL/min (mobile phase velocity 0.1 cm/s), V_s 2.4 cm/s. Each scan 8.3 s; interval between unidirectional scans 22.6 s, Analytical Foundry detector, spatial resolution 0.04 mm. The scan numbers appear (odd numbered scans imply away from home) on *top* of each trace. Peak 0 is the void.

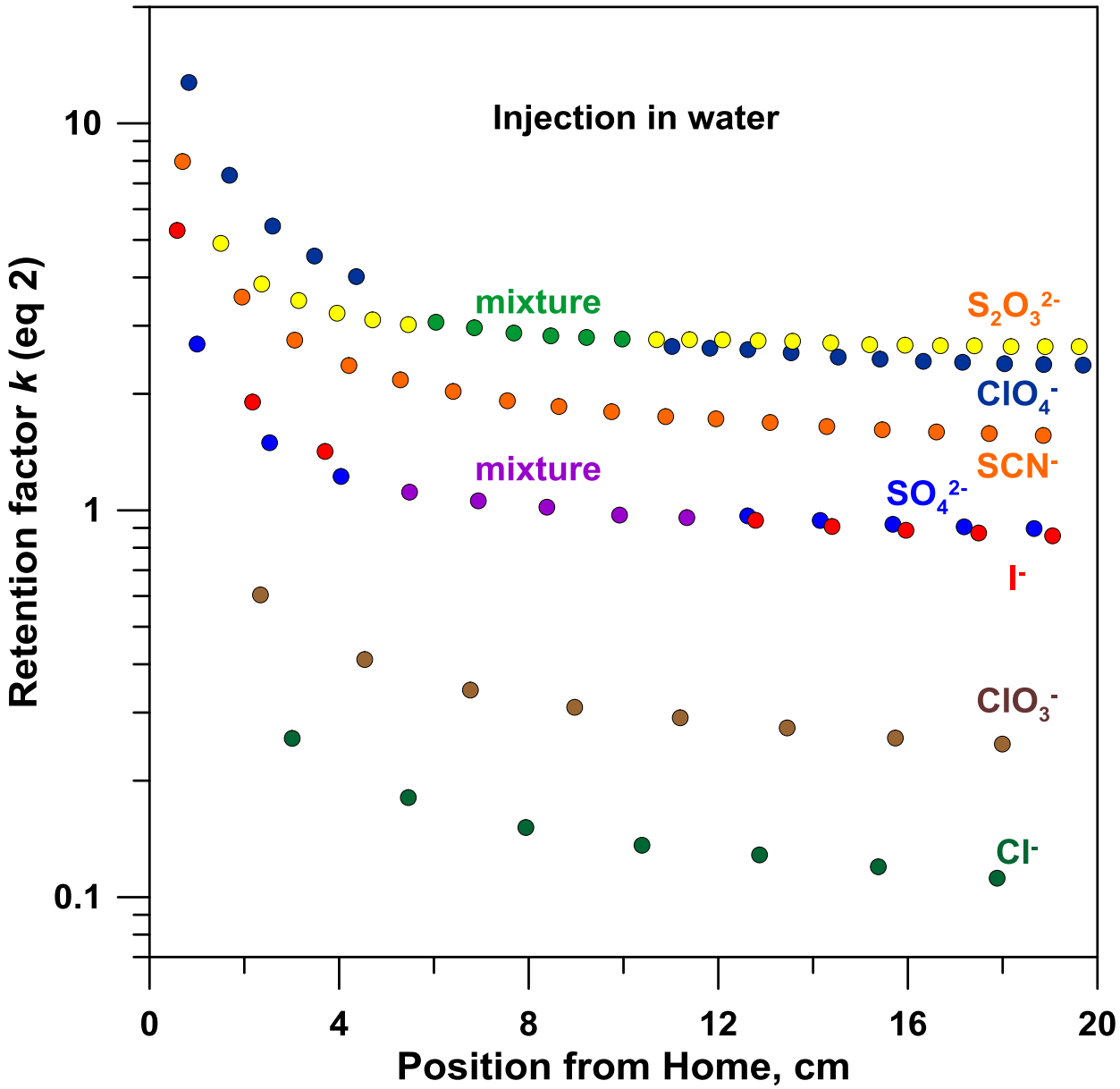

Figure 5-5. Retention factors calculated according to Eq. 2 for the data in Figure 5-4

At the beginning of the scan window the retention factors for all analytes are much higher than at the end. This is due to initial separation in the absence of eluent. One reason for this is that sample is dissolved in water, there is essentially no eluent in the beginning and the eluent gradually penetrates into and mixes with the sample zone, virtually creating a gradient. The second reason is that any departure from laminar flow leads to better mass transport to the wall. In the present system, after sample introduction, flow abruptly starts from essentially zero. The higher *k* value in the inlet zone reflects better mass transfer to the wall before laminar flow fully develops.

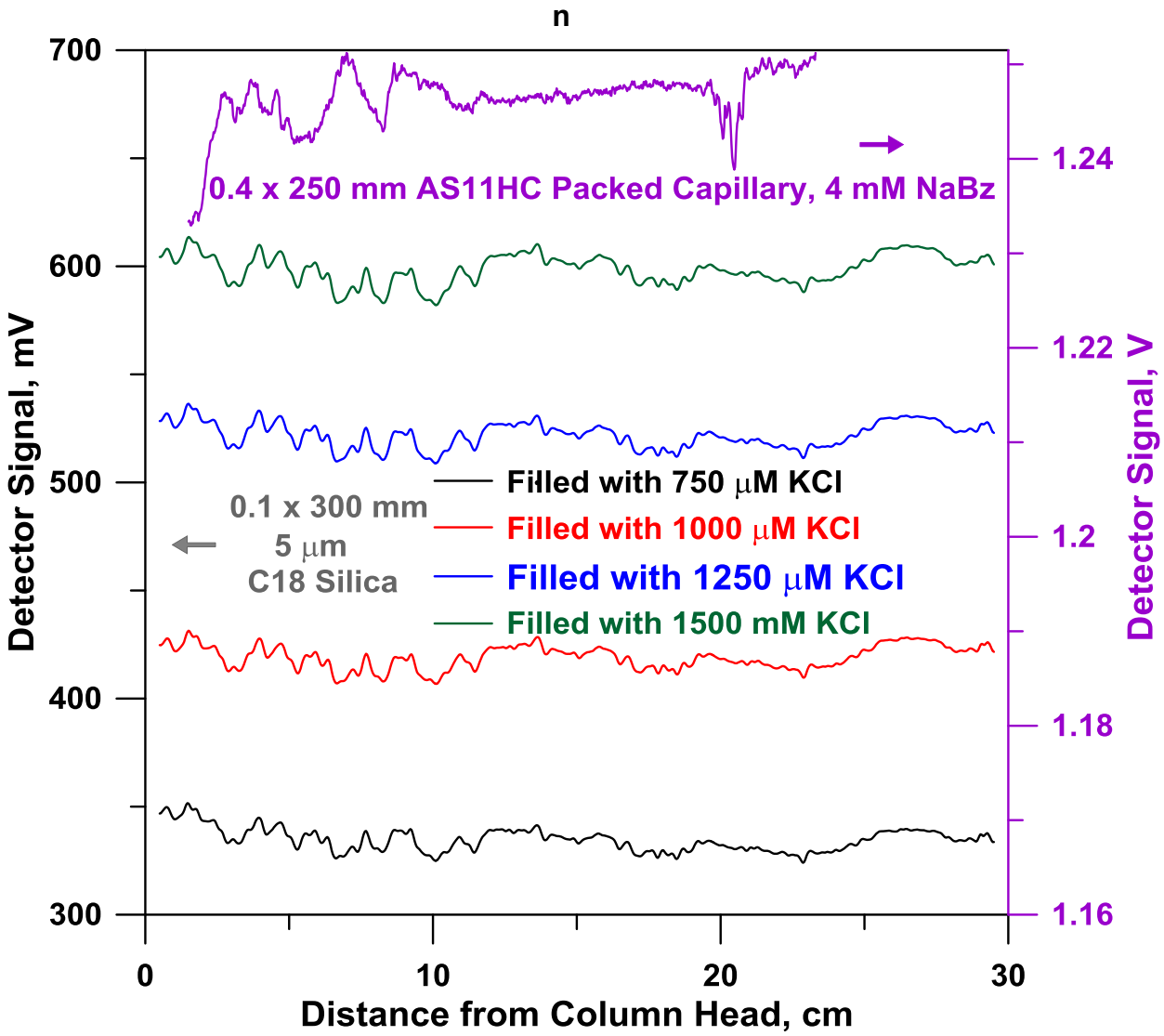

Figure 5-6. Packed column scans to determine packing uniformity

The bottom four scans (left ordinate) are of the same column filled with KCl solutions of different concentrations. Sufficient solution was passed through each time to have a new medium each time. The top scan is that of a larger i.d. packed capillary anion exchange column.

Chapter 6 Portable Lightweight Ion Chromatograph

Brian N. Stamos, Weixiong Huang, Purnendu K. Dasgupta*

Department of Chemistry and Biochemistry, University of Texas, Arlington, TX 76019

*Corresponding author: Phone (817) 272-3171, Email: Dasgupta@uta.edu, Fax: (817) 272-3806

6.1 Abstract

We report a battery powered ion chromatograph that weighs less than 3 kg with on-board rechargeable Li-ion batteries that provide power for 18 hours of operation. It is contained in an Aluminum case measuring 30 x 25 x 16 cm. Separation relies on open tubular chromatographic columns which eliminate the need for high pressure pumps, drastically reducing weight and complexity. Eluent consumption is less than 100 µL per separation. Eluent is supplied from a pressurized vessel connected to a compressed gas cylinder, similar to ones used to inflate bicycle tires, via a voltage-controlled electronic pressure controller. Flow rates are typically < 200 nL/min which allows a single 16-20 g gas cartridge to perform hundreds of separations. The flow rate is linearly proportional to applied pressure. A release valve provides for rapid reduction of pressure. Three low power miniature solenoids, which can operate up to 800 psi, provide variable volume injection capability and further reduce weight and size. Both pressure and injection times are used to control injection volume, typically in the pL – nL range, depending on the capillary size (typically 10-30 µm) in ID. Typical column lengths are 30-75 cm and 100-150,000 plates/m are generated. Separation of 5 common anions takes less than 5 min, with the separation window itself being less than 2 min. The limits of detection are in the low µM range. The design also includes a novel admittance detector design with full microprocessor control. Additional configuration and data readout can be performed with a USB-connected computer.

6.2 Introduction

Field portable analytical instrumentation has been a growing area over the past few decades. Aside from defense and homeland security related uses, the focus has generally been on the analysis of soil composition both in regards to nutrients and pollution, and testing of water quality. Portable instrumentation obviates the need for sample collection, transport and storage. Compact power and size-efficient instrumentation is also the key to planetary exploration knowledge. The Sample Analysis at Mars (SAM) instrument carried by the Curiosity Mars rover contains a mass spectrometer, gas chromatograph and laser spectrometer. All told, the rover contains 11 different instruments and instrument suites. Perchlorate is of particular interest as large concentrations on the surface of Mars were measured by the Phoenix lander.[167] This has apparently been confirmed by the instruments on the Curiosity rover as well.[168] The Atacama Desert represents the closest terrestrial habitat to that of Mars[169] with less than 2 mm of precipitation annually[170] in addition to relatively large amounts of perchlorate present in the soil. The ability to analyze complex samples and to operate without human involvement, in addition to low weight and power consumption, are crucial in these applications.

There has long been interest in field portable ion chromatographs with examples dating back to 1987 by Tsitouridou et al.[171] These early systems did not feature suppression nor were they what would be considered lightweight. The first portable system that would be recognized as a modern ion chromatograph came in 1998 from Boring et al.[172] This system was the first to feature an electrodialytic eluent generator

in addition to a hollow fiber suppressor. This design however still used packed capillary columns requiring a heavy syringe pump. Total weight without batteries was 10 kg with a power requirement of ~17.5 W. In that same year Kappes et al.[173] introduced the first field portable capillary electrophoresis (CE) instrument. Compared to packed columns, CE has the advantage of using open tubular capillaries and requiring no pumps but a high voltage source. Weight and complexity are drastically decreased without the need for a pump. Including batteries the entire system weighed 7.5 kg. Kiplagat et al.[174] introduced the first portable open tubular ion chromatograph (OTIC) in 2010. The system could only separate cations. As the entire system was manually operated there was little power consumption. There was however no eluent generator/suppressor meaning that only non-suppressed IC could be performed. Samples had to be manually injected. Weight however came in at 2.5 kg including a netbook for acquisition. The most recent and complex publication for a field portable IC comes from Elkin. Weight was sacrificed for the ability to continuously collect and analyze water samples for 27 days or about 1370 injections. The system weighed 27.5 kg with batteries and solar cells.

In this paper we present a fully field portable open tubular ion chromatograph that weighs less than 1 kg with an additional 2 kg of batteries that can power it for 18 hours of continuous use. On a spacecraft it will tap into an existing power bus; even on earth many applications will permit to be umbilically connected for power to an automobile.

6.3 Experimental Section

6.3.1 Chemicals

Sodium salicylate (as eluent) and chloride, chlorate, perchlorate, iodide, thiocyanate, sulfate and thiosulfate, as sodium or potassium salts as test anions were all reagent grade and used as received (www.fishersci.com). House distilled water, passed through an ARIES water purification system (www.ariesfilterworks.com) provided water of 18.2 MΩ*cm^{-1} specific resistance. All solutions were filtered with (0.2 μm) before use.

6.3.2 Instrumentation

The pressure source was a bottle of compressed gas duster (Keyboard cleaner, Office Depot, etc). The pressure vessels were machined from poly(methyl methacrylate) (PMMA) with an internal volume of 10 mL and tested to a pressure of 100 psi. All tubing used was PEEK purchased from IDEX (www.idex-hs.com). The miniature electronic pressure controller (990-005103-050) (EPC) was obtained from Parker (www.paker.com). The solenoid valves (INKX0508600A) were purchased from the Lee Company (www.theleeco.com). The solenoid valves are actuated using Texas Instruments (www.ti.com) DRV8841 integrated circuit chips in a half bridge driving configuration. The columns consisted of polyimide-coated fused silica capillaries (15 μm I.D. and 365 μm O.D.), PMMA capillaries (15 μm I.D. and 365 μm O.D.) purchased from Polymicro (www.polymicro.com) or Cyclo Olefin Polymer (COP) capillaries (19 μm I.D., 360 μm O.D.) extruded by Paradigm Optics

(www.paradigmoptics.com) coated with AS18 latex (www.dionex.com) after sulfonation as previously reported[175].

Detection was carried out using a in-house built admittance detector (AD) similiar to a design previously reported[176]. The major change was that a square wave excitation signal was provided by a Cypress Programmable System on Chip (PSoC5LP), programmable from 50 Hz – 1 MHz at 0-5 V p-p. Any DC bias in the signal was removed through a 44 nF capacitor in series and then amplified by a dual JFET operational amplifier (TL082CN, www.ti.com) to 30 V p-p.

All data were recorded using the onboard 20-bit ΔΣ analog to digital converter (ADC) of a Cypress PSoC (www.moeller.io). Power was supplied by three 15 V lithium battery packs with a capacity of 3000 mAh in series to provide -15, +15 and +30 V with additional potentials supplied through buck converters (LM2596, www.ti.com). Constant current for the suppressor and eluent generator were supplied by integrated circuit current sources (LM334, www.ti.com) with digital potentiometers (AD5293-20, www.analogdevices.com) for microprocessor controllable output.

6.3.3 System Control

The system can be controlled with the onboard PSoC preprogrammed. Alternatively it can be connected through USB to a personal computer running a custom LABView (www.nationalinstruments.com) program to control it. The PSoC not only records the voltage signal from the admittance detector through its 20-bit ΔΣ ADC but also

controls the solenoid valves, the gas valve, the EPC and the current through the suppressor/eluent generator.

6.3.4 Atacama Desert Sample Preparation and Analysis

Samples were sieved to obtain a <2 mm fraction. This fraction was then thoroughly ground with a mortar and pestle. 1 g of crushed soil fraction was then extracted with 20 g of Milli-Q water and diluted 10 times. Samples were spiked with 12.5 µL of 1 mg/L $^{35}Cl^{18}O_4$ as the internal standard.

The IC-MS/MS analysis protocol used an IC-25 isocratic pump with an EG40 electrodialytic eluent generator, 2 mm bore AG21/AS21 guard and separation column sets housed in a LC30 temperature controlled oven (30 °C), ASRS-Ultra II anion suppressor in external water mode, and a CD-25 conductivity detector, all from ThermoFisher/Dionex. Around the elution window of perchlorate (t_R ~45 min), 40 min after injection, a diverter valve directed the CD25 effluent to a tandem mass spectrometer (Thermo Scientific Quantum Discovery Max with a heated ESI probe and enhanced mass resolution). Electrodialytically generated high purity KOH eluent was used in gradient mode at a concentration of 5 mM to 80 mM and a flow rate of 0.35 mL/min. Eluent generation, sample injection (5 µL), electrodialytic suppression, autoranging conductivity detection and data acquisition were all conducted under Excalibur/Chromeleon software control. Perchlorate was quantified by the −99 → −83 Th (m/z) transition ratioed to the −107 → −89 Th internal standard transition. All data were interpreted in terms of a 5-point calibration with check standards run daily.

Any sample falling outside the calibration range was reanalyzed after appropriate dilution. All samples were minimally analyzed in triplicate.

6.4 Results and Discussion

6.4.1 System Design and Operation

A simplified drawing of the portable ion chromatograph (PIC) is shown in Figure 6-1. The pressure is supplied from either a compressed air canister or from a compressed N_2 cylinder depending on field use or laboratory use. Canned compressed gas electronics dusters contain di- tri- or tetrafluoroethane, these are inert water-insoluble gases that do not add to background conductivity. Such cans provide pressures greater than 60 psi and can last for several hundred injections. The pressure source is connected to the electronic pressure controller (EPC) to modulate the applied pressure to the pressure vessels (PV) Typically between 14 and 50 psig. Pressure Vessel 1 (PV1) contains the eluent, typically sodium benzoate (NaBz), sodium salicylate (NaSal) or sodium hydroxide (NaOH) while PV2 holds the sample to be injected. The gas valve (GV) can be used to quickly vent the pressure in the PVs. To save weight and power consumption, there is no traditional six-port injection valve. Instead, three solenoid valves (SV) 1-3 control the injection and chromatographic process. The separation column is connected to a PEEK T at the injection end and terminates in an admittance detector.

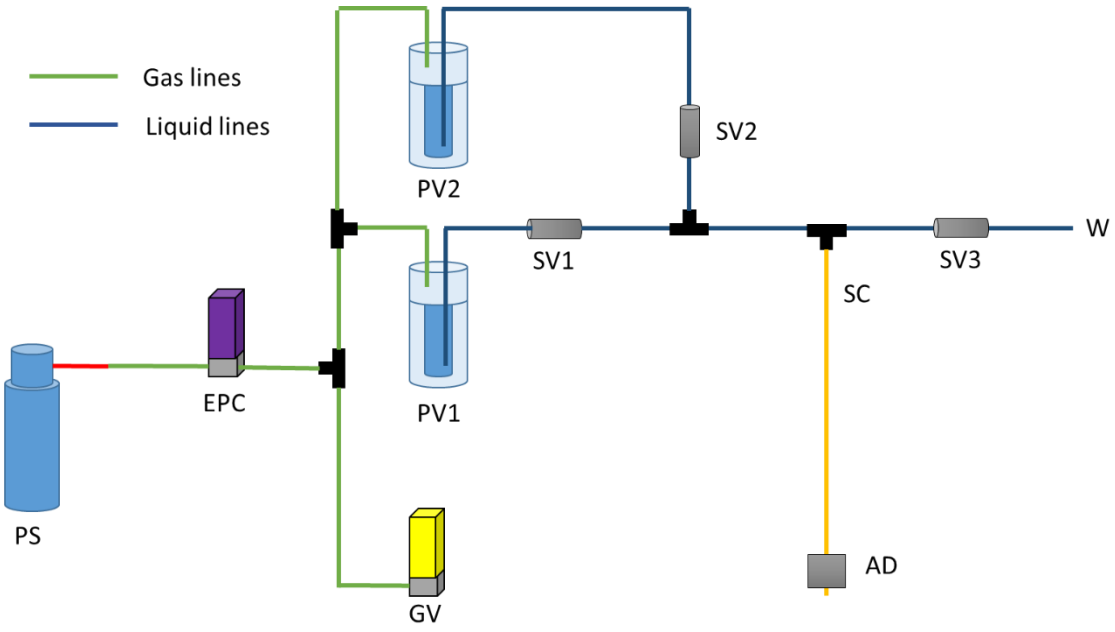

Figure 6-1. Instrument Schematic.
Pressure supply (PS), Electronic Pressure Controller (EPC), Gas Valve (GV), Pressure Vessels (PV), Solenoid Valve (SV), Waste (W), Seperatory Column (SC), Admittance Detector (AD).

An overview of the typical sequence of operations performed during a single sample analysis is given in Table 1. The first step prepares the system for injection by stabilizing the pressure and ensuring that all solenoid valves are in the correct position. Injection is performed in 4 discreet steps. See SI figure 6-3 for clarification. In the analyte sample plug loading step, SV2 and SV3 are opened and pressure is applied to PV2 which pushes the sample to the head of the column. In the injection step, SV2 and SV3 are closed and SV1 is opened. The amount of sample injected is based on both the pressure applied as well as the time it is applied. Injection volumes are typically 0.2-1 nL based on sample concentration and column bore. After injection, SV1 and SV3 are opened to allow eluent to flush out the sample. Finally, only SV1 is opened, forcing the eluent through the column to begin the

separation. The recording of data is also commenced at this point. After the run is finished, SV1 is closed and GV is opened to release pressure. This is done to ensure that when a new run is started the applied pressure is accurate. Finally, all valves are closed and the pressure is set to 0.

The entire instrument including the batteries is in a 12 x 6 x 6 in case and weighs under 3 kg. The batteries are sufficient for over 18 hours of continuous running. The design can be altered to run at a constant pressure with slightly larger solenoid valves, reducing the total fabrication cost to construct to less than $500.

Table 6-1

Step	Operation	Duration	Settings					
			SV1	SV2	SV3	GV	Pressure	Acquire
1	Stabilization for injection preparation	10 s	Closed	Closed	Closed	Closed	14 psi	No
2	Analyte sample plug loading	750 ms	Closed	Open	Open	Closed	14 psi	No
3	Analyte injection	Variable	Open	Closed	Closed	Closed	Variable	No
4	Eleunt flush to remove sample plug	750 ms	Open	Closed	Open	Closed	14 psi	No
5	Separation	Variable	Open	Closed	Closed	Closed	Variable	Yes
6	Release excess pressure	1 s	Closed	Closed	Closed	Open	0 psi	No
7	Return to pre-run conditions	1 s	Closed	Closed	Closed	Closed	0 psi	No

6.4.2 Power Consumption

Table 6-2
Power requirements

Component	Power use (mW)
Solenoid Valve	44
Solenoid Driver	41
Pressure Regulator	864
PSoC	77
Detector	204

Power consumption must be left to a minimum so that they instrument can run for as long as possible on battery supply. From Table 6-1, the total power consumption is 1.23 W during the time chromatography is actually conducted, with one energized solenoid valve. Slightly more power is used during the injection step, but this is a short event and contributes little to the overall power consumption. When idle, power consumption can be reduced to 241 mW by closing all solenoid valves, shutting off the pressure regulator, and putting both the solenoid driver and PSoC to a sleep mode.

6.4.3 Excitation Frequency Optimization

The optimum excitation frequency was determined in an automated fashion by changing excitation frequency in steps while 0.92 nL of 500 µM KCl was repeatedly injected in to a 19 µm i.d. 360 µm o.d. silica capillary. Both maximum signal response as well as signal to noise were evaluated, shown in Figures 6-5 and 6-6. Optimum excitation frequency was found to be 1350 Hz for both maximum peak height and highest signal to noise ratio under these conditions.

6.4.4 Injection Reproducibility

Initially samples were manually loaded with SV1 and SV3 open. The variances in the injected amount were significant; it was difficult to manually control both the pressure applied as well as the length of time that the analyte is loaded. The addition of a second pressure vessel (PV2) allowed a controlled time and pressure to be used. This also made it possible to perform multiple injections of the same

analyte without human intervention. Performance was tested with 2 mM NaBz as eluent and a 60 cm 19 µm i.d. 360 µm o.d. PMMA capillary. Concentration linearity was tested by injection 0.92 nL of F, Cl, NO_2, Br, and NO_3 in concentrations of 100-600 µM for F, 50-300 µM for all other anions as shown in Figure 6-8. Linearity (r^2) was >0.99 for all analytes.

A sub-nanoliter sample (0.92 nL) composed of 200 µM F, Cl, NO_2, Br, and NO_3 were injected 10 times, see Figure 6-7 for chromatogram. For all analytes the % relative standard deviation (%RSD) peak area was < 2%; Table 6-3. Injection time linearity was measured by peak area with injections lasting for 0, 500, 1000, 1500 and 2000 ms or corresponding to 0, 0.2, 0.4, 0.6 and 0.8 nL as seen in Figure 6-9. For all injected analytes, the linear coefficient of determination (r^2) was >0.99. Note that the 0 ms injection time does not correspond to zero volume being injected; a finite amount diffuses into the column as the analyte is moves past the head of the column. From Figure 6-9, this volume was calculated to be 10 pL. It would be apparent that this volume would be linearly related to the actual sample volume that goes past the column head, other things being equal, as this governs the transit time across the column head.

6.4.5 Applications

In September of 2014, 12 samples were collected from the Atacama Desert near Yungay at a site labeled Yungay South.

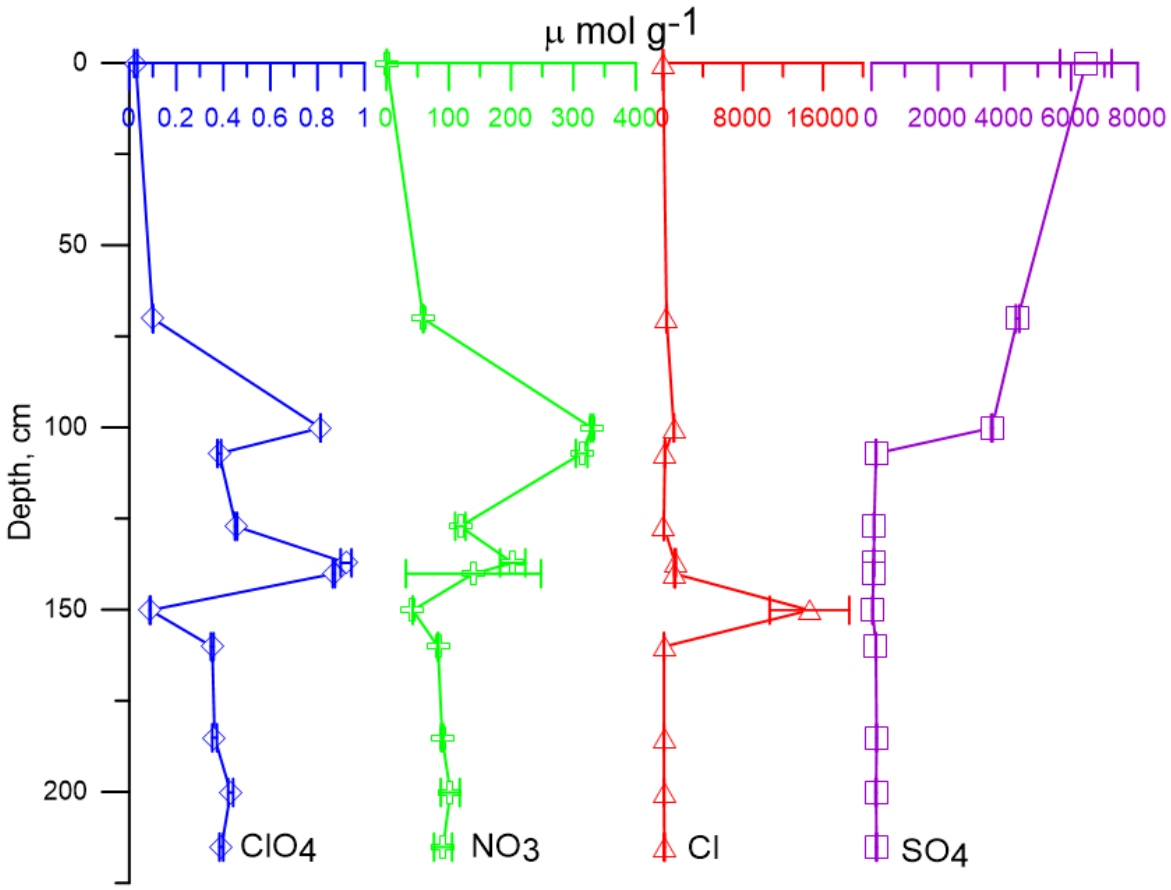

Figure 6-2. Ion concentration depth profile.

Chloride, nitrate and sulfate anions were measured with IC and perchlorate with IC/MS-MS (perchlorate). Of these, sulfate and chloride were the predominant species. Sulfate is the least soluble of the anions and is maximally present at the surface and after 100 cm where there is a dramatic drop off in concentration. The more soluble chloride is present in all samples except the surface, with a primary maximum at ~150 cm (often called the halite layer) and a small secondary maxima at ~100 cm. Despite being more soluble than chloride, nitrate is found only in relatively small quantities in the halite layer, with maxima at 100 and 135 cm. Perchlorate similarly has two maxima at 100 and 135 cm. Perchlorate was below the limit of detection of the portable instrument.

Each sample extract (0.92 nL) was injected on a 19 µm I.D. 360 µm I.D. PMMA capillary column. The Atacama Desert samples from the halite layer (1 g/20 mL water, 1000 times further dilution) were run to demonstrate field usability (Figure 6-10). Carryover was detected in these early run samples, and was corrected in later laboratory testing.

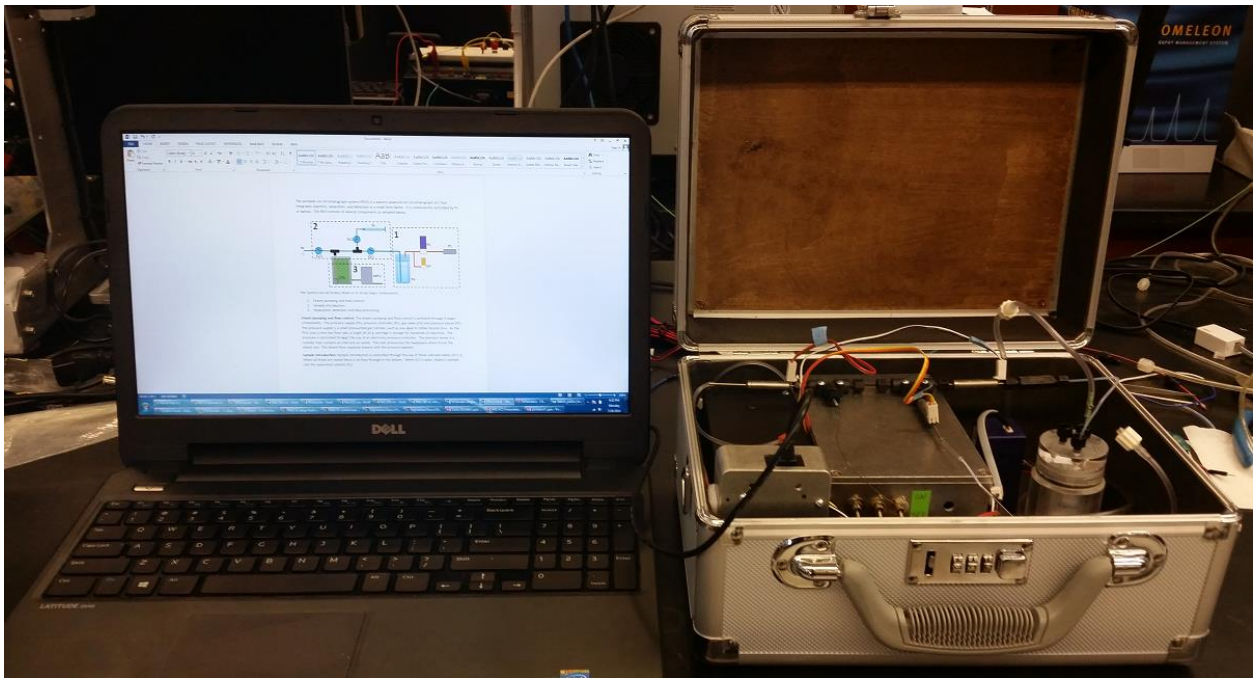

Figure 6-3. Image showing the portable IC next to a 15” laptop for scale.

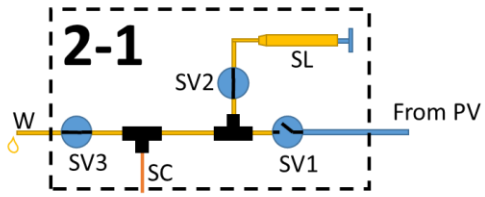

To introduce sample, solenoid valves (SV) 2 and 3 are opened. The sample loader (SL) can then push sample to the head of the separation column (SC)

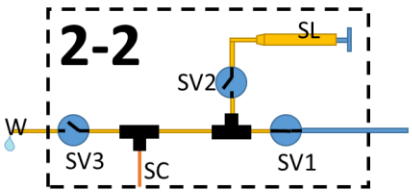

SV 2 and 3 are then closed and 1 opened to push the sample into the column. Sample injection volume is dependent on pressure and time. 1-2 nL is typical.

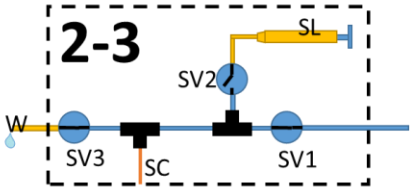

After injection SV1 and SV3 are opened to clear out the residual sample.

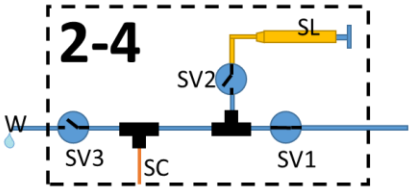

Once eluent is at the head of the column, SV3 is closed to begin separation

Figure 6-4. Injection sequence.

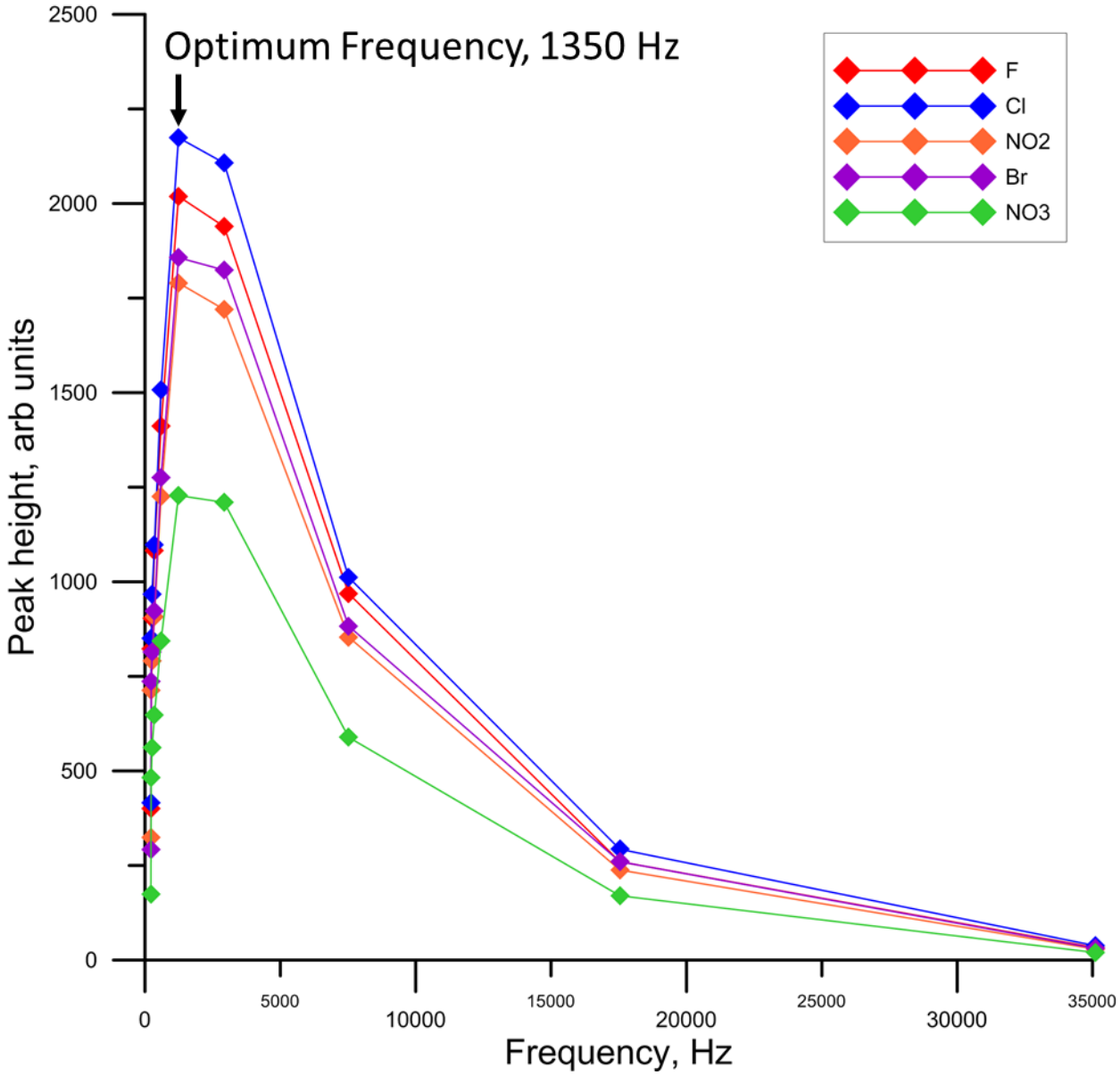

Figure 6-5. Peak heights vs. Admittance Detector frequency.

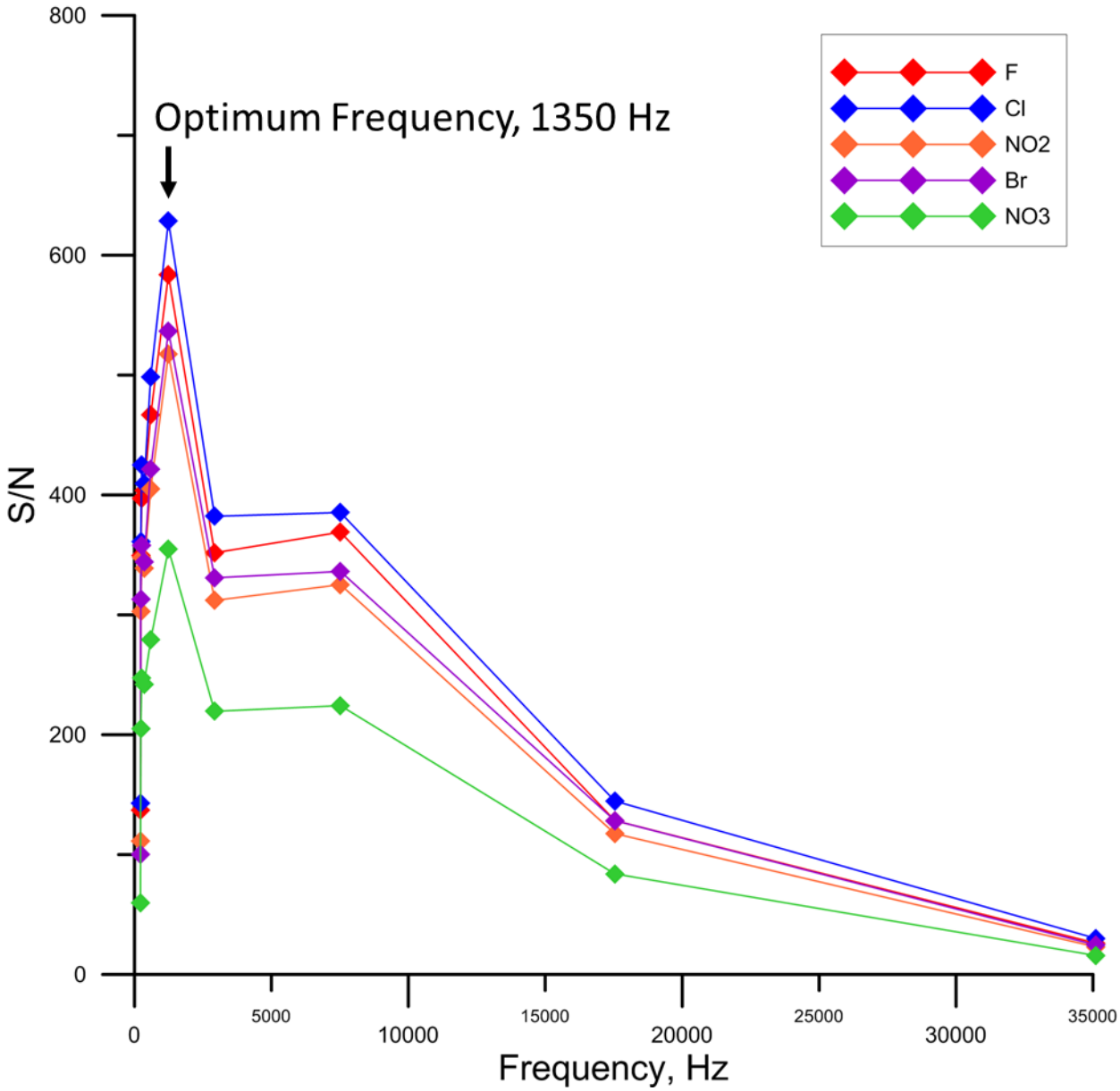

Figure 6-6. Signal to noise for peaks versus Admittance Detector frequency.

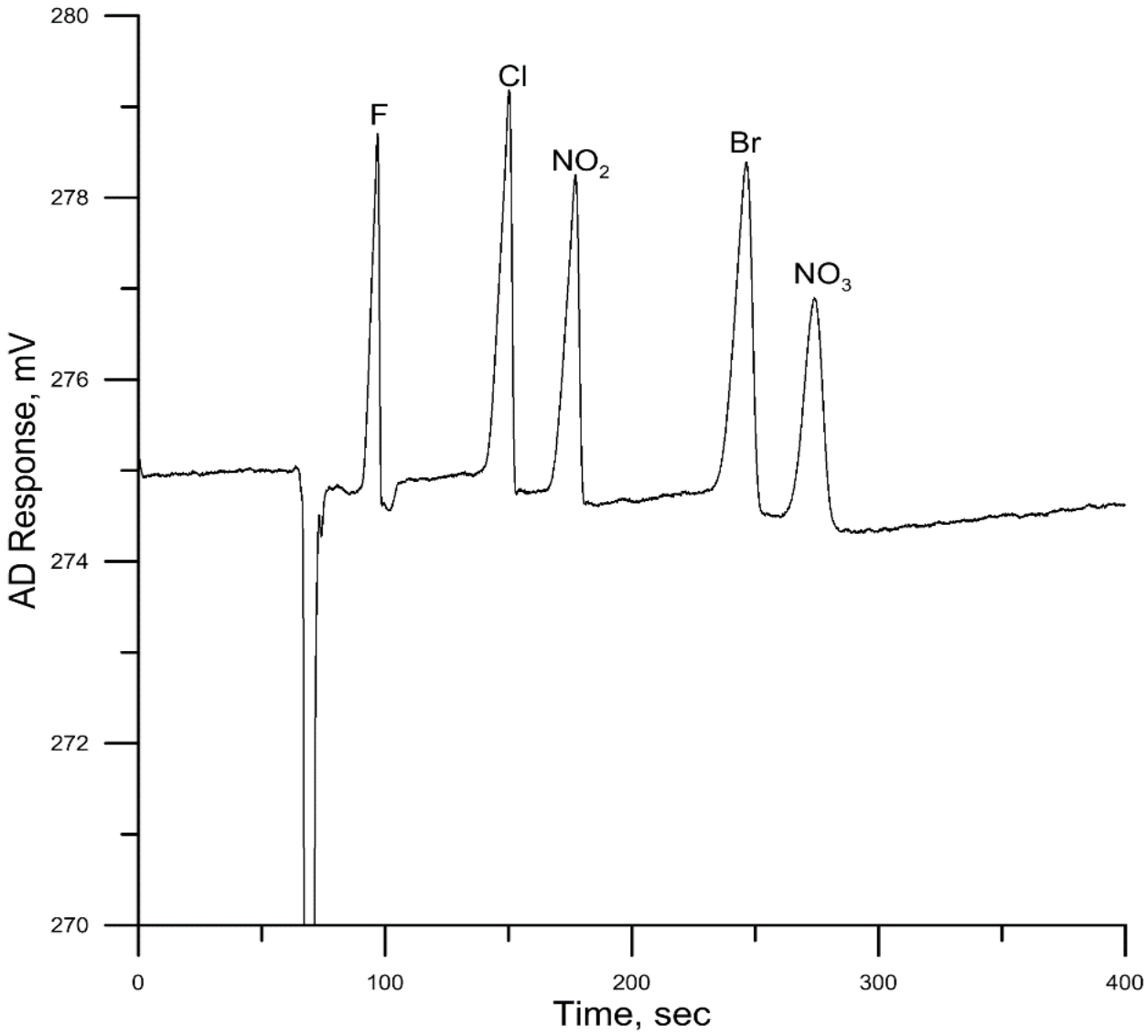

Figure 6-7. Typical non-suppressed chromatogram of F, Cl, NO_2, Br and NO_3.

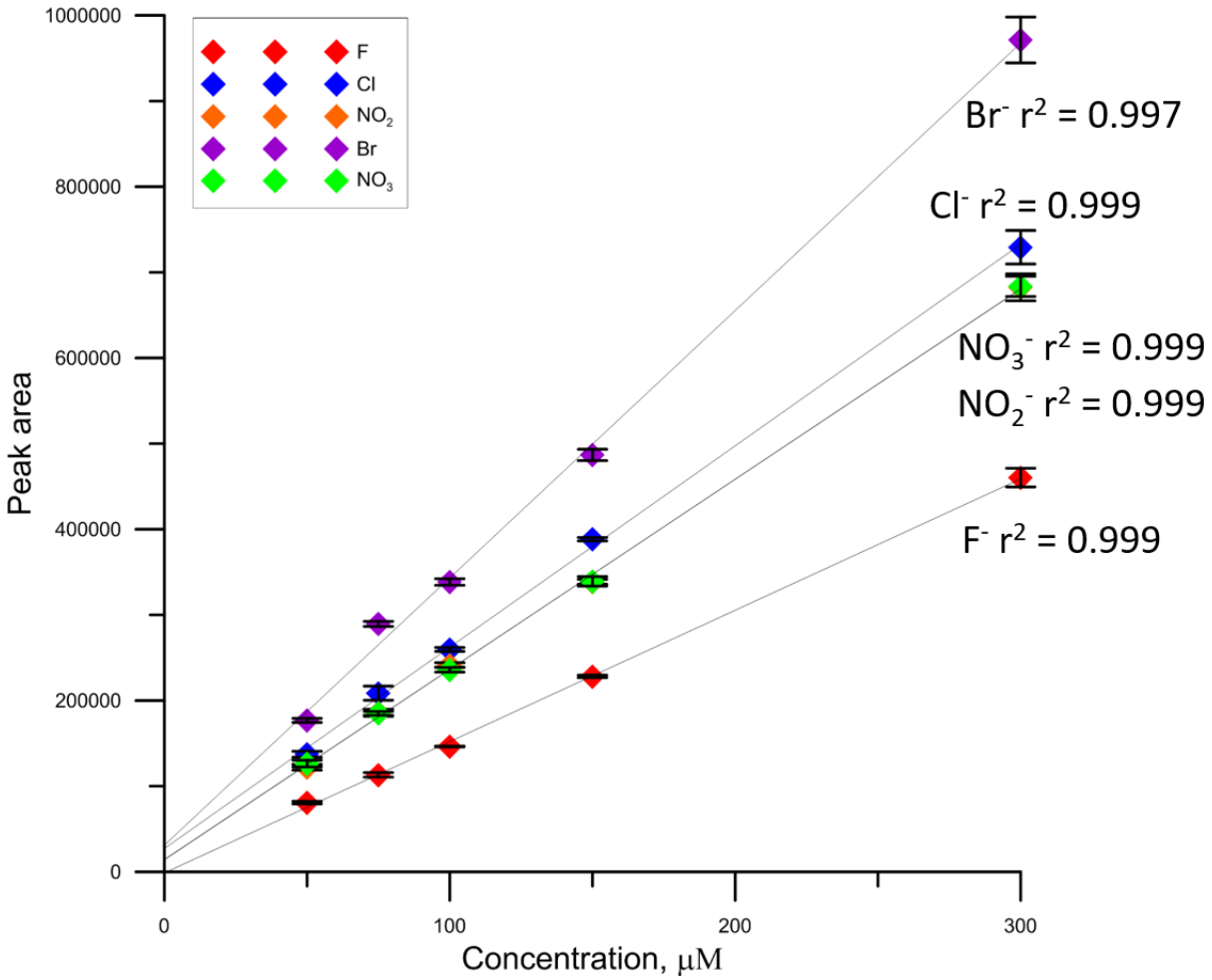

Figure 6-8. Peak area versus concentration to show linearity.

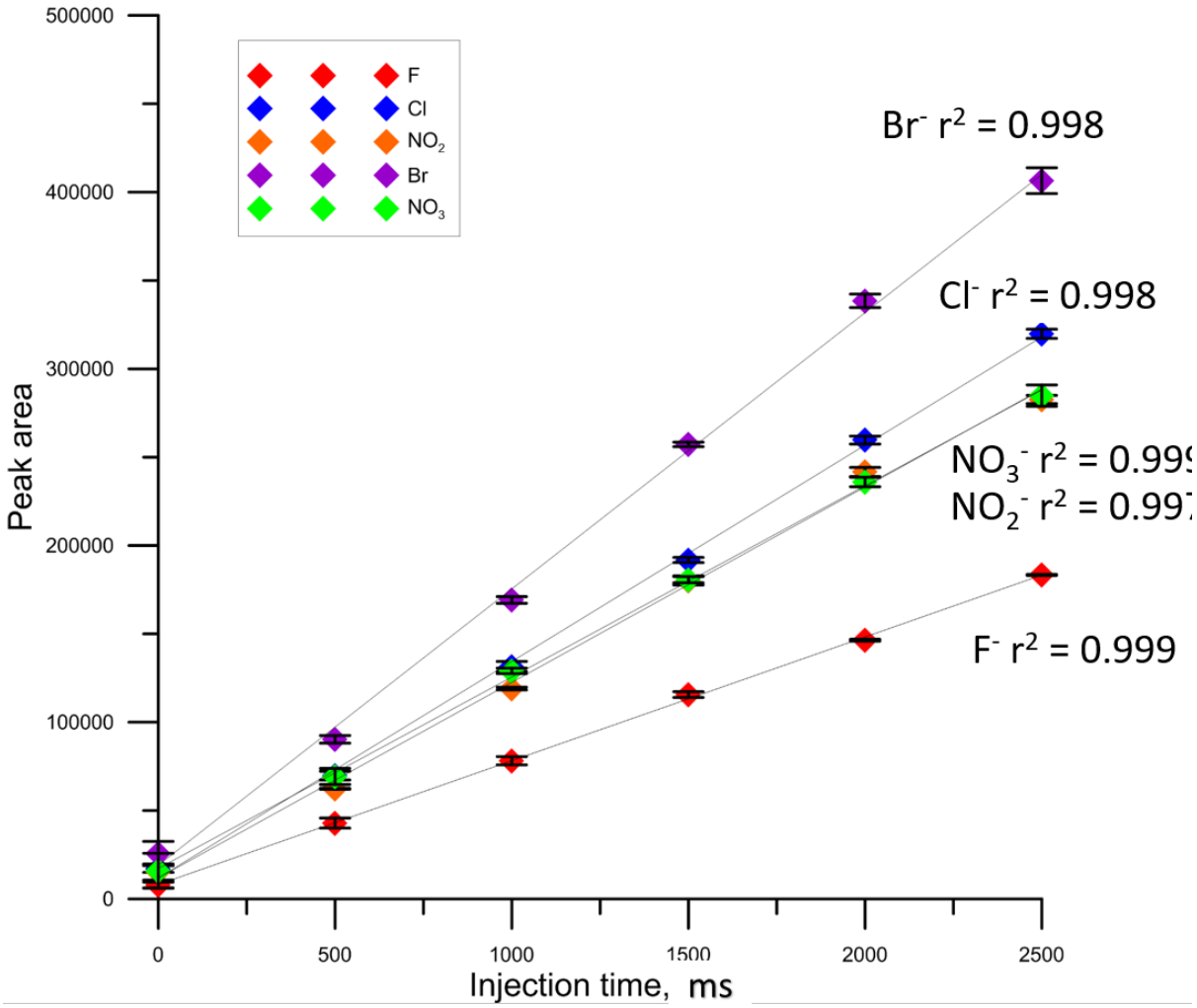

Figure 6-9. Linearity of injection time shown as peak area vs. injection time.

Table 6-3. %Residual Standard Deviation (%RSD) for 5 anions based on peak area, n = 10.

Sample	F	Cl	NO2	Br	NO3
1	1604	1692	1328	1305	822
2	1586	1646	1311	1292	801
3	1580	1668	1283	1308	811
4	1610	1658	1315	1312	814
5	1609	1700	1330	1323	834
6	1601	1683	1322	1296	829
7	1630	1735	1353	1346	843
8	1620	1717	1325	1326	843
9	1636	1667	1313	1283	830
10	1625	1700	1331	1326	848
Stdev	18.24189	27.61722	17.9966	18.94466	15.41464
Average	1610.778	1686	1320.333	1312.444	828.1111
%RSD	1.13%	1.64%	1.36%	1.44%	1.86%

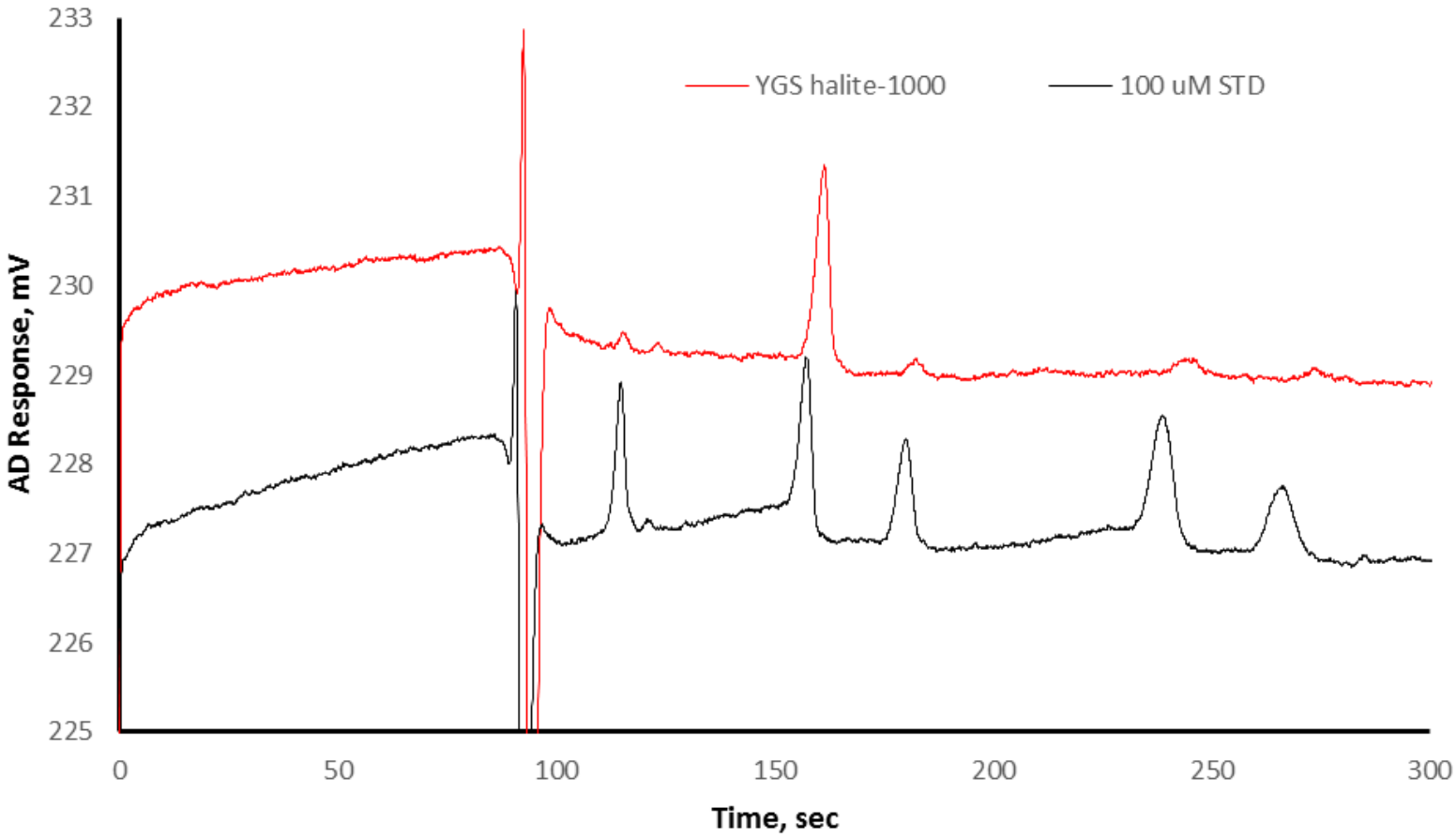

Figure 6-10. Example chromatogram of an injection of an Atacama Desert sample, results produced on site.

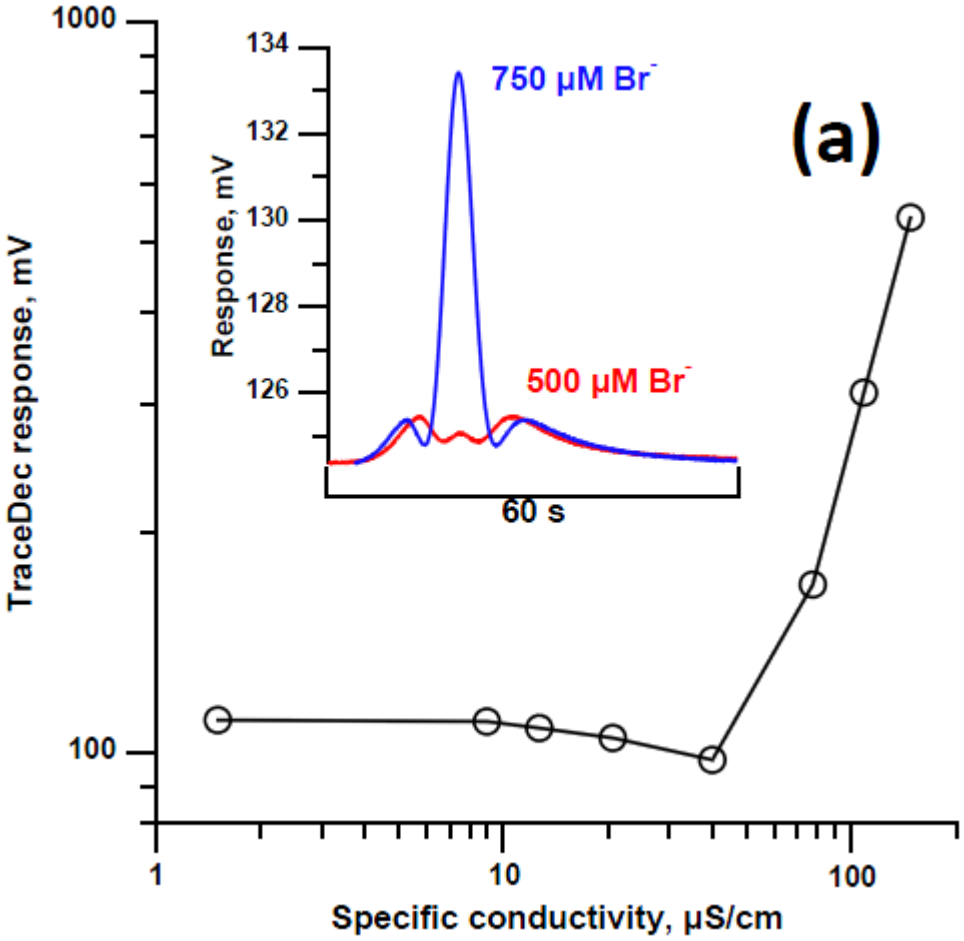
1000
100
TraceDec response, mV
1
10
100
Specific conductivity, µS/cm
134
132
130
128
126
Response, mV
750 µM Br-
500 µM Br-
60 s
(a)

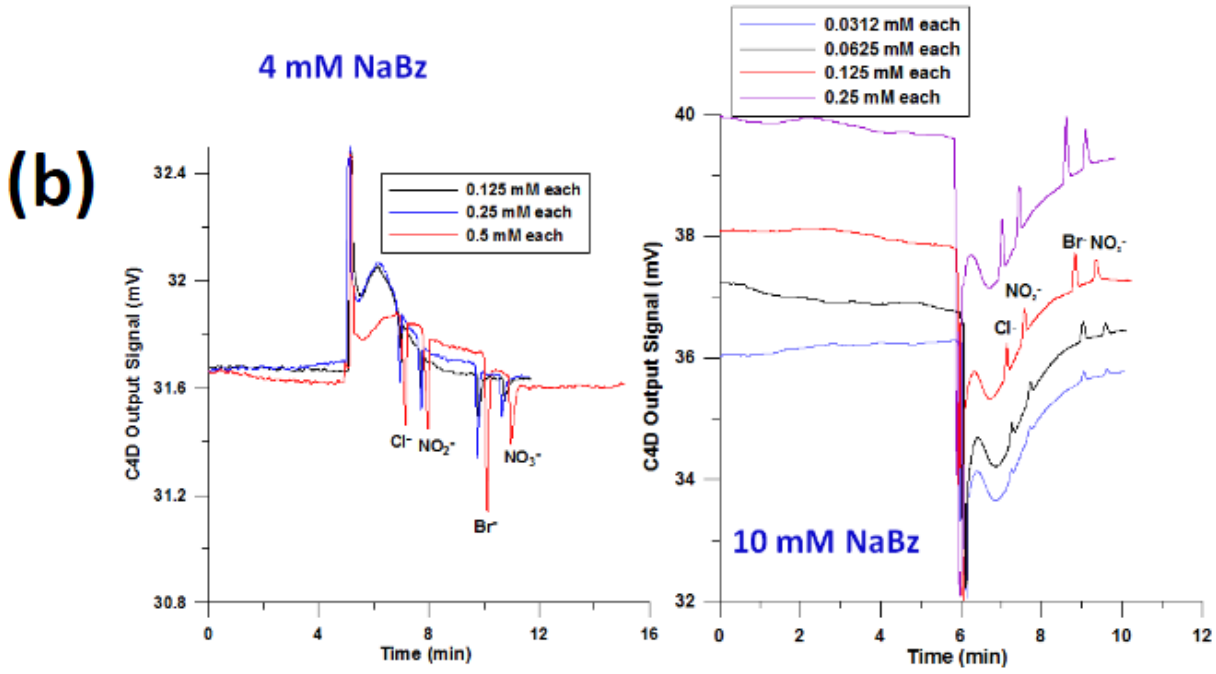

Figure A-S1. (a): Calibration curve obtained by flowing KCl solution of different concentrations first through a conductivity detector and then through a PMMA capillary (*ro* = 170 µm, *r* = 8 µm) with a commercial admittance detector. The insert is chromatographic response to injections of 0.5 and 0.75 mM Br- from a suppressed Dionex IC, a portion of the suppressor effluent was spilt through the above PMMA capillary. Commercial detector 150 kHz, gain 200%, Attenuation 0 dB. The batwing feature and abrupt change in response is common. (b): Negative (left) and positive (right) peaks were obtained OTIC on a AS18 coated PFSC (*ro* = 180 µm, *r* = 2.5 µm). Sodium benzoate was used as eluent: 4 mM (left) and 10 mM (right). Flow rate was 1.2 nL/min, and ~100 pL sample was injected. Detector condition is the same as (a).

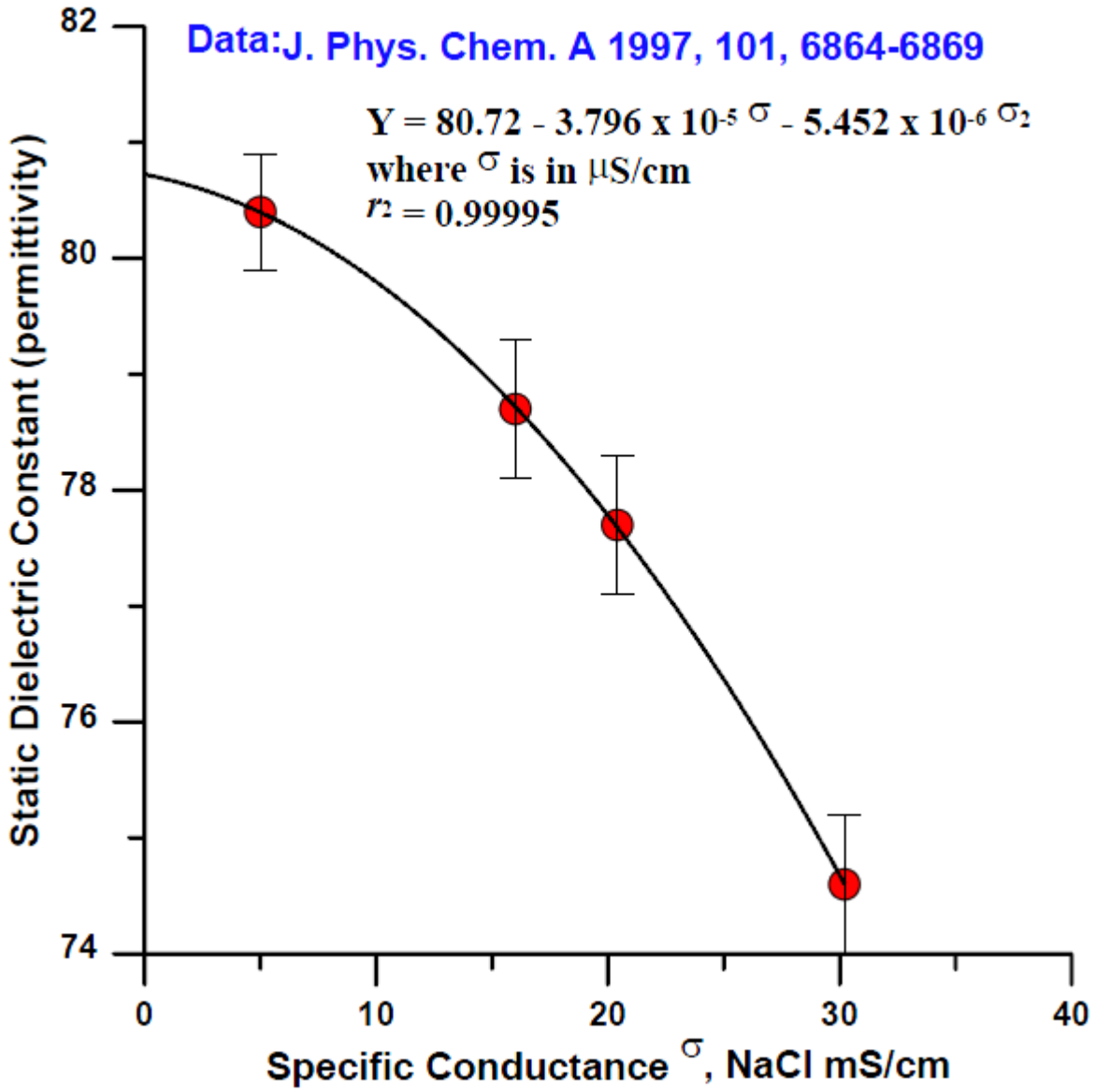

Figure A-S2. Low frequency relative permittivity of NaCl solutions. The best fit quadratic equation is used in our model.

ELECTRODES AND CONNECTIONS

Woods metal alloy melting in hot water was sucked into a PTFE tubing (1.2 mm I.D. x
1.9 mm O.D. x 3 cm length, PTFE 17 gauge SW, Zeus, http://www.zeusinc.com/), in which the capillary of interest was placed in the center in advance. After the alloy cooled down and solidified, the inside capillary was pulled out to form a well-fitting channel. The alloy could be cut into a desired length with a razor blade, after pushed out of the PTFE tubing. A crimp-snap connector (CST-100, P/N 770601-1, TE Connectivity, http://www.te.com/) was modified to hold the electrode. A hook hided inside the connector was drew out to allow the electrode passing through. The

electrode was not soldered with the hook for its replacement or movement, but the conductivity was checked prior to every test. The crimp-snap connector for holding the electrode was fixed by soldering with a female BNC connector that was mounted on the wall of the metal box.

ELECTROLYTE CONCENTRATIONS

The concentrations used were approximately 0, 0.05, 0.1, 0.15, 0.2, 0.4, 0.6, 0.8, 1.0,
1.2, 2, 4, 6, 8, 10 mM KCl.

CAPACITANCE MEASUREMENT

The current passing through a dry capillary was attributed solely to the crosstalk between two electrodes, i.e., the stray capacitance. Capillaries of different diameters and material were tested with or without a Faraday shield. The distance between electrodes was changed. The probe frequency (sine, 27 V p-p) was swept linearly from 0.1 kHz to the high limit bandwidth of the preamplifier over 20 s with appropriate transimpedance gain. Frequency was swept in the linear mode (20 s/sweep) within three different overlapping frequency ranges (100-5000 Hz, 1-50 kHz and 10-500 kHz)

To estimate the wall capacitance, the current frequency relationship of a PFS capillary filled with Woods metal was measured electrodes. The electrodes were 5 mm apart; a Faraday shield was also present. Under these conditions, the stray capacitance was too small to measure.

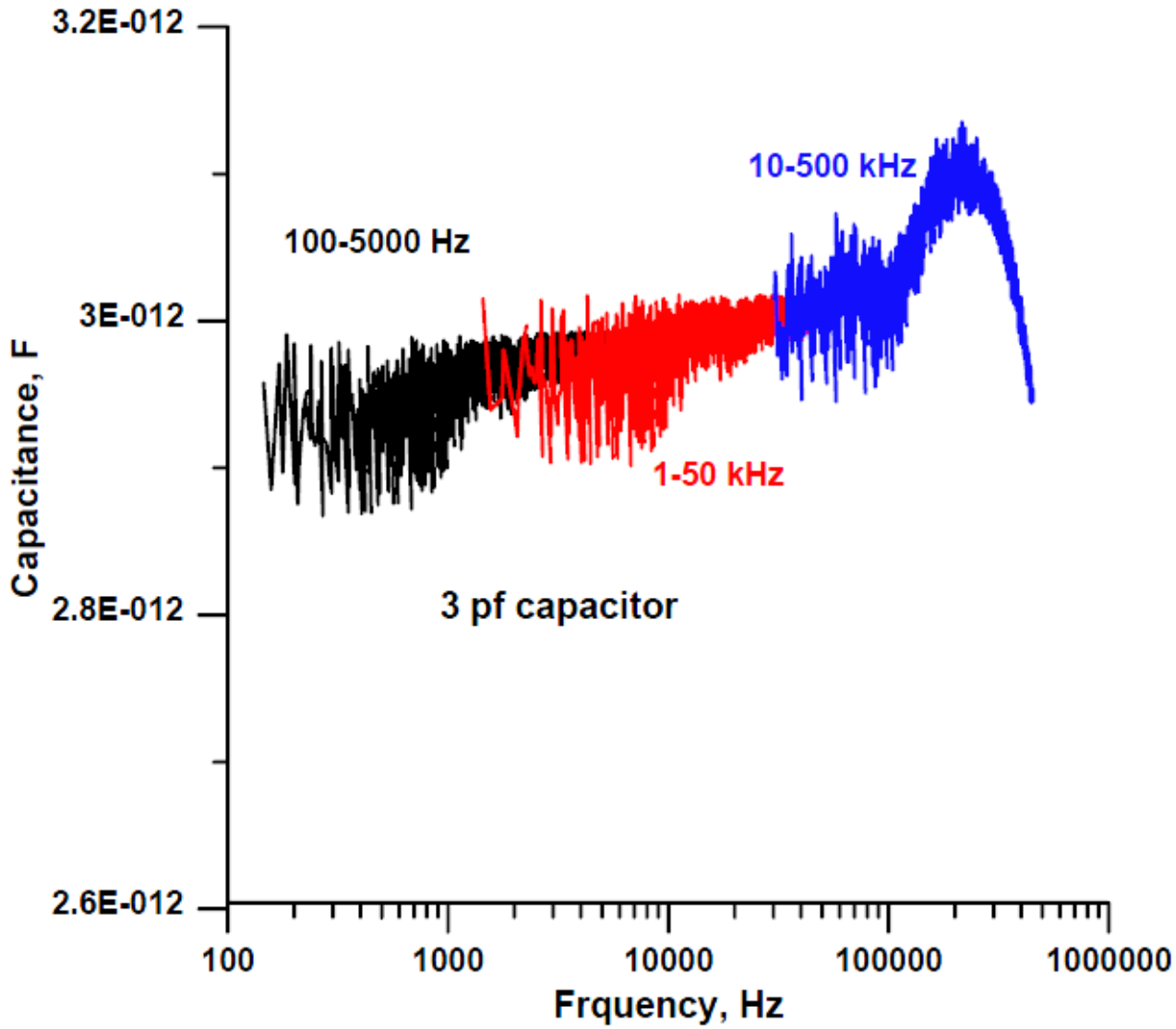

Figure A-S3. Capacitance measurement of a reference capacitor

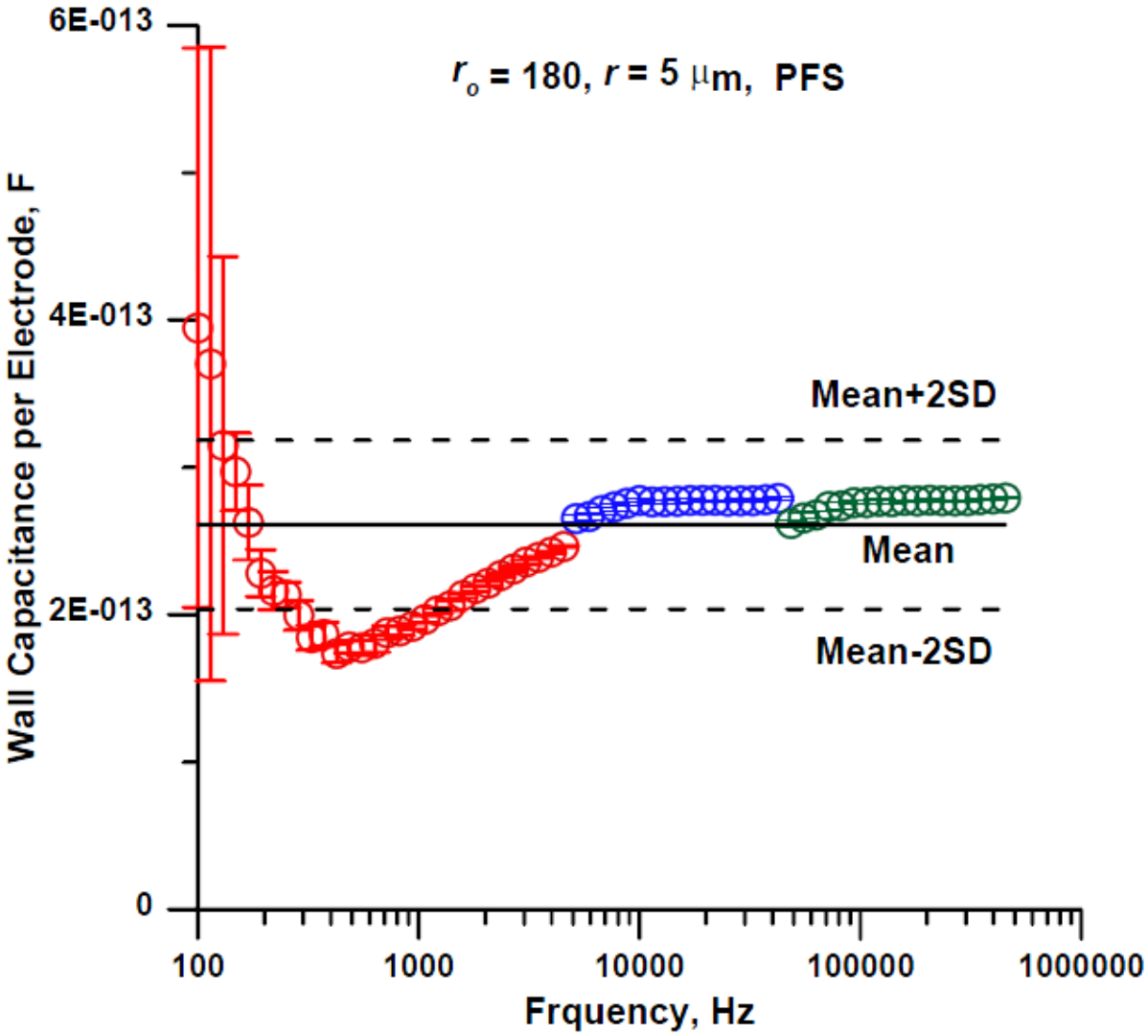

Figure A-S4. Measured wall capacitance of a polyimide-coated fused silica capillary, 5
μm in inner radius. Cast metal electrodes, 10 mm length.

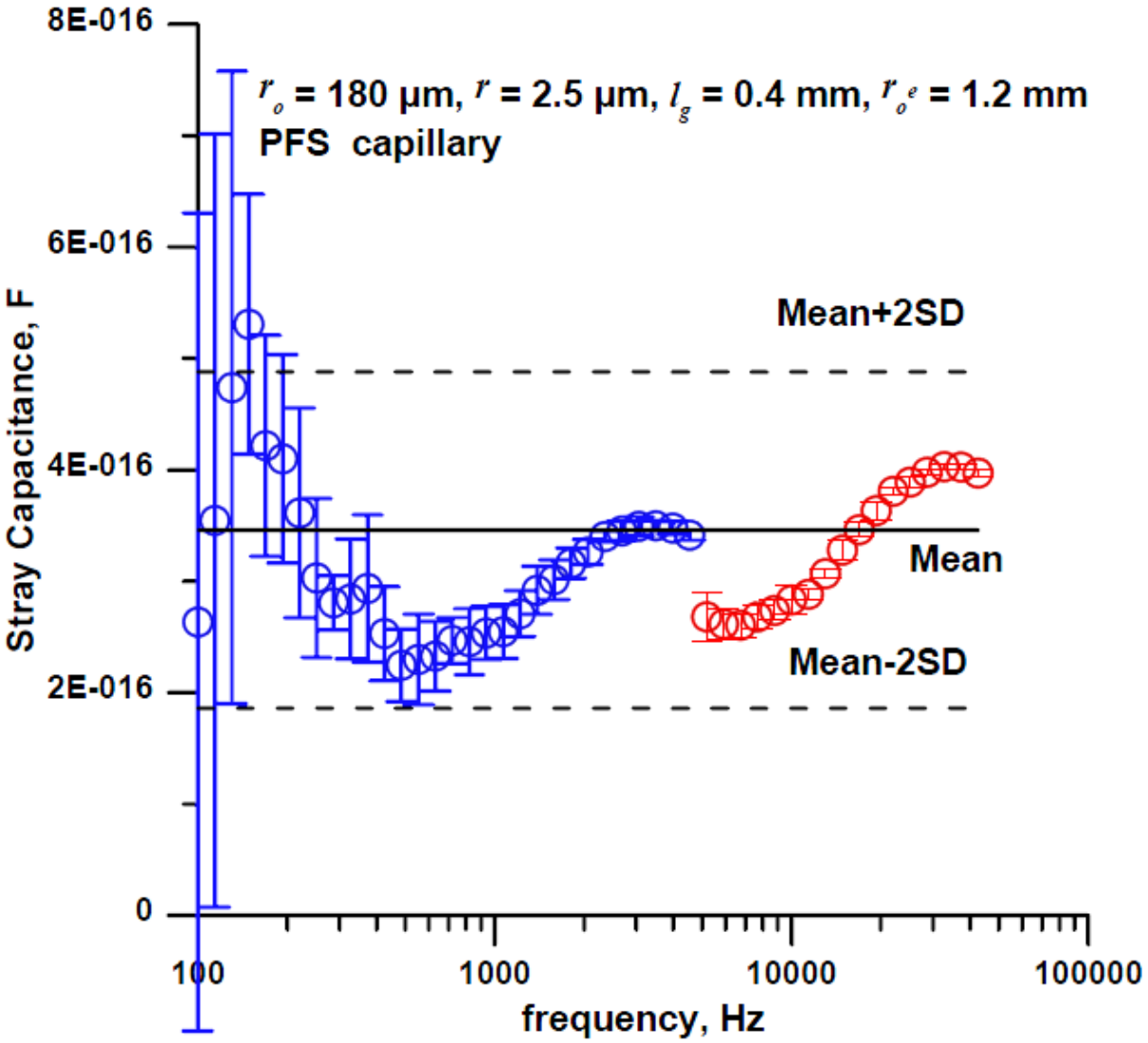

Figure A-S5. Measured stray capacitance of a fused silica capillary. Mu-metal Faraday shield (*te* = 0.13 mm), thickness including paper insulation 0.36 mm, capillary passage aperture 0.4 mm.

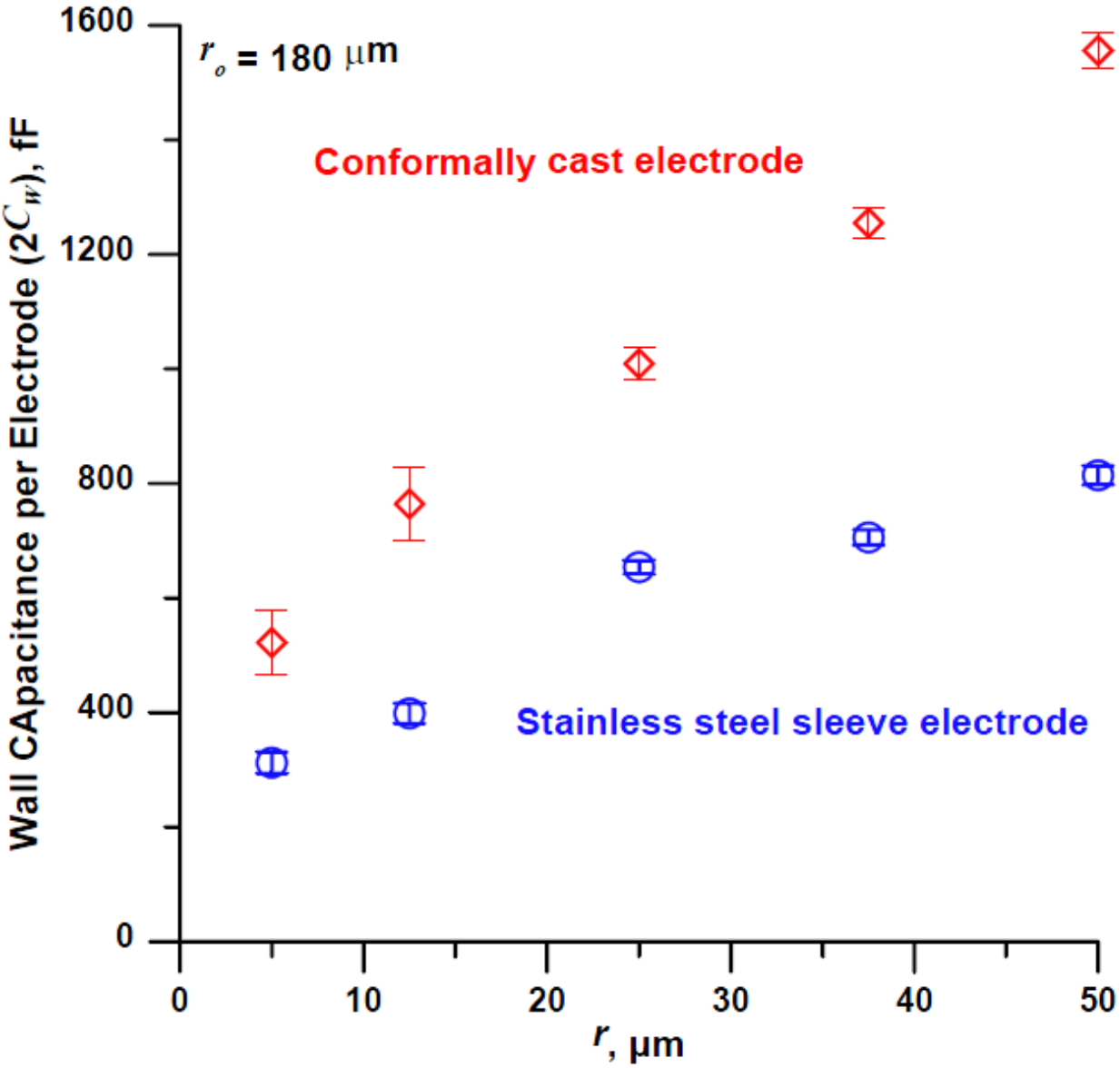

Figure A-S6. Under otherwise identical conditions stainless steel sleeve electrodes produce lower wall capacitances than cast electrodes. Electrode lengths 10 mm.

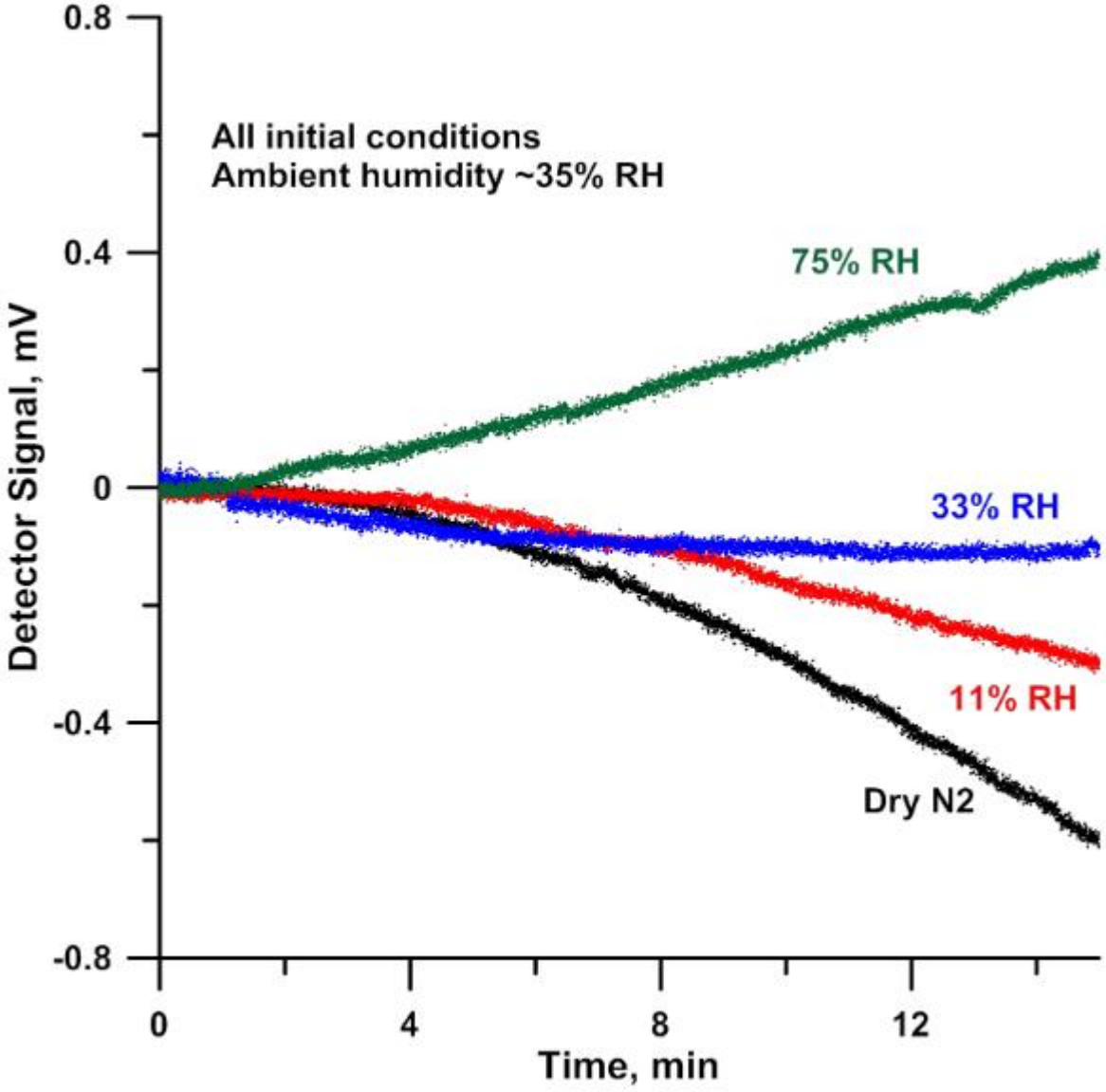

Figure A-S7. Baseline drift in a commercial detector as the humidity is varied around the detector head. *r* = 10 μm, *ro* = 182 μm, dry gas-filled.
Commercial detector. No Filter, No Offset, Frequency: “High”; Voltage: 0 dB; Gain:200%

Table 1-S1. Stray capacitance, *ro* = 180 μm, *lg* = 0.4 mm

r, µm	C_s, fF
5	0.346±0.071
12.5	0.440±0.065
25	0.300±0.063
50	0.263±0.041
90	0.333±0.078
125	0.268±0.058

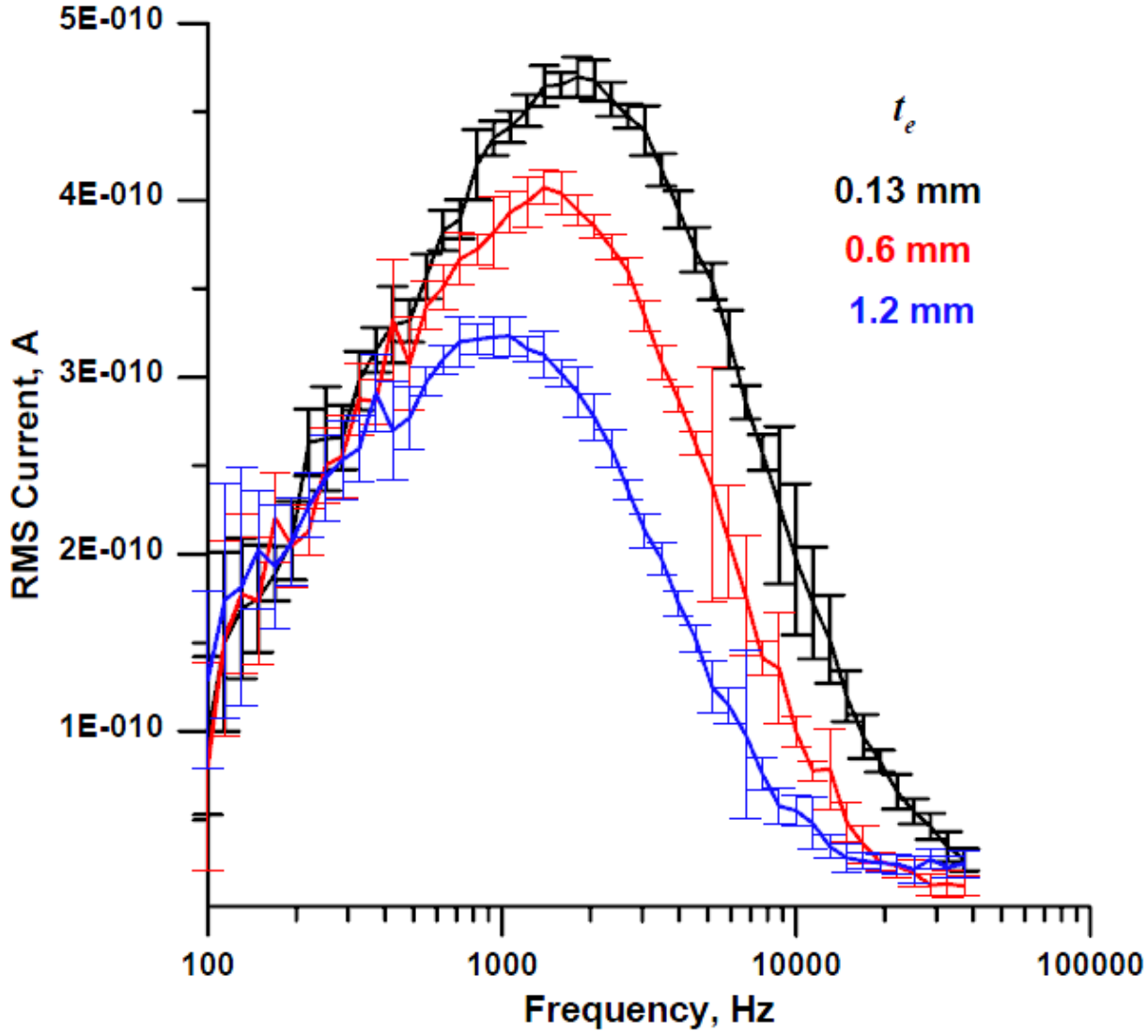

Figure A-S8. Effect of shield thickness of *r* = 12.5 µm, *ro* = 182 µm PFSC. The net response to 100 µM KCl with variations in 0.13 mm (black), 0.6 mm (red) and 1.2 mm (blue) shield thickness. *lg* = 2 mm, other conditions as in Fig. 3.

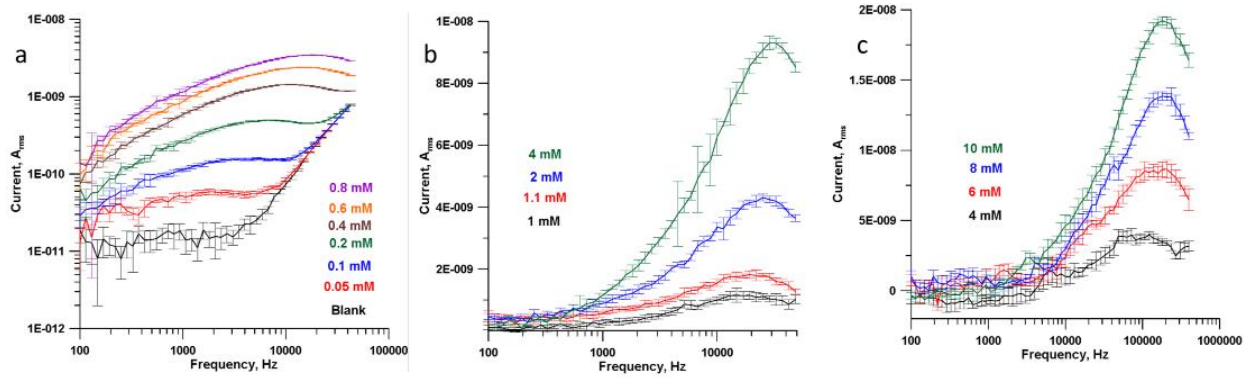

Figure A-S9. Current-frequency plots of *r* = 5 µm, *ro* = 182 µm PFSC. Conditions: Sample: KCl solution; sine wave 27 V p-p; electrode length: 10 mm; electrode distance: 0.4 mm; shield thickness: 0.13 mm; gain: (a) 1 V/nA, (b) 100V/µA, (c) 40V/µA

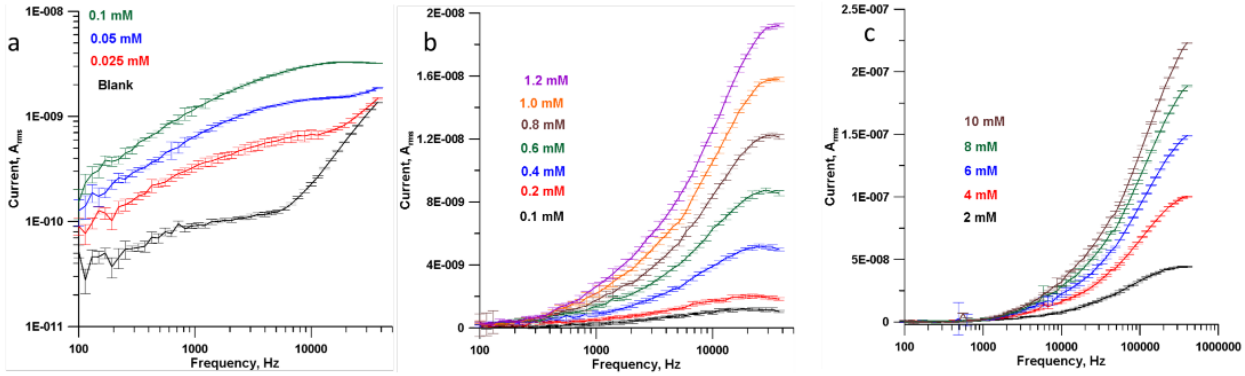

Figure A-S10. Current-frequency plots of *r* = 12.5 µm, *ro* = 182 µm PFSC. Conditions: Sample: KCl solution; sine wave 27 V p-p; electrode length: 10 mm; electrode distance: 0.4 mm; shield thickness: 0.13 mm; gain: (a) 1 V/nA, (b) 100V/µA, (c) 10V/µA.

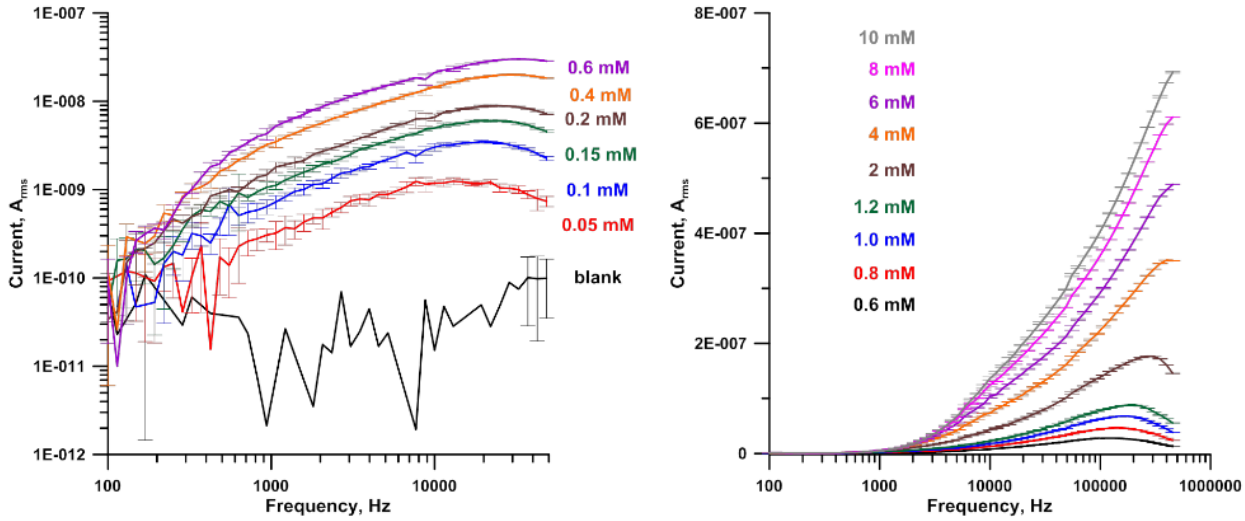

Figure A-S11. Current-frequency plots of *r* = 25 µm, *ro* = 182 µm PFSC.

Conditions: Sample: KCl solution; sine wave 27 V p-p; electrode length: 10 mm; electrode distance: 0.4 mm; shield thickness: 0.13 mm; gain, (a) 10V/nA, (b) 1V/μA

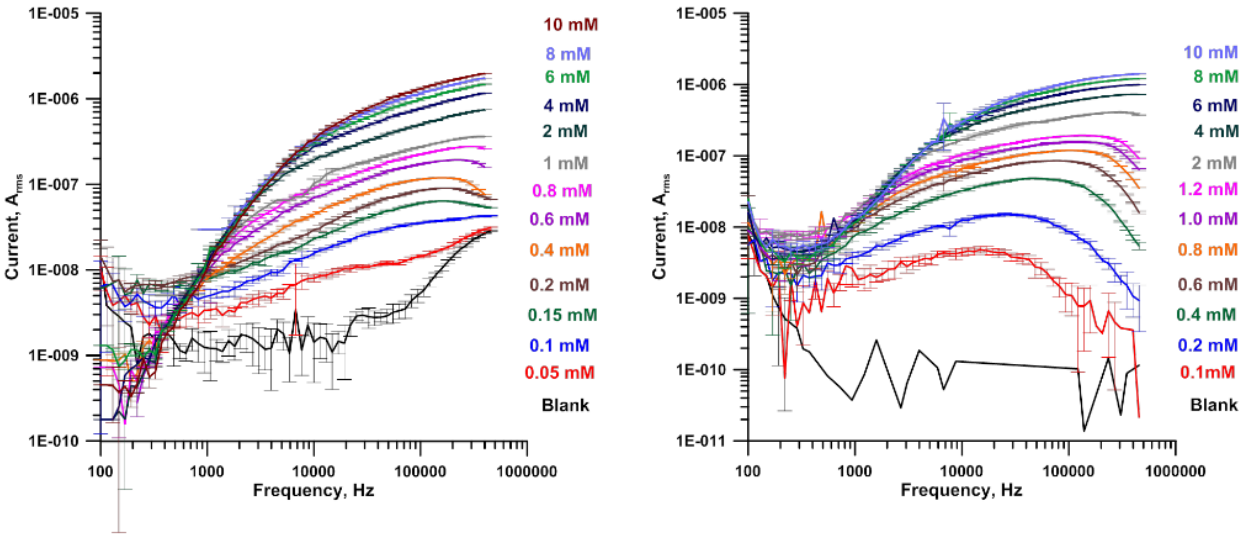

Figure A-S13. Current-frequency plots of *r* = 50 μm, *ro* = 182 μm PFSC. Conditions: Sample, KCl solution; sine wave 27 V p-p; electrode length: 10 mm; shield thickness: 0.13 mm; electrode distance: (a) 0.4 mm, (b) 2 mm; gain: 1V/μA for both.

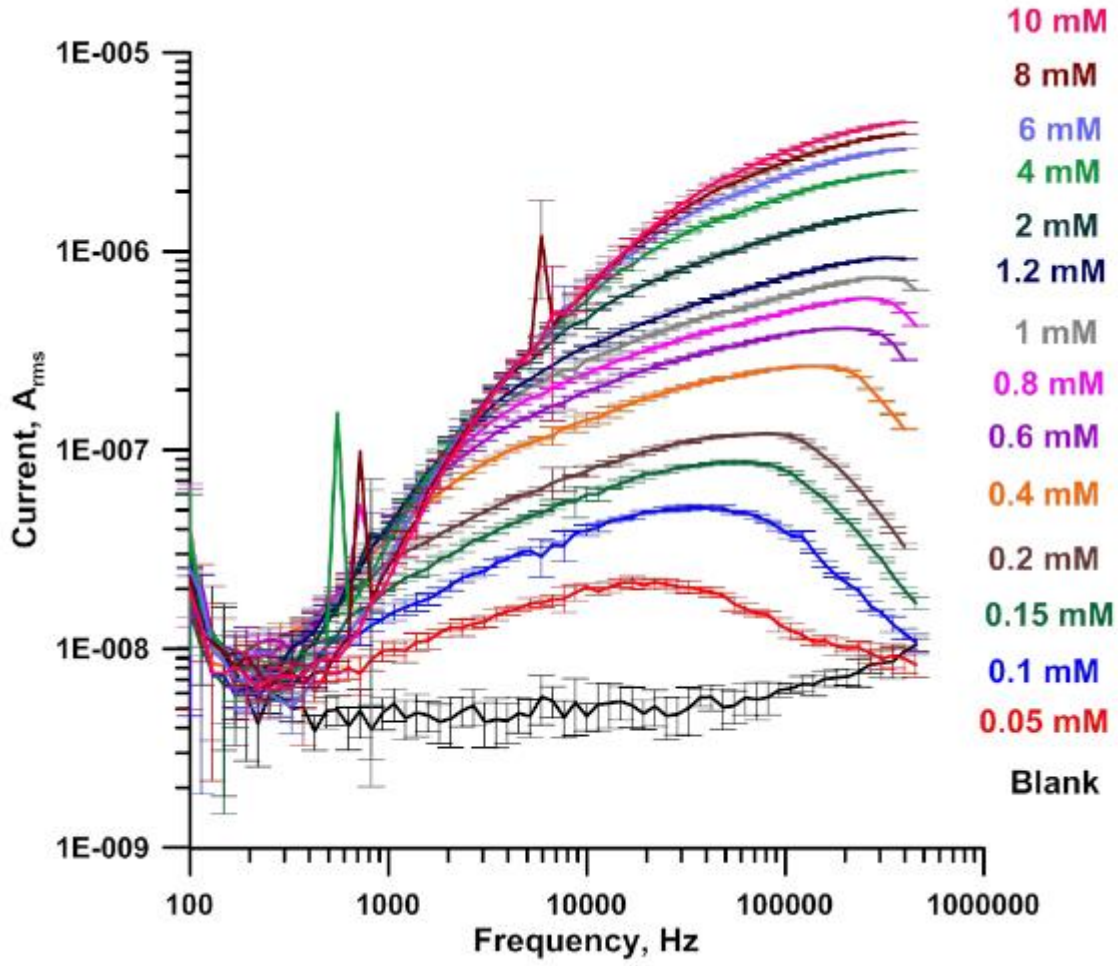

Figure A-S14. Current-frequency plot of *r* = 90 µm, *ro* = 182 µm PFSC. Conditions: Sample: KCl solution; sine wave 27 V p-p; electrode length: 10 mm; shield thickness: 0.13 mm; electrode distance: 2 mm; gain: 0.5 V/µA.

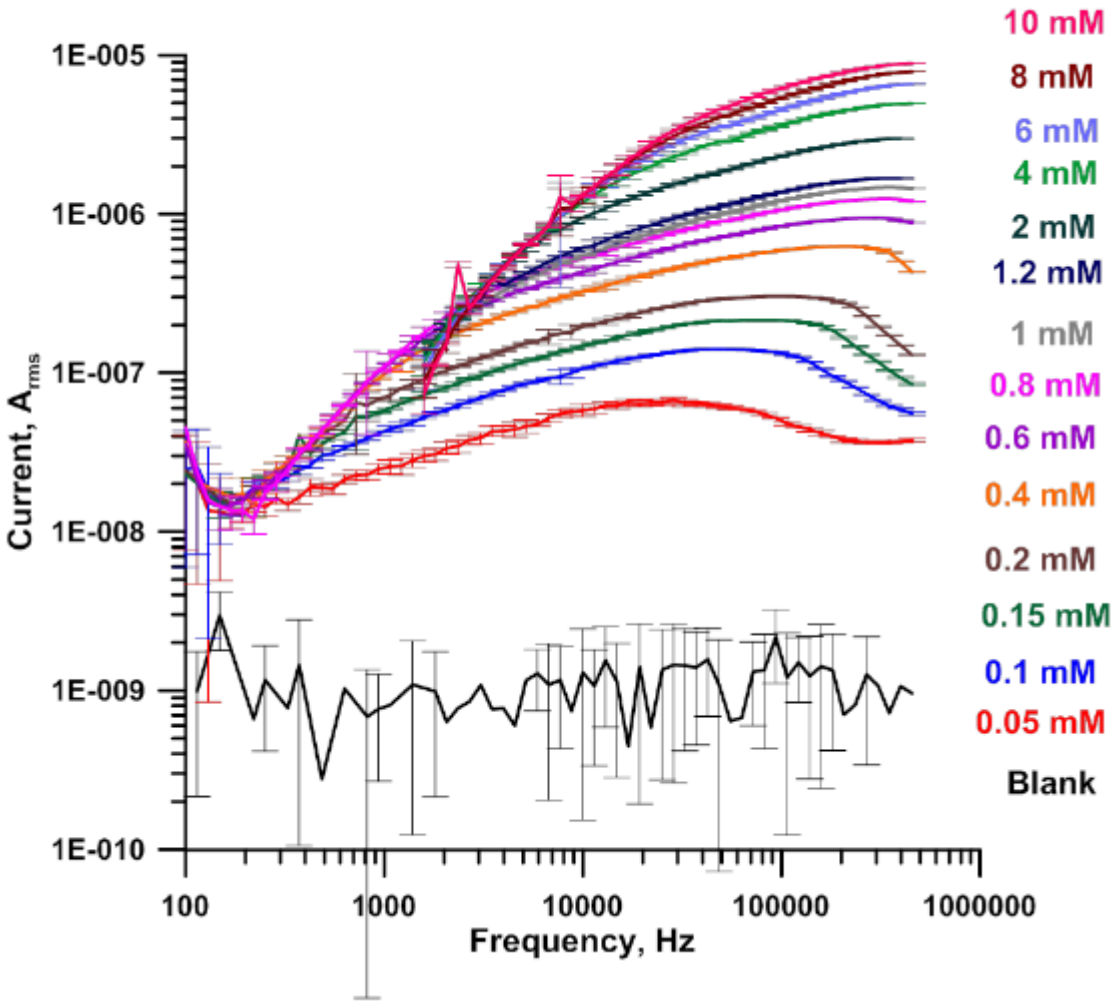

Figure A-S15. Current-frequency plot of *r* = 125 µm, *ro* = 182 µm PFSC. Conditions: Sample: KCl solution; sine wave of 27 V p-p; electrode length: 10 mm; shield thickness: 0.13 mm; electrode distance: 2 mm; gain: 0.5 V/µA.

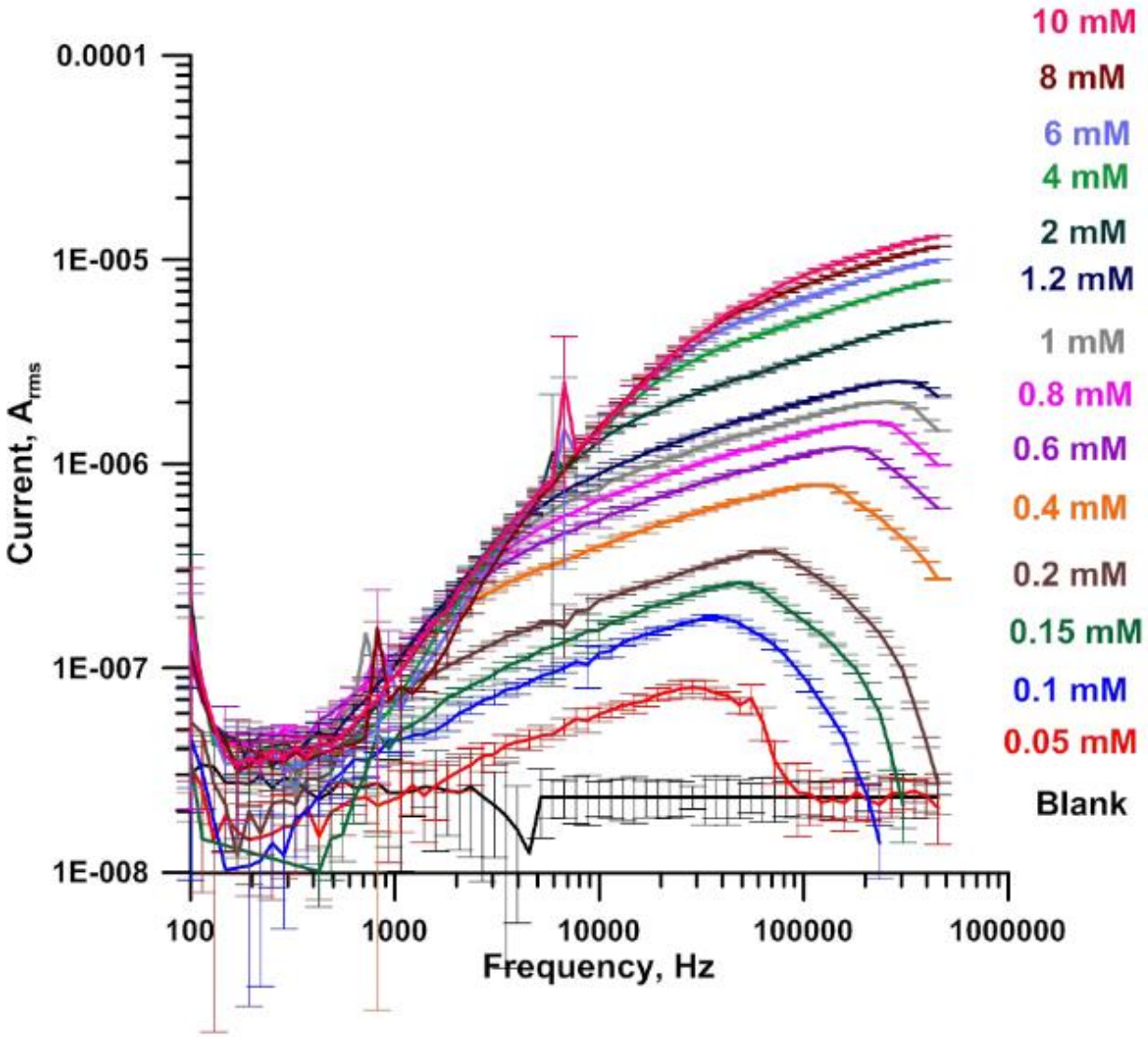

Figure A-S16. Current-frequency plot of *r* = 160 μm, *ro* = 210 μm PFSC. Conditions: Sample: KCl solution; sine wave 27 V p-p; electrode length: 10 mm; shield thickness: 0.13 mm; electrode distance: 2 mm; gain: 100 V/mA

Table S2. Linearity behavior of system in Figure 3

	i vs σ			*log i vs log* σ		
	r^2	slope x 10^{11}	intercept x 10^{11}	r^2	slope	intercept
0.5 kHz	0.9935	1.0	-3.7	0.9989	0.81	9.28
1.0 kHz	0.9944	1.6	-6.7	0.9998	1.23	-11.2
2.5 kHz	0.9898	2.9	-16	0.9992	1.36	-11.2
4.0 kHz	0.9854	3.6	-23	0.9935	1.27	-11.0
10 kHz[a]	0.9958	5.7	-66	0.9973	1.54	-11.3
25 kHz[b]	0.9928	6.6	-83	0.9964	1.37	-11.0
40 kHz[b]	0.9796	5.4	-14	0.9652	0.99	-10.3

[a]Highest 5 concentrations
[b]Highest 4 concentrations

Table S3, Output current and relative sensitivity (1/*i* d*i*/dσ) of a small Bore (*r* =7.5 µm) capillary operated at high *Rcell*
For specific values of specific conductance σ the current *i* was measured (the specific values of σ used are listed in newly added table, Now Table S3. The true differential d*i*/dσ cannot of course be calculated, it was really Δ*i*/Δσ calculated as (*i*2-*i*1)/((σ2-σ1). When d*i*/dσ or more correctly Δ*i*/Δσplotted against σ the value of σ used is the average of σ2 and σ1. Similarly to calculate 1/*i* d*i*/dσ the i in the denominator was the average *i*, (*i*1+*i*2)/2.

	σ µS/cm	Average σ µS/cm	0.5 kHz	1.0 kHz	2.5 kHz	4.0 kHz	10 kHz	25 kHz	40 kHz
i, A	2.3		(1.00±0.38)E-11	(1.56±0.58)E-11	(1.87±0.99)E-11	(3.13±0.57)E-11	(1.22±0.04)E-10	(6.07±0.02)E-10	(1.17±0.06)E-09
$\frac{1}{i}\frac{di}{d\sigma}$		8.7	(1.31±0.30)E-01	(1.28±0.07)E-01	(1.32±0.11)E-01	(1.21±0.05)E-01	(6.79±0.30)E-02	(1.34±0.14)E-02	(7.62±0.66)E-03
i, A	15.1		(1.11±0.09)E-10	(1.57±0.06)E-10	(2.25±0.06)E-10	(2.49±0.09)E-10	(3.08±0.07)E-10	(7.20±0.05)E-10	(1.29±0.06)E-09
$\frac{1}{i}\frac{di}{d\sigma}$		20.2	(5.45±1.72)E-02	(6.44±1.32)E-02	(7.44±0.60)E-02	(8.07±0.27)E-02	(7.97±0.15)E-02	(2.79±0.09)E-02	(8.29±0.86)E-03
i, A	25.3		(1.98±0.08)E-10	(3.12±0.05)E-10	(5.02±0.05)E-10	(6.02±0.08)E-10	(7.35±0.06)E-10	(9.61±0.04)E-10	(1.40±0.01)E-09
$\frac{1}{i}\frac{di}{d\sigma}$		28.8	(5.52±1.66)E-02	(4.40±1.28)E-02	(4.80±0.42)E-02	(5.04±0.35)E-02	(5.55±0.12)E-02	(3.63±0.10)E-02	(1.48±0.10)E-02
i, A	32.3		(2.93±0.17)E-10	(4.26±0.06)E-10	(7.05±0.06)E-10	(8.61±0.07)E-10	(1.09±0.01)E-09	(1.24±0.01)E-09	(1.56±0.01)E-09
$\frac{1}{i}\frac{di}{d\sigma}$		37.9	(2.17±0.77)E-02	(3.11±1.18)E-02	(3.61±0.35)E-02	(3.80±0.19)E-02	(4.16±0.06)E-02	(3.66±0.07)E-02	(2.21±0.06)E-02
i, A	43.4		(3.73±0.16)E-10	(6.04±0.07)E-10	(1.06±0.01)E-09	(1.32±0.01)E-09	(1.74±0.01)E-09	(1.87±0.01)E-09	(1.99±0.01)E-09
$\frac{1}{i}\frac{di}{d\sigma}$		58.9	(2.09±0.18)E-02	(1.99±0.50)E-02	(2.03±0.07)E-02	(2.07±0.05)E-02	(2.25±0.05)E-02	(2.41±0.01)E-02	(2.13±0.01)E-02
i, A	74.4		(7.29±0.25)E-10	(1.14±0.04)E-09	(2.03±0.01)E-09	(2.57±0.01)E-09	(3.61±0.01)E-09	(4.11±0.01)E-09	(3.96±0.01)E-09

σ is specific conductance; all conditions as in Fig. 3.

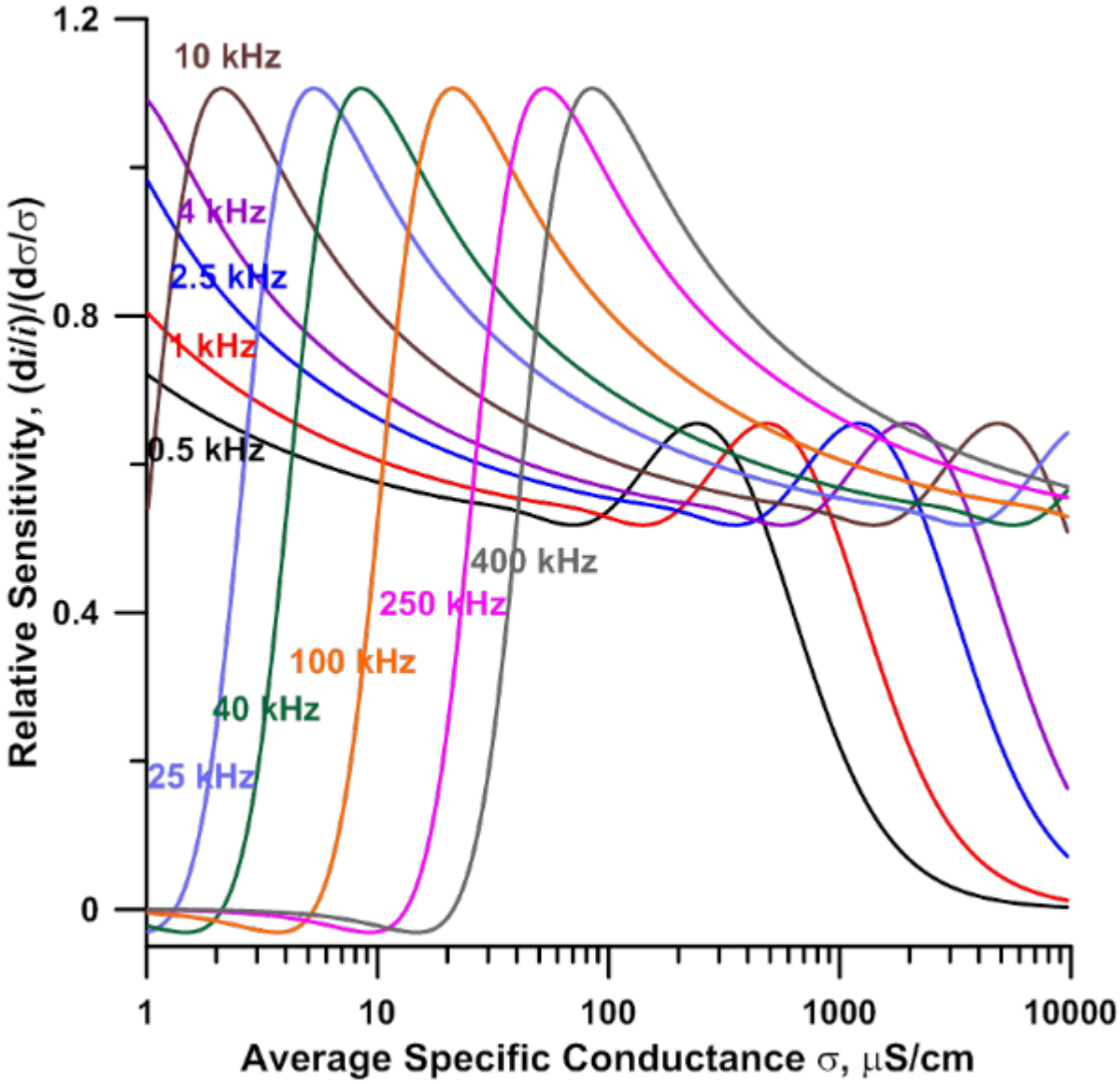

Figure A-S17. Relative sensitivity as a function of specific conductance at different frequencies.

Flat regions indicate a linear response. Simulation parameters are as in Figure 3e: *ro* = 182 μm, *r* = 7.5 μm. *Ft* = 0.4. Sine wave 27 V p-p; *lg* = 0.4 mm; *le* = 10 mm; *te* =0.13 mm.

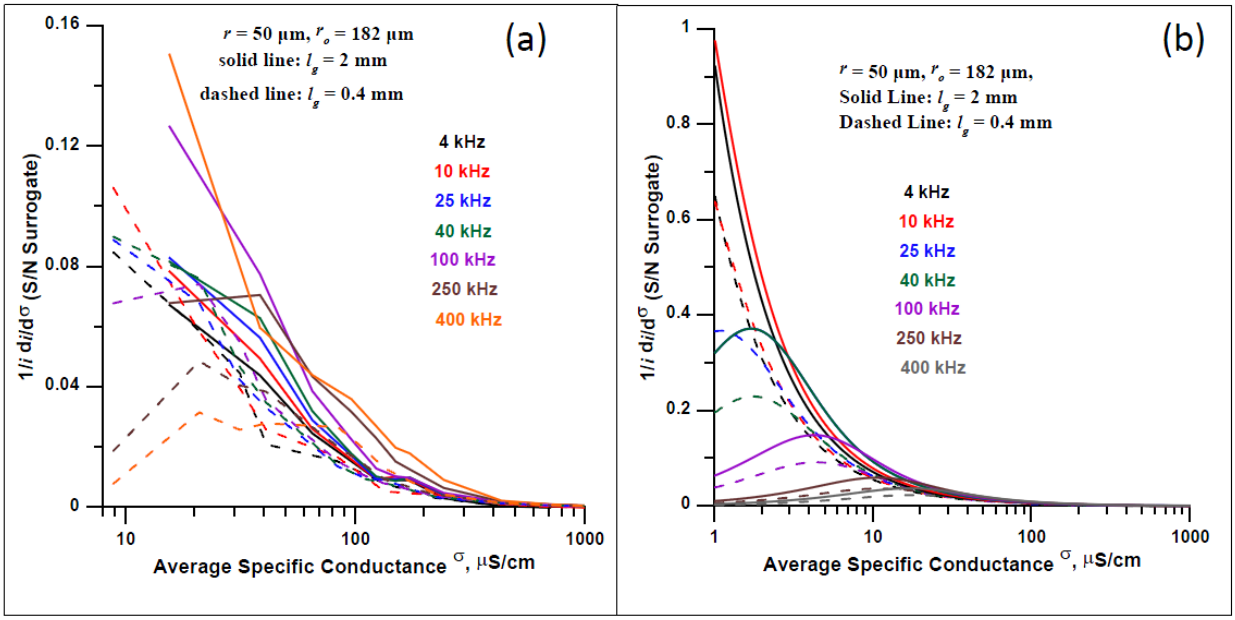

Figure A-S18. Represents the response to background and as such is a *de facto* measure of S/N. (a) Experimental (b) Model results

Table S4. Effect of electrode separation (*lg*)

		25 µm ID x 365 µm OD, FSC	25 µm ID x 365 µm OD, FSC	25 µm ID x 365 µm OD, FSC
	Electrodes distance	**0.4 mm**	**2 mm**	**5 mm**
<10 µS/cm	Frequency, kHz	4.4-28.2	0.61-4.5	0.13-0.95
	Response, A/(µS/cm)	(1.80±0.14) E-10	(2.94±0.22) E-11	(9.06±0.81) E-12
	Background, A	(1.70±0.26) E-9	(2.20±0.16) E-10	(7.22±0.58) E-11
44 µS/cm	Frequency, kHz	12.4-38.2	3.2-24.2	0.58-7.0
	Response, A/(µS/cm)	(9.19±3.31) E-11	(7.39±0.53) E-11	(3.04±0.21) E-11
	Background, A	(3.09±1.09) E-9	(2.13±0.29) E-9	(8.17±1.08) E-10
74 µS/cm	Frequency, kHz	15.3-38.3		
	Response, A/(µS/cm)	(1.13±0.09) E-10		
	Background, A	(6.65±0.32) E-9		
130 µS/cm	Frequency, kHz	16.6-38.3	5.3-34.4	1.9-42.9
	Response, A/(µS/cm)	(1.14±0.10) E-10	(4.70±0.46) E-11	(1.14±0.31) E-11
	Background, A	(1.34±0.07) E-8	(3.16±0.34) E-9	(8.82±3.05) E-10
220 µS/cm	Frequency, kHz			3.2-21.5
	Response, A/(µS/cm)			(2.42±0.18) E-11
	Background, A			(2.93±0.29) E-9
420 µS/cm	Frequency, kHz	182-400	33.2-196	
	Response, A/(µS/cm)	(1.74±0.14) E-10	(3.81±0.29) E-11	
	Background, A	(6.83±0.36) E-8	(9.30±0.94) E-9	
700 µS/cm	Frequency, kHz	205-400	66.8-316	9.8-84.6
	Response, A/(µS/cm)	(1.56±0.13) E-10	(4.61±0.35) E-11	(1.47±0.10) E-11
	Background, A	(1.17±0.06) E-7	(1.98±0.27) E-8	(6.57±0.67) E-9
1270 µS/cm	Frequency, kHz	235-400	75.5-400	16.6-125
	Response, A/(µS/cm)	(1.12±0.13) E-10	(5.16±0.36) E-11	(1.61±0.13) E-11
	Background, A	(1.94±0.10) E-7	(4.60±0.43) E-8	(1.49±0.14) E-8

Sample: KCl solution; PFSC; sine wave 27 V p-p; electrode length: 10 mm; shield thickness: 0.13 mm

Table S5. Optimum detection frequency, background current and response of r < 50µm PFSCs (*ro* = 182 µm)

σ		r = 5 μm	r = 7.5 μm	r = 12.5 μm	r = 25 μm	r = 38 μm	r = 50 μm
	Optimum Frequency	1.3-7.1	2.7-16.2	4.4-28.2	8.8-37.4	16.0-107	33.0-208
<10 μS/cm	Response $di/d\sigma$	(8.66±0.65) E-12	(3.90±0.32) E-11	(1.80±0.14) E-10	(2.15±0.17) E-10	(2.42±0.17) E-10	(1.88±0.15) E-9
	Background i	(8.33±0.78) E-11	(3.88±0.88) E-10	(1.70±0.26) E-9	(1.63±0.11) E-9	(2.46±0.16) E-9	(1.98±0.38) E-8
	Optimum Frequency	5.0-25.3	9.0-42.9	12.4-38.2	14.7-75.2	71.5-394	32.2-264
44 μS/cm	Response $di/d\sigma$	(3.03±0.23) E-11	(7.02±0.52) E-11	(9.19±3.31) E-11	(3.59±0.26) E-10	(1.01±0.08) E-9	(9.59±0.75) E-10
	Background i	(9.20±0.29) E-10	(2.89±0.14) E-9	(3.09±1.09) E-9	(1.31±0.14) E-8	(2.94±0.11) E-8	(9.30±1.13) E-8
	Optimum Frequency	7.6-37.4	12.8-48.6	15.3-38.3	17.4-91.3	102-400	174-400
74 μS/cm	Response $di/d\sigma$	(3.15±0.24) E-11	(2.48±0.18) E-11	(1.13±0.09) E-10	(3.23±0.26) E-10	(1.30±0.08) E-9	(2.76±0.21) E-9
	Background i	(1.80±0.10) E-9	(1.12±0.07) E-9	(6.65±0.32) E-9	(2.23±0.30) E-8	(6.37±0.27) E-8	(1.43±0.14) E-7
	Optimum Frequency		14.8-66.7	16.6-38.3	100-344	139-400	301-400
130 μS/cm	Response $di/d\sigma$		(3.25±0.28) E-11	(1.14±0.10) E-10	(6.96±0.57) E-10	(1.41±0.12) E-9	(3.04±0.34) E-9
	Background i		(2.77±0.27) E-9	(1.34±0.07) E-8	(5.36±0.38) E-8	(1.45±0.04) E-7	(3.15±0.05) E-7
	Optimum Frequency	13.7-49.6	78.6-239		177-400	340-400	218-400
220 μS/cm	Response $di/d\sigma$	(2.00±0.17) E-11	(3.38±0.24) E-11		(7.61±0.57) E-10	(1.94±0.20) E-9	(2.33±0.21) E-9
	Background i	(2.54±0.14) E-9	(4.38±0.21) E-9		(1.12±0.10) E-7	(4.12±0.05) E-7	(5.23±0.26) E-7
	Optimum Frequency	17.4-68.1	127-400	182-400	321-400	258-400	192-400
420 μS/cm	Response $di/d\sigma$	(1.61±0.12) E-11	(3.91±0.31) E-11	(1.74±0.14) E-10	(6.18±0.68) E-10	(1.02±0.08) E-9	(1.27±0.11) E-9
	Background i	(6.26±0.52) E-9	(1.26±0.43) E-8	(6.83±0.36) E-8	(2.54±0.05) E-7	(6.88±0.38) E-7	(8.69±0.66) E-7
	Optimum Frequency	81.8-322	150-400	205-400	293-400	223-400	180-400
700 μS/cm	Response $di/d\sigma$	(1.73±0.14) E-11	(4.35±0.28) E-11	(1.56±0.13) E-10	(4.46±0.37) E-10	(7.42±0.58) E-10	(1.01±0.08) E-9
	Background i	(5.87±0.33) E-9	(2.45±0.08) E-8	(1.17±0.06) E-7	(4.08±0.12) E-7	(9.26±0.68) E-7	(1.20±0.09) E-6
	Optimum Frequency	74.0-400	186-400	235-400	276-400	229-400	158-400
1270 μS/cm	Response $di/d\sigma$	(1.78±0.12) E-11	(4.01±0.30) E-11	(1.12±0.13) E-10	(2.54±0.23) E-10	(5.08±0.43) E-10	(7.50±0.58) E-10
	Background i	(1.52±0.12) E-8	(4.88±0.22) E-8	(1.94±0.10) E-7	(6.10±0.36) E-7	(1.28±0.10) E-6	(1.66±0.15) E-6

Table S6. Optimum detection frequency, background current and response of PFSCs

		r = 50 μm, r_o = 182 μm	r = 90 μm, r_o = 182 μm	r = 125 μm, r_o = 182 μm	r = 160 μm, r_o = 210 μm
	Optimum Frequency	5.8-31.5	12.2-85.1	12.5-146	17.0-60.1
<10 μS/cm	Response $di/d\sigma$	(3.01±0.21) E-10	(2.90±0.24) E-9	(8.79±0.70) E-9	(9.40±0.84) E-9
	Background i	(2.13±0.17) E-9	(2.66±0.15) E-8	(6.58±0.51) E-8	(9.24±0.61) E-8
	Optimum Frequency	24.7-148	105-282	152-400	86.8-208
44 μS/cm	Response $di/d\sigma$	(1.11±0.09) E-9	(5.54±0.44) E-9	(1.24±0.10) E-8	(1.60±0.15) E-8
	Background i	(2.76±0.38) E-8	(1.69±0.21) E-7	(4.15±0.47) E-7	(4.95±0.64) E-7
	Optimum Frequency	42.4-227	216-388	254-400	149-289
74 μS/cm	Response $di/d\sigma$	(1.31±0.11) E-9	(6.29±0.62) E-9	(1.23±0.11) E-8	(1.69±0.17) E-8
	Background	(5.83±0.97) E-8	(2.96±0.33) E-7	(7.53±0.34) E-7	(8.19±1.23) E-7
	Optimum Frequency	91.2-350	333-400	186-400	281-423
130 μS/cm	Response $di/d\sigma$	(1.39±0.11) E-9	(6.96±0.89) E-9	(7.24±0.55) E-9	(1.85±0.23) E-8
	Background i	(1.22±0.21) E-7	(6.20±0.26) E-7	(1.33±0.03) E-6	(1.60±0.18) E-6
	Optimum Frequency	209-400	169-400	131-400	331-400
220 μS/cm	Response $di/d\sigma$	(1.96±0.17) E-9	(5.41±0.45) E-9	(9.45±0.70) E-9	(2.19±0.20) E-8
	Background i	(2.54±0.21) E-7	(1.11±0.05) E-6	(2.11±0.11) E-6	(3.26±0.06) E-6
	Optimum Frequency	225-400	127-400	155-400	222-400
420 μS/cm	Response $di/d\sigma$	(1.07±0.09) E-9	(2.83±0.23) E-9	(6.08±0.46) E-9	(9.05±0.73) E-9
	Background i	(5.56±0.08) E-7	(1.88±0.15) E-6	(3.73±0.20) E-6	(6.01±0.35) E-6
	Optimum Frequency	145-400	147-400	201-400	200-400
700 μS/cm	Response $di/d\sigma$	(8.55±0.65) E-10	(2.40±0.20) E-9	(5.13±0.40) E-9	(6.66±0.49) E-9
	Background i	(8.07±0.47) E-7	(2.67±0.19) E-6	(5.47±0.24) E-6	(8.15±0.60) E-6
	Optimum Frequency	139-400	179-400	93.2-400	200-400
1270 μS/cm	Response $di/d\sigma$	(6.45±0.44) E-10	(1.82±0.15) E-9	(3.33±0.21) E-9	(4.71±0.33) E-9
	Background i	(1.21±0.07) E-6	(3.93±0.21) E-6	(7.11±0.90) E-6	(1.12±0.08) E-5

Unit: frequency, kHz; response, $A_{rms}/(\mu S/cm)$; background, A_{rms}; Sample: KCl solution; sine wave, 27 V p-p, electrode length: 10 mm; electrode distance: 2 mm; shield thickness: 0.13 mm.

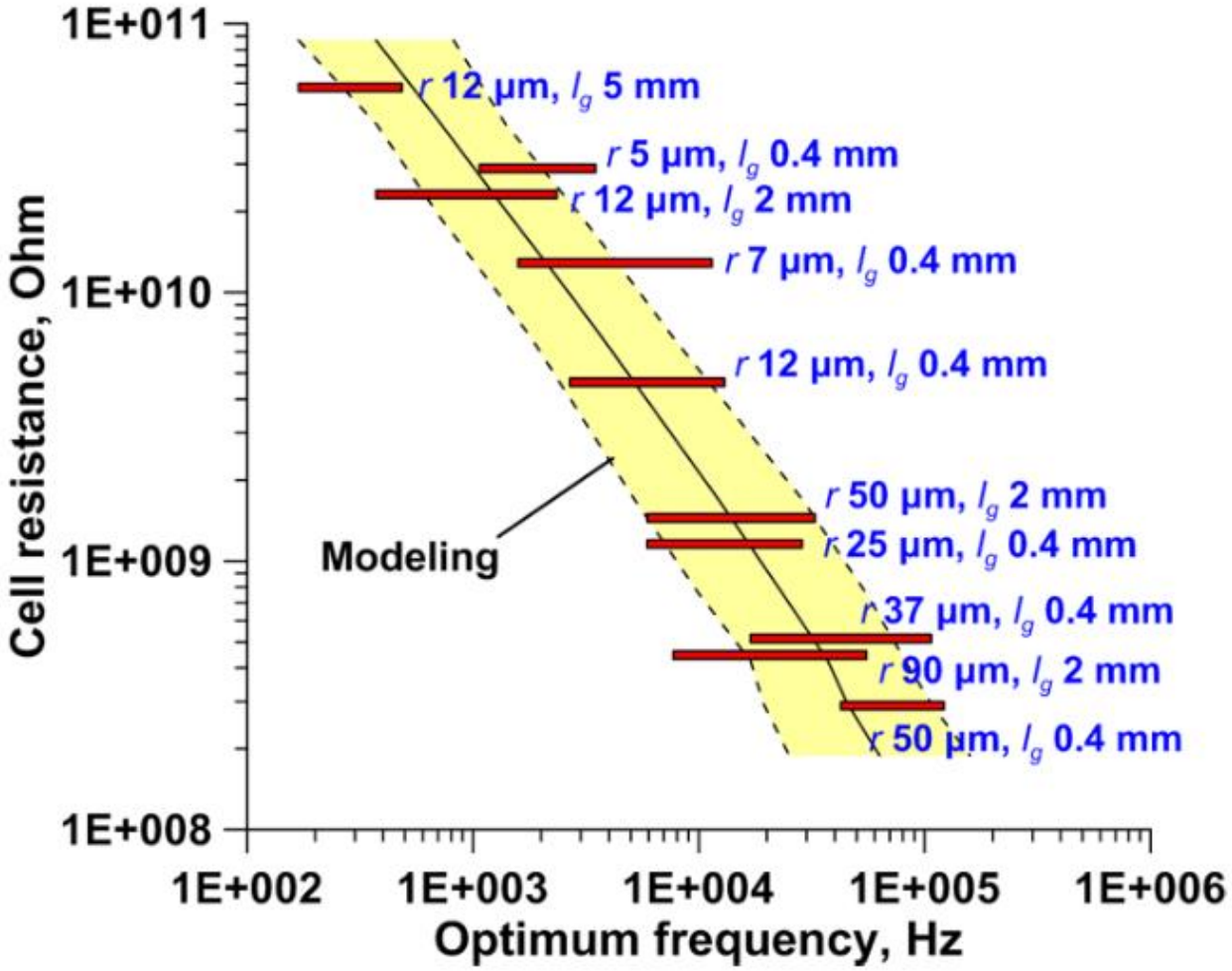

Figure A-S19. Comparison of optimum frequencies for various values of *Rcell* for different capillaries

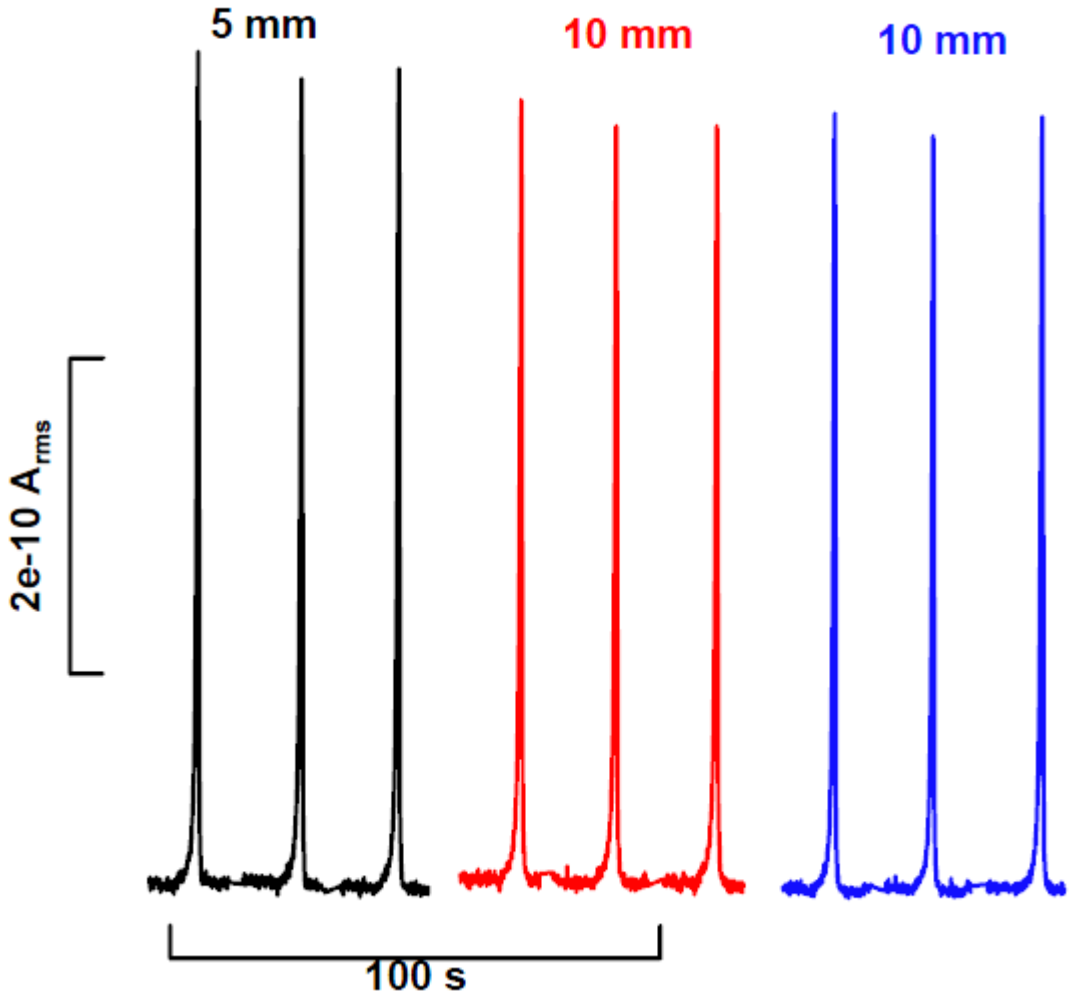

Figure A-S20. Response of 0.2 mM KCl injected into DI water carrier with different electrode lengths.
r = 5 µm, *ro* =182 µm PFSC; detector located 24.5 cm from injection point; injection volume 0.17 nL (equals 2.2 mm capillary length); flow rate, 13.8 nL/min; sine wave 27 V p-p, 1 kHz; *lg* = 0.4 mm; *te* = 0.13 mm; cast Woods metal electrodes.

Table S7. Effect of capillary wall thickness (ro - r)

	r = 50 μm	r_o = 182 μm	r_o = 100 μm
<10 μS/cm	Optimum Frequency, kHz	5.8-31.5	5.5-28.0
	Response, A/(μS/cm)	(3.01±0.21) E-10	(4.43±0.38) E-10
	Background, A	(2.13±0.17) E-9	(4.19±0.33) E-9
	$\frac{1}{\bar{i}}\frac{di}{d\sigma}$	0.141±0.015	0.106±0.012
44 μS/cm	Optimum Frequency, kHz	24.7-148	26.5-156
	Response, A/(μS/cm)	(1.11±0.09) E-9	(1.42±0.11) E-9
	Background, A	(2.76±0.38) E-8	(4.26±0.45) E-8
	$\frac{1}{\bar{i}}\frac{di}{d\sigma}$	(4.01±0.65) E-2	(3.33±0.44) E-2
74 μS/cm	Frequency, kHz	42.4-227	63.0-256
	Response, A/(μS/cm)	(1.31±0.11) E-9	(1.41±0.14) E-9
	Background, A	(5.83±0.97) E-8	(7.38±1.39) E-8
	$\frac{1}{\bar{i}}\frac{di}{d\sigma}$	(2.24±0.42) E-2	(1.90±0.41) E-2
130 μS/cm	Frequency, kHz	91.2-350	142-395
	Response, A/(μS/cm)	(1.39±0.11) E-9	(1.59±0.14) E-9
	Background, A	(1.22±0.21) E-7	(1.46±0.28) E-7
	$\frac{1}{\bar{i}}\frac{di}{d\sigma}$	(1.15±0.21) E-2	(1.09±0.23) E-2
220 μS/cm	Frequency, kHz	209-400	234-400
	Response, A/(μS/cm)	(1.96±0.17) E-9	(2.46±0.21) E-9
	Background, A	(2.54±0.21) E-7	(3.23±0.19) E-7
	$\frac{1}{\bar{i}}\frac{di}{d\sigma}$	(7.69±0.93) E-3	(7.61±0.79) E-3
420 μS/cm	Frequency, kHz	225-400	135-400
	Response, A/(μS/cm)	(1.07±0.09) E-9	(1.42±0.10) E-9
	Background, A	(5.56±0.08) E-7	(7.04±0.29) E-7
	$\frac{1}{\bar{i}}\frac{di}{d\sigma}$	(1.93±0.16) E-3	(2.02±0.16) E-3
700 μS/cm	Frequency, kHz	145-400	121-400
	Response, A/(μS/cm)	(8.55±0.65) E-10	(1.07±0.08) E-9
	Background, A	(8.07±0.47) E-7	(1.05±0.06) E-6
	$\frac{1}{\bar{i}}\frac{di}{d\sigma}$	(1.06±0.10) E-3	(1.01±0.09) E-3
1270 μS/cm	Frequency, kHz	139-400	186-400
	Response, A/(μS/cm)	(6.45±0.44) E-10	(7.58±0.60) E-10
	Background, A	(1.21±0.07) E-6	(1.56±0.07) E-6
	$\frac{1}{\bar{i}}\frac{di}{d\sigma}$	(5.32±0.49) E-4	(4.86±0.44) E-4

Sample, KCl solution; PFSC; applying wave, sine wave of 27 V amplitude; electrode length, 10 mm; electrode distance, 2 mm; shield thickness, 0.13 mm;

Table S8. Comparison of Capillaries of Different Material

		r =7.5 µm r_o = 182 µm PFS	r =8 µm r_o = 175 µm PMMA	r =25 µm r_o = 182 µm PFSC	r =26 µm r_o = 180 µm PTFE	r =12,5 µm r_o = 182 µm PFSC	r =12,5 µm r_o = 180 µm PEEK
	Electrode length (l_e, mm)	5	5	10	10	5	5
<10 µS/cm	Frequency, kHz	2.2-13.6	1.8-12.7	8.8-37.4	9.8-44.5	3.6-25.9	3.7-24.4
	Response, A/(µS/cm)	(2.96±0.23) E-11	(2.60±0.20) E-11	(2.15±0.17) E-10	(2.54±0.19) E-10	(1.49±0.11)E-10	(2.26±0.17)E-10
	Background, A	(3.01±0.62) E-10	(2.14±0.12) E-10	(1.63±0.11) E-9	(2.00±0.15) E-9	(1.17±0.10)E-9	(9.71±0.88)E-10
44 µS/cm	Frequency, kHz	8.0-42.2	7.7-37.9	14.7-75.2	19.3-88.5	11.1-40.0	14.6-40.0
	Response, A/(µS/cm)	(6.27±0.51) E-11	(6.30±0.44) E-11	(3.59±0.26) E-10	(3.46±0.30) E-10	(8.28±0.59)E-11	(1.54±0.11)E-10
	Background, A	(2.43±0.10) E-9	(2.00±0.15) E-9	(1.31±0.14) E-8	(1.39±0.20) E-8	(2.50±0.17)E-9	(4.95±0.18)E-9
74 µS/cm	Frequency, kHz	10.4-40.0	10.8-32.0	17.4-91.3	11.1-100	14.7-40.0	17.6-40.0
	Response, A/(µS/cm)	(2.13±0.24) E-11	(2.16±0.19) E-11	(3.23±0.26) E-10	(2.56±0.20) E-10	(1.07±0.08)E-10	(1.43±0.12)E-10
	Background, A	(1.24±0.06) E-9	(8.81±0.58) E-10	(2.23±0.30) E-8	(2.17±0.31) E-8	(5.34±0.24)E-9	(9.40±0.37)E-9
130 µS/cm	Frequency, kHz	14.5-43.5	11.1-38.3	100-344	176-400	17.3-37.5	14.1-40.0
	Response, A/(µS/cm)	(3.31±0.27) E-11	(3.14±0.31) E-11	(6.96±0.57) E-10	(5.38±0.40) E-10	(1.09±0.09)E-10	(1.25±0.48)E-10
	Background, A	(2.89±0.13) E-9	(2.41±0.11) E-9	(5.36±0.38) E-8	(4.60±0.09) E-8	(1.19±0.05)E-8	(1.56±0.60)E-8
220 µS/cm	Frequency, kHz	92.8-245		177-400	231-400	14.0-38.3	
	Response, A/(µS/cm)	(2.65±0.22) E-11		(7.61±0.57) E-10	(7.38±0.59) E-10	(1.09±0.42)E-10	
	Background, A	(2.90±0.15) E-9		(1.12±0.10) E-7	(1.41±0.10) E-7	(1.98±0.75)E-8	
420 µS/cm	Frequency, kHz	94.1-400	94.0-400	321-400	344-400		18.7-400
	Response, A/(µS/cm)	(3.74±0.26) E-11	(3.22±0.21) E-11	(6.18±0.68) E-10	(6.55±0.70) E-10		(2.15±0.18)E-10
	Background, A	(1.02±0.04) E-8	(8.21±0.70) E-9	(2.54±0.05) E-7	(2.87±0.01) E-7		(9.11±0.42)E-8
700 µS/cm	Frequency, kHz	135-400	129-400	293-400	279-400	181-400	202-400
	Response, A/(µS/cm)	(4.29±0.30) E-11	(4.02±0.34) E-11	(4.46±0.37) E-10	(3.82±0.37) E-10	(1.54±0.13)E-10	(1.97±0.17)E-10
	Background, A	(2.20±0.06) E-8	(1.87±0.07) E-8	(4.08±0.12) E-7	(4.25±0.25) E-7	(1.01±0.05)E-7	(1.49±0.08)E-7
1270 µS/cm	Frequency, kHz	177-400	156-400	276-400	252-400	191-400	193-400
	Response, A/(µS/cm)	(3.93±0.29) E-11	(4.13±0.35) E-11	(2.54±0.23) E-10	(2.37±0.20) E-10	(1.14±0.10)E-10	(1.46±0.11)E-10
	Background, A	(4.62±0.12) E-8	(4.26±0.13) E-8	(6.10±0.36) E-7	(5.97±0.41) E-7	(1.74±0.13)E-7	(2.43±0.16)E-7

Each comparison pair is color-coded. Sample: KCl solution; PFSC; sine wave of 27 V p-p; electrode distance: 0.4 mm; shield thickness: 0.13 mm

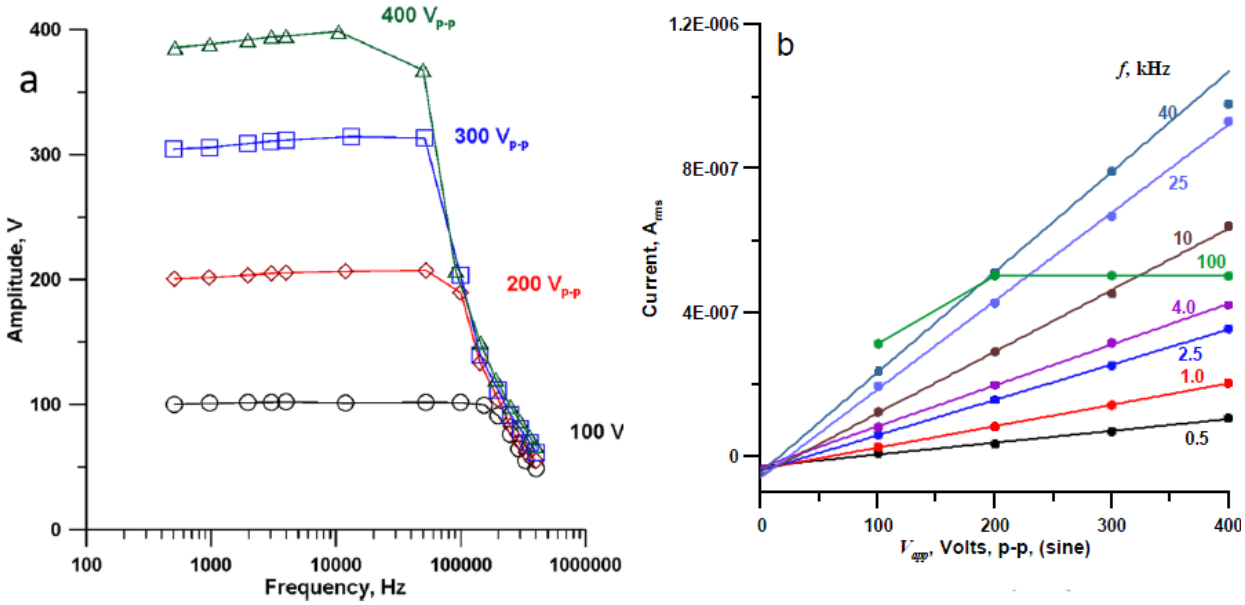

Figure A-S21. The frequency response of the PA15 boost amplifier (a) and effect of input voltage to output current of the CCD (b).
Measured current for 1 mM KCl solution; *ro* = 182 µm, *r* = 12.5 µm, other conditions as in Figure 3. Plot b indicates a small negative bias current. Both plots indicate no GBW limitation to 40 kHz.

Appendix B Supporting Information for Chapter 2

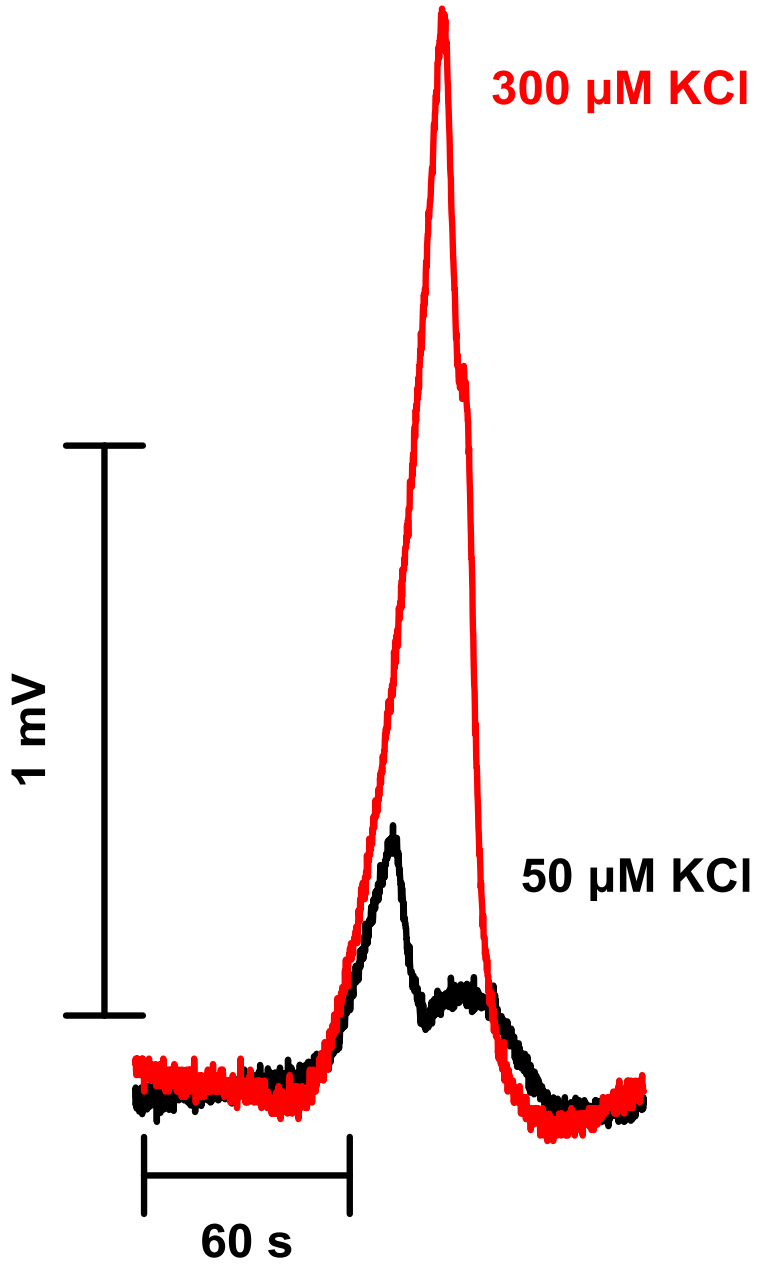

Figure B-S1. During several initial injections of KCl into a water carrier flowing through the capillary
(r = 1 μm, r_o = 75 μm, see Figure 3 for other conditions), a split peak was produced. This gradually disappeared. We interpret this as the wall is initially in the H^+-form. K^+ in part is exchanged for H^+ and the two elute separately (HCl, then KOH+KCl) leading to split peaks. When the wall is fully converted to the K^+-form, “normal” peaks appear.

Appendix C Supporting Information for Chapter 3

Table C-S1. OTIC program sequence for sample injection and separation, one cycle

step	Duration Time	SV1	SV2	IV	Pressure	comment
1	1 s	off	Off	load	P_{inj} (typical, 14 psi)	System initialization; apply pressure to the system; Sample has been loaded in IV before running the program
2	1 s	off	Off	injection	P_{inj}	Switch IV to make the sample loop to connect to the eluent line
3	800 ms	on	Off	injection	P_{inj}	Open SV1 to move the undiluted sample zone to the Tee
4	t_{inj} (100-5000 ms)	off	Off	Injection	P_{inj}	Close SV1 for introducing sample into the capillary column
5	3 s	on	Off	Injection	P_{inj}	Open SV1 again for cleaning the remaining sample in the Tee and the line
6	1 s	off	Off	load	P_{sep} (14-100 psi)	Close SV1 and increase the pressure for beginning the separation; trigger data acquisition
7	t_{sep}	off	Off	load	P_{sep}	Separation step. The duration time (t_{sep}) is depended by the duration time of chromatography and column equilibrium.
8	800 ms	off	On	load	P_{inj}	Open SV1 for release tank pressure (when $P_{sep} > P_{inj}$)
9	1 s	off	Off	load	P_{inj}	Return to the initial status for next cycle

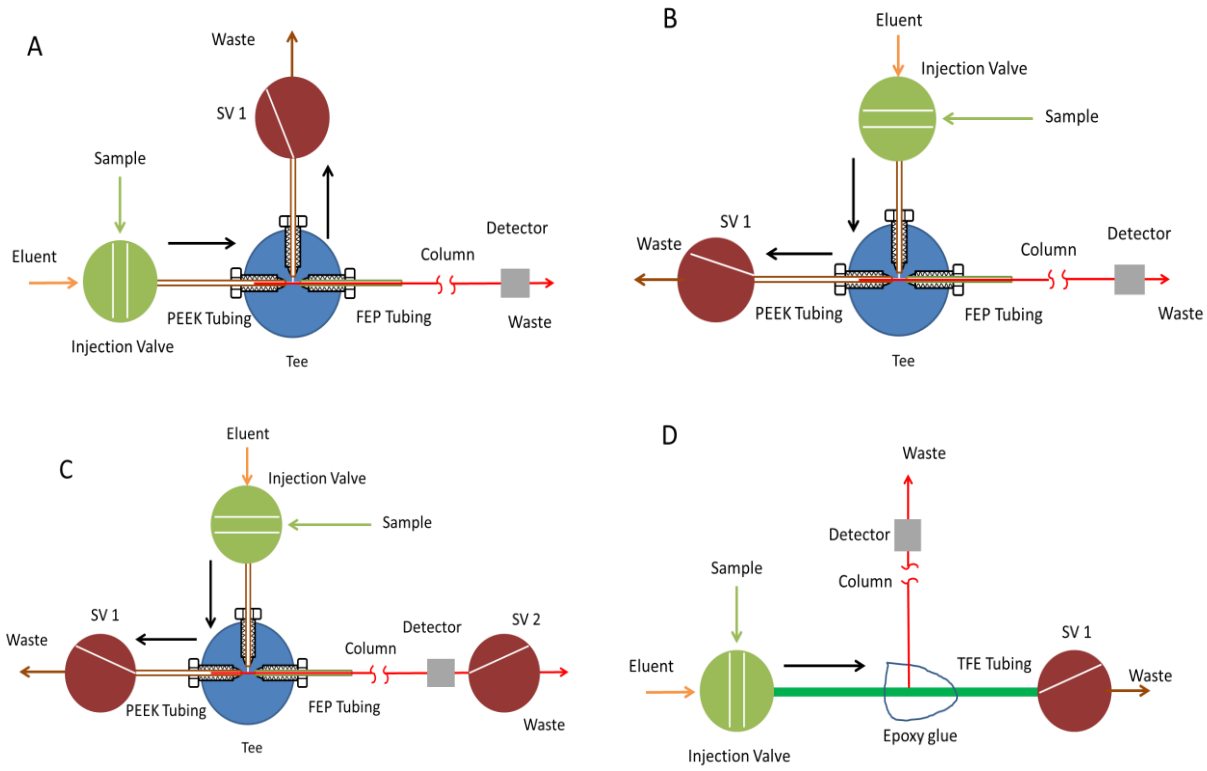

Figure C-S1. Comparison of autoinjected volumes (V_{aut}) with different configurations
(r = 9.8 μm, L= 70 cm, PMMA): **A.** The capillary column is inserted into the eluent inlet tubing through the tee, V_{aut} = 279 pL; **B.** The capillary column is inserted into the eluent outlet tubing, V_{aut} = 38 pL; preferred configuration; used in this work; **C.** The capillary column is inserted into the eluent outlet tubing. The outlet of column was connected to an additional valve (SV2); when the sample is passing through the tee, SV2 was shut off to prevent flow into the column, V_{aut} = 51 pL; **D.** custom tee: hole drilled through a PEEK tube wall, column connected through the hole and epoxy adhesive was used to fix the column, V_{aut} = 149 pL;

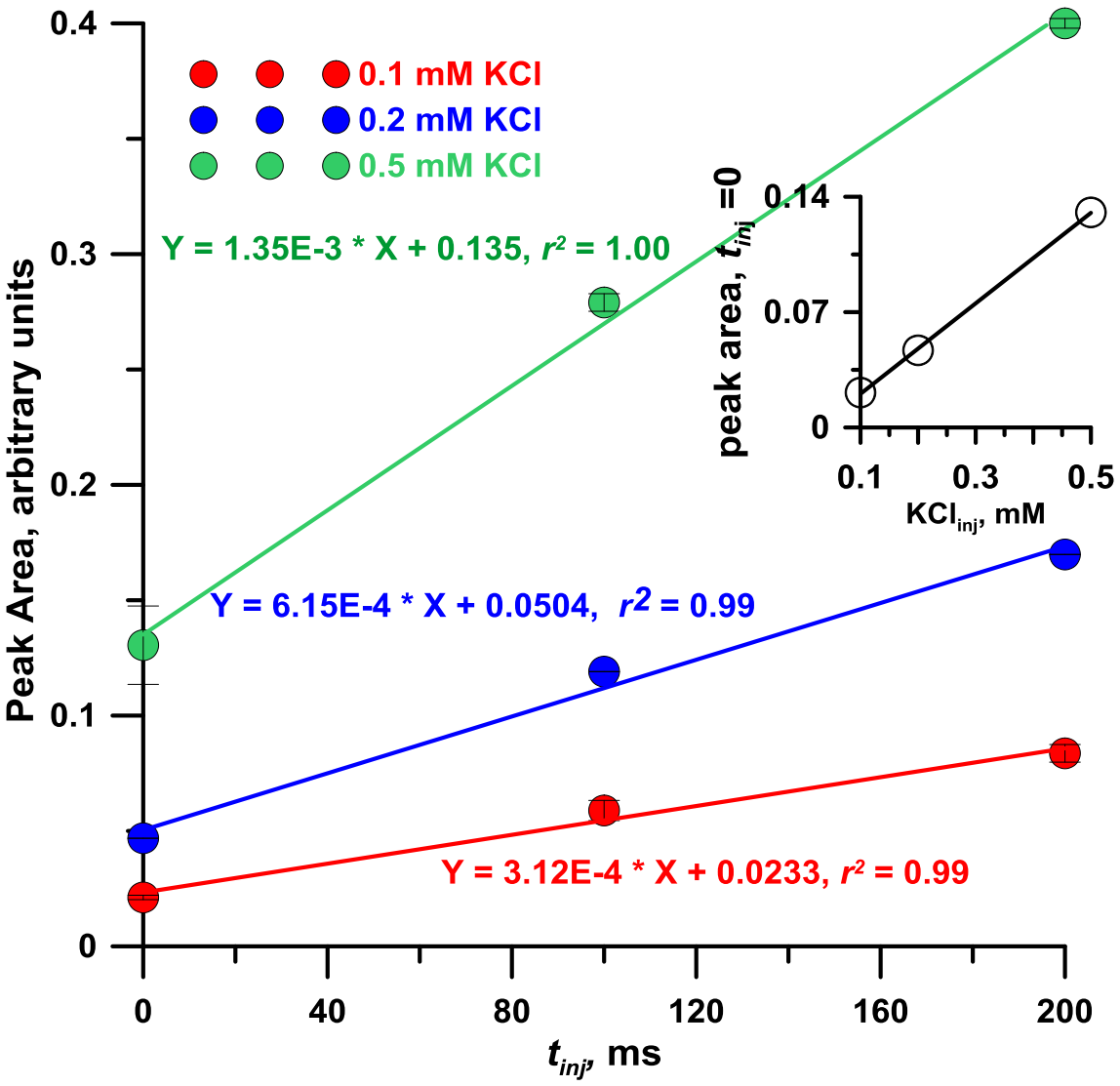

Figure C-S2. The Peak Area of Cl^- at different injection times

(n=3). Conditions: Triplicate injection, 1 mM NaBz eluent, r =9.8 μm, L = 70 cm, P_{Elu}

30 psi, 63 nL/min.

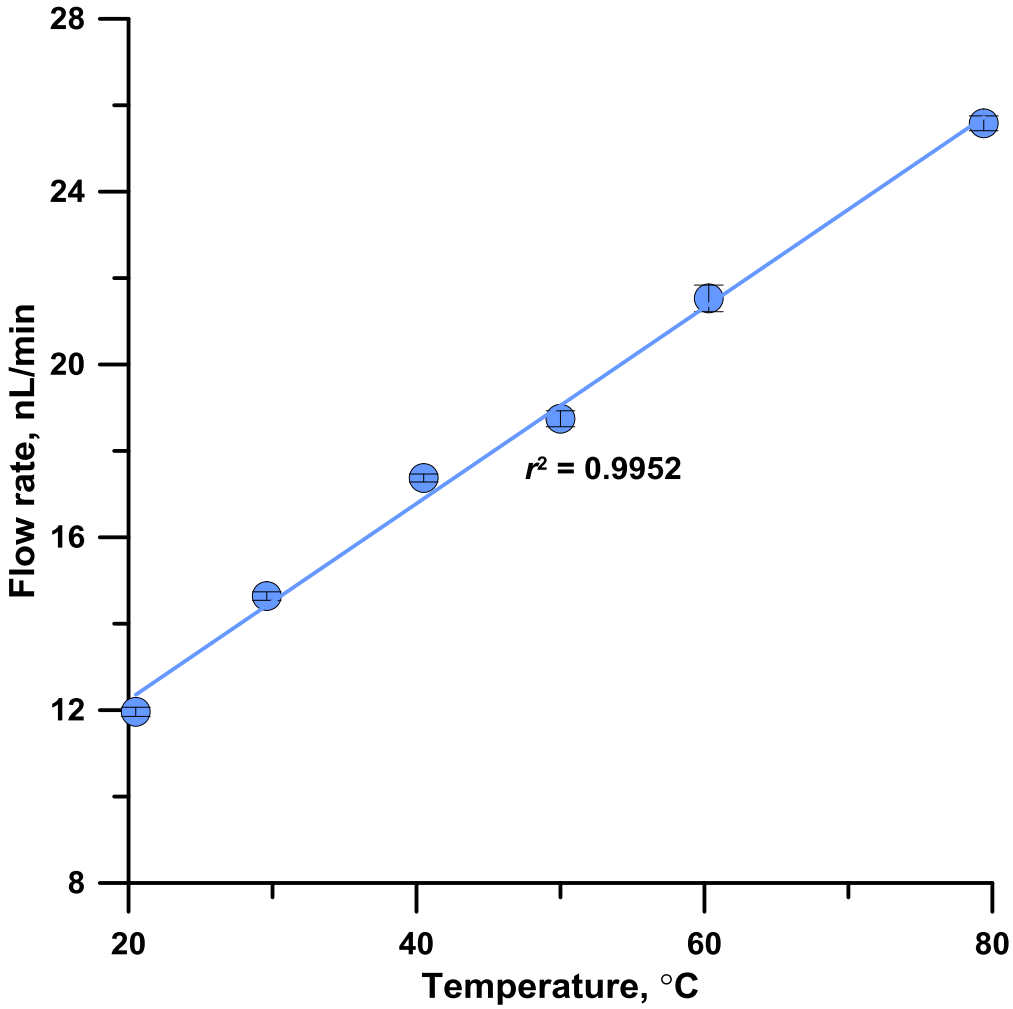

Figure C-S3. Silica capillary, r = 5 μm, L= 55 cm.

2 mM sodium benzoate, pressure fixed at 55 psi. Flow rates were measured gravimetrically.

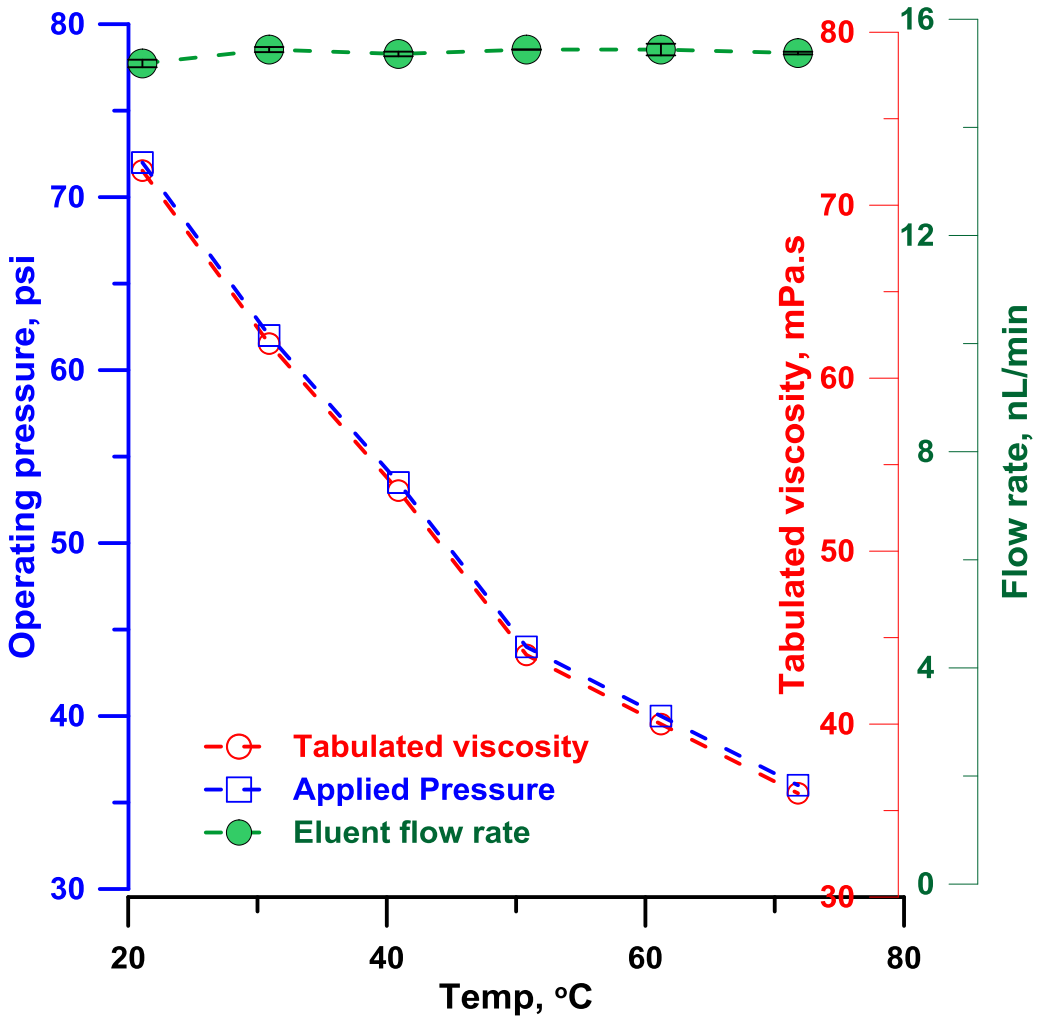

Figure C-S4. Maintaining constant flow rate by varying applied pressure as temperature varies**.**

Silica capillary, r = 5 μm, L= 55 cm, 2 mM Na-Benzoate. Flow rate measured gravimetrically.

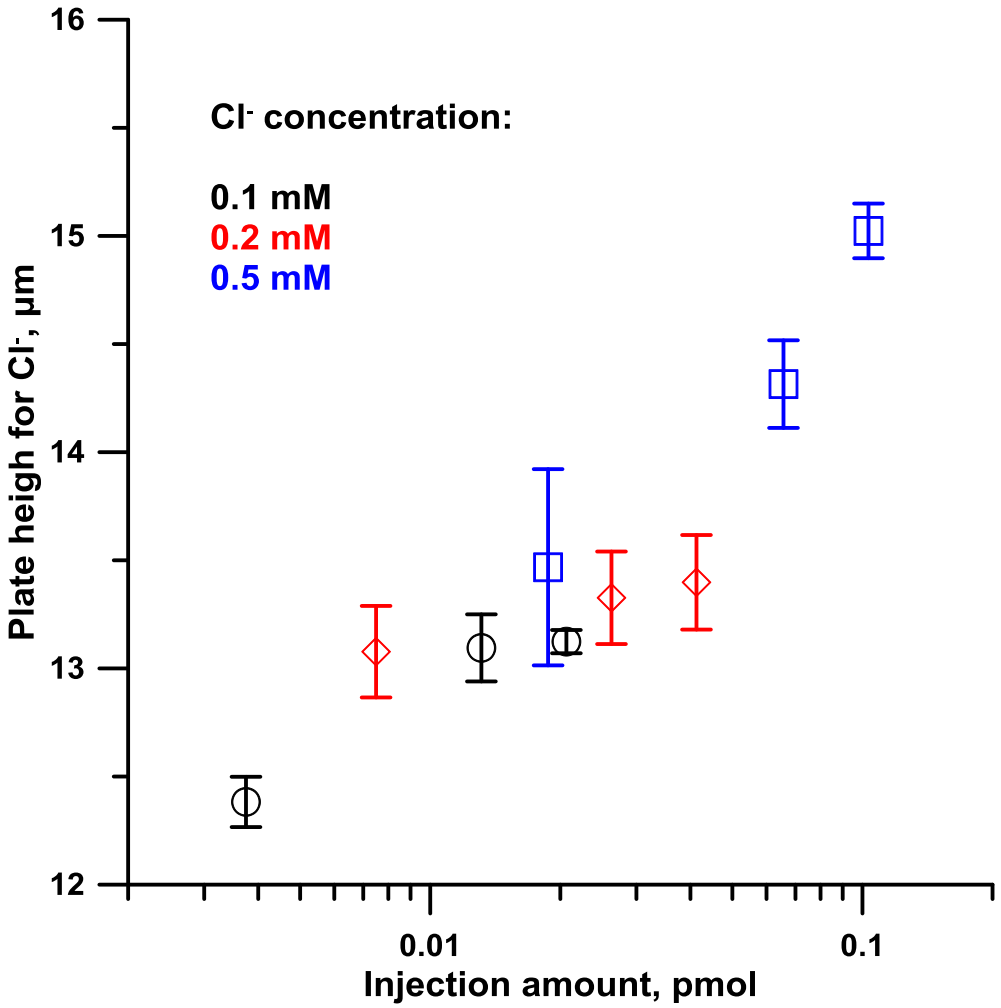

Figure C-S5. Plate height of Cl^- as a function of amount injected.

0.1, 0.2 or 0.3 mM KCl was injected for 0 (autoinjection), 100 or 200 ms at 14 psi.

Triplicate injection, 1 mM NaBz eluent, r = 9.8 µm, L = 70 cm, P_{Elu} = 30 psi, 63 nL/min

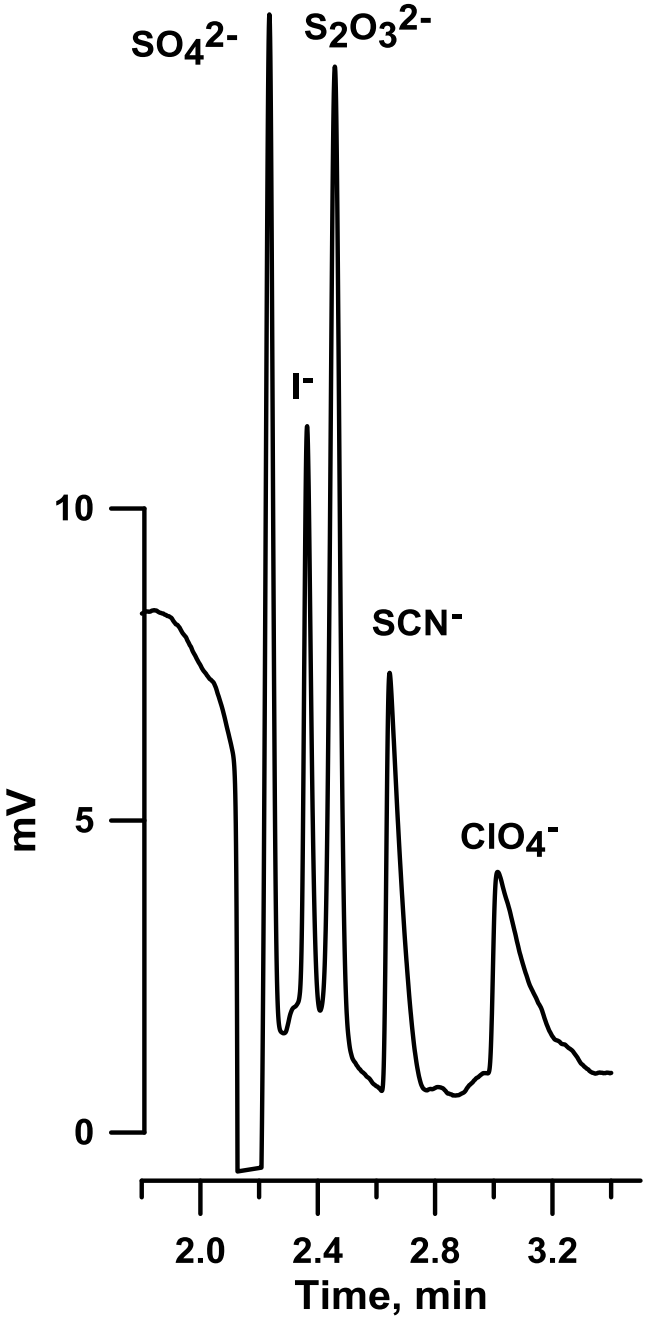

Figure C-S6. Chromatogram of strongly retained anions.

r = 9.8 µm, *L* = 70 cm; Eluent, 2 mM phthalate, pH= 7.4; samples, 200 µM SO_4^-, I^-, $S_2O_3^-$; 500 µM ClO_4^-, SCN^-; injection volume 100 pL; P_{Elu} =45 psi, linear velocity 0.54 cm/s (96 nL/min).

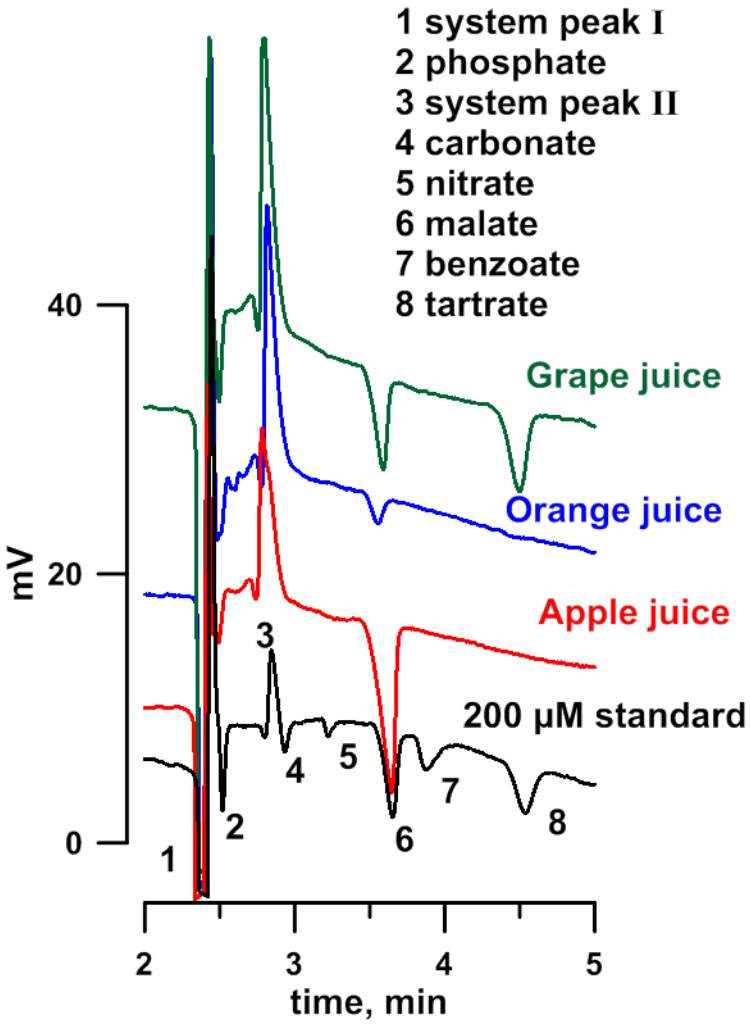

Figure C-S7. Chromatograms of separation typical organic acids in fruit juice samples.

Conditions: (r =8.5 µm, L = 59 cm long; injection volume, 1.8 nL; Eluent, 1 mM Na_2SO_4 + 1mM NH_4OAc, pH = 5.0 (adjusted with HOAc); P_{Elu} =40 psi, linear velocity 0.40 cm/s (26 nL/min). standard concentrations: 200 µM each analyte. Citrate takes too long under these conditions and is better eluted with a phthalate eluent.

Table C-S2. Inorganic and organic anions concentration in samples

	Chloride	Nitrate	malate	tartrate	citrate
Grape juice	4.226±0.023	0.256±0.012	1.190±0.080	18.42±1.34	0.545±0.152
Apple juice	0.891±0.020	0.252±0.015	24.58±0.74	ND	ND
Orange juice	1.378±0.037	ND	0.066±0.007	ND	13.48±0.48
Mineral water	0.146±0.006	0.076±0.003	3.050±0.285	ND	ND

Concentrations given in mM, uncertainties represent ±1 SD (n=3).

Inorganic anions were determined with a benzoate eluent, citrate was determined with a phthalate eluent, other organic acids were determined with a acetate buffered sulfate eluent (see Figure S7).

Table C-S3. Analytical parameters for the separation of inorganic anions and organic anions

	Linear range (μM)	R	RSD [b] (%)	LOD_1 [c] (μM)	LOD_2 [d] (μM)
F^-	10-400	0.9972	4.92	2.6	1.8
Cl^-	5-250	0.9980	3.37	1.4	0.8
NO_2^-	5-250	0.9985	4.82	1.9	1.0
Br^-	5-250	0.9994	3.22	1.5	0.7
NO_3^-	5-250	0.9993	3.00	2.3	1.0
SO_4^{2-}	10-400	0.9997	0.68	-	3.3
$H_2PO_4^-$	40-400	0.9979	7.46	-	11.1
Malate	40-400	0.9994	3.53	-	12.6
Benzoate	100-400	0.9971	7.33	-	28.5
Tartrate	70-400	0.9994	4.38	-	21.9
Citrate	100-400	0.9969	5.07	-	32.0

a) Eluent for F^-, Cl^-, NO_2^-, Br^- and NO_3^-: 1 mM benzoate;
Eluent for $H_2PO_4^-$, malate, benzoate, tartrate: 1 mM Na_2SO_4 and 1 mM NH_4Ac, pH = 5.0 (adjusted with HAc);

Eluent for SO_4^{2-} and citrate: 2 mM phthalate with pH 7.0 (adjusted with LiOH);

b) n = 3; sample concentration: 200 μM; Injected sample volume: 1.2 nL;
c) S/N = 3 criterion verified at each stated LOD; injected sample volume: 0.5 nL;
d) Injected sample volume: 1.2 nL

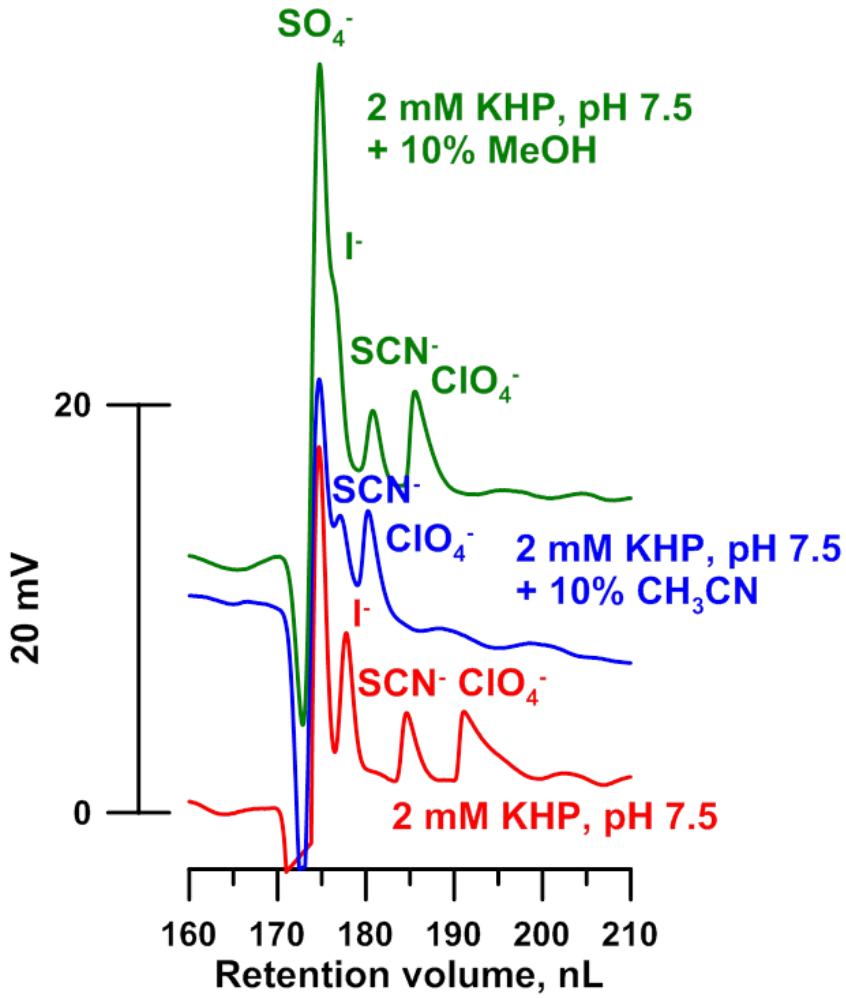

Figure C-S8. PMMA, r = 9.8 μm, L_{eff} = 58 cm. Flow rate: 48 nL/min. 500 μM each I^-, SCN^-; 1 mM each SO_4^{2-}, ClO_4^-, 0.2 nL injection.
Perchlorate asymmetry at 10% height changed from 8.1 to 3.4 to 2.0 in going from pure water to 10% methanol to 10% acetonitrile.

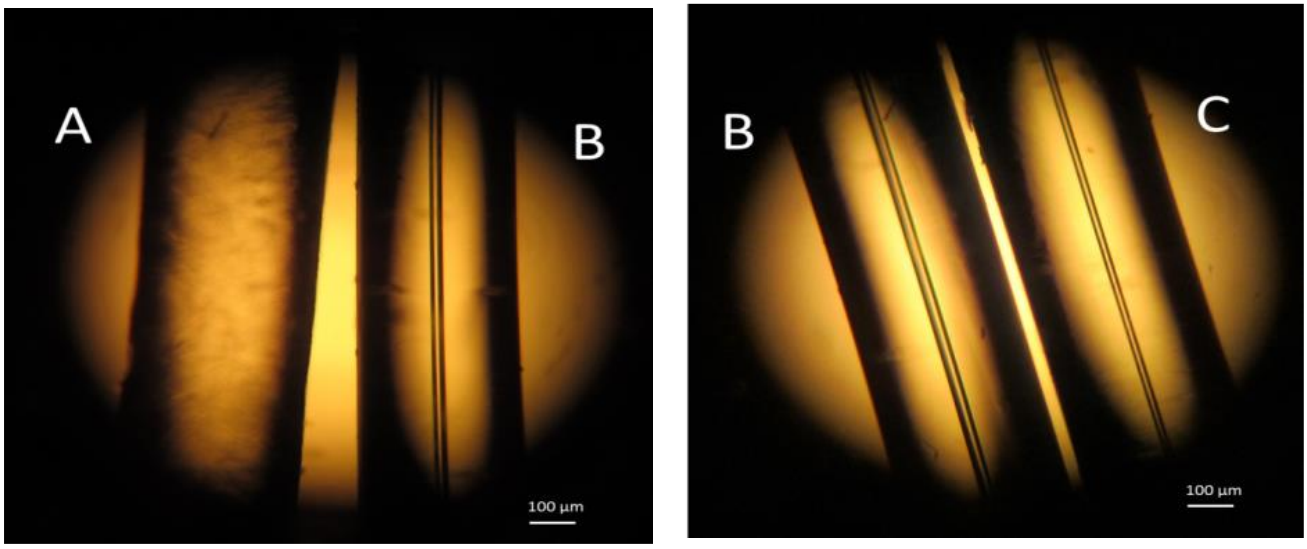

Figure C-S9. A): immersed into 50% (v/v) acetonitrile solution for 10 h; B) original PMMA capillary, without treatment with acetonitrile; C) the channel passed by 30% (v/v) acetonitrile solution for 2 h.

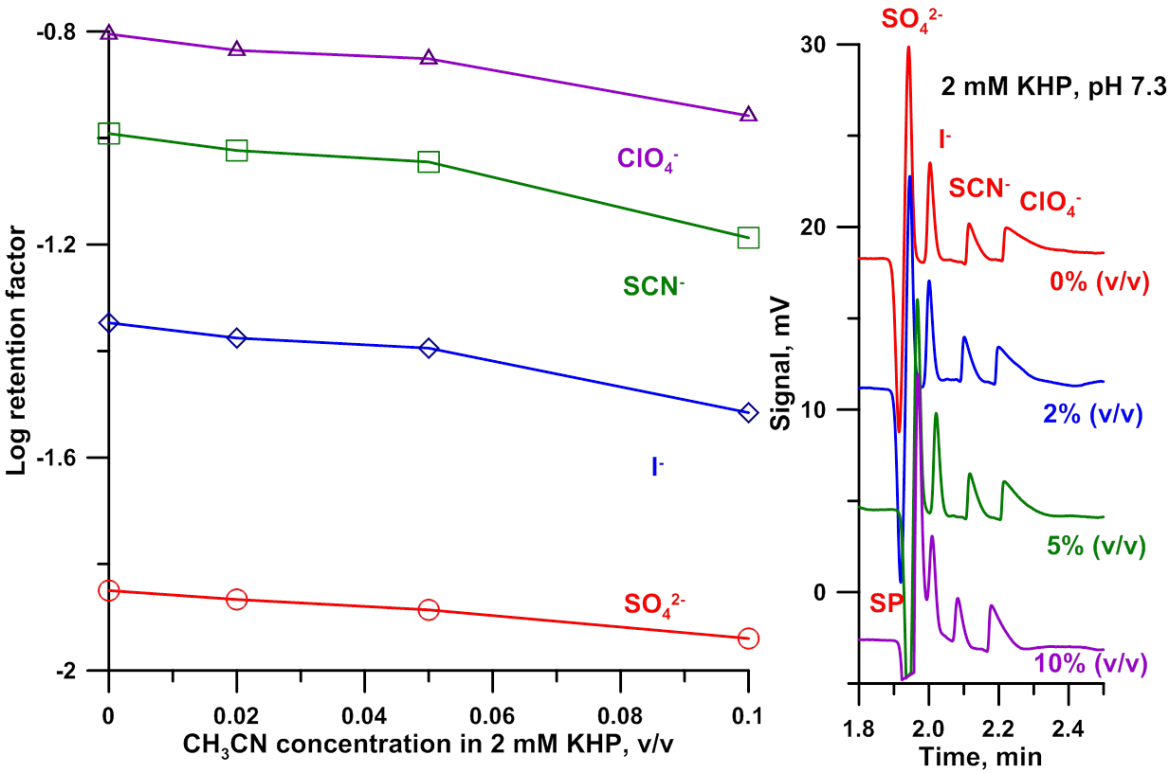

Figure C-S10. Variations in acetonitrile content in an acetonitrile containing phthalate eluent 2 mM phthalate at pH 7.3 plus acetonitrile as indicated
r = 7.2 μm, *L* = 47 cm, PMMA, injection volume,0.25 nL; P_{Elu} 48 psi; linear velocity 0.40 cm/s (44 nL/min). I^- and SCN^- at 0.5 mM, $SO_4^{2-}$and ClO_4^-at 1 mM.

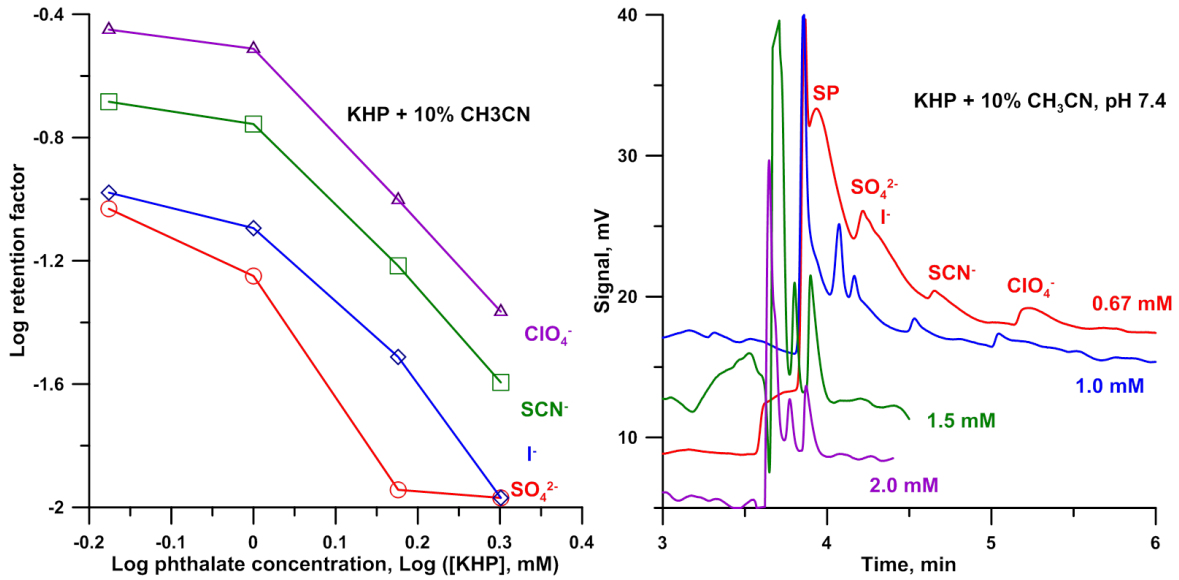

Figure C-S11. Variations in phthalate content in a phthalate eluent (pH 7.4) containing 10%v/v acetonitrile

r = 7.2 μm, *L* = 68 cm, PMMA, injection volume,0.2 nL; P_{Elu} 48 psi, linear velocity 0.32 cm/s (31 nL/min); I^- and SCN^- at 0.5 mM, $SO_4^{2-}$and ClO_4^-at 1 mM**.**

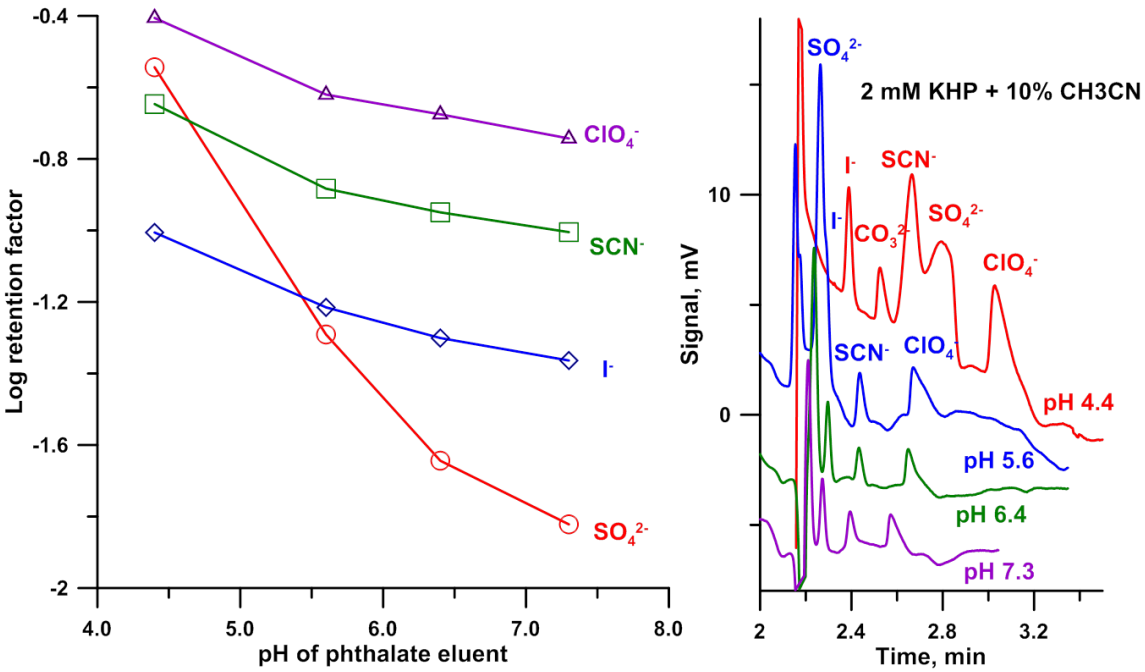

Figure C-S12. Variations in pH in a 2 mM phthalate eluent containing 10%v/v acetonitrile

r =7.2 μm, *L* = 54 cm, PMMA, injection volume, 0.25 nL; P_{elu} 48 psi, linear velocity 0.40 cm/s (38 nL/min); I^- and SCN^- at 0.5 mM, SO_4^{2-} and ClO_4^- at 1 mM.

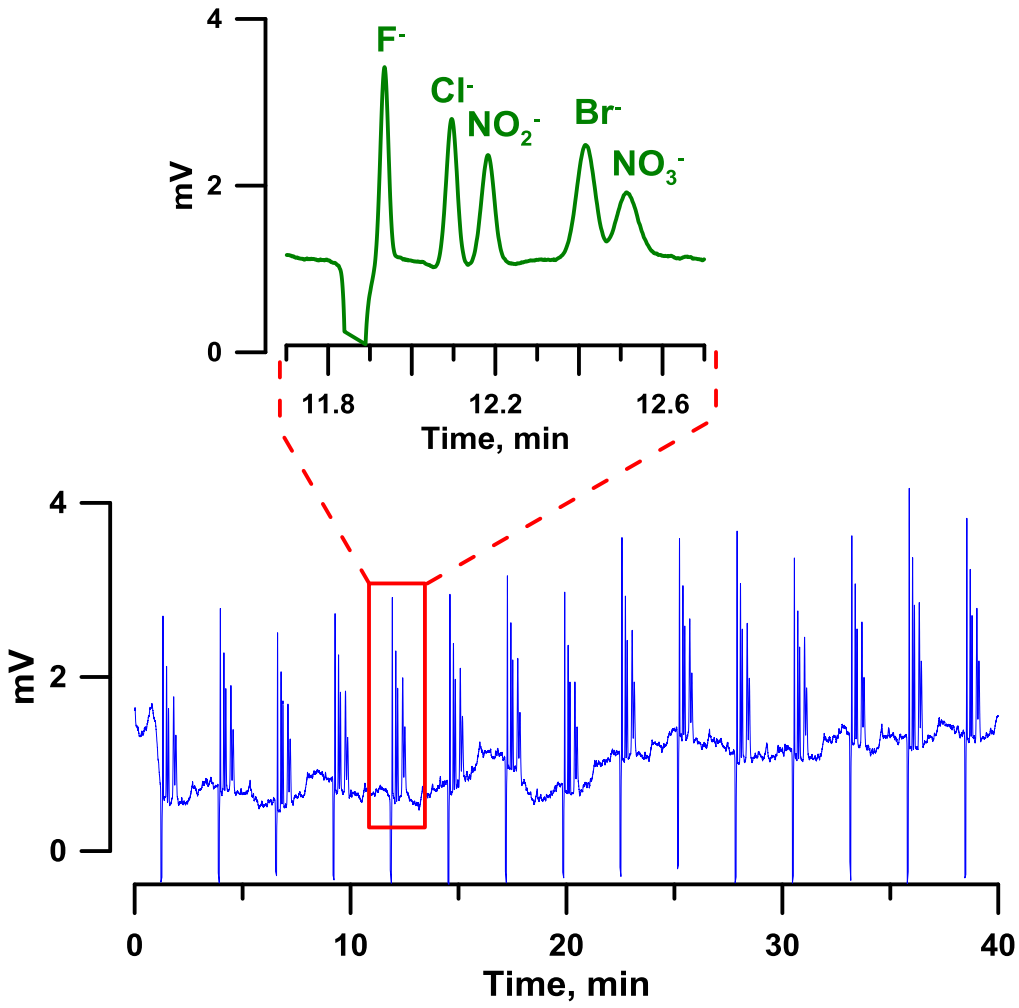

Figure C-S13. Fast separation (1 min window) of five ions
r = 9.8 μm, *L* = 80 cm, PMMA , injection volume, 0.48 nL; samples, 200 μM F-; 100 μM

of Cl^-, NO_2^-, Br^-, NO_3^-; P_{Elu} =100 psi, linear velocity 1.07 cm/s (191 nL/min).

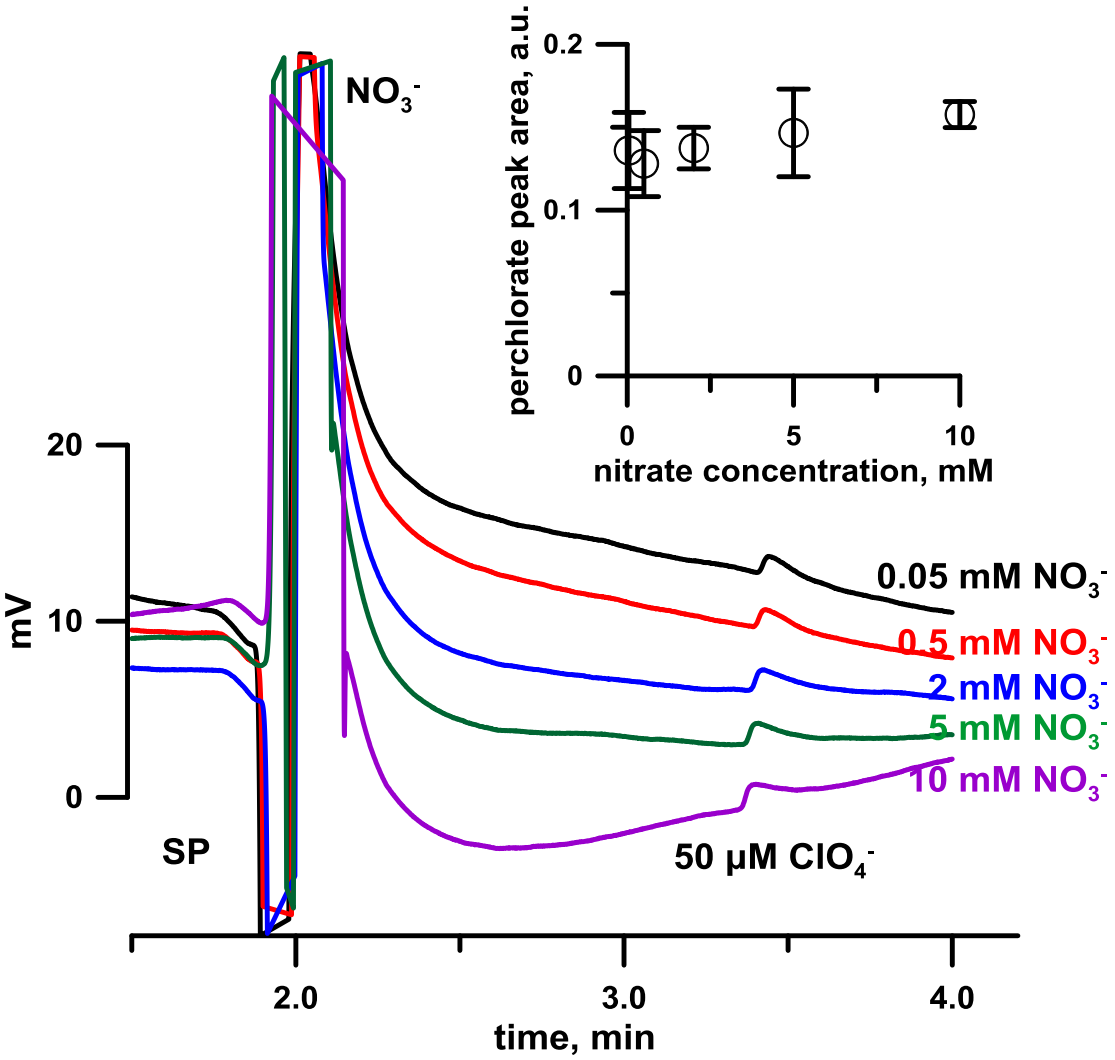

Figure C-S14. Chromatograms for the separation and quantitation of ClO_4^- in the presence of varying amounts of NO_3^- (up to 200x)
The inset shows the constancy of the ClO_4^- peak area. r = 7.3 μm, L = 40 cm, PMMA, 50 μM ClO_4^- in presence of 50 -10,000 μM NO_3^-; 2 mM potassium phthalate (pH 7.4) with 10% (v/v) acetonitrile. Injection volume, 4.11 nL; P_{Elu} =40 psi, linear velocity 0.32 cm/s (32 nL/min).

Baseline Correction procedure. As experiments were done without temperature control and electrical properties such as conductance are highly temperature dependent, at high sensitivities baseline drift was significant. As the periods for a chromatogram were short the drifts were mostly linear (not always) and we simply assumed the baseline drifted linearly from the start (before any peaks) to the end (after complete elution of all analytes). This was then subtracted from the raw data.

Appendix D Supporting Information for Chapter 4

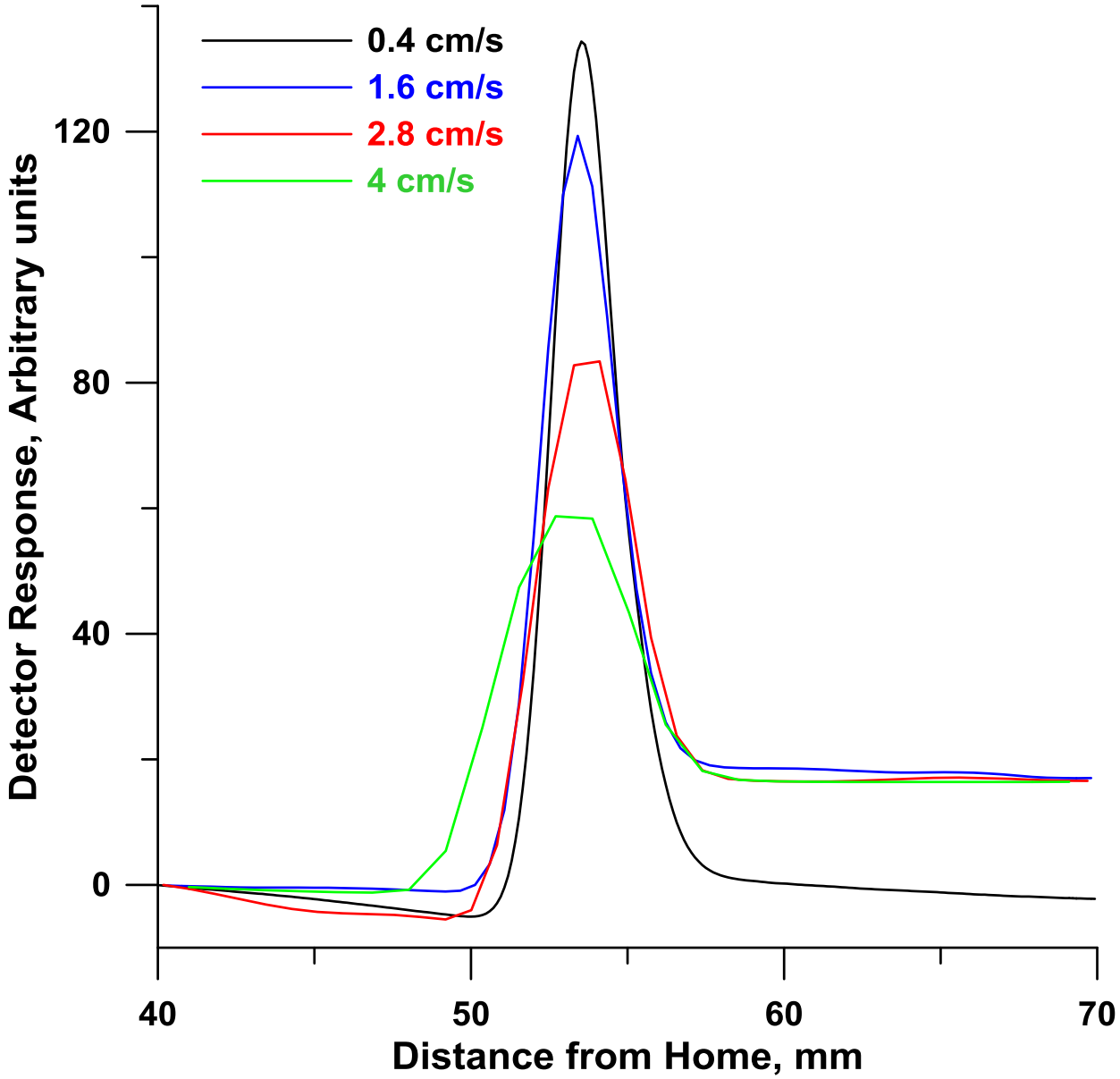

Figure D-S1. Tracedec AD response to injections of 0.95 nL of 500 µM KCl at scanning speeds of 0.4 cm/s (black), 1.6 cm/s (blue), 2.8 cm/s (red) and 4 cm/s (green). Note that at the higher scanning speeds the baseline never returns to the starting value.

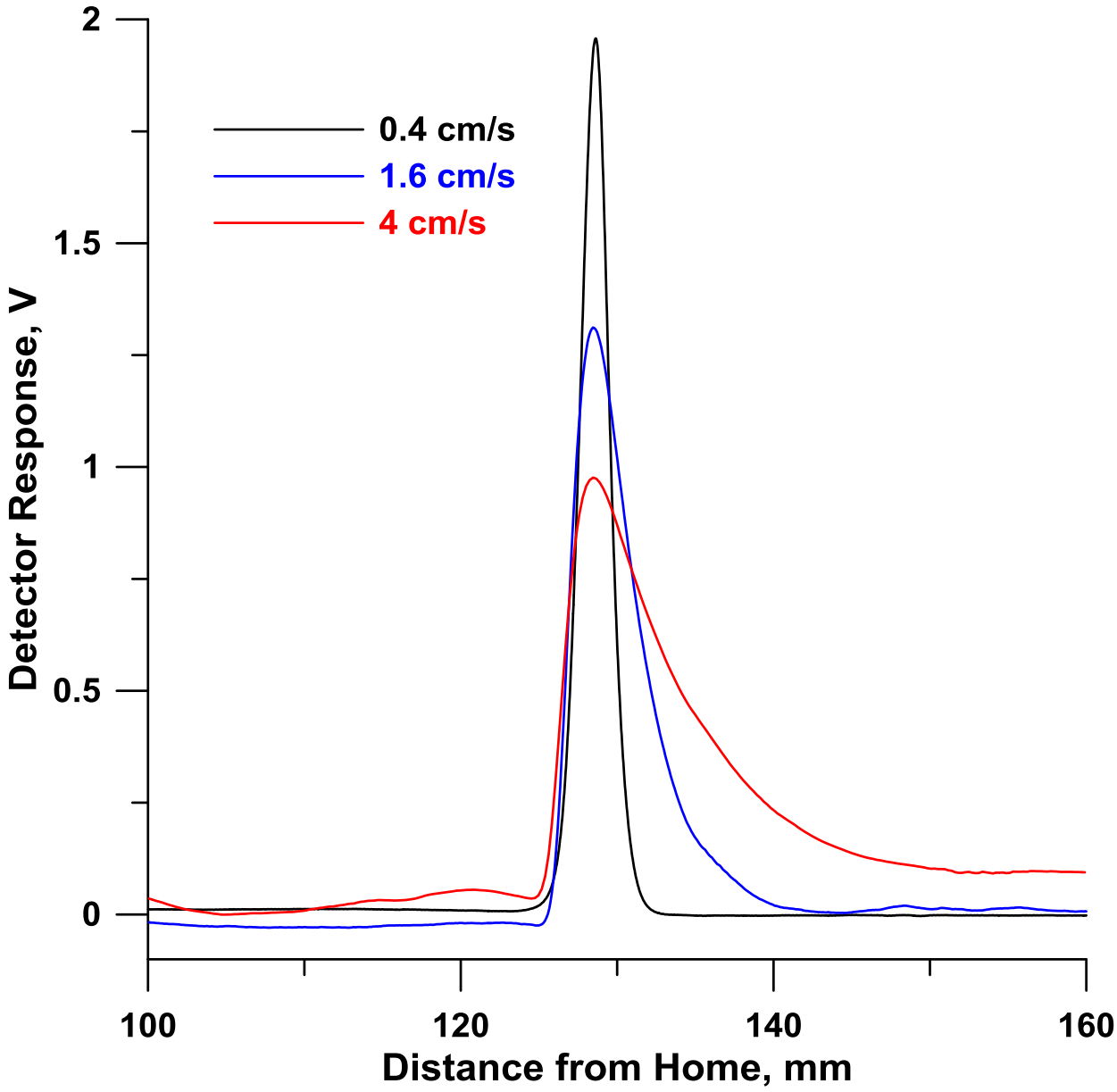

Figure D-S2. AF AD response (time constant 0.25 s) to injections of 500 µM KCl at scanning speeds of 0.4, 1.6 and 4.0 cm/s.
A more challenging condition than Figure S1 was used: 0.18 nL injection was used with a 11 µm ϕ capillary. Data acquisition rate 1 kHz. Return to baseline is improved compared to Figure S1 but at the highest scan speed, this is still an issue.

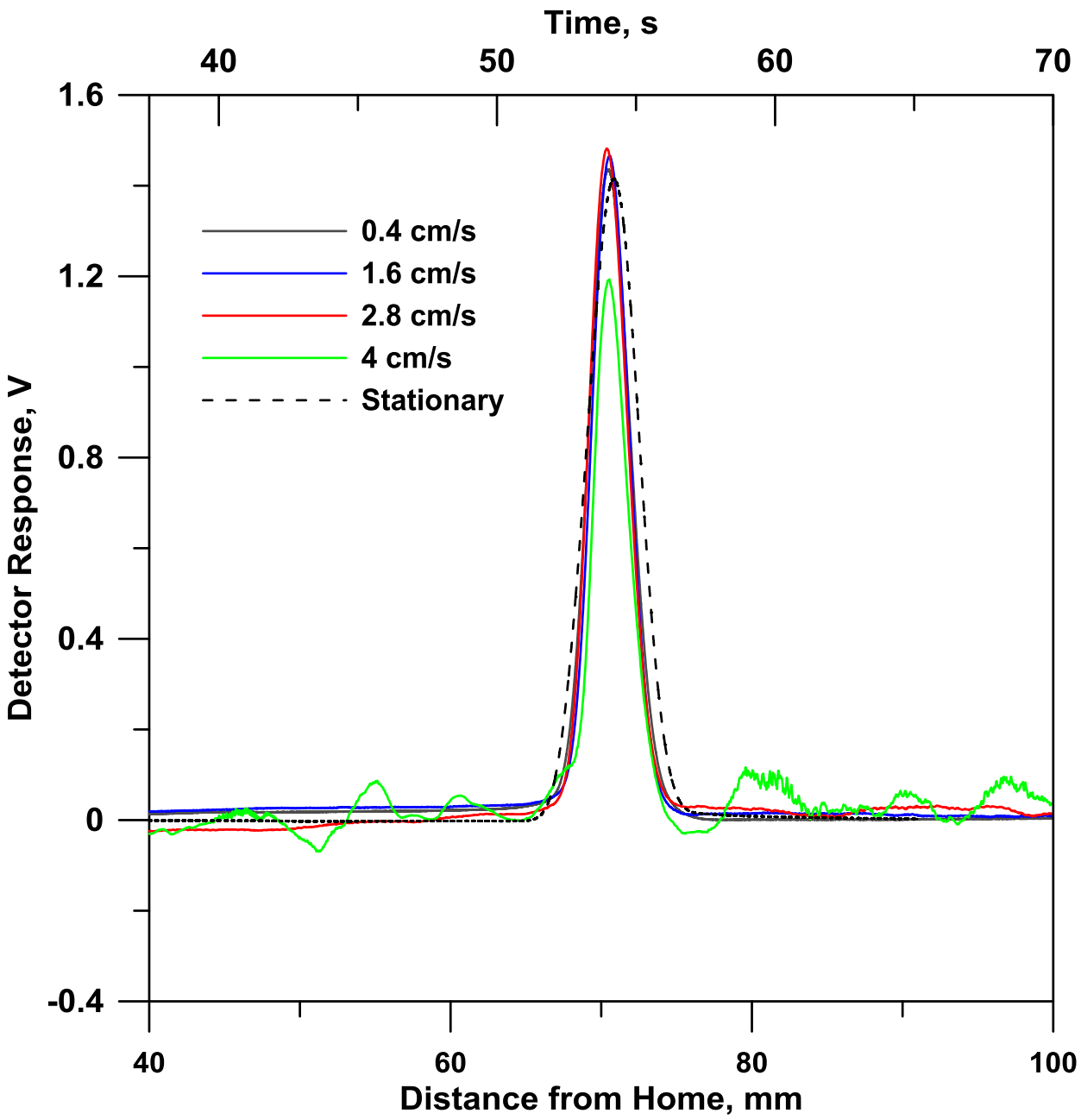

Figure D-S3. AF AD response (time constant 25 ms) to injections of 500 µM KCl at scanning speeds of 0.4, 1.6 and 4.0 cm/s

Conditions same as in Figure S2. Return to baseline is further improved compared to Figure S2. With increasing speed, the peak areas did not decrease much until the highest speed: 6.66, 6.15, 6.15, and 5.16 area units from the lowest to the highest speed. The baseline noise is clearly the highest at the highest speed (4.5 mV specified as standard deviation after drift correction) and lowest at the lowest (0.37 mV) but inconsistent at the intermediate speeds (1.45 and 0.96 mV at 1.6 and 2.8 cm/s, respectively). The stationary detector noise was 0.22 mV, the top abscissa scale pertains to the stationary detector, positioned at ~7 cm from home.

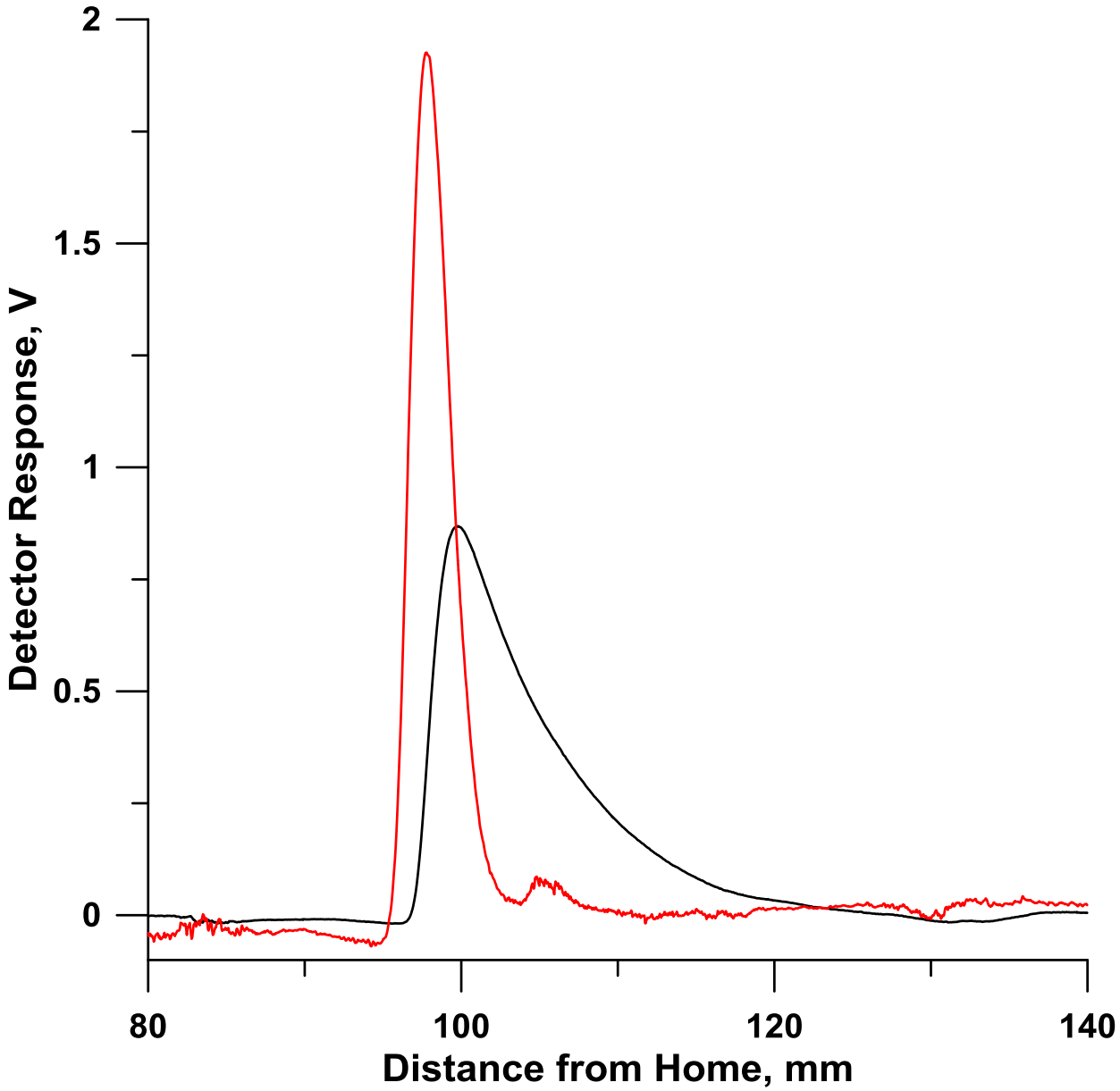

Figure D-S4. Comparison of AF AD responses with two different response times (red 25 ms, black 250 ms)
With 4 cm/s scanning speed, 1 kHz data acquisition rate. Other conditions as in Figure S2.

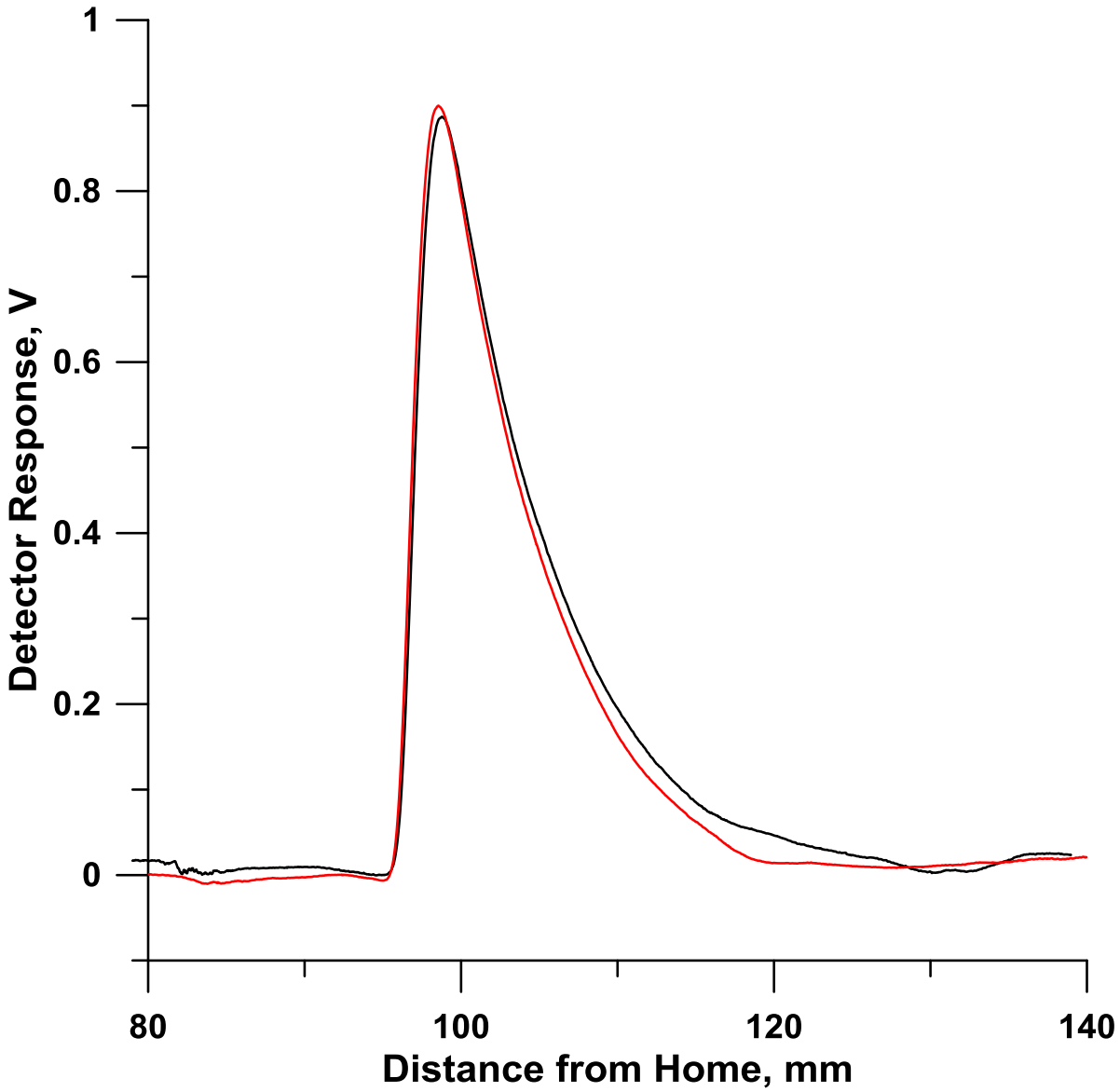

Figure D-S5. AF AD responses as a function of data acquisition rate. Black 1000 Hz, Red 500 Hz.

Other conditions as in Figure S2.

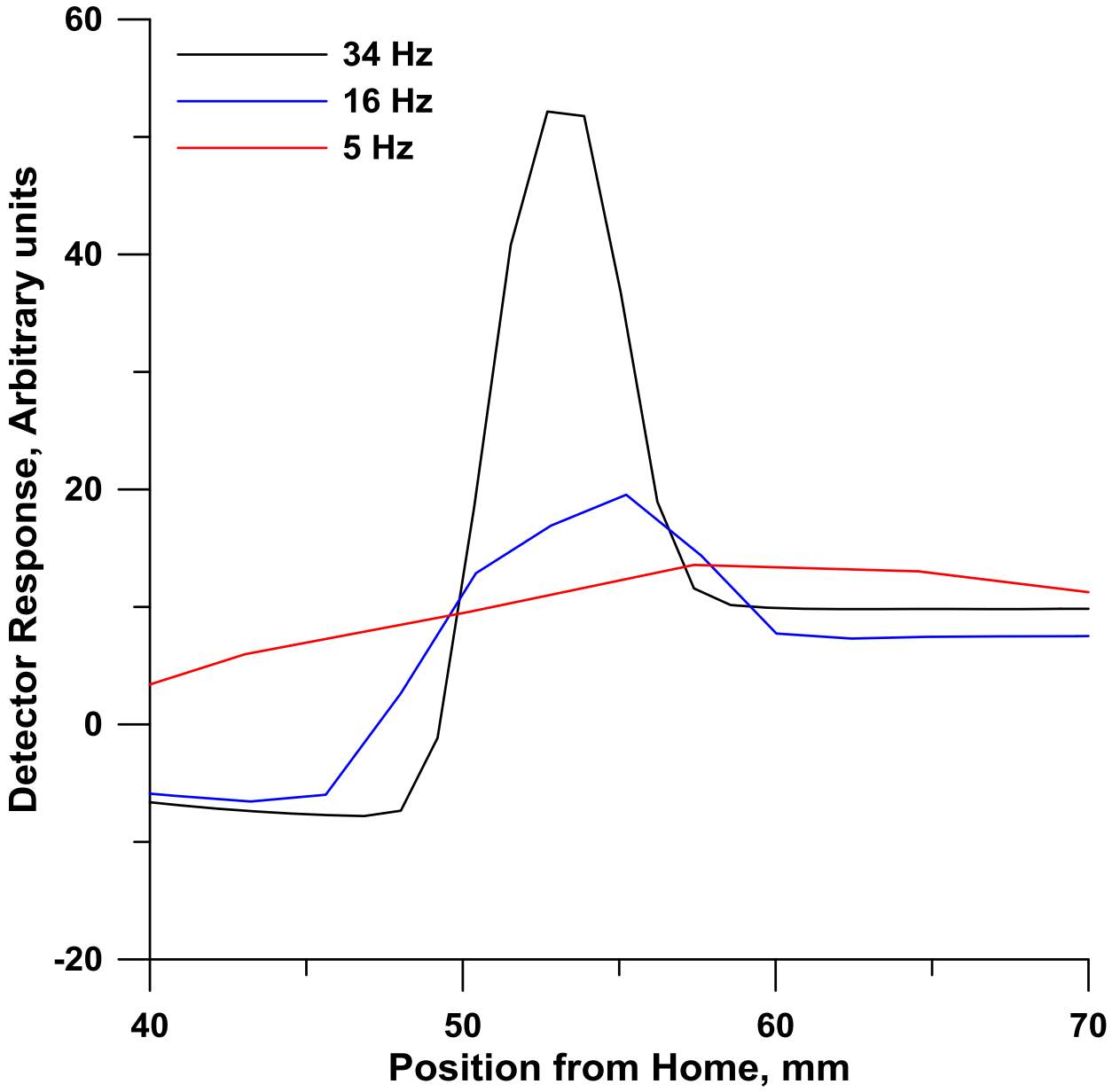

Figure D-S6. TraceDec responses as a function of data acquisition rate from 5.6-34 Hz Scanning speed 4 cm/s. Other conditions as in Figure S1.

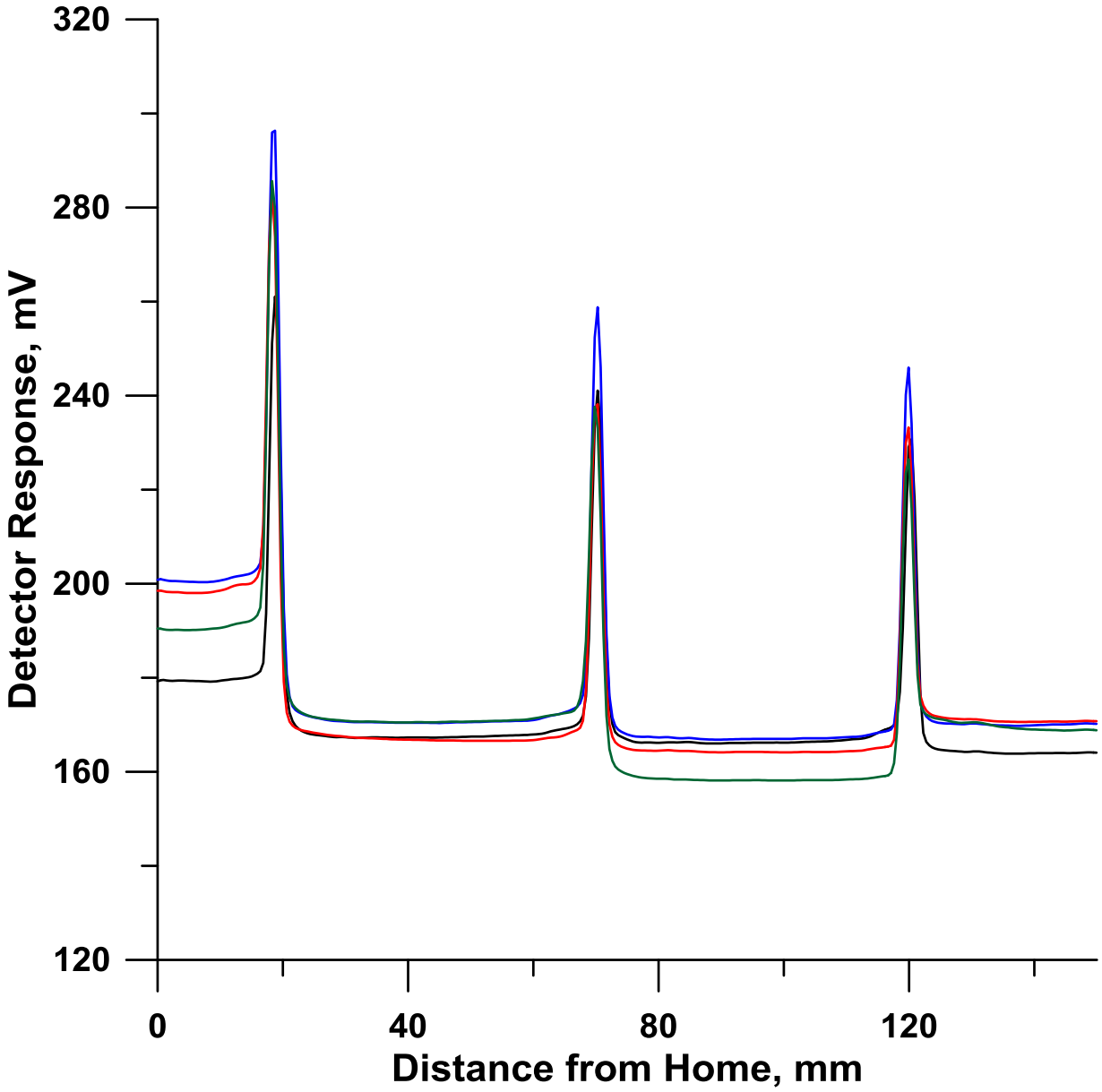

Figure D-S7. Three marks made on a silica capillary scanned four times with the Tracedec AD at a speed of 1.6 cm/s
The response from the paint marks remains relatively consistent.

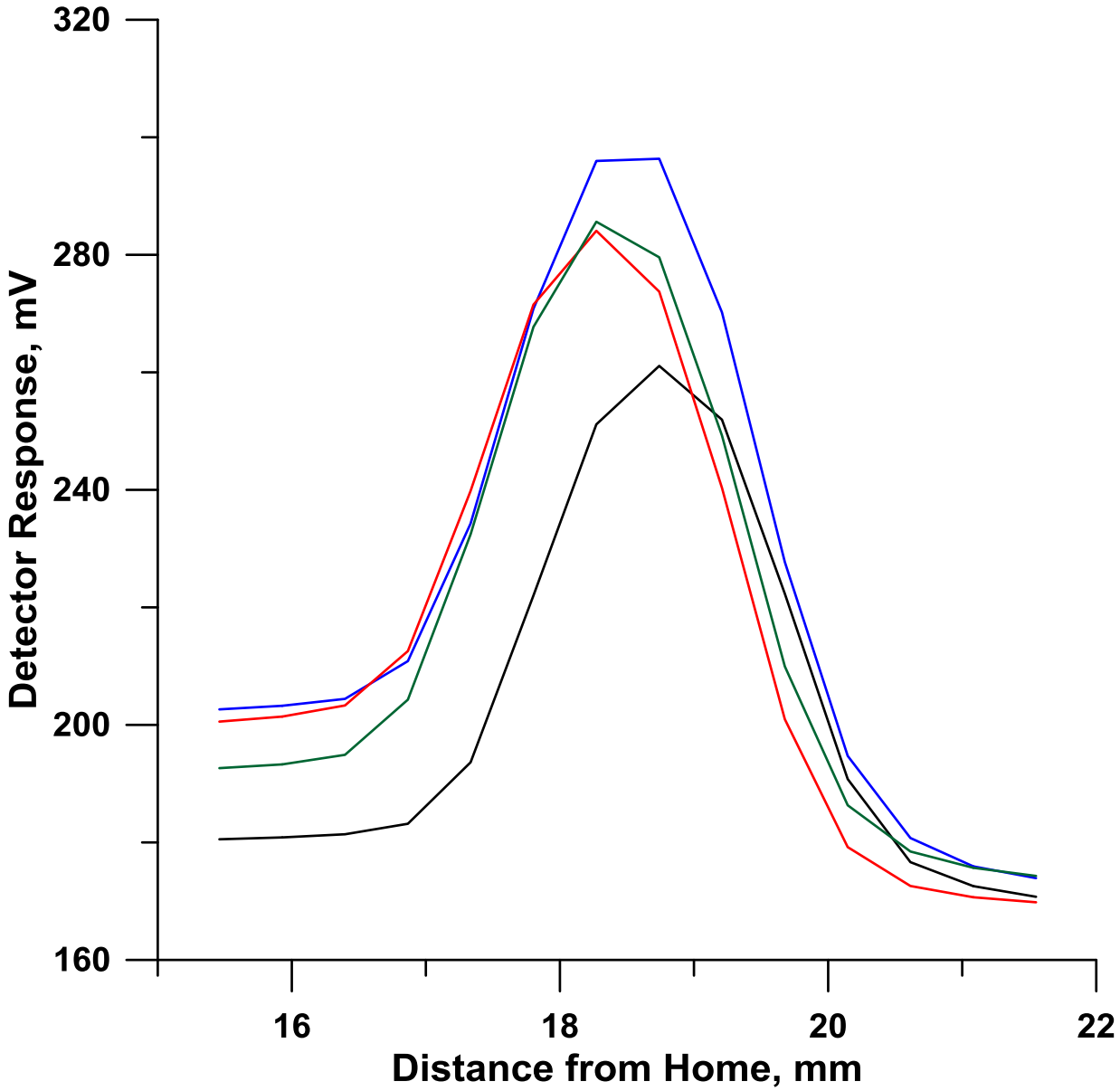

Figure D-S8. A zoomed in view of the first mark from the Figure 5-S7
At this level of magnification, it becomes readily apparent that the peak shape reproducibility is poor in addition to the difficulty of determining the true beginning and end.

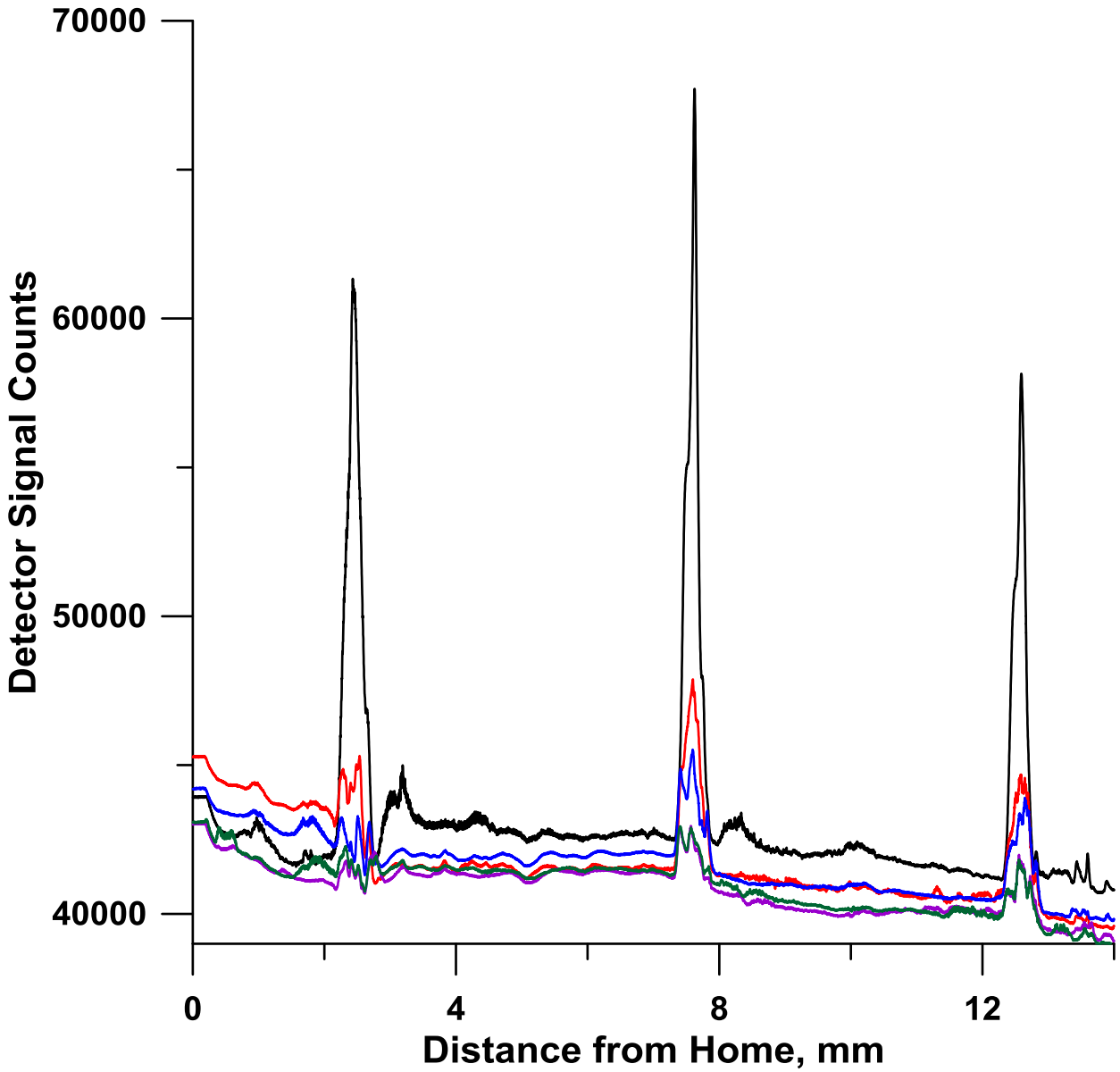

Figure D-S9. Three marks made on a silica capillary scanned five times with the AF AD at a speed of 1.6 cm/s
The response from the paint marks consistently decreases with each progressive scan. At 2.8 cm/s, the marks are immediately removed.

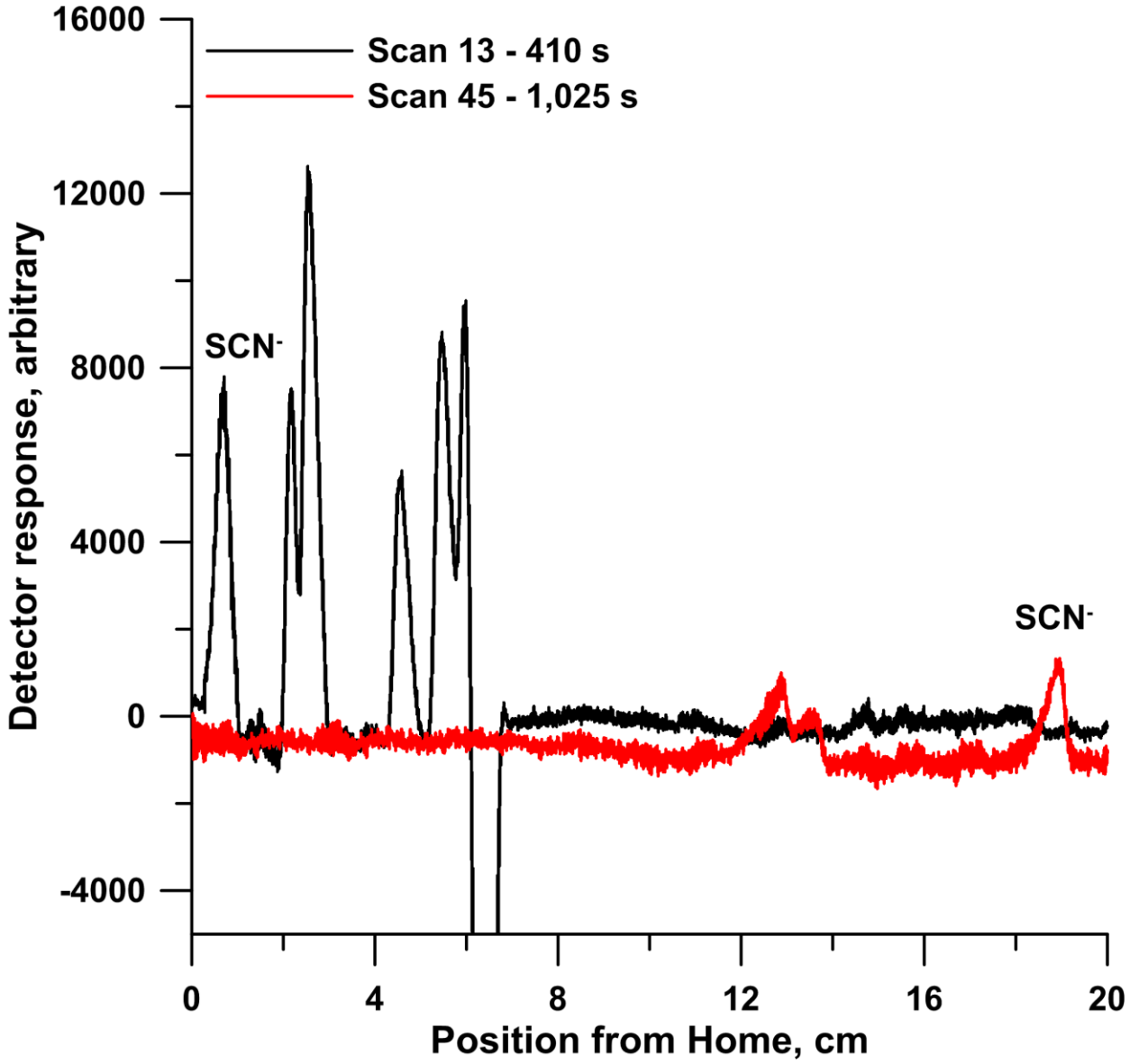

Figure D-S10. Two scans performed as thiocyanate just enters the scan window (black) and right before it leaves it (red)
At the beginning of the scan window, thiocyanate is already baseline separated with a peak height of 7775. It takes over ten minutes for it to reach the end of the scan window with the peak height decreasing to 2261. Detection at the beginning of the column not only saves time but increases the SNR by eliminating additional dispersion.

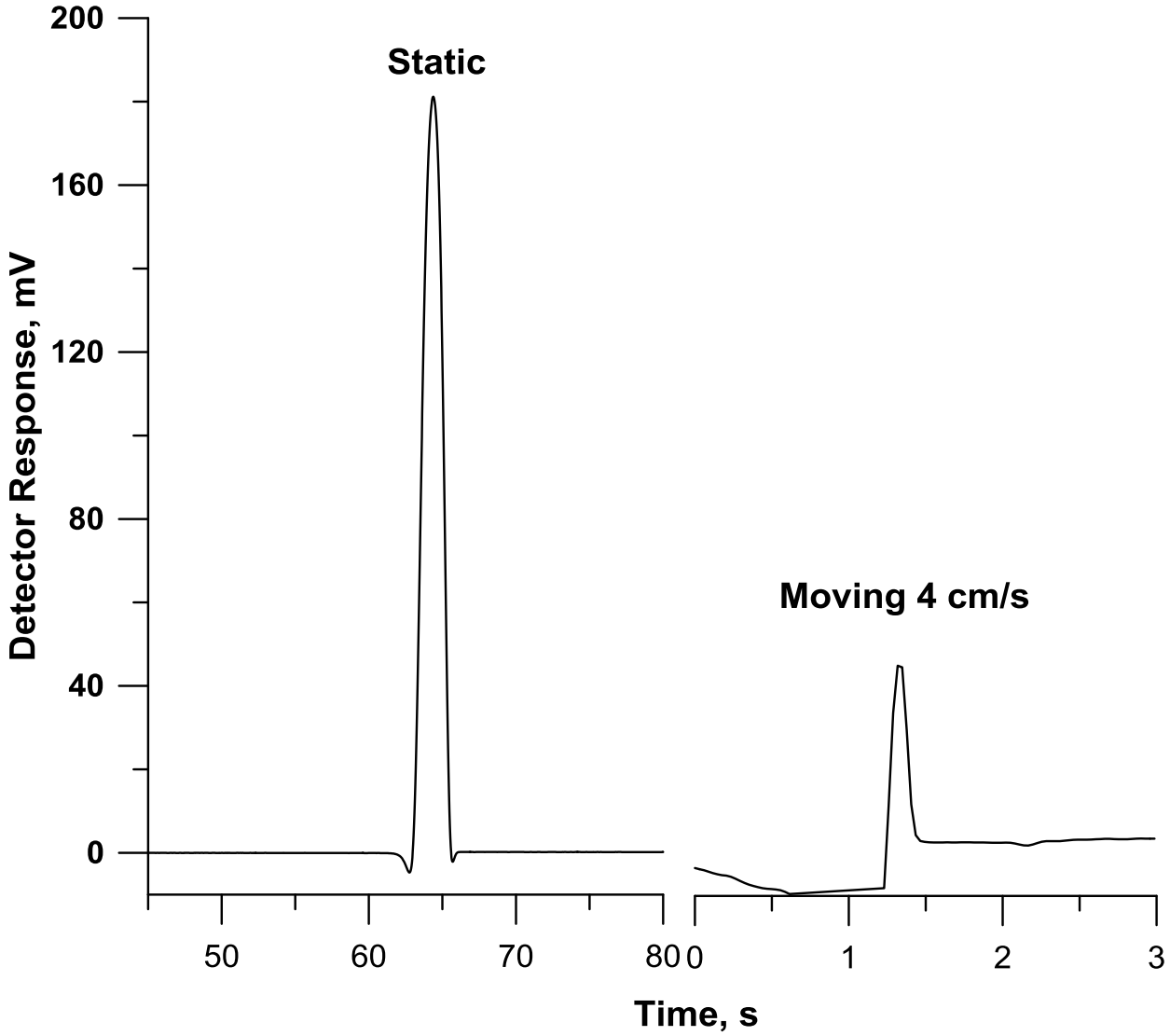

Figure D-S11. The difference between stationary and scanning detection can be significant for some detectors

Injection of 0.95 nL of 500 µM KCl into a water carrier on a 21 µm I.D. 360 µm o.d. COP capillary. TraceDec AD, *f* = 34 Hz. Detection was made in the same location on the tube to provide comparable dispersion.

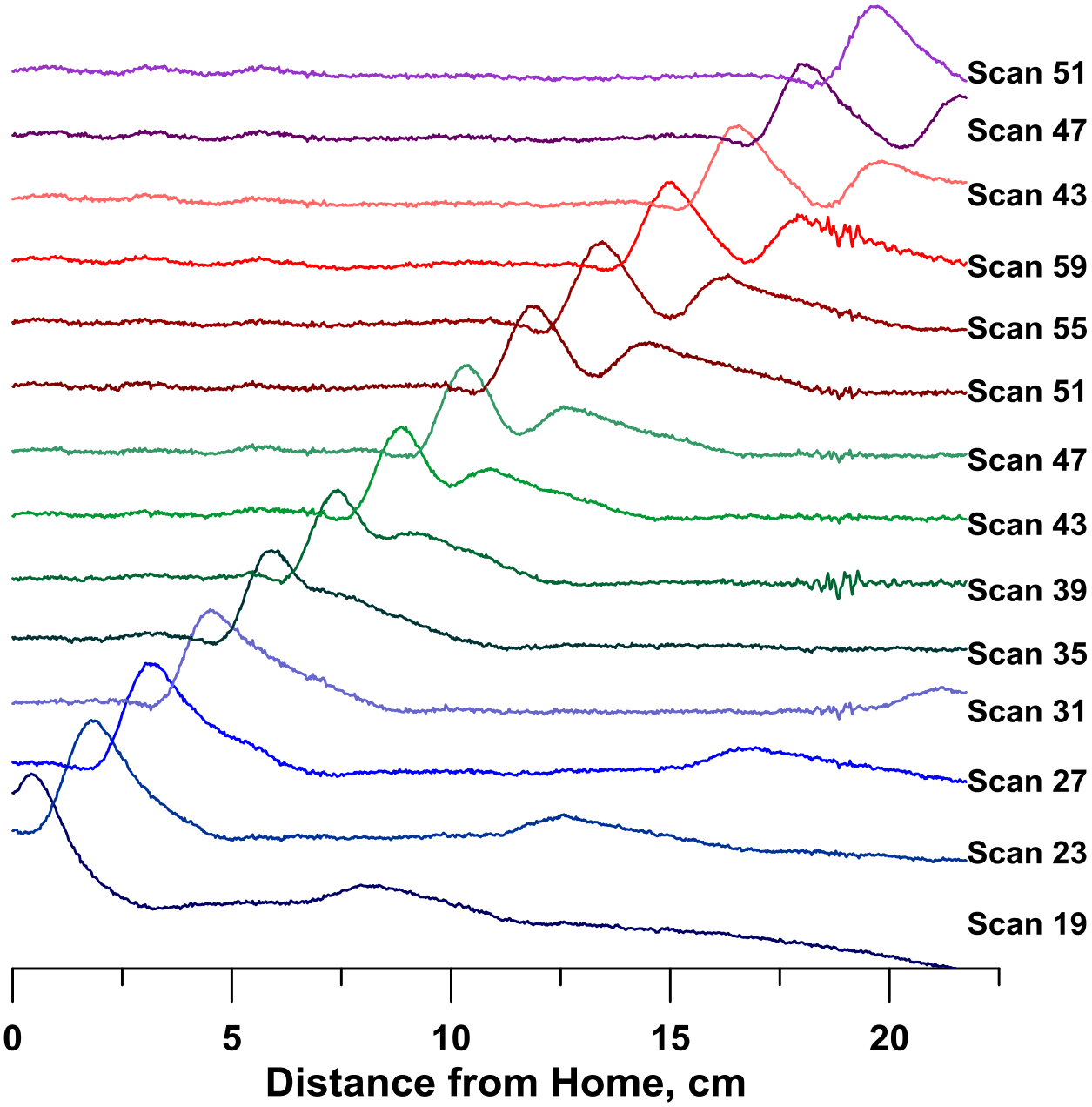

Figure D-S12. Progression of scans performed on a Dionex AS11-HC 0.4x250 mm capillary column without suppression

1.5 µL injection of 500 µM Cl, 1 mM BrO_3,; 4 mM sodium benzoate eluent, 10 µL/min. First indication of separation occurs in scan 35 and is not completed until scan 59. Some ~0.5 cm of the column remains within the fittings at each end; when the quadrupole electrode reaches the end fittings the detector, the contact point is ~1.5 cm from the end fittings. Thus, "Home" above connotes ~2 cm from the beginning of the column and a total of 21 cm is scanned. V_S 20 mm/s. AF AD transimpedance amplifier gain 0.5 V/µA, optimum probe frequency determined to be 80 kHz. Data acquisition rate

80 Hz, spatial resolution 250 µm. Total scan time each way is 11 s with 6 s pause in between.

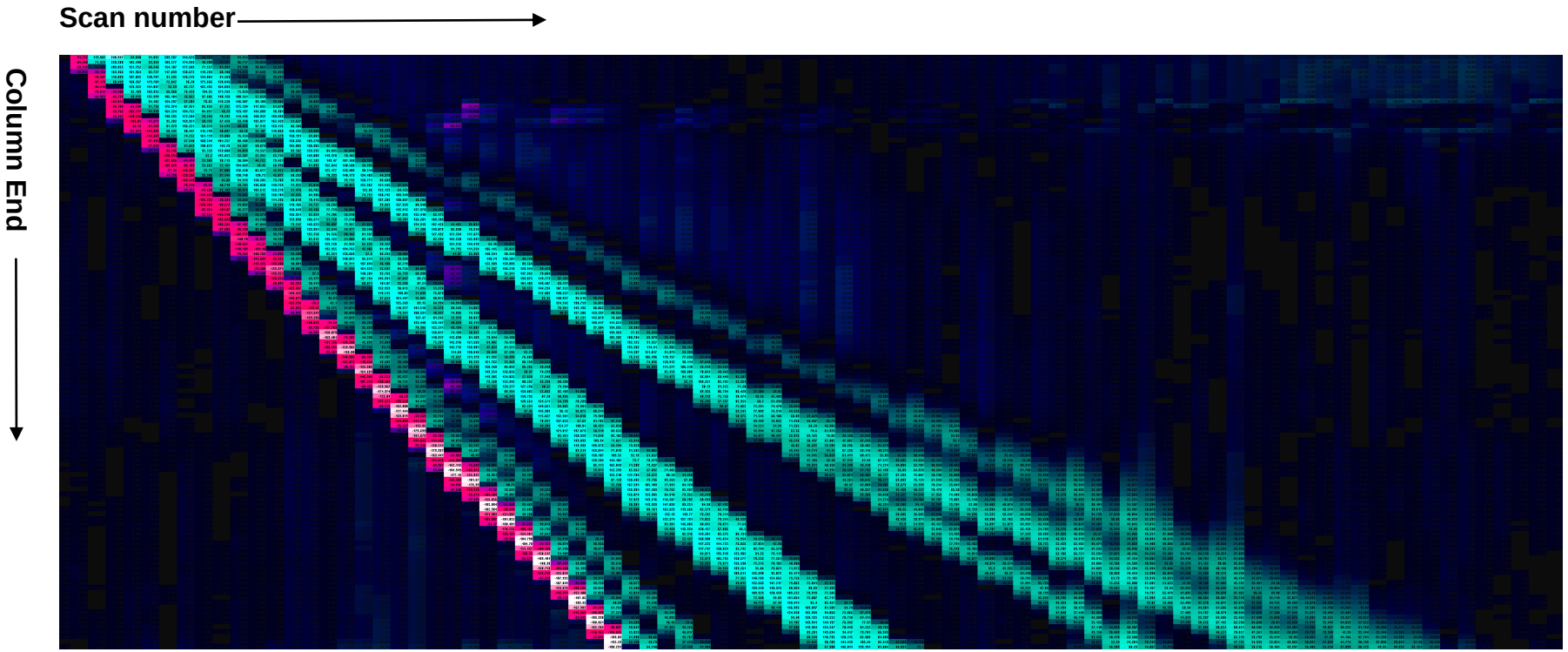

Figure D-S13. A conditionally formatted Excel worksheet bearing the data in Figure 5-4
The lowest numbers (negative in the preset case) appear in red, numbers near zero (baseline) appear in black while positive numbers appear in green. The speed with which a given band is moving through the column is indicated by its slope. In this depiction, the negative void dip in red moves the fastest and exits the view window first. Analytes 1 and 2 start their journey together but ~25% through the scan window their separation is complete and they thence proceed separately. Analytes 3 and 4 separate almost immediately after entering the view window. Analytes 5 and 6 do not separate until about midway through the scan window while Analyte 7 first enters our view already separated from the others.

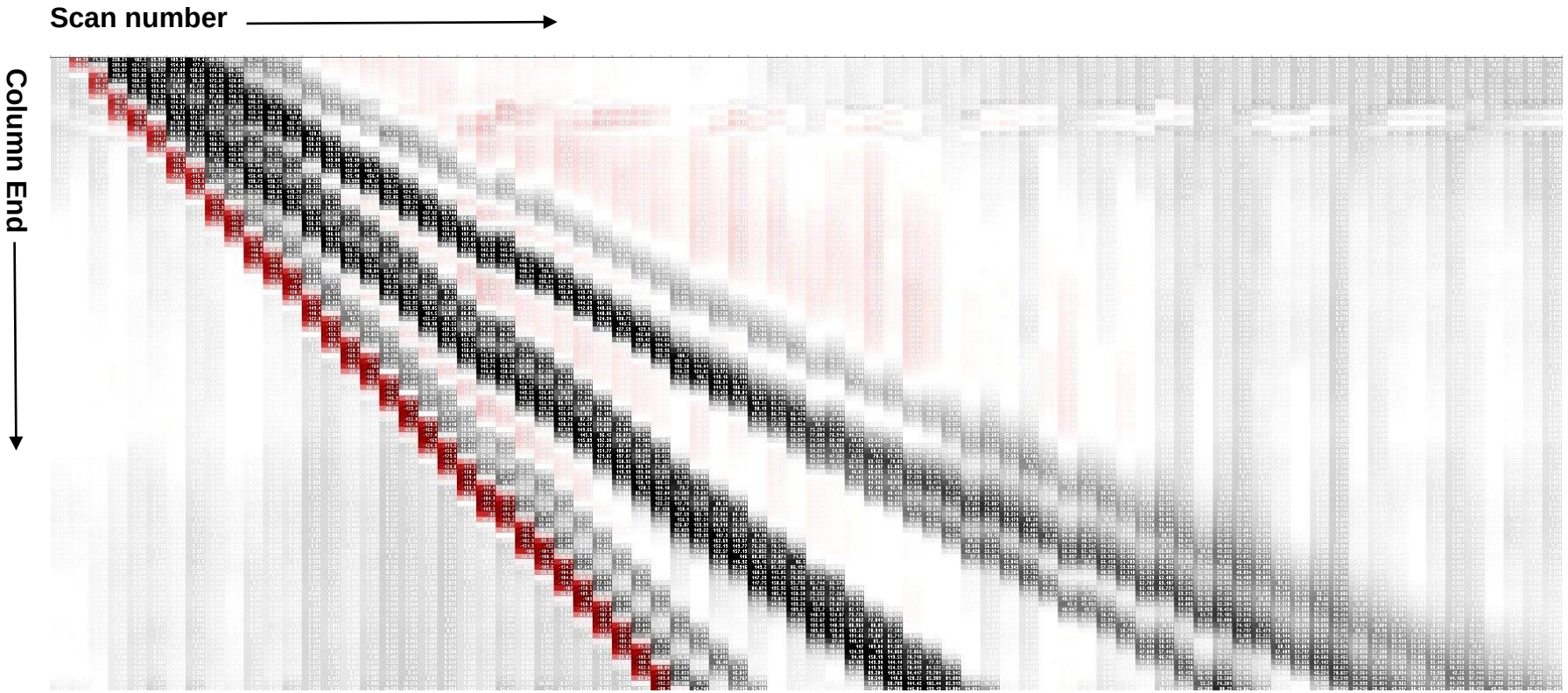

Figure D-S14. Same as Figure 5-S13, only different color scheme in conditional formatting
Going from red(negative) to white (near zero) to black (positive).

Derivation of Equation 2.

Whereas *k* is defined as

$$k = \frac{d_{m,t}}{d_{a,t}} \quad \ldots(s1)$$

$d_{a,t}$ is measured but $d_{m,t}$ is not measured what is measured is $d_{m,t'}$ (see main text).

If the mobile phase velocity is V_m, taking into account the additional distance the void moves between *t* and *t',*

$$d_{m,t'} = d_{m,t} + V_m(t - t') \quad ...(s2)$$

t - *t'* is the time taken for the scanner head to go from $d_{a,t}$ to $d_{m,t'}$, therefore

$$t - t' = \frac{d_{m,t'} - d_{a,t}}{V_s} \quad ...(s3)$$

Incorporating eq. s3 into s2,

$$d_{m,t} = d_{m,t'} - \frac{V_m}{V_s}(d_{m,t'} - d_{a,t}) \quad ...(s4)$$

Therefore

$$R_f = \frac{d_{m,t}}{d_{a,t}} = \frac{V_s d_{m,t'} - V_m(d_{m,t'} - d_{a,t})}{V_s d_{a,t}} \quad ...(s5)$$

or

$$R_f = \frac{(V_s - V_m)d_{m,t'} + V_m\, d_{a,t}}{V_s d_{a,t}} \quad ...(s6)$$

Thence

$$k = R_f - 1 = \frac{(V_s - V_m)d_{m,t'} + V_m\, d_{a,t}}{V_s d_{a,t}} - \frac{V_s d_{a,t}}{V_s d_{a,t}} \quad ...(s7)$$

or

$$k = \frac{(V_s - V_m)(d_{m,t'} - d_{a,t})}{V_s d_{a,t}} \quad ...(s8)$$

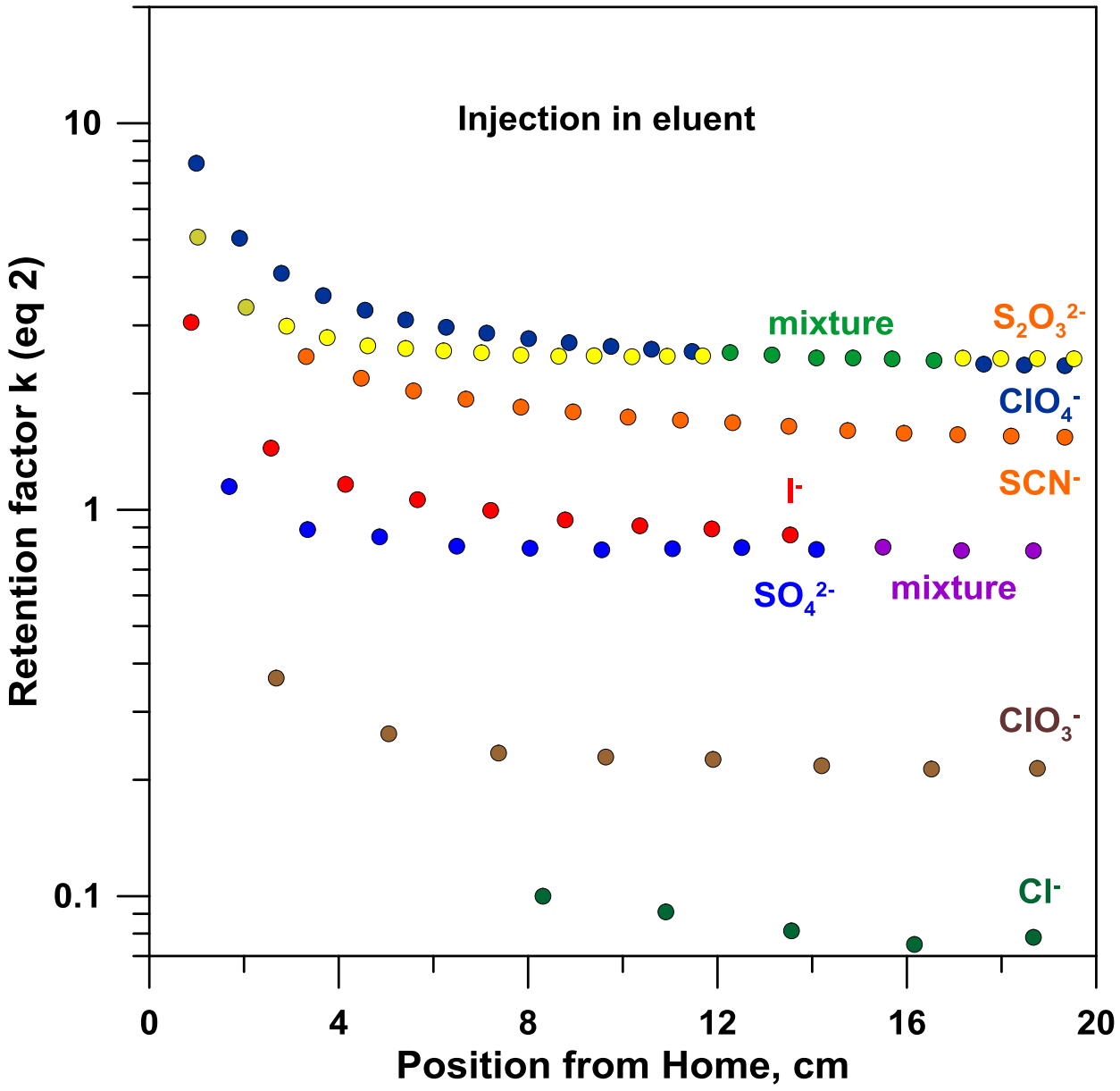

Figure D-S15. Retention factors calculated according to Eq 2 with the same conditions as Figure 5-5 but with injected anions in 6 mM sodium salicylate, same as the eluent The retention factors at the beginning of the scan window are lower than those when injected in water. Note that as the analytes approach the end of the scan window they reach *k* values equivalent to those when injected in water. Thiosulfate/perchlorate and iodide/sulfate merge later as well. Note logarithmic ordinate.

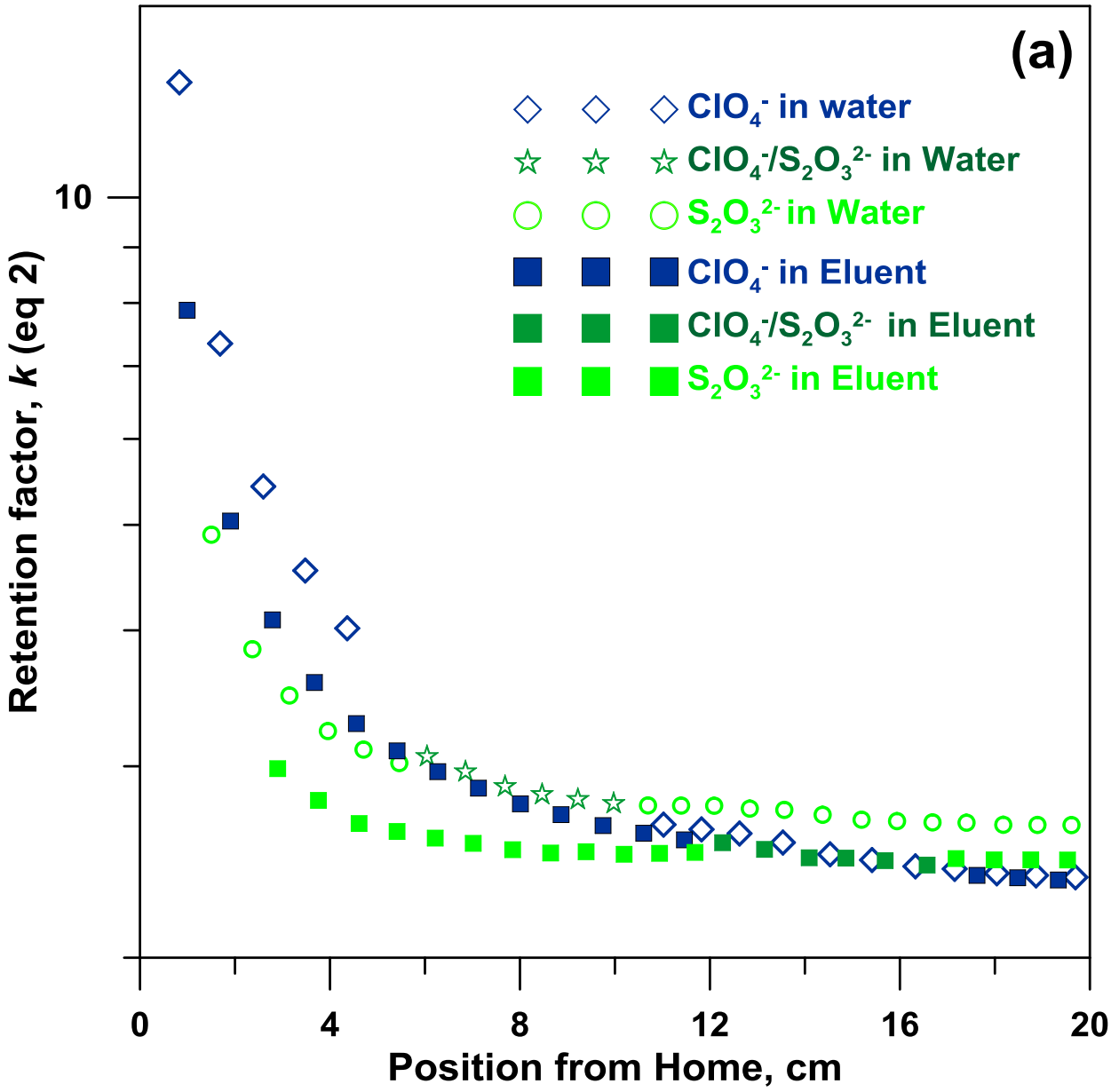

Figure D-S16a. The movement of perchlorate and thiosulfate dissolved both in eluent (filled symbols) and water (open symbols)
In all cases the high initial retention (higher when sample dissolved in water) decreases quickly. While perchlorate starts out with greater retention than thiosulfate, the two merge (at ca 6 and 12.5 cm for the sample in water and eluent, respectively) and perchlorate thereafter moves out ahead. Note logarithmic ordinate. See also Figure S18 and Figure 4.avi. Note logarithmic ordinate.

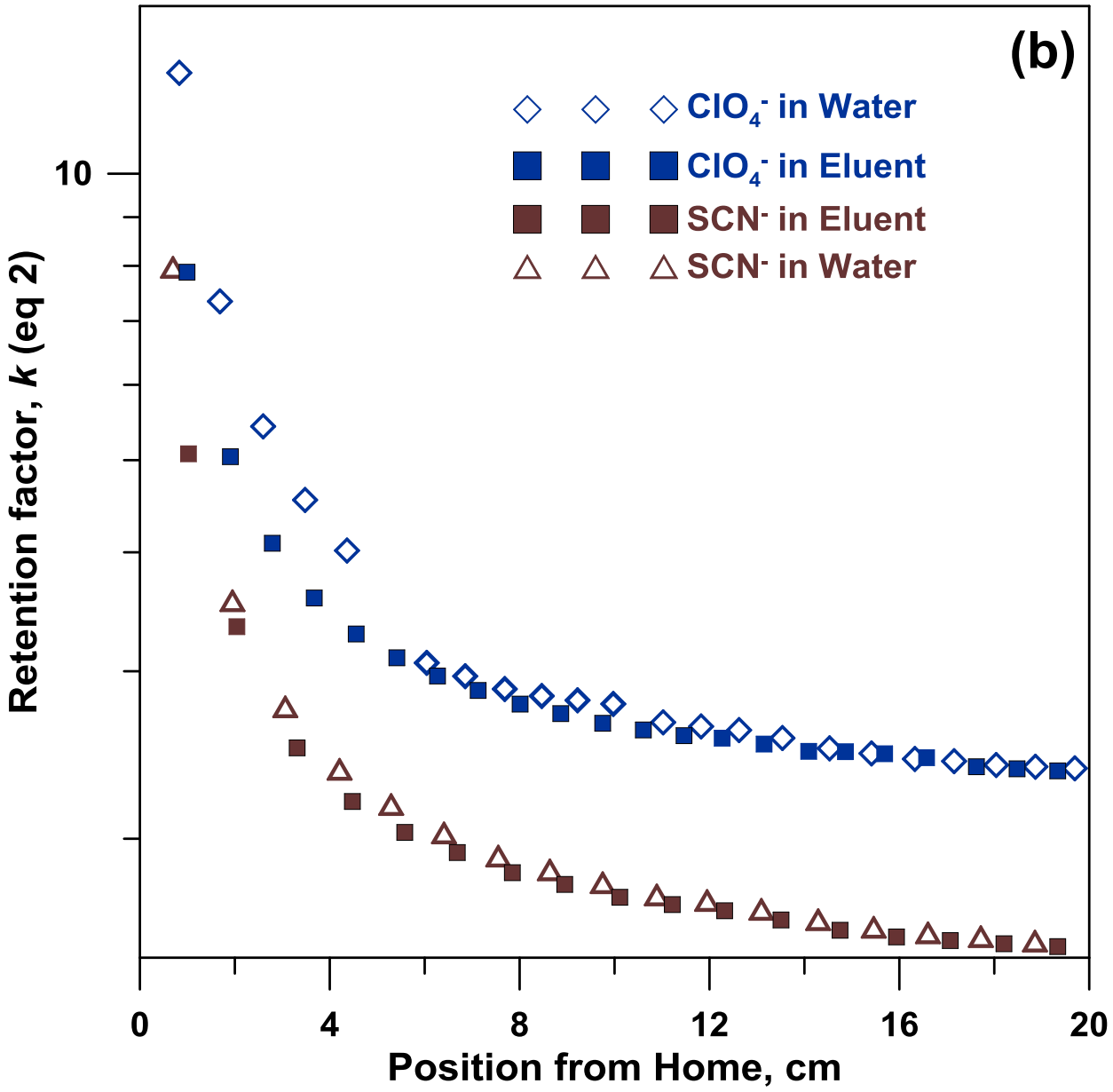

Figure D-S16b. The movement of perchlorate and thiocyanate dissolved both in eluent (filled symbols) and water (open symbols)
The former starts out with greater retention but retention quickly becomes almost the same in both cases. Note logarithmic ordinate.

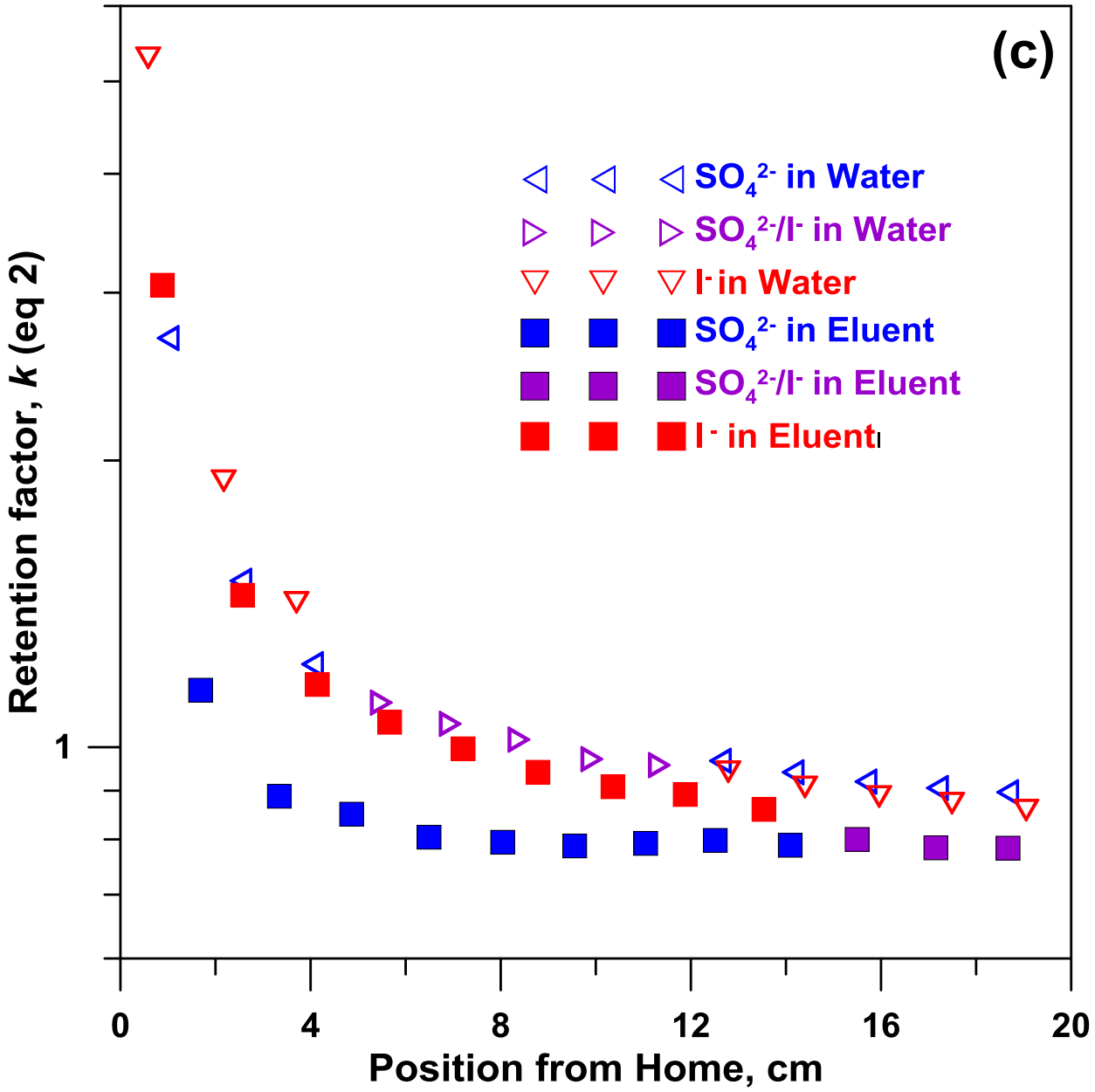

Figure D-S16c. The movement of iodide and sulfate dissolved both in eluent (filled symbols) and water (open symbols)
In all cases the high initial retention (higher when sample dissolved in water) decreases quickly. While iodide starts out with greater retention than sulfate, the two merge (at ca 5 and 15.7 cm for the sample in water and eluent, respectively) and iodide thereafter moves out ahead (for the sample in eluent case, it happens past the view window). Note logarithmic ordinate.

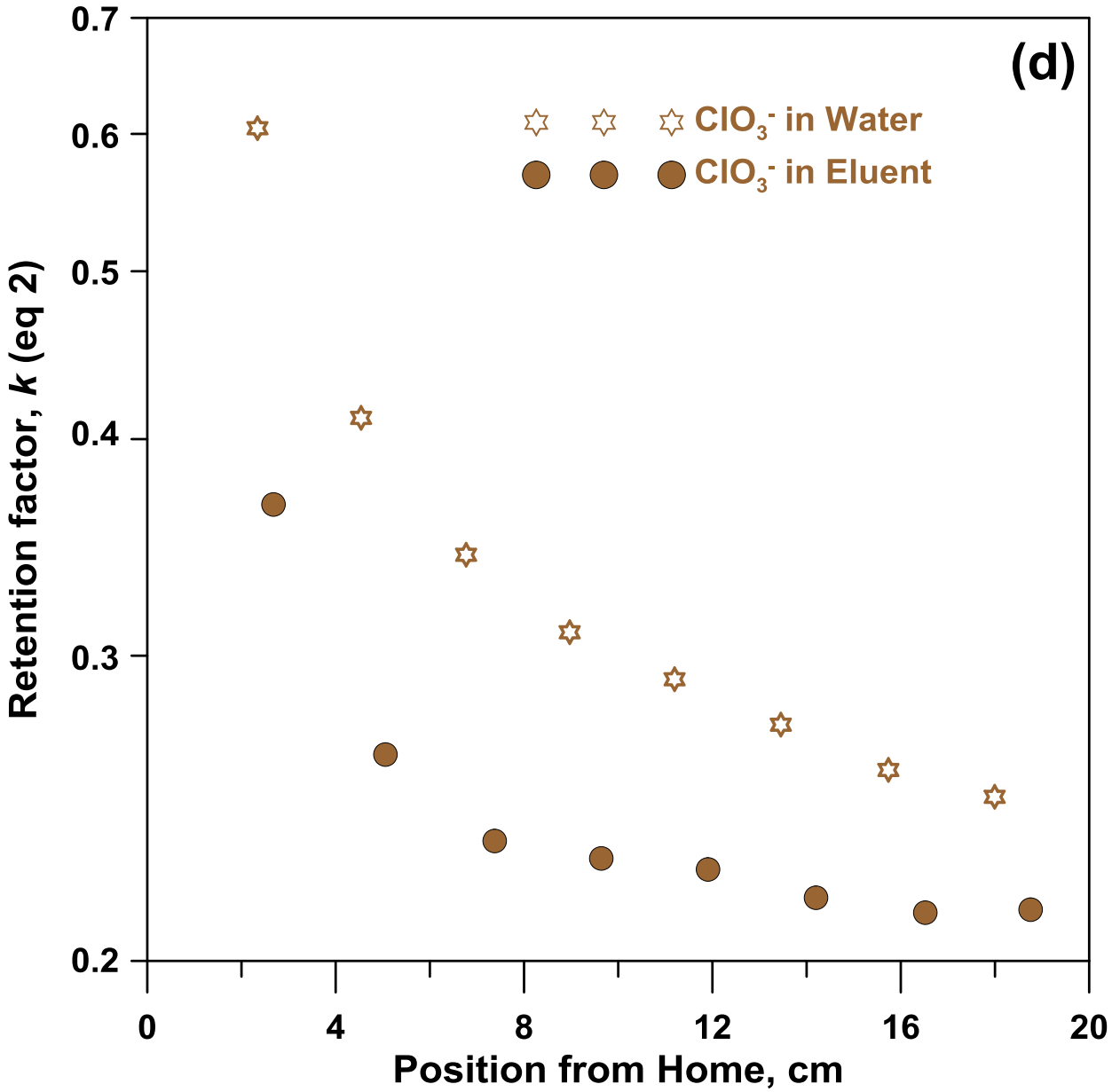

Figure D-S16d. The retention of a relatively little retained ion like chlorate, whether dissolved in water (open symbols) or eluent (filled symbols), begins to converge after some distance from the inlet
Note logarithmic ordinate.

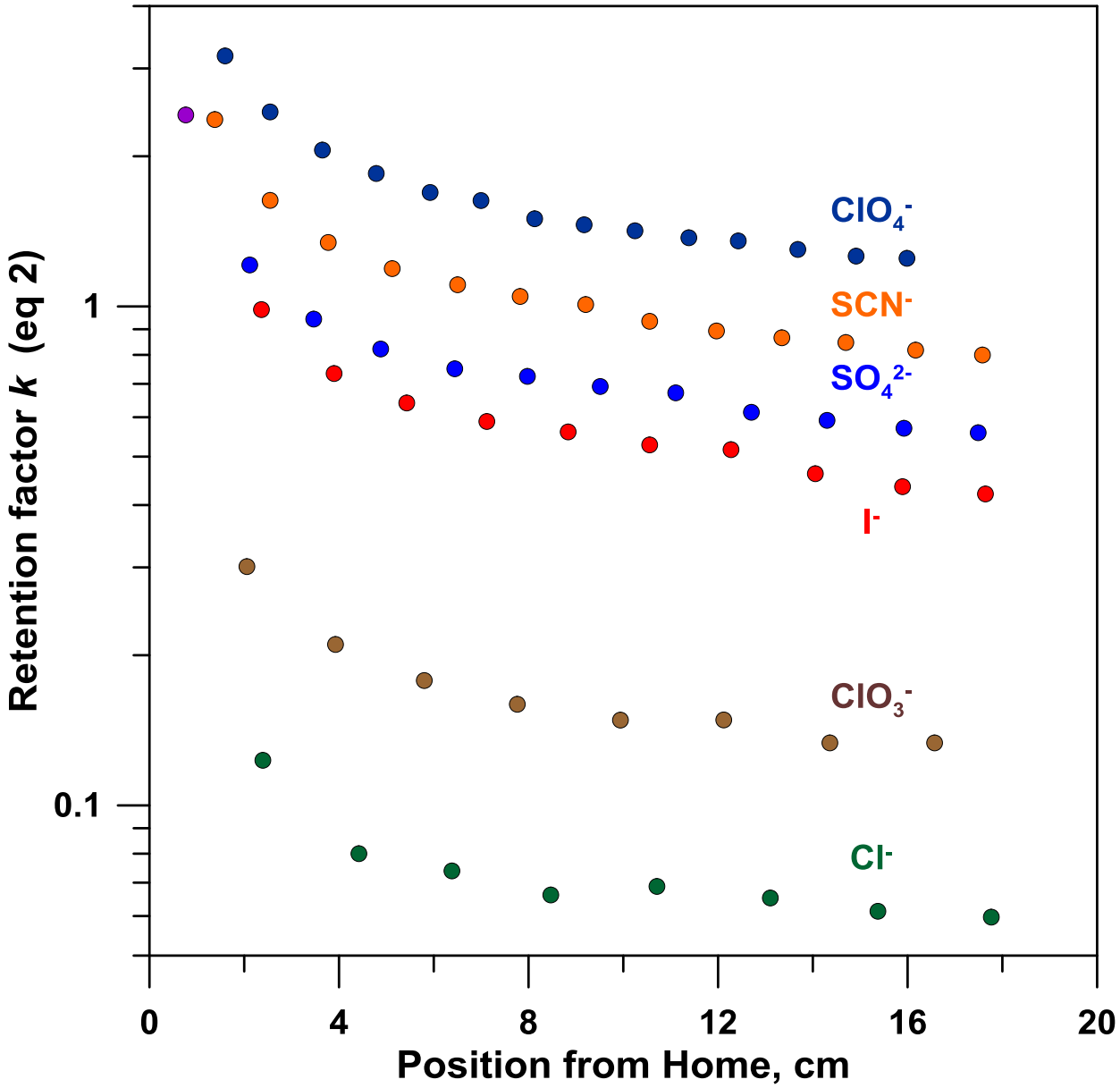

Figure D-S17. This experiment was identical to that in Figure 5-5, with the same eluent, same linear velocity of the eluent, sample dissolved in water except that the column had a inner diameter of 21 µm instead of 11 µm
Note that the *k* values are vastly lower than those in Figure 5 due to the much different phase ratio. Note also that the “inlet effect region” is longer than that for the narrower bore column.

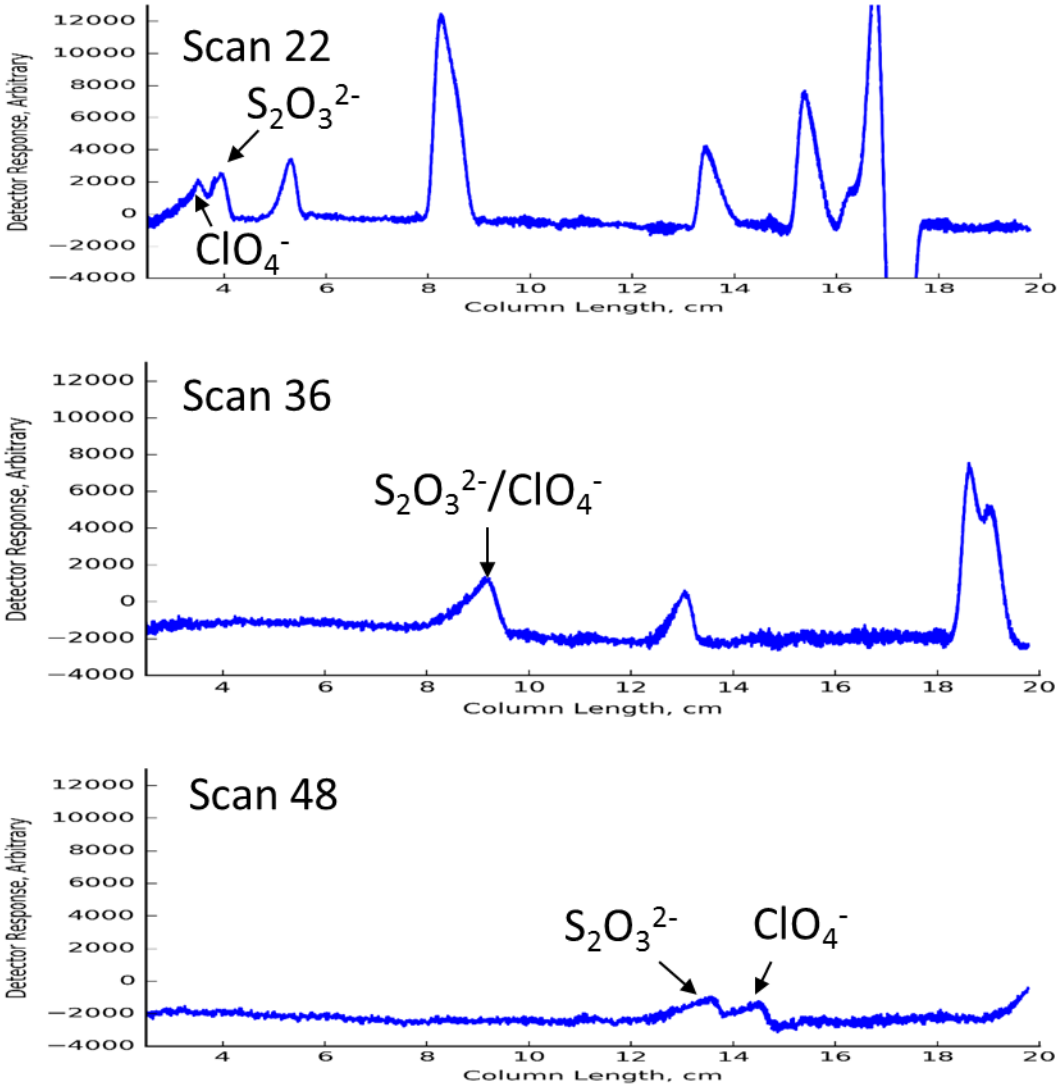

Figure D-S18. Same conditions as Figure 5-5.
Three scans showing the elution order reversal of thiosulfate and perchlorate. Initially thiosulfate is ahead, but by the end of the detection window perchlorate has passed it.

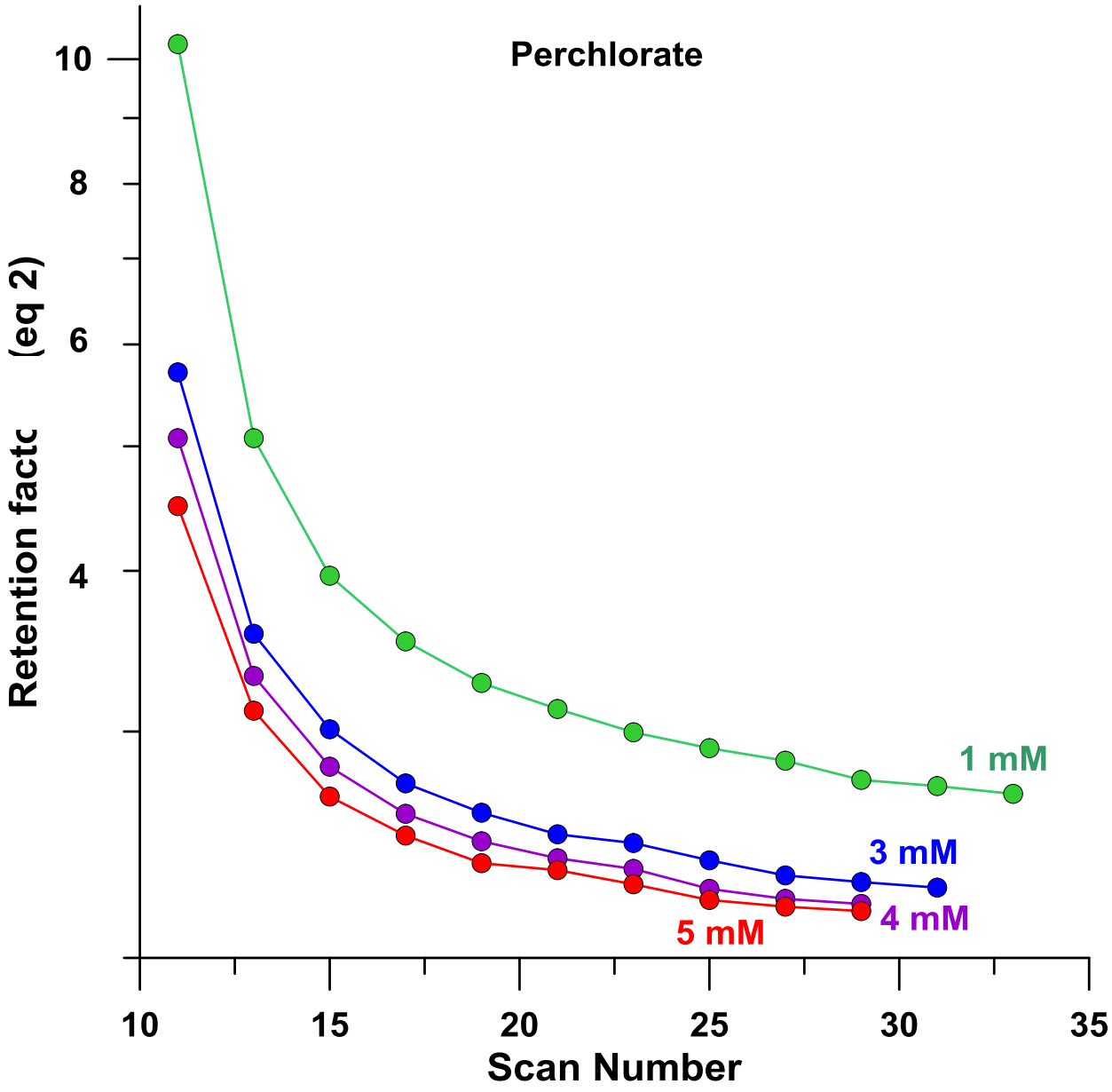

Figure D-S19. Repeated scans on 20 cm length of an 11 μm i.d., 360 μm AS18 latex coated silica capillary of total separation column length 60 cm

Injections: 430 pL of 1, 3, 4, and 5 mM ClO_4^-. Eluent, 6 mM sodium salicylate; flow rate, 5.2 nL/min (mobile phase velocity 0.1 cm/s), V_s 2.4 cm/s. Each scan 8.3 s; interval between unidirectional scans 22.6 s, Analytical Foundry detector, spatial resolution 0.04 mm. With increasing concentration of perchlorate the retention factors at the beginning of the scan window decrease. Final *k* values also decrease with increasing concentration showing self-elution.

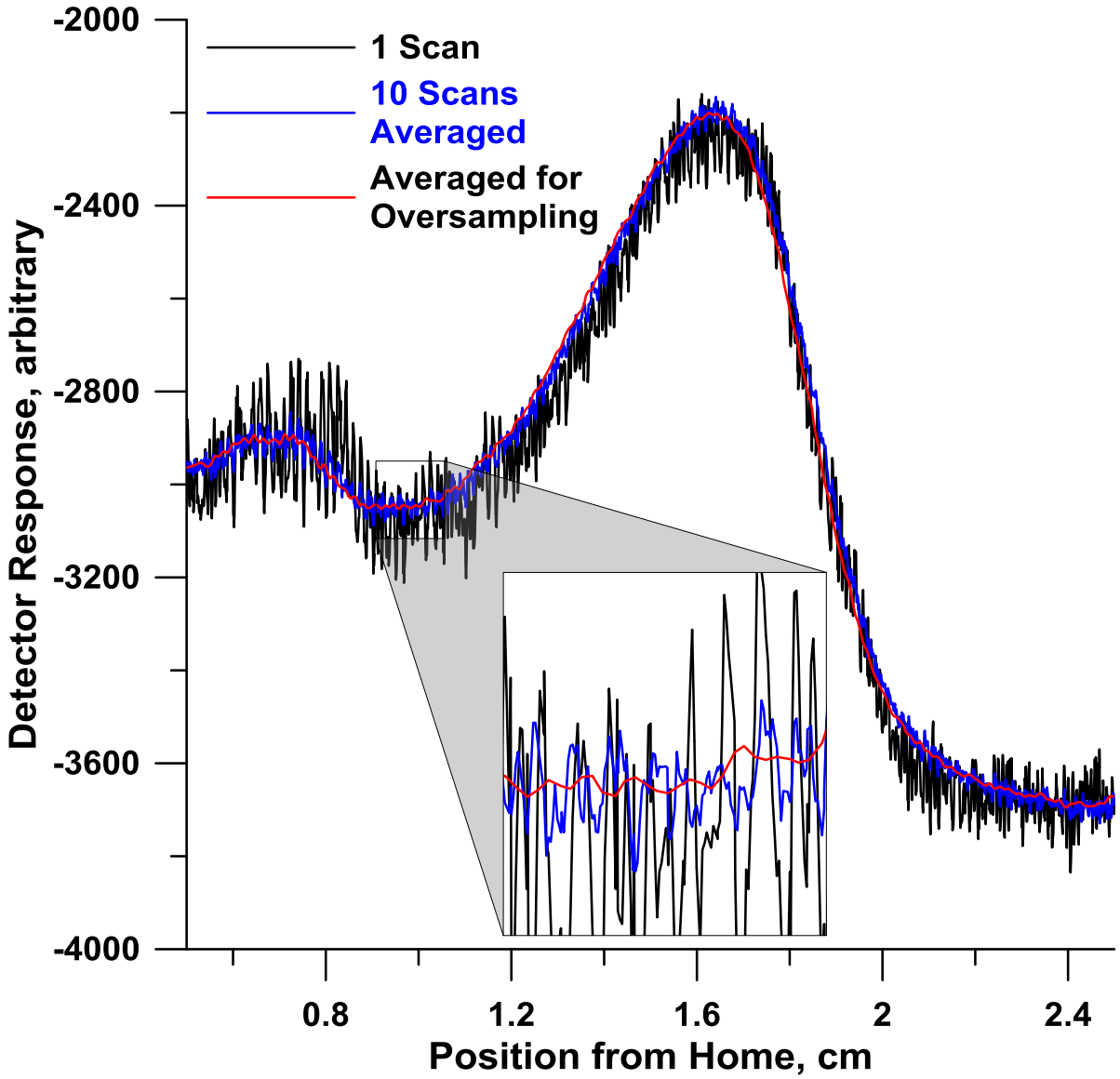

Figure D-S20. Increasing Signal to Noise ratio through stopped-flow multiple scan signal averaging and oversampling

Separation was conducted under conditions of Figure 4. Following the separation of low-levels of thiosulfate from rest of the sample components, a 2.5 cm zone was scanned repeatedly. Ten unidirectional scans at an overall speed of V_s = 0.8 cm/s takes 51 s including return time and stop time before reversing direction. Simply Signal averaging the data reduces the noise level from 877 µV for a single scan to 255 µV for 10 scans. As data are acquired at 1 kHz during the 5 ms stage stops between its 40 µm microsteps, each spatial point is actually sampled 5 times. An appropriate degree of further signal averaging is thus permissible without loss of spatial resolution and lowers the noise much further, achieving a significant gain in the SNR.

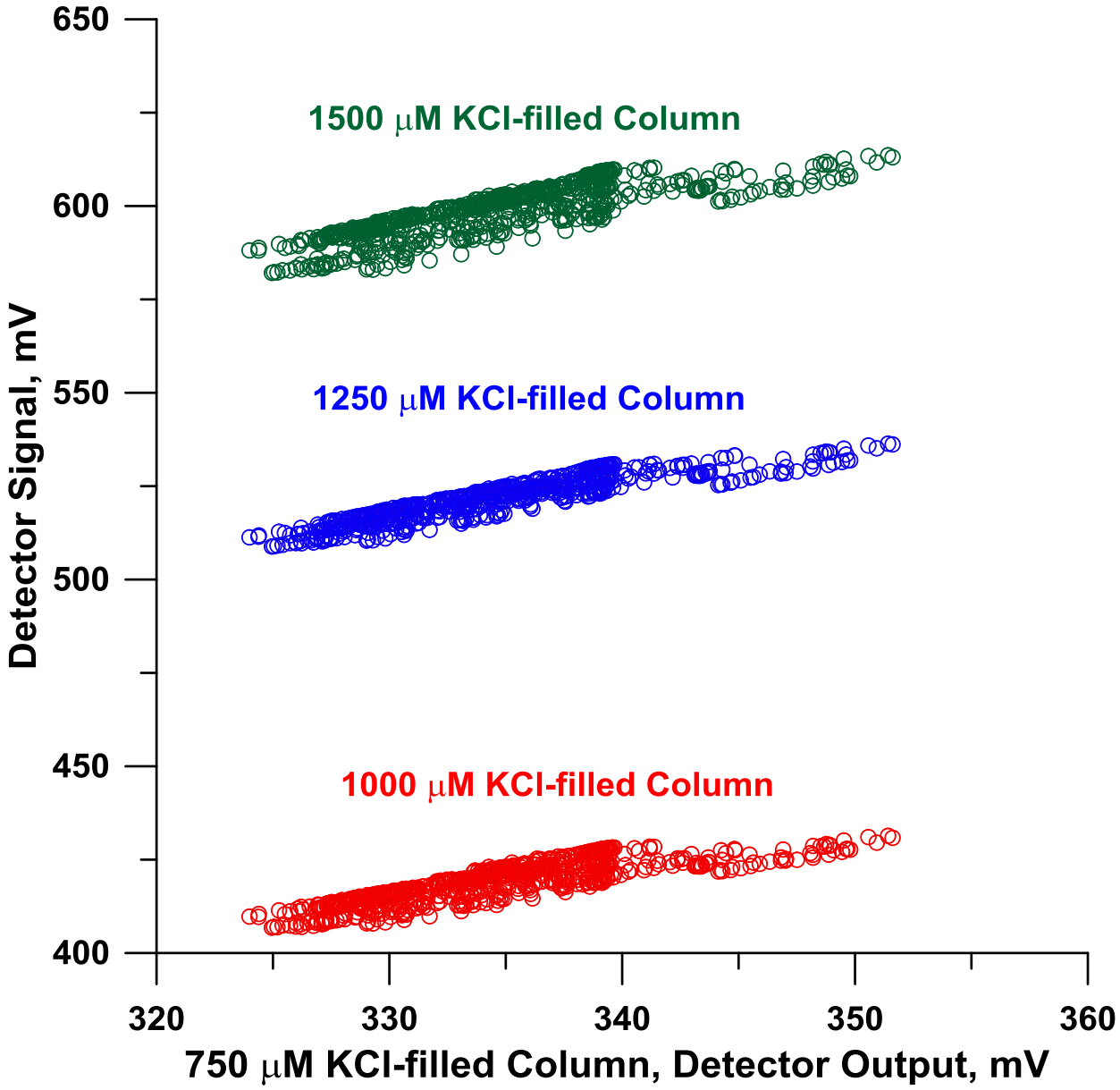

Figure D-S21. Correspondence of data for different KCl solutions used to fill a 0.1 mm id x 300 mm long silica capillary packed with 5 µm C18 silica
Column courtesy of Column Scientific, Xiamen, China.

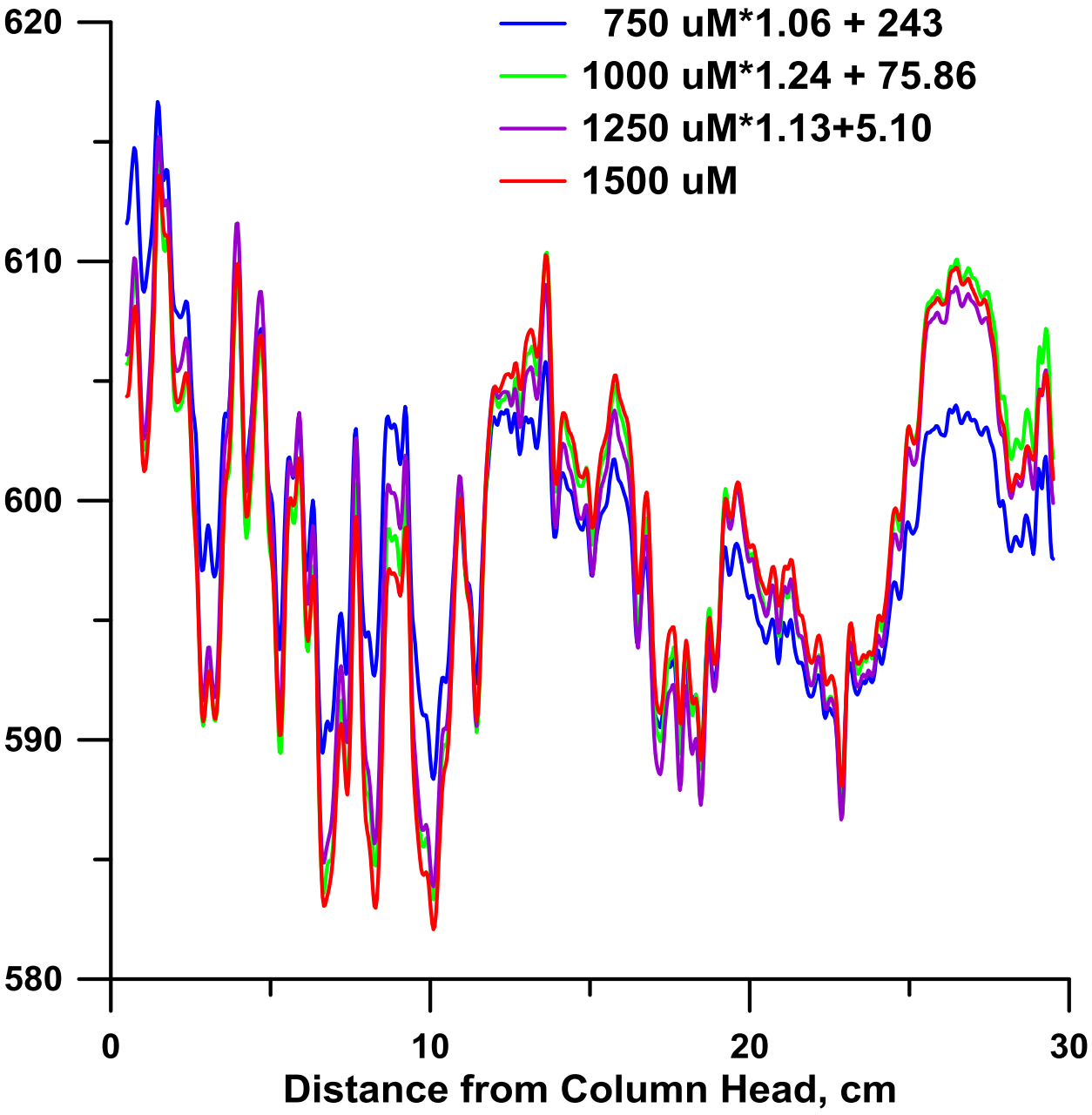

Figure D-S22. Correspondence of data obtained with 0.1 x 300 mm column packed with 5 µm silica particles with 0.75-1.5 mM KCl solutions

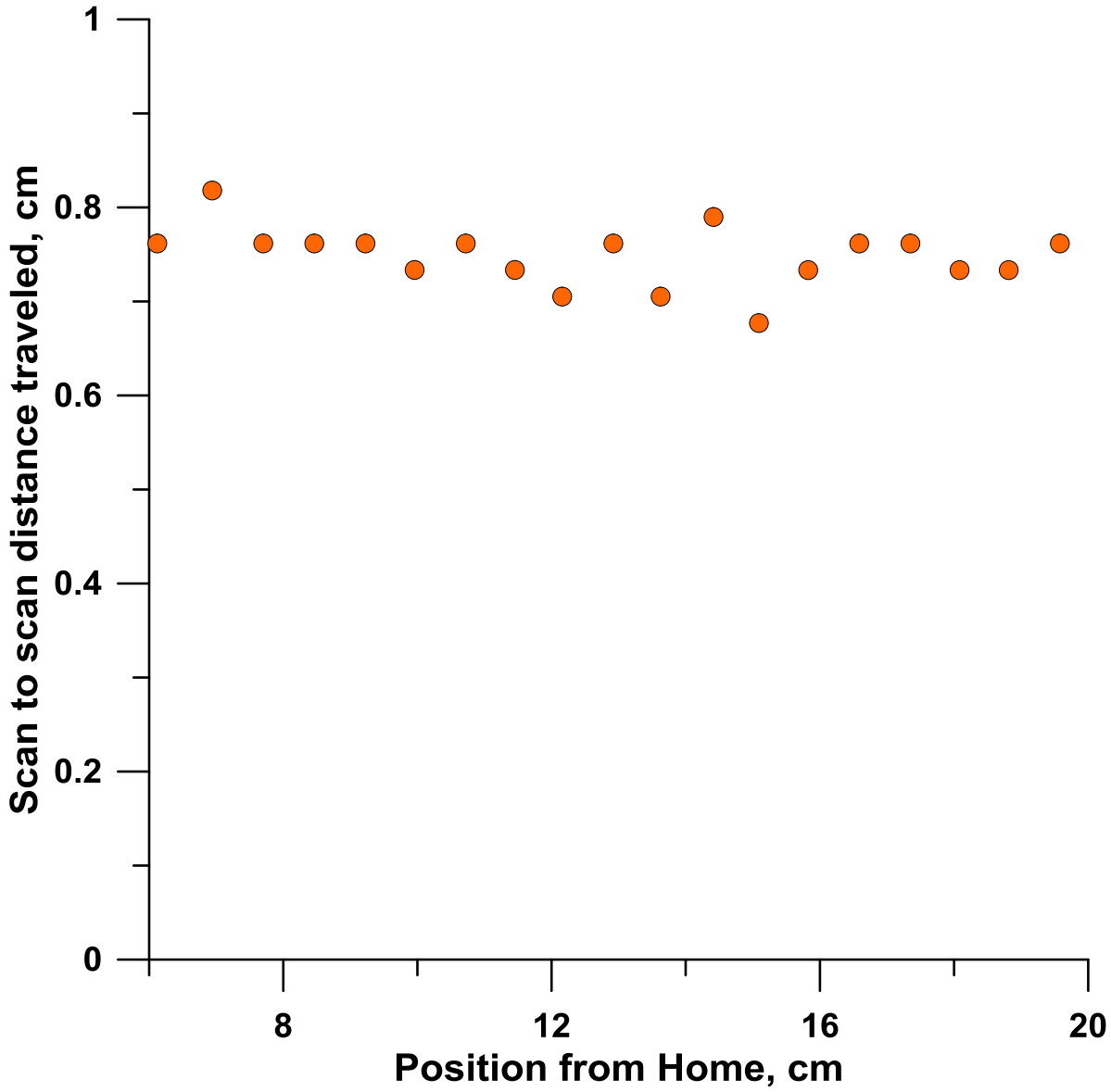

Figure D-S23. Uniformity of retention at different positions in the column
Past the inlet effect zone, as probed with SCN^-. Experimental conditions as in Figure 4. Note that the spatial retention variations appear to be different for different analyte ions (not shown here) suggesting retention is governed by more than one type of interaction and/or inhomogeneity among individual latex particles.

Appendix E. Xeropreservation of functionalized lipid biomarkers in hyperarid soils in the Atacama Desert

Mary Beth Wilhelm[a, b, *], Alfonso F. Davila[c, b], Jennifer L. Eigenbrode[d], Mary N. Parenteau[c,e], Linda L. Jahnke[e], Xiao-Lei Liu[f], Roger E. Summons[f], James J. Wray[a], Brian N. Stamos[g], Shane S. O'Reilly[f], Amy Williams[h]

a School of Earth and Atmospheric Sciences, Georgia Institute of Technology, Atlanta, GA 30332 b Space Science and Astrobiology Division, NASA Ames Research Center, Moffett Field, CA 94035

cSETI Institute 189 N Bernardo Ave, Mountain View, CA 94043

d Planetary Environments Laboratory, NASA Goddard Space Flight Center, Greenbelt, MD 20771

e Exobiology Branch, NASA Ames Research Center, Moffett Field, CA 94035

f Department of Earth, Atmospheric, and Planetary Sciences, Massachusetts Institute of Technology, Cambridge, MA, 02141

g Department of Chemistry and Biochemistry, The University of Texas at Arlington, Arlington, Texas 76019

h Department of Physics, Astronomy, and Geosciences, Towson University, 8000 York Road, Towson, MD 21252

* (Corresponding author, Telephone: (650) 604-0489; Email: marybeth.wilhelm@nasa.gov)

Submitted to Proceedings of the National Academy of Sciences of the United States of America

E.1 Abstract

Our understanding of long-term organic matter preservation comes mostly from studies in aquatic systems. In contrast, taphonomic processes in extremely dry environments are relatively understudied and are poorly understood. We investigated the accumulation and preservation of lipid biomarkers in hyperarid soils in the Yungay region of the Atacama Desert. Lipids from seven soil horizons in a 2.5 m vertical soil profile were extracted and analyzed using GC-MS and LC-MS. Diagnostic functionalized lipids and geolipids were detected, and increased in abundance and diversity with depth. Deeper clay units within the soil have fossil organic matter (radiocarbon dead) that has been protected from exposure to rainwater since the onset of hyperaridity _2 million years ago.

We show that these clay units contain lipids in an excellent state of preservation with functional groups and unsaturated bonds I carbon chains. This indicates that minimal degradation of lipids has occurred in these soils since the time of their deposition at least 2 Ma. The exceptional structural preservation of biomarkers is likely primarily due to the long-term hyperaridity that has minimized microbial activity and enzymatic action, a taphonomic process that we term xeropreservation (i.e. preservation by drying). The degree of biomarker preservation allowed us to reconstruct major changes in ecology in the Yungay region that reflect a shift in hydrological regime from wet to dry since the Neogene. Our results suggest that hyperarid environments, which comprise 7.5% of the continental landmass, could represent a rich and relatively unexplored source of paleobiological information.

E.2 Introduction

Understanding taphonomic processes and the conditions conducive to long term preservation of organic matter has been critical for reconstructing the evolutionary history of life on Earth[177] and in developing strategies to search for evidence of life elsewhere[178, 179]. Microbial processes mediate the majority of organic matter decomposition [180-184], with only approximately 0.1% of the global net primary production preserved in the sediment record [185-188]. This limits the quantity and quality of molecular fossils (aka biomarkers) that become preserved after organisms die.

Long-term preservation of biomarkers is enhanced when fast sedimentation or mineral encapsulation impede or mitigate microbial attack [189,190], or under environmental conditions that limit microbial activity and retard organic degradation, such as low temperature and humidity [191,192] . In this paper, we focus on the preservation of biomolecules in an environment that has been extremely dry (i.e. hyperarid) over geologic timescales. While hyperarid deserts represent 7.5% of the Earth's continental landmass[193] and fossils are known to be preserved in them[194], biomarker degradation and taphonomic processes over geological timescales in a hyperarid environments has not been previously investigated. We hypothesized that typical pathways of organic matter degradation would be inhibited in long-lived hyperarid regions where low water activity suspends microbial activity and greatly reduces enzyme action [195,196].

We investigated the accumulation and degree of preservation of biomolecules in million-year-old hyperarid soils in the Atacama Desert, the oldest, continuously dry desert on Earth[197]. We focused our investigation on lipids because they have functional groups that are susceptible to microbial attack, but also contain recalcitrant hydrocarbon cores

that can be preserved over geologic time scales, recording the presence and activity of organisms living millions to billions of years ago as well as the history of diagenetic conditions since the time of deposition [177, 178].

E.3 Study Site

The Yungay region of the Atacama Desert experiences <2 mm of precipitation annually[198], with rain events often interspaced by a decade or more. The Aridity Index, defined as the ratio of mean annual precipitation to potential evapotranspiration in this region is approximately 0.004 which is 30 times more arid than the Mojave or Gobi Deserts[199]. Surface soils in the

Yungay region primarily experience water activities that range from 0.01-0.52 over the course of a diurnal cycle[200], well below 0.6, the threshold for microbial growth[196]. The extreme aridity Significance Fossil organic matter records past climatic and ecological conditions, yet 99.9% of organic matter is destroyed in most environments and eludes preservation in the geologic record. This is particularly true for information-rich labile biomolecules, which are typically degraded or recycled in time scales of days to weeks. We report the excellent preservation of functionalized fatty acids and other labile lipids in clay soils older than 2 million years in the hyperarid core of the Atacama Desert, due to protection from rainwater and the resulting lack of microbial degradative activity. This novel taphonomic process, which we term xeropreservation, suggests that hyperarid deserts could host an exceptionally preserved paleobiological record that is relatively unexplored on Earth, and potentially

Mars.

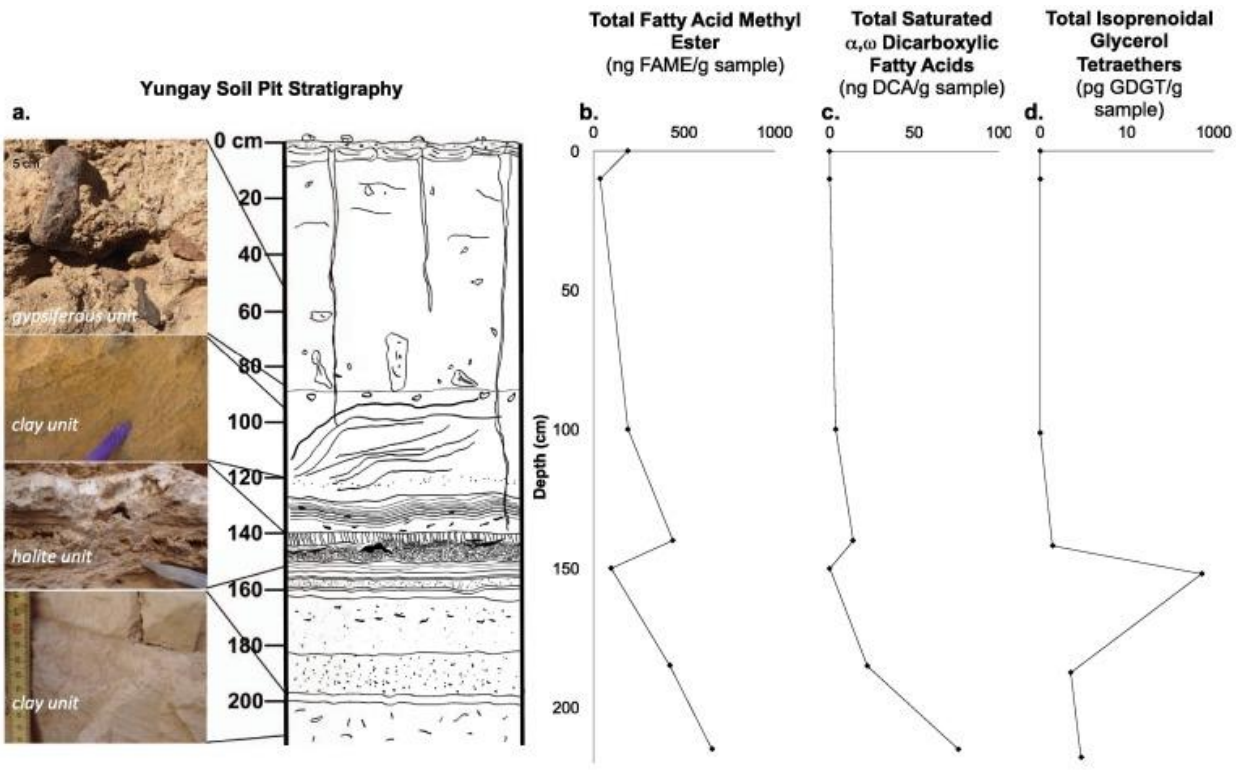

Figure E-1. Yungay Soil Pit Stratigraphy & Key Lipid Abundances
a) The soil pit contains three major units: gypsiferous soils (0- 90 cm depth), clay-rich units (> 90 cm depth), and a 10 cm-thick halite unit that interrupts clay units at 150 cm depth. Gypsiferous soils are matrix-supported and contain angular lithics. A clay unit at 100 cm depth contains centimeter-sized laminations composed of course sand. A clay unit at 140 cm depth contains fine sub-cm sized laminations (Fig. S3).

The massive, well-cemented halite unit (140-150 cm) has two major morphologies: vertical, crystalline structures and mottled halite. Beneath are alternating bands of well-sorted clay units and contain fibrous plant fragments (cm-size) that become more concentrated with depth. A more detailed description of the stratigraphic profile is provided by [207, 209]. b, c, d) Total abundances of FAME, DCA, and Isoprenoidal GDGT

were found to increase with depth with the exception of the halite unit (150 cm). Isoprenoidal GDGT and DCA were absent from upper gypsiferous soil. Isoprenoidal GDGTs are plotted on a logarithmic scale due to the presence of a high relative abundance of Archaeol in the halite unit causes an absolute lack of habitation by plants or animals and can only support a sparse microbial population in surface soils that are primarily derived from atmospheric inputs [200-203]. This region has been arid to semiarid since the late Jurassic (150 Ma), and has experienced continuous hyperaridity for the last _2 Ma[204-206]. Fluvial incision and deposition ceased at Yungay near the Plio-Pleistocene boundary coinciding with transition to hyperarid climatic conditions within the region. Subsequent to drying, landforms have retained and accumulated the Aeolian deposits of atmospheric salts and dust in the upper meter of the soil column[207]. We sampled a 2.5 m stratigraphic sequence in a soil pit that was previously dug by[208], and can be generally categorized into three major units (Fig. 1A): gypsiferous soils in the top 90 cm, clay-rich units below 90 cm depth, and a 10 cm thick wellcemented, massive halite unit that interrupts the clay units at 140-150 cm depth. Within the top 2 meters of soil, 87% of the halite is located in this unit[207]. Sparse plant material is found in the clay units below the massive halite unit[209]. Landform ages in this region are_2 My based on cosmogenic radionuclide concentrations in surface boulders and Ar isotopes in interbedded volcanic ash deposits[209]. During this time, atmospheric salts have been vertically redistributed in the top _1.5 meters of unaltered fluvial deposit and dust derived silicate matrix due to episodic wetting events[207,209], and according to[207,209], the massive, well-cemented halite unit at 140-150 cm signals the maximum depth of rainwater percolation and salt distillation over the last 2 Ma. This is further supported by

the low concentrations of soluble ions, including chloride, in layers below the halite (Fig. S1). Hence, the massive, well-cemented halite unit has acted as an impermeable unit precluding clay layers beneathfrom exposure to rainwater and other modern surficial processes[207]. Consequently, organic matter in the deeper clay layers are of fossil origin, older than 2 My, and represent a rare opportunity to investigate the degradation of lipid biomarkers over million-year timescales in the absence of water.

E.4 Results

The abundance and diversity of functionalized lipid groups increased with depth throughout the profile (Fig. 1b and 2). The most abundant class of lipids detected were fatty acid methyl esters (FAMEs), which are formed through the transesterification of esterified fatty acids (e.g. complex membrane-bound polar lipids, acylglycerols, steryl esters) as well as methylation of free fatty acids (FFA)[210]. Between 20 and 62 unique FAMEs were detected in each sample with alkyl chain lengths between 13 and 34 carbons, including methyl-branched FAMEs (terminal branched and mid-chain). The FAME profile composition was markedly different between horizons (Fig. 2), with diversity and abundance increasing with depth (Fig, 1b & 2). FAMEs were particularly abundant in the clay layers, with a maximum concentration in the deepest layer analyzed (215 cm) of 742 ng g-1 soil, comprised of 62 unique FAMEs. The abundance of FAMEs in the gypsiferous soil was lower by a factor of 4 or more. Deeper clay

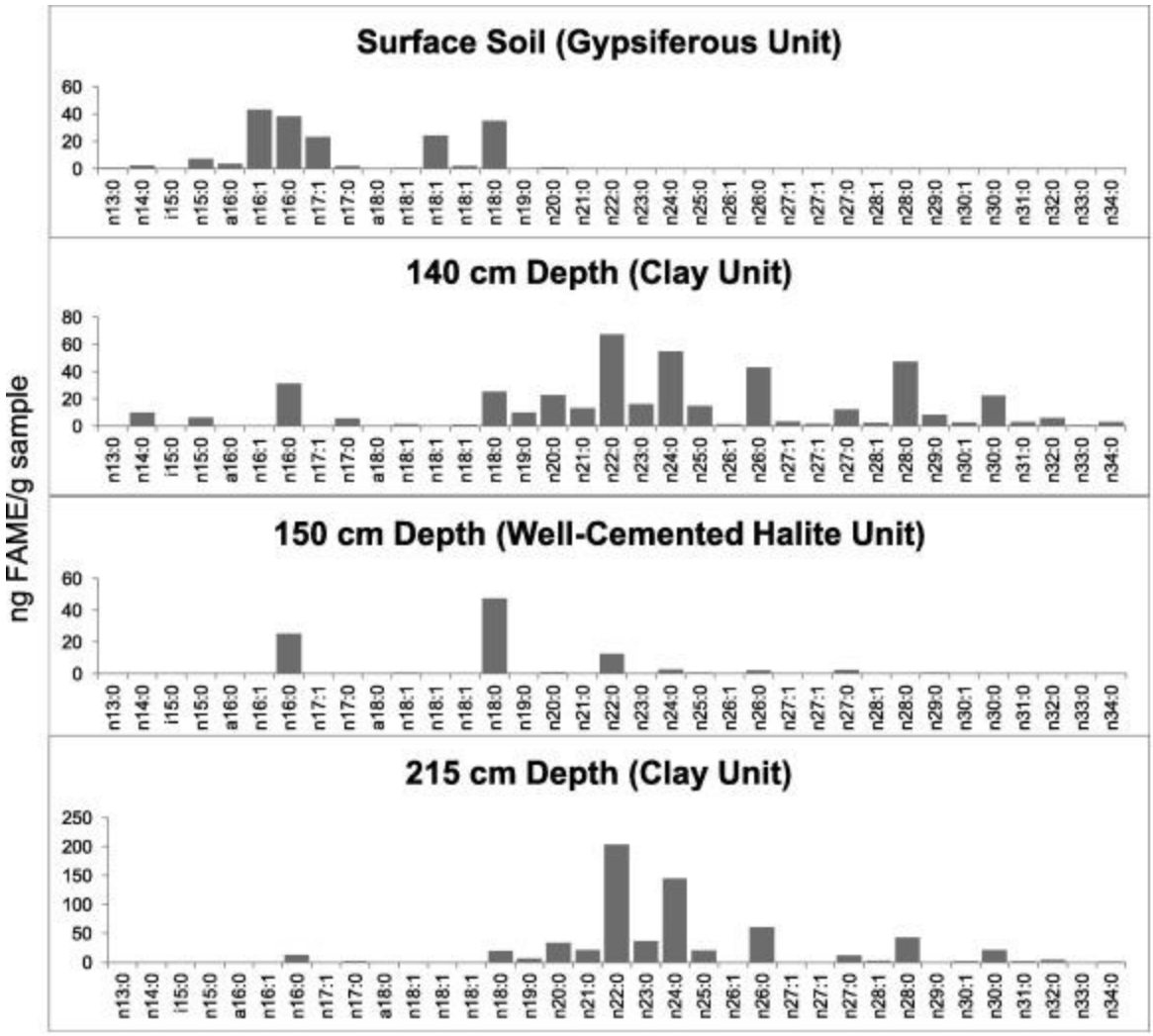

Figure E-2. Fatty Acid Methyl Ester (FAME) Profiles for Representative Yungay Pit Samples: Upper gypsiferous soils were dominated by n-16:0 and n-18:0 FAMEs. On the other hand, clay units were dominated by n-22:0 and greater chain length FAMES and contain a greater diversity in FAME content. The deepest clay unit had the greatest total FAME abundance. The wellcemented halite unit was dominated by n-16:0 and n-18:0 FAMEs. The vertical scale changes between plots.

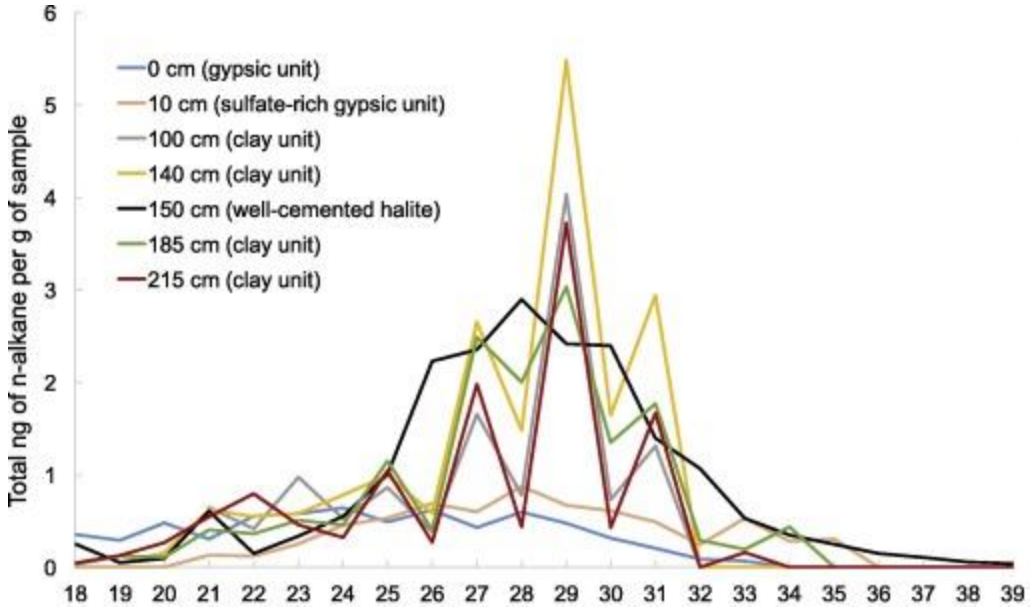

Fig. E-3. n-Alkane Content in Yungay Pit Soils: The straight chain n-alkane content of Yungay soils reveals two distinct patterns.
Clay rich units exhibit an odd-over-even chain length preference.

Conversely, gypsiferous soils and the halite unit exhibit a slight even-over-odd chain length preference. layers contained FAMEs with unsaturated bonds in their alkyl chains (Fig. 2). Small amounts of silylated fatty acids were also detected in soils 100 cm and below, reflecting free fatty acids not methylated during our acid methanolysis procedure (Table S4). Additionally, α- and β- monohydroxy monocarboxylic fatty acids were detection that contain a hydroxyl (OH) group exposed to the external environment and is available to be chemically altered. Based on the diagnostic fragment ions at m/z 175 and 159, α-hydroxy fatty acids were the more abundant member. The upper gypsiferous soils were dominated by n-C16:0 and n-C18:0 FAMEs, and contained both iso and antiso FAMEs (Fig. 2). N-alkanes were also present in these units and had an unusual, slight even-over-odd chain length preference in the C25-C33 range (Fig. 3). Contamination from petroleum can be excluded by the absence of phenanthrene and

other polycyclic aromatic hydrocarbons in the samples[211,212]. Hydroxy fatty acids were not detected in the gypsiferous soils, with the sole exception of a single chain length class (n-C16:0) found in the surface soil (Table S2). Additionally, no archaeal lipids were detected within gypsiferous units.

Conversely, the clay-rich units contained a higher abundance of lipids and included lipid classes that were not detected in the upper gypsiferous soils. The FAME profile in these units was dominated by n-C22:0 and C24:0 FAMEs (Fig. 2). Dimethyl esters of saturated α,ω-dicarboxylic fatty acids (DCA) were detected in all samples below 100 cm depth, with abundance and chain length ranges increasing with depth. The deepest clay unit had the largest abundance, and also the largest range in chain length (C9-C31) (Fig. 1c; Table S1), while only trace amounts of C22 DCA was observed in the halite unit. α- and β-monohydroxy monocarboxylic acids were also present in clay units with a relatively high abundance of n-24:0. A clay-rich sample at 185 cm depth had the highest total abundance of this lipid class as well as the greatest diversity, with chain lengths that ranged from C15 to C33. N-alkanes in these clay units contained an odd-over-even chain length preference (Fig. 3). Isoprenoidal glycerol dialkyl glycerol tetraethers (GDGTs) (Fig. 1d) and non-isoprenoidal, branched GDGTs were detected in clay-rich layers below 100 cm depth (Table S3), but not in the upper gypsiferous soils. An isoprenoidal GDGT (GDGT-0) was extracted from a clay-rich unit at 140 cm depth, and three additional isoprenoidal GDGTs (GDGT-1, GDGT-2, and crenarchaeol) along with five non-isoprenoidal GDGTs were identified in the clay-rich units at 185 cm and 215 cm depth respectively (Fig. S2 and Table S3). Branched GDGTs were found in greater abundance than isoprenoidal GDGTs. Significantly, the well-cemented halite unit at

140-150 cm depth contained a GDGT profile distinctive from both the gypsiferous and clay-rich units. It was characterized by a relatively high abundance of isoprenoidal glycerol diether, archaeol (481 pg/g of soil), a lesser abundance of isoprenoidal GDGT-0, and the halophilic archaeal biomarker, C20-C25 extended archaeol (Table S3).

E.5 Discussion

Biomarker preservation under prolonged hyperarid conditions Fatty acids are rapidly destroyed by biological degradation such as aerobic and anaerobic respiration, fermentation, and photoheterotrophy (6, 11), and incubation experiments with phytoplankton have demonstrated complete degradation over the course of a few weeks[213]. Hence, in most environments, the presence of labile lipids such as FFAs and FAMEs is indicative of extant communities or of recent biogenesis (36). Surprisingly, the concentration of FAMEs (Fig. 1b and 2) and FFAs (Table S4) in Yungay soils was not only found to increase with depth in the soil sequence, but FFAs and FAMEs retained labile features such as unsaturated bonds in the alkyl chains within the deeper, sealedoff clay units. In addition, α- and β- monohydroxy monocarboxylic acids were primarily found in clay-rich units below 100 cm depth (Table S2), despite this class of fatty acid's susceptibility to rapid diagenesis[211] and hydroxyl group loss[214].

Given the short residence time of labile fatty acids in most environments, their detection throughout the soil profile suggests that they either represent extant biomass, or exceptionally wellpreserved functionalized fossil lipids. We considered evidence for both scenarios. The Yungay region is one of the driest areas in the Atacama Desert. The water activity in the surface soils is well below the threshold for metabolic growth and enzymatic activity[200], and should remain very low and constant below a depth of 1 m[215].

The extremely dry conditions are reflected in the low biomass (103-105 cells cm-3) in surface soils[200,216,217], and low organic carbon content (<102 ppm)[200,207], which is "radiocarbon dead" (older than 40,000 years) below a depth of 100 cm[209]. In addition, the D/L ratio of aspartic acid in the top cm of soil indicates significant racemization of biologically produced amino acids, and yields ages of 103 to 105 years[218]. Together, these data argue against substantial biological activity or recent biogenesis of lipids, even in the topmost gypsiferous soils. Instead, functionalized lipids in the topmost soils likely represent relatively modern atmospheric inputs, a conclusion supported by the fact that the majority of cultivable isolates found in these soils are root-associated microbes in an environment where there has not been plant growth in millions of years[202]. On the other hand, the deeper clay layers that contain the highest concentration and diversity of lipids, have been isolated from rainwater as well as modern surface inputs for a period of hundreds of thousands to a few-million years by the massive halite unit at 140-150 cm depth, which is is a marker of maximum water percolation[207]. Soluble ion distribution in the soil profile (Fig. S1) reaffirms that there has been little or no percolation of rainwater through this halite unit (see below). Therefore, we argue that the functionalized lipids in the deeper clay units, and especially the archaeal and plant lipids found to be absent from the upper gypsiferous and surface soils, are fossils of organisms in an excellent state of chemical and structural preservation since their time of deposition. The remarkable degree of preservation of functionalized fatty acids and other lipids over several million years in hyperarid soils can be explained by the extremely low water activity, a taphonomic process that we term xeropreservation (preservation by drying). Low water activity in soils arrests

biological activity and suspends or greatly reduces chemical degradation, inhibiting modification of a cell's own lipid membrane as well as the action of heterotrophs. In particular, low water activity can inactivate or slow the reaction rate of the cell's own lytic enzymes, or those of heterotrophs, that degrade organic moieties upon cell death[219] (11, 19, 43). By halting aerobic or anaerobic metabolic activity, labile lipids such as fatty acids can be preserved. Such excellent lipid biomarker preservation is comparable to other geological samples that have been subjected to rapid dehydration, such as in polymerized resins like amber[(220-222)], and opens the possibility for extreme longevity of other labile biomarkers such as ancient DNA. Additionally, the structural and chemical integrity of labile lipids throughout the soil profile suggests that chemical oxidation of these biomolecules has been limited despite the photochemical formation and accumulation of reactive oxidant species in these hyperarid soils[223]. Again, this is likely due to the extremely low water availability in these soils, a factor exacerbated with depth, which limits soil organic oxidant chemistry.

Additionally, there are a number of abiotic conditions known to increase preservation of organic matter. Clay minerals present in the soil may play a role enhancing the preservation of organics (e.g., polar lipids) through interaction with charged mineral surfaces[(178, 179, 190)]. Entombment by chemical precipitates is another mechanism of microbial fossilization[(190, 224, 225)]. The many salts observed at Yungay could have served a similar function by encasing microorganisms or organic matter, thereby leading to increased chance of long-term preservation. It is also possible that the environmental conditions microorganisms were exposed to prior to drying had some effect on the degree of preservation of intracellular biomolecules. Stress (e.g. osmotic stress,

decreases in pH, and starvation) has been shown to induce a number of survival strategies including modifications in cell membrane fatty acid composition[226], which afford protections to microorganisms that increase recovery after drying[227]. The possibility that cellular modifications from environmental stressors before drying offer increased long-term preservation should be investigated further. Microbial diversity and paleoenvironmental reconstruction based on lipid biomarkers Certain lipids have been used as taxonomic markers for particular groups of microorganisms[228]. Some recent work has called into question the utility of this approach, specifically as it relates to methylated hopanoids[229, 230]. However, ester-linked membrane fatty acids are commonly used to assess microbial diversity[231], since the fatty acid chain length, number and position of double bonds, cyclopropane rings, and position of methyl branches allow for distinction between aerobes, anaerobes, sulfate-reducing bacteria, cyanobacteria, actinomycetes, fungi, protozoa, plants, and green algae[232]. The excellent preservation of the labile and refractory lipids allowed us to characterize taxonomic groups present in each stratigraphic unit, perform paleoenvironmental reconstructions based on known habitats of these groups, and assess environmental change over time. We broadly used FAMEs, isoprenoidal glycerol ethers, DCAs, and alkanes to distinguish between bacteria, archaea, and higher organisms such as plants throughout the soil profile.

FAME profiles in the upper gypsiferous soils were indicative of a predominant bacterial source[233, 234]. The slight even-overodd carbon chain length preference in alkanes was unusual, and could indicate a distinctive microbial origin or alteration of algal detritus[235]. The lack of archaeal lipids from the gypsiferous soils was consistent with previous work

that noted an absence of archaeal groups based on 16S RNA analyses[217]. These data support the idea that the Yungay region soils contain a population primarily consisting of bacteria. On the other hand, clay-rich units below 100 cm depth and contained lipid biomarkers not detected in the soils above, including lipids that are typically diagnostic of plants. The long-chain DCAs detected are likely derived from plant biopolymers such suberin and cutin[236] The odd-over-even chain length preference seen in C24-C32 n-alkanes is a common biosignature of terrestrial plants[(211, 236-238)]. The finding of plant-derived lipids in the clayrich units is consistent with the finding of cm-long fragments of fibrous plant material in samples at 185 cm and 215 cm depth[207].

The presence of α- and β-Monohydroxy monocarboxylic acids almost exclusively in the clay units also points to past inputs of biological lipids. While monohydroxy monocarboxylic acids can form from the decomposition of FAMEs, the profile of α- and β- Monohydroxy monocarboxylic acids in the clays differs from that of the FAME profiles and is suggestive of a unique source instead of a diagenetic product. This class of lipid is common in soil, marine, and lacustrine sediments[(211, 233)], and occur in a wide range of taxonomic groups, or can be produced as intermediates in the alpha- and beta-oxidation of monocarboxylic acids, so their exact source is difficult to determine, although the most abundant monohydroxy monocarboxylic acid found (n-24:0) is known to occur in certain seagrass species[236]. Isoprenoidal GDGTs, a class of membrane lipids diagnostic for archaea[(239, 240)] were also found in the clay units, along with branched GDGTs that are sourced from bacteria[241]. Nonisoprenoidal, branched GDGTs are proposed bacterial lipids[241]. Their greater abundance versus isoprenoidal GDGTs in the lower clay units is is consistent with a dominant bacterial signal. Furthermore, this

signal is inconsistent with offshore marine sources[240]. This, along with the absence of GDGTs in the upper gypsiferous soils suggests that both bacterial and archaeal GDGTs are syngenetic to the host clay unit. Together with the evidence for plant biomarkers, the presence of bacterial and archaeal GDGTs indicates a wetter environment towards the bottom of the soil profile, capable of supporting a more diverse ecosystem than that existing under the current hyperarid environmental conditions.

Finally, the well-cemented halite unit at approximately 140- 150 cm depth contained a GDGT profile distinct from both the gypsiferous and clay-rich units. The relatively high abundance of archaeol; a lesser abundance of isoprenoidal GDGT-0; and the presence of the biomarker C20-C25 extended archaeol (Table S3) are all diagnostic of halophilic archae[(242-245)]. The occurrence of the halite unit between two layered clay units (Figs. 1 and S3) and the halophilic archaeal lipid biomarkers found within the halite unit are consistent with formation in a small-scale evaporitic environment under a wetter climate regime. In this scenario, the buried halite layer could represent a paleo-surface horizon formed during a period of intense evaporation. This is in contrast to the proposed "wash-down" origin of the halite layer, whereby the salt-rich horizon formed from the episodic vertical transport of atmospheric salt during infrequent rain events and subsequent reprecipitation[(207, 209)]. The presence of diagnostic archaeal lipids found only in the halite unit, and the presence of undisrupted fine laminations in the clay unit immediately above (Fig. S3), both suggest that rainwater percolation might not be the sole mechanism responsible for the formation of the halite unit. However, soluble ion concentrations (Fig. S1) do indicate that atmospherically-derived salts have been solubilized by rainwater and reprecipitated for the most part above the halite unit (at 100

and 137 cm depth, see supplementary information appendix for expanded results and discussion). Thus, the halite unit still marks the maximum depth for percolation of rainwater as suggested by[207, 209]. The wetter climate regime in the Yungay region inferred from the lipid biomarkers in the clay and halite units could be related to permanent El Niño-like conditions inferred for the central Atacama 5.6-4.7 Ma[246], or with short, punctuated wet climate intervals during the last _5 Ma[247], a timing that is consistent with the estimated age of the soil profile (_ 2 Ma). In summary, extreme and prolonged dryness in the last 2 Myr has been responsible for the preservation of labile biomarkers in hyperarid Atacama soils. This is likely due to the low water activity in the soils, which prevents any significant microbial activity or chemical degradation of organic compounds. The exceptional preservation of functionalized and more fragile or labile lipids, especially at the bottom of the soil profile that has been sealedoff from rainwater over a million-year time scale, is comparable to the preservation of other labile biomarkers in deep-frozen permafrost or in polymerized resins like amber, and allowed us to reconstruct significant taxonomic changes that point to a shift in the hydrologic regime over the last 2-6 My.

E.6 Methods

E.6.1 Sample Collection

We collected seven samples from the soil pit in Yungay. Samples were collected in September 2014, before the rain event that occurred in March 2015. Due to the extremely low inventory of biomass in Atacama soils (26), samples were collected by scientists wearing full-body, sterile, clean-room suits (<1 colony forming unit per 10,000 garments), masks, glasses, and gloves to minimize the introduction of emitted

anthropogenic biological contaminants[248] during sampling. To remove surface contamination and expose fresh faces of the different soil horizons, approximately 20 cm of the pit wall was removed using a solvent-cleaned chisel (details of cleaning protocols are available in the SI). Samples were then collected in the soil pit from the bottom up using a solvent-cleaned drill bit to loosen the material.

A solvent-cleaned spoon was used to scoop samples into glass jars that had been heated to 500ºC for greater than 8 hours. Each sample was collected using a unique drill bit and spoon to minimize cross contamination. Samples were kept frozen until being returned to NASA Goddard Space Flight Center for storage at -20°C.

E.6.2 Abbreviated Lipid Analyses

For each unique sample, approximately 100 g of soil was homogeneously powdered with a solvent washed and ashed ceramic mortar and pestle. Soil samples were extracted using a modified Bligh and Dyer protocol[249, 250]. The protocol was modified primarily to minimize transfer steps and thus minimize loss from these organically lean soils. The monophasic extraction mixture of HPLC-grade water, methanol, and methylene chloride was split by further addition of methylene chloride and water to a final volume ratio of 1:1:0.9. This mixture was gravimetrically separated and the resultant total lipid extract (TLE) was collected, a portion set aside, and evaporated under a stream of N2 until a final volume of 40 µL was achieved. The TLE was subjected to a medium acid methanolysis[251] to cleave esterlinked membrane fatty acids and to methylate FFA. This produced a total FAME. The extract was subsequently derivatized using bis-(trimethylsilyl) trifluoroacetamide (BSTFA) for silylation of hydroxyl

groups and remaining FFA. An aliquot of the derivatized TLE (20% of total) was analyzed on an

Agilent 5975C gas chromatograph-mass spectrometer (GC-MS) (chromatographic conditions available in the SOM). The lipids were quantified relative to an internal standard (5α-cholestanol, 12.5 ng on column). A portion of each TLE (10% of total) was also analyzed for glycerol di- and tetraethers on a 1260 Infinity series liquid chromatograph-mass spectrometer (LC-MS) (chromatographic conditions available in the SOM).

E.7 Conclusions

This study demonstrates that the range of stability for labile, functionalized lipid biomarkers in clays is on the order of a few million years under extreme hyperarid conditions. Xeropreservation of biomolecules could represent an important, unexplored source of paleobiological information in the Atacama region in northern Chile, including Miocene sediments with marine vertebrates and invertebrates (18) and Jurassic and Cretaceous sediments with dinosaur remains[252, 253] and in other hyperarid desert environments. Xeropreservation could also be important with respect to the search for evidence of life on Mars. The finding of >2 My wellpreserved lipids in Atacama soils supports lipid biomolecules as an ideal target biomarker in the ongoing search for extant and ancient life on Mars, where arid to hyperarid conditions have dominated the environment for approximately the last two billion years and perhaps only geologically recently has the window for habitability closed[199].

E.8 Acknowledgements

This work was supported primarily by the National Science Foundation Graduate Research Fellowship Program under Grant No. DGE-1148903 to M.B.W. Additional support was provided by a NASA Astrobiology Institute Early Career Collaboration Award to M.B.W. A.F.D. acknowledges funding from the NASA Astrobiology Institute (NAI Grant NNX15BB01A to the SETI Institute). M.N.P. was supported by NASA Exobiology grant NNX15AM17G. R.E.S. acknowledges support from the NASA Astrobiology Institute (NNA13AA90A) Foundations of Complex Life, Evolution, Preservation, and Detection on Earth and Beyond. X.-L.L. and RES were further supported by the Simons Foundation Collaboration on the Origins of Life (SCOL). S.O.R. was supported by the EU Marie Curie Actions Program and the Irish Research Council (ELEVATE Career-Development Fellowship). We thank Carolyn Colonero and Kate French of MIT for technical assistance and Terry Jordan, Lujendra Ojha, Max Bernstein, and Raechel Harnoto for helpful discussions.

E.9 Supplemental Information

S1. Expanded Laboratory Methods

E-S1.1 Additional Sampling Notes

Clean room suit, gloves, glasses, and facemasks were donned before entering soil pit. The walls of pit were cleared with clean chisel, removing approximately 1–2 feet of soil material. Clean drill bits were used for each unique sample location, and samples were collected from the deepest layer up. Drill bits were used to loosen the material, and then a clean sampling spoon was used to scoop soil into ashed jars. Surface soils and sulfate-rich sample from 10 cm depth were collected about 50–100 m away from soil pit where there was no visible foot traffic.

E-S1.2 Tool Cleaning Protocols

Glass jars (Qorpak 8 oz clear straight sided round with green polypropylene cap and PTFE disc attached, cleaned and certified for semi-volatiles) were washed in Method Smarty soap, rinsed three times with tap water, then rinsed three times with distilled water (18.3 Mohm), dried overnight, then ashed at 500 °C overnight (> 8 h).

Lids were wiped with a Kimwipe soaked in methanol to remove dust. Then the lid was attached to clean jar and shaken with methanol, acetone, then hexanes. Lids never came into contact with the sample; ashed ultra high vacuum aluminum foil (All-Foils Inc.) was placed over ashed glass jars before the lid was attached.

Sampling spoons were scrubbed with a brush with Simple Green detergent. They were then rinsed three times with tap water, three times with distilled water, methanol, acetone, and hexanes.

Drill bits and chisels were put into a dishwasher with Method Smarty Soap. They were heavily scrubbed with Simple Green detergent, then rinsed in tap water and distilled water. They were sonicated in a methanol bath for 15 minutes, and then were then rinsed with methanol immediately after being pulled from the bath. They were then rinsed three times with methanol, acetone, then hexanes.

E-S1.3 Lipid Extraction

Glass jars containing samples were removed from the –20 °C freezer and were kept for 30 minutes to 1 hour at room temperature to prevent condensation of moisture onto soil directly. Soils were not lyophilized, in order to reduce the exposure time to the laboratory environment to minimize contamination risk and due to the extremely low water content in the hyperarid soils. Preliminary samples that were lyophilized to estimate water content in soil showed only 1.4% reduction in mass due to water loss.

Between 100 and 200 g of soil was removed from glass jars and then powdered with a solvent-rinsed and then ashed ceramic mortar and pestle. Three extractions were then performed on 70-90 g of a powdered sample, 40 mL of HPLC-grade H_2O, 100 mL of methanol, and of 50 mL of methylene chloride. After addition of solvents, the resultant slurry was sonicated and stirred. The mixture was then left to settle until solvent became mostly clear. Clear solvent was poured into a new flask.

Solvent extracts were then added to separatory funnel with 180 mL of extract and 47 mL of methylene chloride and inverted two times to mix. Water (47 mL) was then added to drive methanol into the aqueous phase. The methylene chloride layer was slowly drained into a new flask. The methanol and water phase was discarded. The resulting extract was evaporated and transferred into smaller vials until ~100 µL remained. Care was taken to minimize the number of containers used in the evaporation process and to thoroughly rinse and sonicate the sides of all vessels after draining to recover any lipid left behind. 10% of the total lipid extract was set aside for LC–MS (1/100 of 10% of the total lipid extract was injected on the LC–MS).

The total lipid extract was then reacted with commercial methanolic HCl 0.5N (Supelco, LC08137B) following the Kates, 1986 procedure. This simultaneously adds a methyl group to free fatty acids, and also tranesterifies complex lipids (phospholipids, triacylglycerols, steryl esters). This breaks the ester bond liberating the previously esterified fatty acids and then methylates them. Acid methanolysis gives a 'total' solvent-extractable fatty acid pool. One microliter of a 1 microgram per microliter 5α-cholestan-3β-ol standard was then added.

The derivatized portion was silylated with bis-(trimethylsilyl)trifluoroacetamide (Fluka, Lot # BCBL7513V). This step silylated OH groups on hydroxyl FAMEs and should have also silylated any other hydroxyl lipids (sterols, alkanols) had they present. The final volume was 40 µL, which contained 30% of the derivatized total lipid extract. 1/40th of this volume was then injected into the GC–MS.

E-S1.4 GC–MS

GC-MS was performed on an Agilent 5975C inert XL MSD system equipped with an Agilent DB-5MS column (60 m × 250 µm × 0.25 µm, Agilent, Santa Clara, CA, USA) with helium as carrier at 1 mL/min. We separated lipids by the following protocol: the oven temperature was held at 70 °C for 2 min and then increased from 70 °C to 130 °C at 10° C per min, then increased to 310 °C at 4 C per min and held at this temperature for 37 min.

E-S1.5 LC–MS

Following a LC–MS version of the tandem column protocol (Becker et al.., 2013), lipid analyses were performed on an Agilent 1260 Infinity series liquid chromatography system coupled to a 6130 quadrupole mass spectrometer via APCI interface. Separation of compounds was achieved with two ACQUITY UPLC BEH Hilic Amide columns (2.1 × 150 mm, 1.7 µm, Waters, Eschborn, Germany) maintained at 50 °C. The solvent gradient program used a constant flow rate of 0.5 mL/min and: 1. a linear change from 3% B to 20% B in 20 minutes; 2. a linear increase to 50% B at 35 minutes; 3. a linear increase to 100% B at 45 minutes, holding for 6 minutes; and 4. a decrease to 3% B for 9 minutes to re-equilibrate the column, where A was *n*-hexane and B was *n*-hexane/isopropanol (90:10). APCI source conditions were positive ion mode, drying gas (N_2) temperature 350 °C, vaporizer temperature 380 °C, drying gas flow rate 6 L/min, nebulizer gas (N_2) pressure 30 psi, capillary voltage 2000 V, corona current 5 µA. Glycerol di- and tetraethers were detected by both full scans and selected ion monitoring. Lipids were identified on the basis of accurate mass (better than 1 ppm), retention time, and diagnostic fragments, and quantified by $[M+H]^+$, with an extraction window of individual ion

chromatograms being ± 0.01 *m*/*z* units. We used C_{46} GTGT as an injection standard to determine the concentration of glycerol ether lipids.

E-S2. Anion Profiles in Yungay

E-S2.1 Methods

Samples were sieved to obtain a < 2 mm fraction. This fraction was then thoroughly ground with a mortar and pestle. One g of crushed soil fraction was then extracted with 20 g of Milli-Q water and diluted an additional 10 times. Samples were spiked with 12.5 µL of 1 mg/L 35Cl18O4 as the internal standard.

The IC-MS–MS analysis protocol used an IC-25 isocratic pump with an EG40 electrodialytic eluent generator, 2 mm bore AG21/AS21 guard and separation column sets housed in a LC30 temperature controlled oven (30 °C), ASRS-Ultra II anion suppressor in external water mode, and a CD-25 conductivity detector, all from ThermoFisher/Dionex. Around the elution window of perchlorate (t_R ~45 min), 40 min after injection, a diverter valve directed the CD25 effluent to a tandem mass spectrometer (Thermo Scientific Quantum Discovery Max with a heated ESI probe and enhanced mass resolution). Electrodialytically generated high purity KOH eluent was used in gradient mode at a concentration of 5 mM to 80 mM and a flow rate of 0.35 mL/min. Eluent generation, sample injection (5 µL), electrodialytic suppression, autoranging conductivity detection and data acquisition were all conducted under Excalibur/Chromeleon software control. Perchlorate was quantified by the −99 → −83 Th (*m*/*z*) transition ratioed to the −107 → −89 Th internal standard transition. All data were interpreted in terms of a 5-point

calibration with check standards run daily. Any sample falling outside the calibration range was reanalyzed after appropriate dilution. All samples were minimally analyzed in triplicate.

E-S2.2 Results

Chloride, perchlorate, nitrate and sulfate anions were interrogated via IC and perchlorate anions through IC/MS-MS (Supplementary Fig. 1). Of these, sulfate and chloride were the predominant species. Sulfate is the least soluble of the anions and is maximally present at the surface with penetration down to 100 cm where there is a dramatic drop in concentration. The more soluble chloride anion is present in all samples except the surface, showing a primary maximum at 150 cm (the halite layer) and a smaller secondary maximum at 100 cm. Despite being more soluble than chloride, nitrate is found only in relatively small quantities in the massive, well-cemented halite unit, with maxima at 100 and 137 cm. Similarly, perchlorate has two maxima at 100 and 137 cm.

E-S2.3 Discussion

Chloride concentration significantly decreases below 150 cm, while the nitrate and perchlorate anions slightly increase and stabilize in concentration. This reaffirms that 150 cm is the depth of maximum percolation as previously proposed (Ewing et al.., 2006; 2008) as percolating rainfall would have solubilized and subsequently carried chloride to the clay layers below. There are also relative maxima in the perchlorate, nitrate, and chloride profiles at 100 cm. It is possible that this depth represents percolation from smaller rain events. The changes in the anion chemistry throughout the soil profile likely do not necessarily represent the percolation depth throughout its history, but instead

represent the percolation depth at and after the establishment of the chloride-rich layer that acts to inhibit the flow of water downward 2 Ma ago or earlier.

Significantly, the relative maxima in nitrate and perchlorate at 137 cm depth are offset from the chloride maximum at 150 cm. Given nitrate is more soluble than chloride, it is unexpected that that these maxima are offset, and that only a relatively small quantity of nitrate is detected in the halite unit. This discrepancy gives additional credence to the idea that the halite unit may have originally formed by a process different than the previously proposed “wash down” model. It is likely that some of the chloride present in this unit was derived through the solubilizing of atmospherically-derived halite that was deposited by wind and subsequent washing down through the profile by wetting events. But, the presence of relatively abundant halophilic archaeal GDGTs, the undisrupted sub-cm laminations present in the layers above the halite unit (Supplementary Fig. 3), and the anion concentration profiles point to an alternative formation mechanism for the halite unit.

E-S2.4 Acknowledgements

This chapter has been previously published and is reprinted with permission according to the authors’ rights of Elsevier. Original work may be found using the citation: Wilhelm, Mary Beth, et al. "Xeropreservation of functionalized lipid biomarkers in hyperarid soils in the Atacama Desert." Organic Geochemistry 103 (2017): 97-104.

Supplementary Figure Captions

Supplementary Fig. E-1. **Anion Profiles in the Yungay Soil Column**: Anion profiles of chloride, perchlorate, nitrate and sulfate with depth in the Yungay. The point at 150 cm was taken from the massive, well-cemented halite unit. See Supplemental Information for further description of these data.

Supplementary Fig. E-2. **Glycerol Ether Lipids Detected in Atacama Samples**: Glycerol ether lipids detected in the Atacama samples. Archaeol and C20-C25 extended archaeol are archaeal diethers. Isoprenoidal and branched GDGTs are archaeal and bacterial tetraethers, respectively.

Supplementary Fig. E-3. **Finely Laminated Soil Unit at 140 cm Depth**: Image of a perchlorate and nitrate-rich soil unit located at 140 cm depth, 10 cm above the massive, well-cemented halite unite. This unit is comprised of silt to fine sand-sized particles that form undisrupted, fine sub-cm sized laminations and contains cm-sized voids. Such laminations are diagnostic of quiescent deposition in a sustained aqueous environment, such as a perennial pond.

Supplementary Fig. E-4. **Centimeter-Sized Fragments of Fibrous Plant Material Found at 215 cm Depth**: An image taken of sample collected from the unit at 215 cm. The arrow points to one of the fibrous cm-sized plant fragments present interspersed throughout this unit, and a likely source for some of the plant lipid biomarkers detected.

Supplementary Table Captions

Supplementary Table E-4. Note these values do not represent the total amount of free fatty acid present in the soils, but instead reflects free fatty acids that remained after acid methanolysis. Some of the FAME content is comprised of what were free fatty acids prior to analysis.

Supplementary Figures

Figure E-S1. Ion Depth Profile.

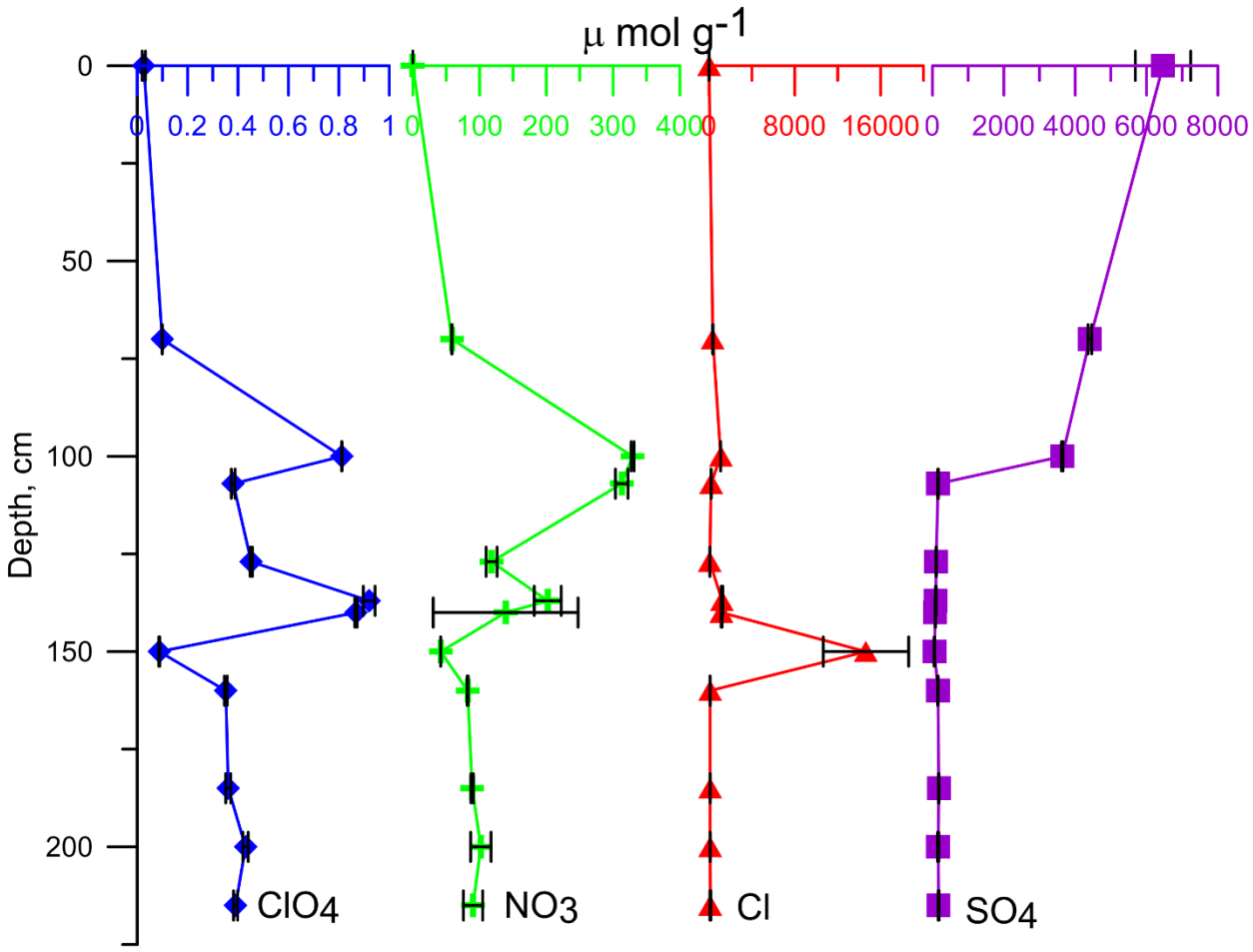

Figure E-S2. FAMES.

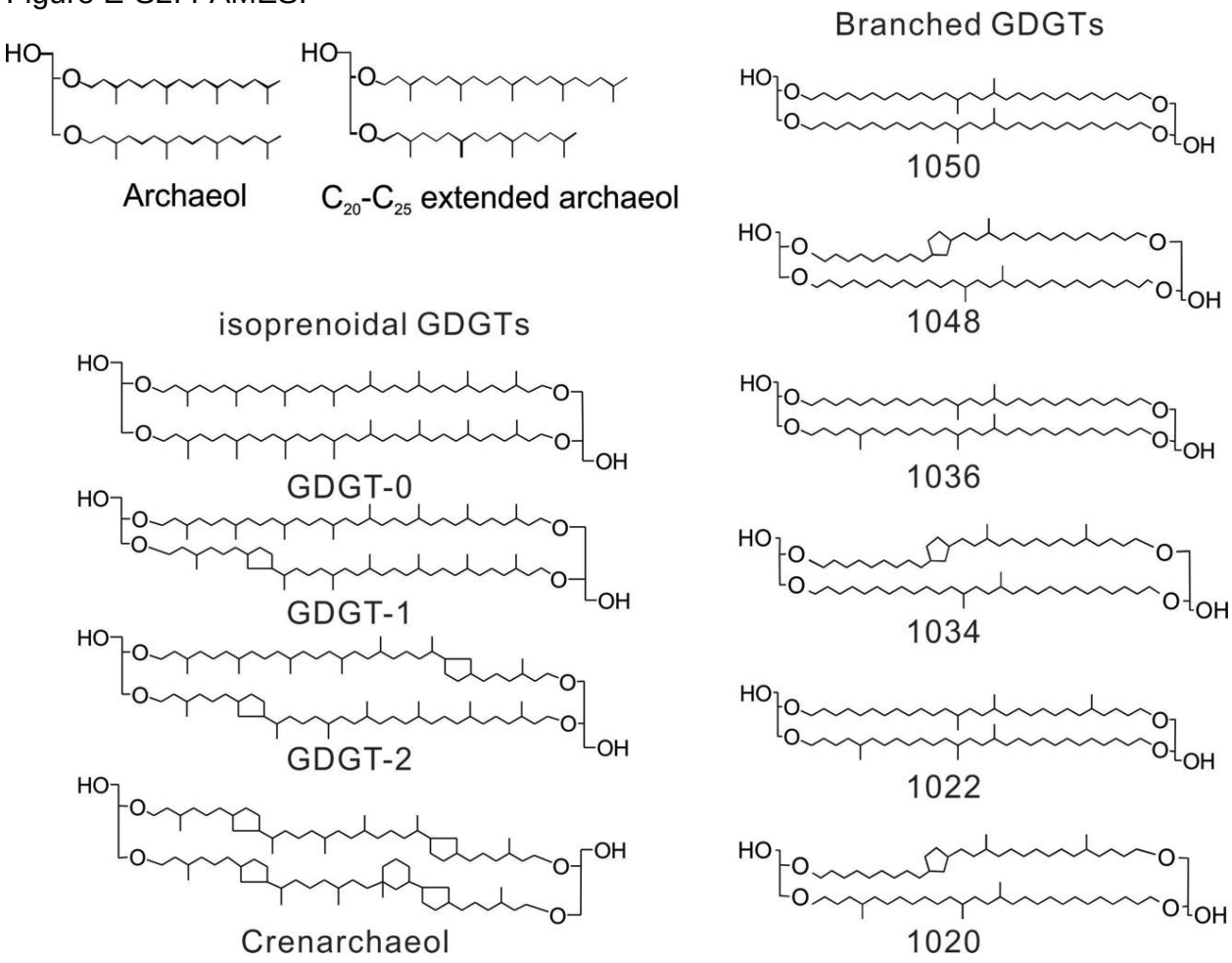

Figure E-S3. Photo of put profile.

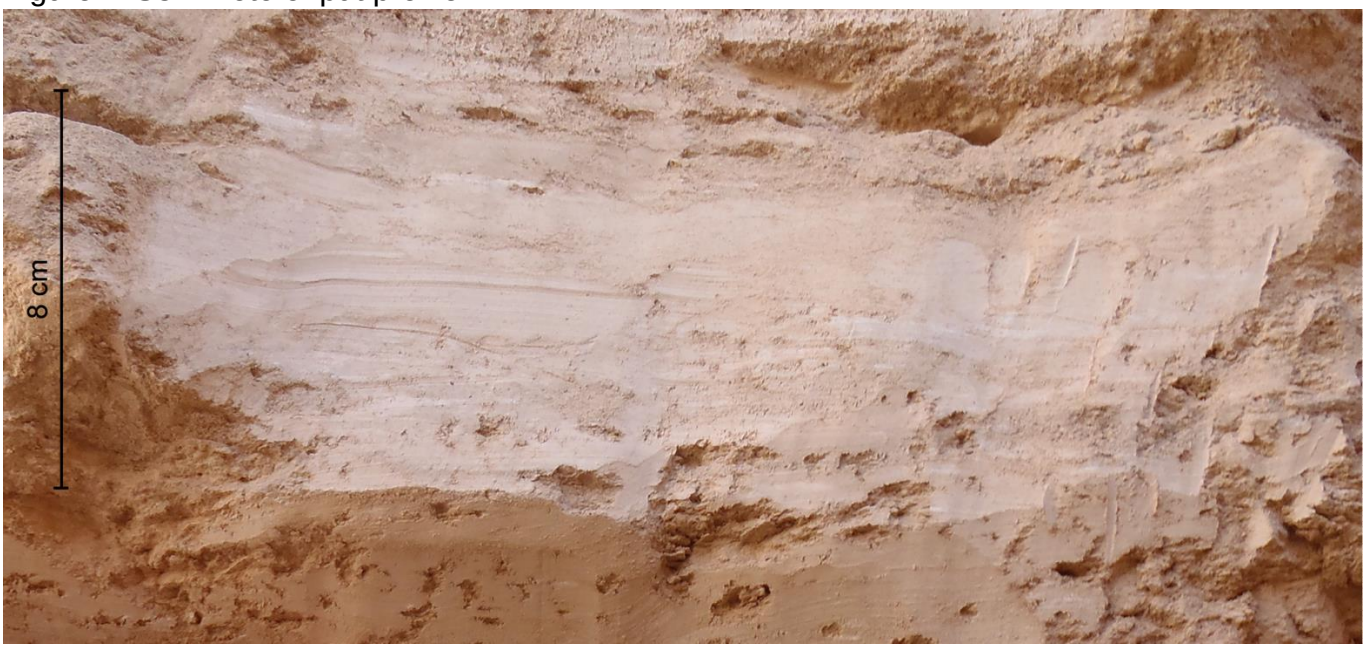

Figure E-S4. Photo of collected material. Plant material highlighted.

Supplementary Tables

Supplementary Table E-1. Saturated α,ω-dicarboxylic fatty acids in Yungay pit soils (ng DCA/g sample)

Carbon Chain Length	**100 cm depth** *(clay unit)*	**140 cm depth** *(clay unit)*	**150 cm depth** *(well-cemented halite)*	**185 cm depth** *(clay unit)*	**215 cm depth** *(clay unit)*
9	n.d.	n.d.	n.d.	n.d.	0.19
10	n.d.	n.d.	n.d.	n.d.	0.08
11	n.d.	n.d.	n.d.	0.06	0.10
12	n.d.	n.d.	n.d.	0.08	0.12
13	n.d.	n.d.	n.d.	0.05	0.15
14	n.d.	0.06	n.d.	0.17	0.25
15	n.d.	n.d.	n.d.	n.d.	0.72
16	n.d.	n.d.	n.d.	0.81	6.68
17	n.d.	1.51	n.d.	0.32	0.80
18	0.20	0.52	n.d.	0.84	4.67
19	n.d.	0.48	n.d.	0.55	2.67
20	0.22	0.68	n.d.	1.08	n.d.
21	0.62	n.d.	n.d.	1.24	0.12
22	0.91	2.06	0.01	3.74	19.47
23	n.d.	n.d.	n.d.	3.35	8.24
24	0.45	1.23	n.d.	3.26	11.37
25	0.27	1.45	n.d.	1.77	3.65
26	n.d.	n.d.	n.d.	0.32	6.49
27	0.31	1.50	n.d.	2.99	3.06
28	0.64	2.17	n.d.	n.d.	4.16
29	n.d.	1.02	n.d.	0.80	1.39
30	n.d.	0.85	n.d.	0.89	1.35
31	n.d.	0.36	n.d.	n.d.	0.33

a) n.d. is not detected from herein.

b) DCAs not detected in samples analyzed from units above 100 cm.

Supplementary Table E-2. Monohydroxy monocarboxylic fatty acids in Yungay pit sils (ng hydroxy fatty acid/g sample)

Carbon Chain Length	**Surface Soil** *(gypsiferous unit)*	**100 cm depth** *(clay unit)*	**140 cm depth** *(clay unit)*	**150 cm depth** *(halite unit)*	**185 cm depth** *(clay unit)*
15	n.d.	n.d.	n.d.	n.d.	0.02
16	0.95	0.32	n.d.	n.d.	0.22
17	n.d.	n.d.	0.09	n.d.	0.10
18	n.d.	0.16	0.12	0.09	0.18
19	n.d.	0.19	0.58	n.d.	0.08
20	n.d.	0.36	0.39	n.d.	0.51
21	n.d.	0.19	0.40	n.d.	0.84
22	n.d.	0.74	1.45	0.25	4.70
23	n.d.	0.77	1.50	0.07	7.37
24	n.d.	n.d.	n.d.	n.d.	32.94
25	n.d.	0.65	1.68	n.d.	8.29
26	n.d.	0.98	3.01	n.d.	11.37
27	n.d.	0.18	0.54	n.d.	1.98
28	n.d.	0.56	1.15	n.d.	3.19
29	n.d.	0.09	0.31	n.d.	1.38
30	n.d.	n.d.	0.30	n.d.	1.81
31	n.d.	n.d.	0.19	n.d.	0.50
32	n.d.	n.d.	0.14	n.d.	0.78
33	n.d.	n.d.	n.d.	n.d.	0.49

Supplementary Table E-3. The occurrence of glycerol tetraethers (GDGTs) in Yungay Pit Soils (pg GDGT/g sample)

				isoprenoidal GDGTs				***branched GDGTs***					
	Archaeol	C20-325 extended Archaeol	GTGT-0	GDGT-0	GDGT-1	GDGT-2	Crenarchaeol	1050	1048	1036	1034	1022	1020
Surface Soil (gypsiferous unit)	n.d.	n.d.	n.d.	n.d.	n.d.	n.d.	n.d.	n.d.	n.d.	n.d.	n.d.	n.d.	n.d.
10 cm depth (gypsiferous unit)	n.d.	n.d.	n.d.	n.d.	n.d.	n.d.	n.d.	n.d.	n.d.	n.d.	n.d.	n.d.	n.d.
100 cm depth (clay unit)	n.d.	n.d.	n.d.	n.d.	n.d.	n.d.	n.d.	n.d.	n.d.	n.d.	n.d.	n.d.	n.d.
140 cm depth (clay unit)	n.d.	n.d.	n.d.	0.19	n.d.	n.d.	n.d.	0.24	n.d.	n.d.	n.d.	n.d.	n.d.
150 cm depth (halite unit)	481	2.66	0.69	39.04	n.d.	n.d.	n.d.	n.d.	n.d.	n.d.	n.d.	n.d.	n.d.
185 cm depth	n.d.	n.d.	n.d.	0.20	0.09	n.d.	0.21	1.06	n.d.	0.82	0.28	0.28	0.10

(clay unit)													
215 cm depth (clay unit)	n.d.	n.d.	n.d.	0.27	0.08	0.22	0.30	0.96	0.40	0.70	0.47	0.39	0.21

Supplementary Table E-4. Free fatty acids in Yungay pit soils detected through derivatization with a silylation agent (ng free fatty acid/g of sample)

Carbon Chain Length	100 cm depth (clay unit)	140 cm depth (clay unit)	150 cm depth (halite unit)	185 cm depth (clay unit)
12	n.d.	n.d.	0.10	n.d.
13	n.d.	0.08	n.d.	0.01
14	n.d.	0.32	0.03	0.04
15	0.12	0.29	n.d.	0.04
16	0.61	0.91	1.53	0.17
17	n.d.	0.62	n.d.	0.16
18	0.62	0.40	0.26	0.12
19	0.08	0.15	n.d.	0.11
20	0.02	0.16	n.d.	0.11
21	n.d.	n.d.	n.d.	0.80
22	0.31	0.41	n.d.	0.35
23	n.d.	n.d.	n.d.	n.d.
24	n.d.	n.d.	n.d.	1.43
25	n.d.	n.d.	n.d.	n.d.
26	0.38	n.d.	n.d.	n.d.
27	n.d.	n.d.	n.d.	n.d.
28	0.20	n.d.	n.d.	n.d.

Appendix F Evaluation of Amount of Blood in Dry Blood Spots. Ring-disk Electrode Conductometry

Brian N. Stamos,[†] Akinde F. Kadjo,[†] C. Phillip Shelor, [†] Jordan M. Berg,[‡*] Benjamin C. Blount[≠] and Purnendu K, Dasgupta[†*]

[†]Department of Chemistry and Biochemistry, University of Texas, Arlington, TX 76019

[‡]Department of Mechanical Engineering, Texas Tech University, Lubbock, TX 79409

[≠]Division of Laboratory Sciences, National Center for Environmental Health, Centers for Disease Control and Prevention, Atlanta, GA 30341

*Corresponding authors: JMB: Phone (806) 834-4332, Email: Jordan.Berg@ttu.edu, Fax: (806) 742-3540; PKD: Phone (817) 272-3171, Email: Dasgupta@uta.edu, Fax: (817) 272-3806

F.1 Abstract

Dried blood spot (DBS) are increasingly being used for quantitative analysis. Typically one or more fixed area punches from the spotted filter are analyzed. The exact amount of blood spotted per unit area can depend on a number of factors. Based on the constancy of blood electrolyte levels, the preferred approach is to measure the sodium concentration in a portion of the aqueous extract. This analysis is typically destructive and is thus wasteful of the limited extract volume. We propose that electrical conductivity of the extract is an equally good but nondestructive measure. A small diameter ring-disk electrode (RDE) configured as a dip-sensor is ideal for conductance measurements in very small volumes. However, for a planar electrode like a RDE, the measured conductance depends on the dimensions of the liquid body extending from the probe. There are no analytical solutions for this geometry. Based on initial modeling results (COMSOL) that match experimental data, we provide a spreadsheet-based estimation approach. Using the RDE dimensions as the input parameters, the procedure determines the depth (D_{99}) of the liquid below the probe at which the measured conductance reaches 99% of the value that would be attained with an infinite liquid depth. Importantly, both model and experiment demonstrate that D_{99} is independent of the value of the specific conductance of the liquid (σ) and for typical probes of small dimension, is small enough to be practical for dip-type measurements in very small volumes of liquid. We demonstrate the use of such probes with actual DBS extracts.

F.2 Introduction

The diagnostic use of dried blood spots (DBS) dates back to over half a century. The first use of DBS was to screen for Phenylketonuria in infants,[254] a method still used today. Typically a small amount of a blood sample (heel prick in infants, finger prick in adults, tail prick in animals) is collected on a paper filter and is either sent for analysis or archived. DBS analysis is used widely to screen for neonatal metabolic disorders.[255] Relative to whole blood or plasma, DBS presents several advantages in sampling, storage, and transport. No centrifugation is needed. The lifetimes of many biomarkers are extended for months to years[256] while facilitating robust and compact storage. DBS sampling is particularly well suited for screening infectious agents, notably the human immunodeficiency virus (HIV); it has thus made a major difference in resource-poor areas for the diagnosis of HIV infection in infants and subsequent care.[257] Dried blood is not considered a biohazard and small sample volumes reduce risks of infection. This particularly helps sampling, storage and transportation.[258] Sampling and archival of DBS for future analysis is thus becoming increasingly popular in large scale clinical and other field use.

DBS sampling was originally introduced for qualitative screening. Over the past two decades, however, advances in trace analysis, especially liquid chromatography-(tandem) mass spectrometry, have led to the use of DBS for quantitative analysis.[259] DBS sampling and analysis has been validated for use in a wide variety of analytes for which whole blood/plasma was once considered the only useful matrix. The applications range from HIV-1N diagnosis to pharmacokinetic and toxicokinetic studies.[260-263] Sample sizes are typically 10–20 µL (most commonly 15 µL) but volumes below 5 µL have also been used. The blood is typically placed directly onto a filter card, made from materials such as S&S 903 filter paper.[264,265] Typically the cards are catalogued and stored at temperatures from ambient to –20 ^{o}C, depending on anticipated storage period.

For analysis, an area of the spot (typ. 3-3.2 mm Φ) is punched out, and extracted in water or water/ethanol mixtures. Unlike qualitative tests, quantitative analysis requires the exact volume of blood represented by the punched out portion be known. One recommendation is to follow a strict protocol where the exact amount of blood being spotted is known.[266-268] In collecting samples, especially in the field, this is a hindrance. One would simply want to cleanse an area, and soak up whatever blood is elicited by a prick with the filter, without having to worry about pipetting an exact volume on the filter. However even when known amounts are so spotted, varying hematocrit levels in different patients give rise to different viscosities, and therefore the same sample volume may not produce the same spot area.[269,270] Reportedly hydrophilic monolithic porous polymer sheets may produce more uniform spot sizes from the same volume of blood than paper filters.[271,272] However, analyte distribution may not be radially uniform across the spot;[273] using any media that promotes chromatography-like retention may make this problem worse. Also, while adherence to strict protocols may be adequate for self-contained studies, hospitals sharing patient samples may use different collection methods. Moreover a strict protocol has rarely been followed for archived samples. Age determination from a victim's blood has long been sought, and accurate quantification of biomarkers would aid greatly in this task. The ability to nondestructively quantify the blood volume represented by an extract will be of benefit in an enormous number of cases.[274,275]

Rather than relying on the combination of (a) spotting a known volume, (b) producing a fixed spot size and (c) assuming spatial uniformity, the weight of the punched out spot has been measured. The success of this strategy relies on substrate uniformity and constancy of the hematocrit concentration. Presently the recommended method is to use the sodium level as an "internal standard", typically measured by flame photometry.[20] For chromatographic analysis of DBS trace constituents, the extraction

volume is small, often in the ~100 μL range. With such a small sample, any destructive analysis for blood volume determination is undesirable. We propose that nondestructive conductivity measurement of the extract can serve the same purpose as measuring sodium. We further propose that a small ring-disk electrode (RDE) dip probe is ideal for making such measurements. To our knowledge, this is not only the first report that uses conductance measurement to quantitate the amount of blood in a DBS punch, but also the first to provide *a priori* the minimum liquid depth necessary to obtain reproducible results with a RDE type conductance probe.

F.3 Perspective

Electrolyte concentrations in human blood maintain a remarkable consistency. In human physiology, the osmolarity is tightly regulated through the Renin-Angiotensin-Aldosterone pathway.[276] The predominant ion in blood, Na^+, has been shown to lie within the 120-150 mM range in 99.5% of > 111,000 blood samples studied.[277] Assuming normal distribution, the normal (95%) limits will be given by 135 ± 10.8 mM, a variation of ± 8.0%. Most standard compilations state much tighter bounds, for example, the normal range for Na^+, K^+,HCO_3^- and Cl- are stated[278] to be 141±6, 4.25±0.75, 25±3 and 100±5 meq/L. Ionized Calcium and magnesium normal ranges span 2.4±0.2 and 1.65±0.25 meq/L.[279] Although chloride is second in concentration to sodium, 50% higher mobility makes it the largest contributor to conductivity. The use of infinite dilution equivalent conductance values for the corresponding ions lead to an overall specific conductance value of 16.4±0.5 mS/cm for the above composition. While the exact value will depend on the dilution factor (which also controls how much the actual equivalent conductance values differ from those at infinite dilution), the relative contributions (Cl^-: 46.7%, Na^+: 43.2%, HCO_3^-: 6.8%, K^+: 1.9%, Ca^{2+}: 0.9% and Mg^{2+}: 0.5%) and the overall relative uncertainty is likely to remain the same. Blood electrolyte

concentration is approximately equivalent to 130±4 mM NaCl based on equivalent conductance at infinite dilution. In a DBS extract, the concentration of NaCl will be several mM and the applicable equivalent conductance values will be much less than those at infinite dilution; the contribution of divalent ions will be especially affected due to electrostatic reasons.

Electrical conductivity measurement of an extract should therefore be applicable to the estimation of blood volume present in the spot extracted. The RDE represents a two-dimensional sensing surface that is easily made in a miniature form. The RDE is used extensively in voltammetric applications (often in a rotating format); this geometry has been widely used for amperometric measurements in a wall-jet configuration. Less conventional uses of the RDE geometry have been in capacitance sensing of soils[280] or liquids,[281] electromigrative injection from a small loop in capillary electrophoresis,[282,283] etc. The use of the RDE geometry for conductivity measurement is scant;[284] in a related geometry a cylindrical electrode (outer surface area active) with a small diameter wire (only tip active) protruding beyond the outer cylinder terminus was shown to be especially tolerant of suspended solids and floating debris.[285] An obvious problem of conductometry with an RDE is that a cell constant cannot be readily defined. It has not been possible to relate the measured conductance *ab initio* to the solution specific conductance based on the sensor dimensions alone. Nevertheless, the geometry is particularly conducive to measuring conductance in small volumes. Indeed the only conductivity detection based capillary electrophoresis system ever commercialized used RDE conductometry.[286]

F.4 Principles and Approaches

The basic configuration of the model system is shown in Figure 1. Note that this limiting model system does not take into account that the conducting electrolyte may extend to the side beyond r_3, i.e., in a practical scenario when such an electrode is dipped into a measurement solution contained in a tube, the electrode will not tightly fit into the tube, there will be solution extending to the sides on the same plane. Further, although the active face of the electrode is two-dimensional, a real three dimensional cylindrical electrode (face RDE, outer cylinder wall insulated) will typically be *dipped* into the solution for measurement, resulting also in solution above the plane of the electrode, around the insulated cylindrical wall.

The sample specific conductance, σ, is related to the measured conductance, G by the relationship

$$\sigma = GK \quad \ldots(1)$$

where K is the probe cell constant. In most conductivity cell designs, the solution to be measured is contained in the space between the two electrodes; to a first approximation, the electric field is wholly contained within this volume. Presence or absence of solution beyond this space has little effect on the measured conductance. With an RDE, this is not the case: it is intuitive that the measured conductance will be greater if the depth D of the solution layer extending from the sensor surface is substantial, rather than infinitesimal. It follows that the “cell constant” is not a constant but depends on the solution depth. Experiments and numerical simulations bear out the intuitive expectation that G would keep increasing with D. But as the field dissipates with distance, increasing D beyond a certain value will have diminishing returns. G will thus asymptotically approach a limiting value G_∞ as D approaches infinity. Conversely, K will decrease with increasing D and also asymptotically approach a limiting value K_∞ as D approaches infinity. Solutions to similar problems have previously been advanced by

finite element[27,28] or similar “annular patch subdomain”[287] methods for capacitance probes. The only extant analytical equation for interdigitated planar electrodes conductometry is applicable solely to infinite solution depth.[288]

An infinite solution depth is not practical. We propose the depth at which 99% of the limiting value of G is reached, D_{99}; as a more usable index, where:

$$G(D_{99}) = 0.99\, G_{\infty} \quad \ldots(2)$$

As long as the sample height is $\geq D_{99}$, the cell conductance can be given by

$$G_{\infty} = (1.005 \pm 0.005)\, G_{\geq D99} \quad \ldots(3)$$

Likewise K_{∞} may then be taken as $0.995 \pm 0.005\, K(D_{99})$. To avoid the need to know the sample volume (depth) precisely, and to reduce conductance variations due to variations in depth, the sample depth should be chosen to be $\geq D_{99}$ so that K and G are insensitive to variations in D. If we can *a priori* know/estimate D_{99} from the sensor dimensions, one can ensure accurate results by ensuring that sufficient liquid is taken for the liquid depth below the probe to be $\geq D_{99}$. Herein we simulate and model the RDE conductance sensor to estimate D_{99} from the RDE dimensions. Thence one can operate comfortably above D_{99} and obtain the correct value of K_{∞} from the measurement of a solution of known specific conductance. Note that the assumed geometry of the model will really provide an upper limit of D_{99}, the existence of the conducting media to the sides, on and beyond the plane of the electrode, can only reduce D_{99}.

Herein we assume that at the applied voltage to the sensor is small enough such that heating due to the passage of current is insignificant. The electrical potential and resulting current densities can be described by Laplace’s equation. While finite-element software of considerable power is available to solve Laplace’s equation for complex geometries and boundary conditions, the learning curve to use such specialized and expensive programs is steep. For simple geometries it is possible to solve Laplace’s

equation using a general-purpose spreadsheet, such as Microsoft Excel™.[289-291] However, adaptive meshing and automated parameter sweep techniques that improve accuracy and ease of use are difficult to implement in a spreadsheet. We have chosen therefore to take a hybrid approach. We first simulate and model using the commercial finite-element package *COMSOL Multi-physics* (hereinafter COMSOL) for a number of RDE dimensions as a function of sample depth. The COMSOL simulation results, are then validated by actual measurements made with the RDE sensors. The COMSOL simulation data are then used to construct a semi-empirical algebraic model of D_{99}. This is then used to provide an initial input to the Excel-based calculator.

F.5 Principles and Approach

The steady-state current density $\boldsymbol{j}$, electric field $\boldsymbol{E}$, and electric potential V are modeled within the sample by the following system of partial differential equations:

$$\nabla \cdot \boldsymbol{j} = 0 \tag{4a}$$

$$\boldsymbol{j} = \sigma \boldsymbol{E} \tag{4b}$$

$$\boldsymbol{E} = -\nabla V \tag{4c}$$

For spatially uniform σ, these yield Laplace's equation,

$$\nabla^2 V = 0 \tag{5}$$

with Dirichlet boundary conditions[292] on the electrode surfaces, and Neumann boundary conditions[39] on the lines of symmetry and insulating surfaces. Because of the cylindrical symmetry of the probe, eq 5 can be considered on a two-dimensional domain. To solve eq 5 using a spreadsheet, the derivatives were approximated using finite-difference formulas. We used fourth-order central differences, with second-order central differences in the cells immediately adjacent to the domain boundary. Gauss-Seidel

iteration with successive over-relaxation was used until satisfactory convergence (see below) occurred to provide the solution.[25]

Once eq 5 is solved to give the potential *V* throughout the domain, the current density can be computed from eq 4b. The total probe current is the integral of the axial component of the current density over the inner electrode area:

$$I = 2\pi \int_0^{r_{inner}} \boldsymbol{j} \cdot \hat{\boldsymbol{z}}\ r dr \quad \text{... (6)}$$

The conductance *G* is then the excitation voltage divided by this current. As with eq 5, this expression can be approximated using discrete approximations to the integral operator. For this study, the integral was computed using the trapezoid rule.[27]

Convergence was tested in two ways. First, the percentage change in the calculated conductance *G* is computed after each of 500 iterations. Second, the percent difference between the current entering the probe through the inner electrode and leaving through the outer electrode is computed. Conservation of charge and the steady-state assumption implies a zero sum. Therefore this value is used as a second convergence measure. When both criteria drop below specified values (typically 0.01% – 1%), the simulation is considered converged. Figure 2 compares the potential field contours by the Excel-based solver to the potential field computed by *COMSOL Multi-physics* for the *standard* (see below) probe dimensions and sample depth.

Determining D_{99} directly using the Excel solver is computationally intensive. On a personal computer, an inconveniently long period is needed because a large range of depths must be simulated to ensure that G_∞ is reached. We define instead a dimensionless quantity *sensitivity*, $S_D^G(D)$, the relative change in G ratioed to a relative change in the depth at a given *D* value. The sensitivity can be computed approximately from the change in *G* (ΔG) at two closely spaced values of *D*:

$$S_D^G(D) \approx \frac{\Delta G}{G} \cdot \frac{D}{\Delta D} \quad \text{...(7)}$$

From simulation results we observed that D_{99} corresponds to a value of D for which $S_H^G(D) \approx 0.05$. Note that had we modeled $G(D)$ to have an exponential dependence on D (that it clearly does as will be shown in the results later) such that

$$G(D) = G_\infty(1 - e^{-kD}) \quad ...(8)$$

k being a constant. In the case of such an explicit function, it is readily calculated for the above situation that

$$D_{99} = 4.605/k \quad ...(9)$$

The sensitivity function at D_{99}, $S_H^G(D_{99})$ is readily computed to be ~0.0466, in agreement with the simulation results.

The sensitivity is a nondecreasing continuous function, so given an interval containing the desired value, the location of the value may be found by bisection search,[27] by the half-interval method with the new interval containing the target. But finding an appropriate starting interval is critical to an efficient bisection implementation. Presently, we accomplished this with a semi-empirical algebraic model to the *COMSOL* simulations data. Let A_1, A_2, and A_3 be the areas of the inner electrode, the annular gap, and the outer electrode, respectively. The normalized dimensionless values of the same areas, $\bar{A}_1$, $\bar{A}_2$, and $\bar{A}_3$, in units of the inner electrode area, can be given as 1, A_2/A_1 and A_3/A_1. We set $\bar{A}_{min} = 10\ \min(1, \bar{A}_3)$ and then define the effective inner and outer electrode areas by $\bar{A}_{1,eff}$= min(1, $\bar{A}_{min}$) and $\bar{A}_{3,eff}$= min($\bar{A}_3$, $\bar{A}_{min}$). A semi-empirical estimate for D_{99} becomes possible:

$$D_{99,est} = 1.31\left(\bar{A}_{1,eff}\bar{A}_2\bar{A}_{3,eff}\right)^{1/6} r_1. \quad (10)$$

The interval (0.7-1.3)$D_{99,est}$ was generally found to give a suitable initial interval for the bisection search. Even with a manual search, simply following the gradient, the monotonicity of $S_H^G(D_{99})$ ensures that a suitable starting interval will eventually be found.

An illustrative example as to how to use the Excel Spreadsheet Elecrosolve.xlsx that is a companion to this manuscript as a supporting information file, is presented in the Supporting Information using the dimensions of our standard probe.

F.6 Experimental Section

F.6.1 Blood Spotting and Processing

Unidentified adult human blood samples (finger prick) were collected from volunteers. In one experiment, triplicate 0, 1, 2, 4, and 8 μL samples from one of the researchers were alternately pipetted into prewashed and dried 1.5 mL micro-centrifuge tubes or spotted on prewashed and dried Whatman No 3 filters.[293] The samples in the vials were diluted respectively with 100, 99, 98, 96, and 92 μL water, capped, allowed to sit for 20 min, vortexed for mixing and conductance measured within 5 min using the standard probe (*vide infra*). The filters were allowed to dry. One-fourth inch (6.3 mm) diameter disks were punched out with a stainless steel punch under dust-free conditions. This punch area was chosen because it was large enough to completely contain the largest amount of blood (8 μL) spotted in these experiments. The punch was transferred to a prewashed and dried 1.5 mL micro-centrifuge tube, 100 μL of water added, the vial capped and allowed to remain for 20 min. After vortex mixing, the conductance was measured with the standard probe without removal of the filter. In another experiment triplicate 2 μL blood samples from 12 volunteers were spotted on filters and then processed as above.

F.6.2 Conductivity Probe Construction and Measurements

Several RDE probes, differing in dimension, were constructed and are referred to as the *macro*, *medium* and *standard* probes, respectively. The *macro* probe was constructed of a 2.77 mm ϕ stainless steel rod insulated with a 0.8 mm thick PTFE sleeve as the center

electrode and inserted inside a 4.4/5.1 mm id/od stainless steel tube insulated on the outside with PTFE heat shrink tubing. The *medium* probe had a 710 µm ϕ stainless steel rod insulated with a 400 µm thick PTFE sleeve as the center electrode and inserted inside a 1600/3200 µm id/od stainless steel tube. The *standard* probe had a 800 µm ϕ center electrode, a 290 µm thick spacer and a 1400/1830 µm i.d./o.d. outer electrode insulated on the exterior by a snug-fit PTFE tube of 2.7 mm outer diameter. This probe was used in all actual DBS/blood measurements. To protect from corrosion in high chloride DBS extracts, the electrodes were electroplated with gold before covering the outside.

Calibrations were conducted at 22 °C. The medium and the macroprobes were inserted upside down into the bottom of a well drilled into an acrylic block such that the snug-fit probe acted as a stopper. The cavity was filled with a known volume of a KCl solution of known specific conductance. The conductance was then measured with a Dionex CDM-1 Conductivity Detector. Aliquots of the solution were then removed in 0.5 µL steps thus changing the liquid height above the probe and the conductance was measured in each step.

F.7 Results and Discussion

F.7.1 Electrode Corrosion and Measurement Conditions

The standard probe was provided with an external union with male nuts, the union terminus sits on the lip of the vial (see Figure S1 and S2 in SI) making it convenient to position it reproducibly, although this is not critical as long the electrode touches the extract and the liquid depth thereafter is sufficient. Some corrosion of the stainless steel electrodes was observed on prolonged use in high chloride solutions with the excitation conditions used (square wave, 3 kHz, 5 V p-p); the need for frequent electrode polishing

to maintain reproducibility was eliminated by electroplating both electrodes with gold. Rapid vertical insertion of the probe into the liquid can trap air bubbles at the interface; this needs to be avoided.

F.7.2 Liquid Depth vs. Conductivity

Experiment vs COMSOL Simulation

The *COMSOL* simulation results are compared with the actual experimental results for the macro probe with 500 μM KCl solution as a function of sample depth *D* in Figure 3. Simulations were carried out up to *D* = 2400 μm while the measurements extended to ~1700 μm. The fit of the experimental data for $D \geq 500$ μm to an asymptotic dependence of *G* on *D* (eq 8) is indicated by the dashed line. The projected G_∞ values are 42.2 and 43.3 μS for the experimental vs. simulation data; the simulated value is 2.6% greater (note however, the simulated value is directly proportional to the assumed value of σ of the solution). Consideration of similar data for the medium probe for the same solution (see Figure S3 in the Supporting Information) shows an even closer match, with the simulated value for G_∞ being ~0.6% lower than the value projected from the experimental data. These results together suggest that there is no systematic bias in the simulation. Two other aspects of the simulation vs. experimental data are noteworthy. At $D \leq 500$ μm, especially at $D \leq 200$ μm, the nonplanarity of the liquid meniscus due to surface tension effects becomes significant compared to the D value in the model that assumes a flat liquid surface. Difference in the model vs. experimental data is therefore significant at small D values; fortunately this has no effect on determining D_{99}. Second, in Figure 3, the approach to G_∞ is clearly faster in the experimental data; D_{99} is lower compared to that predicted by the simulation. This arises from the probe having an outer insulating shield of appreciable thickness, leading to a significant amount of solution extending in the radial dimension beyond the electrode,

whereas the model assumes no peripheral solution. The model therefore can only provide a conservative upper limit for the D_{99}.

F.7.3 Predicting D_{99}. Excel vs. COMSOL Solutions

For most practical situations involving conductance measurement, it is very rare that one relies on the cell constant computed from absolute dimensions of the electrodes/cell. Rather, the cell is calibrated with solutions of known conductance. While we have seen the COMSOL model predicts the absolute conductance value as measured quite well, the real value of a simpler, readily applicable solution is for the method to predict the D_{99} value well. The user would then calibrate the electrode with standards under conditions in which the calibrant solution depth below the electrode surface will equal or exceed D_{99}. Figure 4 shows a comparison of the Excel vs. COMSOL predictions as to how $G\infty$ is attained as a function of depth for the macroprobe. The Excel prediction is ~10% lower than the COMSOL prediction (1500 vs. 1650 μm).

The experimental data and COMSOL simulations for the medium probe are shown in Figure S3. Using an asymptotic fit (eq 8 and 9) we compute D_{99} to be 1700 and 1800 μm, respectively for the experimental data and the COMSOL simulations, in very good agreement. Importantly, for a 100 μL sample using the standard probe in the vials described, the tip is immersed to a depth of ~2 mm below the meniscus and the liquid depth below the tip is ~ 6 mm, more than enough to exceed the calculated D_{99} value of <2 mm, as illustrated in the supporting information using the Excel approach. An extract volume of 100 μL in a typical 1.5 mL micro centrifuge tube provides sufficient liquid depth to use any of RDE sensors described here and stay comfortably above D_{99}.

F.7.4 Real Samples

Does the DBS Extract Reflect A Complete Extraction of Blood Electrolytes?

It was of interest to determine how whole blood directly put in the extraction solvent compares with the same amount of blood put on a filter, dried and extracted. Figure 5 shows that these values are virtually identical, indicating that the electrolyte is efficiently extracted. The conductance variance of the diluted blood samples ranged from 3.7-9.1% (mean±sd 5.4±1.9%); that for the DBS extracts were slightly higher at 2.0-12.1% (mean±sd 7.4±4.2%). Neither variance showed a consistent pattern with the amount of blood taken. A paired t-test indicated at 90+% confidence levels the two sets of values are statistically indistinguishable. As the data in Figure 5 would suggest, the presence of the filter remaining in the solution or any debris therefrom makes no difference in the measured conductance; this was also independently verified by removing the filter.

F.7.5 Relating to NaCl Equivalents Present in the Sample

In principle, all data can be interpreted by the absolute conductance measured by a given probe in a given laboratory but comparability across probes and laboratories require calibration. We presently calibrated the standard probe with 0, 0.1, 0.5, 4.0, 8.0, and 10.0 mM NaCl, the measured conductance values were linearly correlated with the tabulated specific conductance values for these concentrations (r^2 = 0.9992, Figure S4). The relationship between the NaCl concentration and the conductance in this domain is nonlinear but is satisfactorily described by a quadratic relationship (r^2 = 0.9998, Figure S6). Our experiments were conducted in an open laboratory environment in the presence of CO_2. When measured directly at the deionized water system, the conductance measured by the standard probe is essentially zero and when taken in the vial becomes 1.6-1.7 μS within the first two minutes from CO_2 intrusion. For a calibrant like 0.1 mM NaCl, this blank correction is significant. If the vial is not washed, impurities contributed by the vial (which are labeled as sterile but not apparently electrolyte free)

also contributed, in the batch we used the blank conductance was ~5 μS. For real DBS extracts, the conductance is, however, several hundred μS and blank correction has little impact.

F.7.6 Variations in Real Samples

Triplicate 2 μL samples were taken from 12 volunteers. Within-subject variance, which includes effects of operator skill and thence reproducibility in pipetting/spotting,etc. ranged from 2.6-12.2% (mean±sd 6.5±2.7%) while between-subject variance was 17.9% (Figure 6). Granted that this is a very limited number of subjects and the present researchers have no prior experience in sampling and spotting blood, this is still an indication of the degree of accuracy in quantitating the amount of blood taken in a DBS punch one may expect by the proposed approach of conductance measurement.

It is interesting to note from Figure 6 that the mean NaCl equivalent concentration in these blood samples was 140±10 mM, compared to 130±4 mM estimated from literature compilations and infinite dilution equivalent conductance data as previously stated.

F.8 Conclusions

A ring-disk electrode geometry was modeled to determine minimum immersion depth to obtain results accurate to within 1% and found to correlate well with experimental data. Applicability towards quantitation of the amount of blood represented in a DBS punch by nondestructively measuring the conductance of an aqueous extract of the DBS punch was shown. There are presently no comparable data on the uncertainties of similar quantitation via sodium measurements. While we cannot draw conclusions as to comparability in this regard, there is no reason to believe that the results will not be

equivalent. The conductance measurement approach with a small RDE probe has the considerable advantage of zero sample consumption.

F.9 Acknowledgements

This work was supported partially by NSF (CHE-1506572), ThermoFisher/Dionex and the Hamish Small Chair Endowment at the University of Texas at Arlington. This chapter has been reprinted with permission from Brian N. Stamos, Akinde F. Kadjo, C. Phillip Shelor, Jordan M. Berg, Benjamin C. Blount and Purnendu K, Dasgupta. Akinde F. Kadjo, Brian N. Stamos, C. Phillip Shelor, Jordan M. Berg, Benjamin C. Blount, and Purnendu K. Dasgupta “Evaluation of Amount of Blood in Dry Blood Spots. Ring-Disk Electrode Conductometry.” Anal. Chem., 2016

F.10 Supporting Information

As indicated in text. Figures S1-S6. This material is available free of charge via the Internet at http://pubs.acs.org.

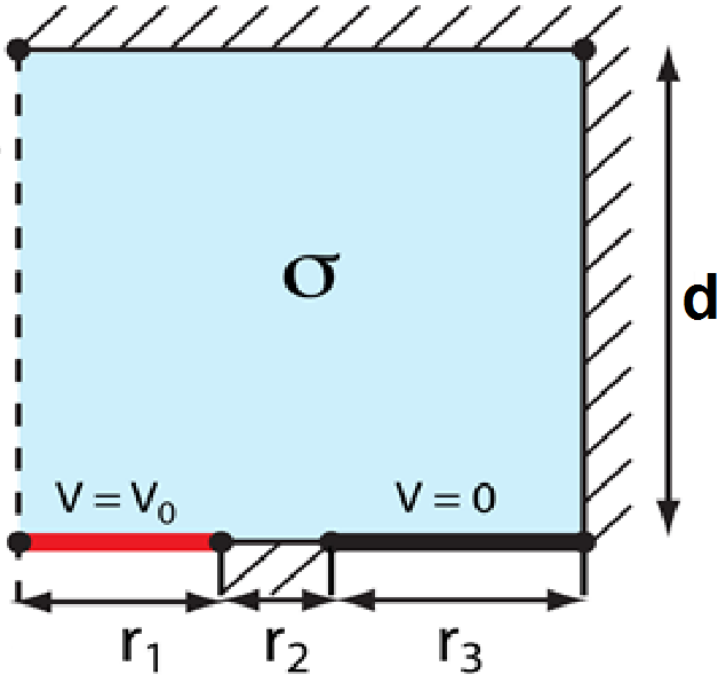

Figure F-1. Electrode configuration and model variables.
The bottom left corner is the center of the RDE; only one half of the RDE is shown. The behavior of the complete electrode assumes mirror symmetry. The diameter of the central electrode (red) is $2r_1$, the width of the gap between the two electrodes is r_2 and the width of the outer electrode is r_3. Atop (or below) the electrode is a homogeneous conducting medium of specific conductance σ that extends to a depth d.

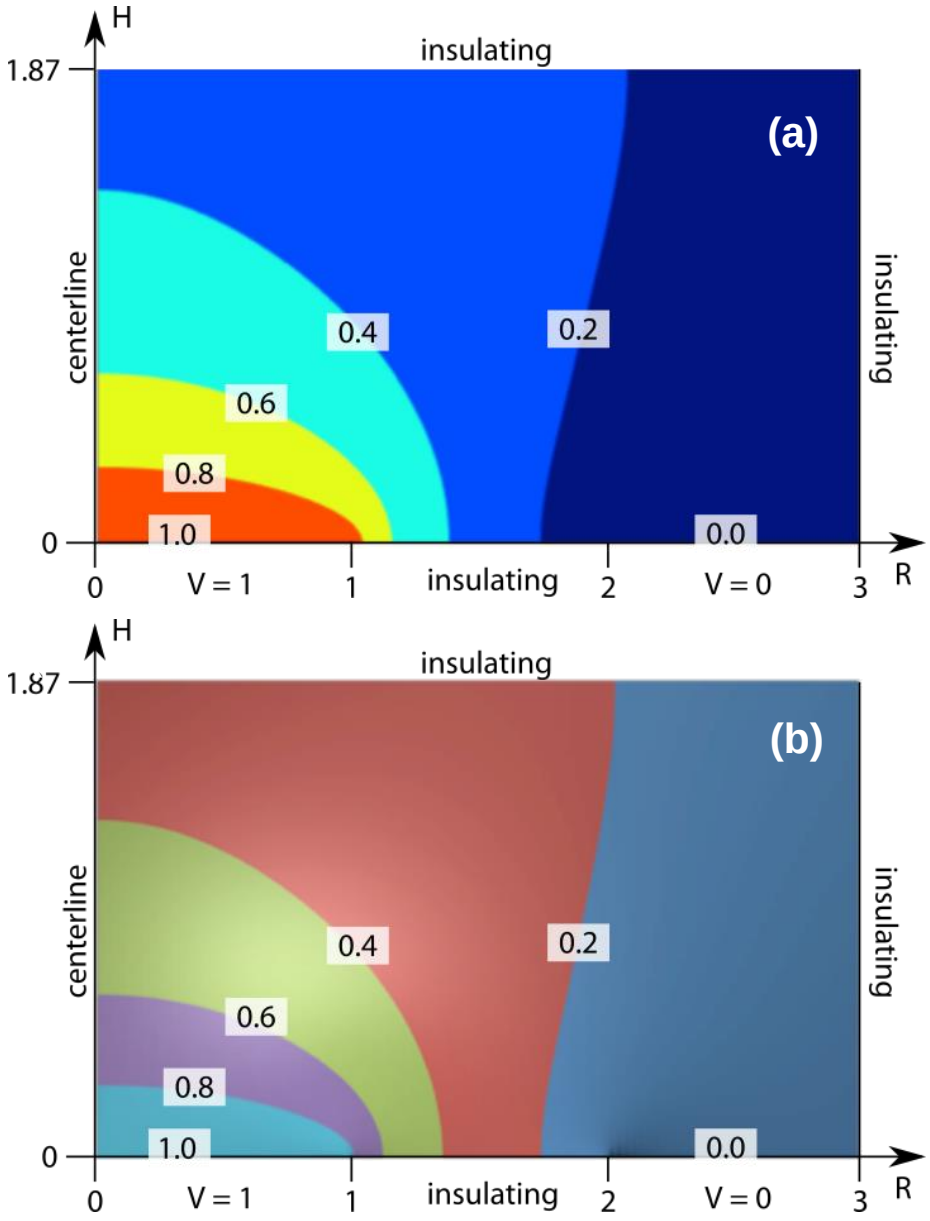

Figure F-2. Potential contour diagrams predicted by COMSOL vs. Excel calculations (solutions to eq 5)for an RDE where the central electrode radius equal the width of the insulator spacer, which in turn equals the width of the outer ring electrode ($r_1 = (r_2 - r_1) = (r_3 - r_2)$).The abscissa is this given in units of r_1. Quantitatively, the resulting values of *G* agreed to better than 5% accuracy.

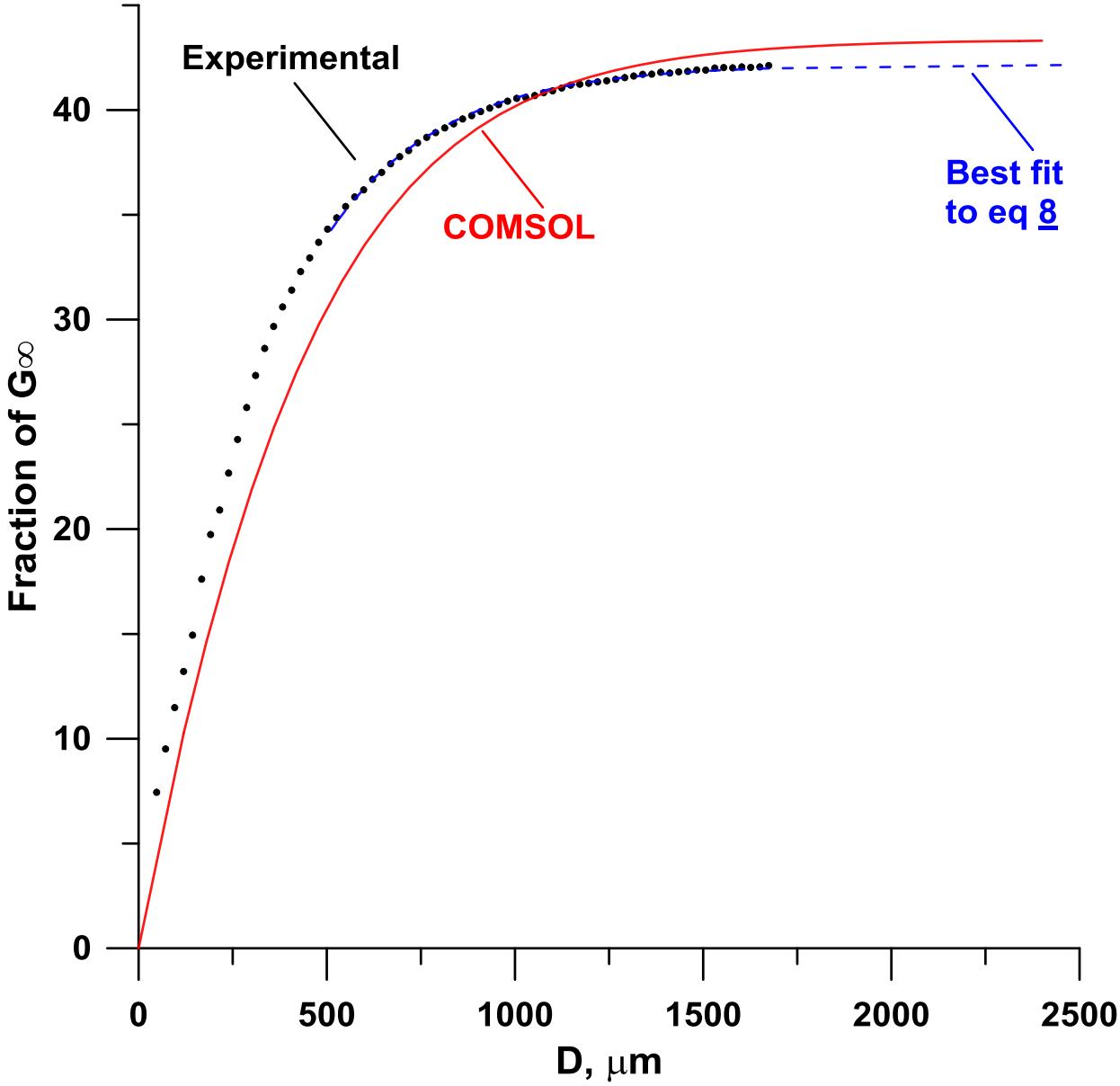

Figure F-3. Comparison of experimental and simulations results for macroprobe conductance versus sample depth for a 500 μM KCl solution.

The blue dashed line is the best fit to eq. 8.

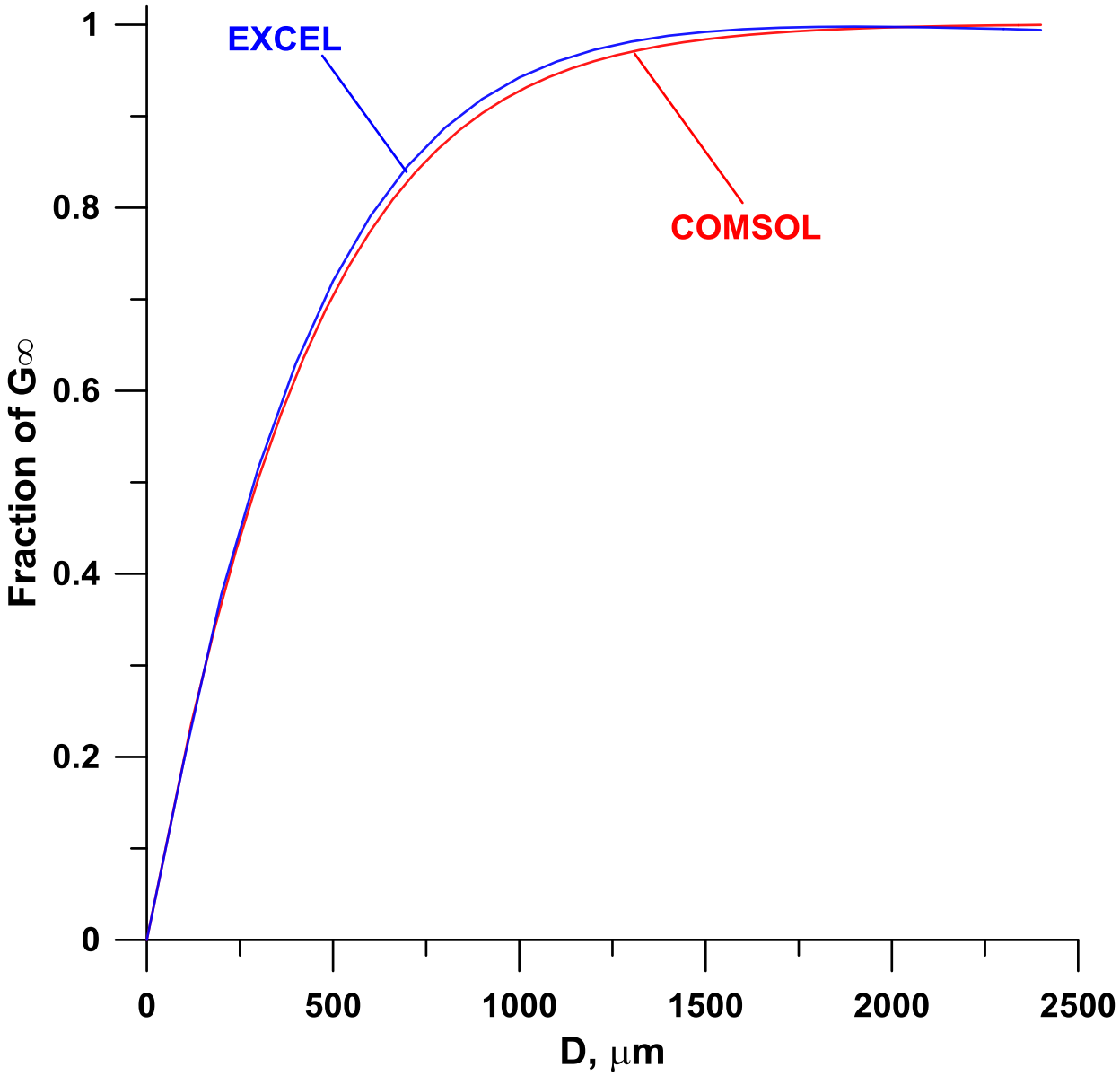

Figure F-4. Comparison of experimental and simulations results for the attainment of the plateau conductance versus sample depth computed for the macroprobe and a 500 μM KCl solution.

The predicted D_{99} values are respectively 1.50 and 1.65 mm for the Excel vs. the COMSOL solutions.

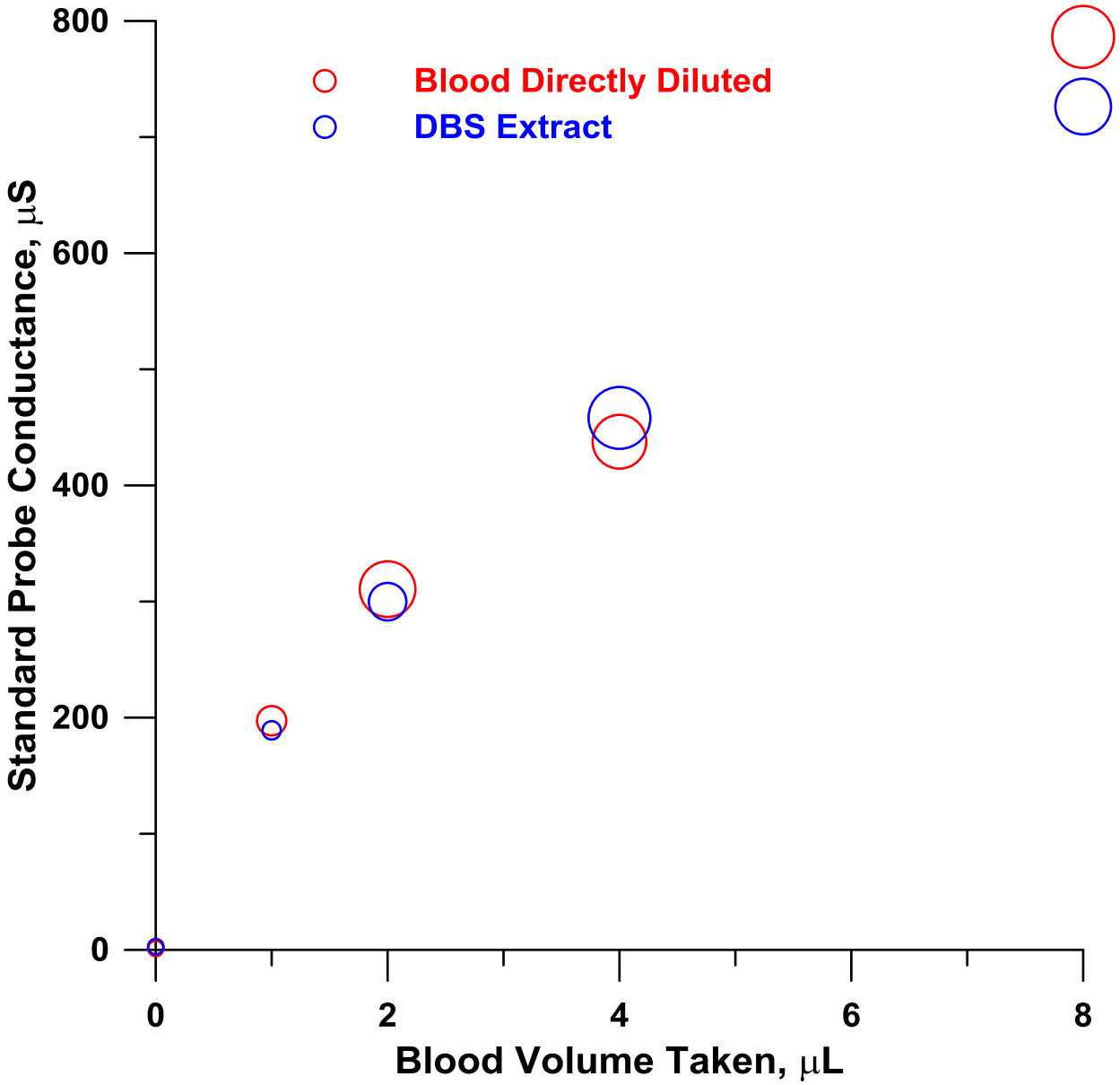

Figure F-5. Measured Conductance values for x = 0-8 μL blood samples diluted with (100- x) μL of water (red circles) or the same blood samples spotted on filter, dried, extracted with 100 μL water and conductance measured (blue circles).

Measurements were made with triplicate samples in each case and the diameter of each circle represents two standard deviations.

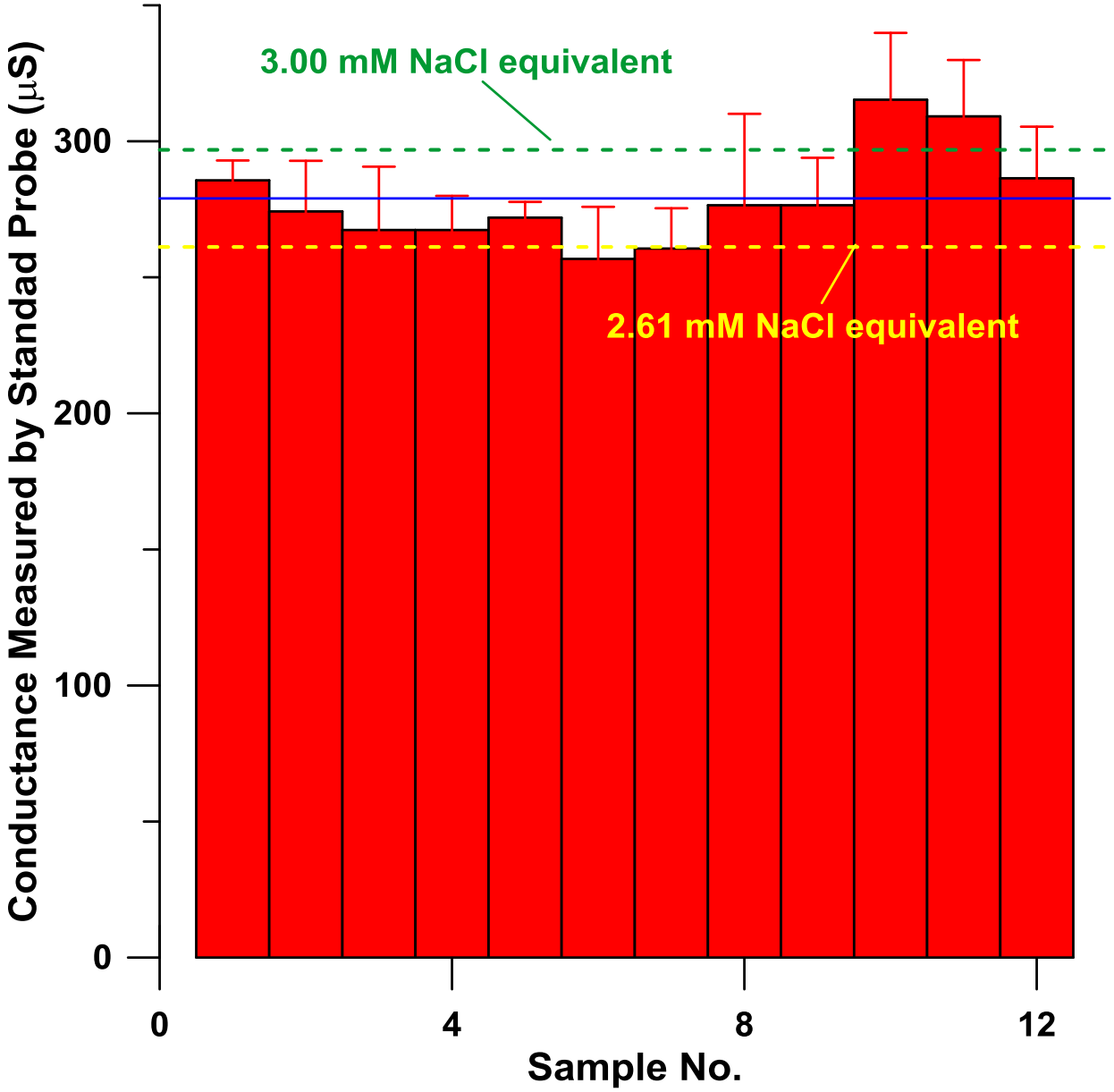

Figure F-6. Conductance measurements of 2 μL blood spot extracts (100 μL water) of 12 healthy individuals.

Error bars (1 standard deviation) for each individual (triplicate samples) are indicated.

The blue line is the sample set mean while the dashed lines depict +/- 1 standard deviation boundaries.

Supporting Information

Model

The steady-state current density ***j***, electric field ***E***, and the electric potential *V* are modeled using equations for charge conservation, $\nabla \boldsymbol{j} = 0$, Ohm's law, $\boldsymbol{j} = \sigma \boldsymbol{E}$, and the definition of electrical potential, $\boldsymbol{E} = -\nabla V$. Dirichlet boundary conditions holds on the inner electrode ($V = V_i$), as well as the outer electrode ($V = 0$). The Neumann boundary condition ($\nabla V * \boldsymbol{n} = 0$) holds on the remaining lines of symmetry and insulating surfaces, where ***n*** is the inward-pointing unit normal vector.

For reasons of numerical conditioning and compactness, these equations are written in terms of dimensionless variables $\bar{r} = r/r_0$, $\bar{z} = z/z_0$, $\bar{\sigma} = \sigma/\sigma_0$, and $\bar{V} = V/V_0$. The following nondimensional equations describe the sample:

$$\nabla \cdot \boldsymbol{j} = 0 \qquad \text{(S1a)}$$

$$\boldsymbol{j} = \sigma \boldsymbol{E} \qquad \text{(S1b)}$$

$$\boldsymbol{E} = -\nabla V \qquad \text{(S1c)}$$

where ∇ denotes the gradient with respect to the nondimensional coordinates. For spatially uniform $\bar{\sigma}$, eqs S1(a)-(c) yield Laplace's equation,

$$\nabla^2 V = 0 \qquad \text{(S2)}$$

Eq S2 is solved to give the nondimensional potential ∇ throughout the domain. Subsequently the nondimensional current density is computed from eq S1b.

It is convenient to choose V_0 to be the input voltage V_i and σ_0 to be the specific conductivity of the solution. Then the nondimensional input voltage and conductivity respectively satisfy $\bar{V}\imath = 1$ and $\bar{\sigma} = 1$. Choosing $r_0 = r_1$ gives $\bar{r}1 = 1$.

The nondimensional current $\bar{\jmath}$ is the integral of the axial component of the nondimensional current density $\bar{\jmath}$ over the inner electrode. With the choice of normalizations above,

$$\bar{\jmath} = 2\pi \int_0^1 \bar{\jmath} * \hat{z}\, \bar{r} d\bar{r} = -2\pi \int_0^1 \bar{\nabla}\bar{\mathrm{V}} * \hat{\mathrm{z}}\, \bar{\mathrm{r}} \mathrm{d}\bar{\mathrm{r}} \ldots \text{(S3)}$$

The dimensionless conductance is $G = j/V_i = j$, and the dimensionless cell constant is $\bar{K} = \frac{\bar{\sigma}}{\bar{G}} = 1/\bar{\jmath}$. Finally, the actual physical variables are recovered by

$$\boldsymbol{E} = (V_0/r_0)\bar{\boldsymbol{E}}, \ldots \text{(S4a)}$$

$$\boldsymbol{j} = (\sigma_0 V_0/r_0)\bar{\boldsymbol{\jmath}}, \ldots \text{(S4b)}$$

$$\boldsymbol{J} = \sigma_0 V_0 r_0 \bar{\boldsymbol{J}}, \ldots \text{(S4c)}$$

$$G = \sigma_0 r_0 \bar{G}, \ldots \text{(S4d)}$$

$$K = (1/r_0)\bar{K}. \ldots \text{(S4e)}$$

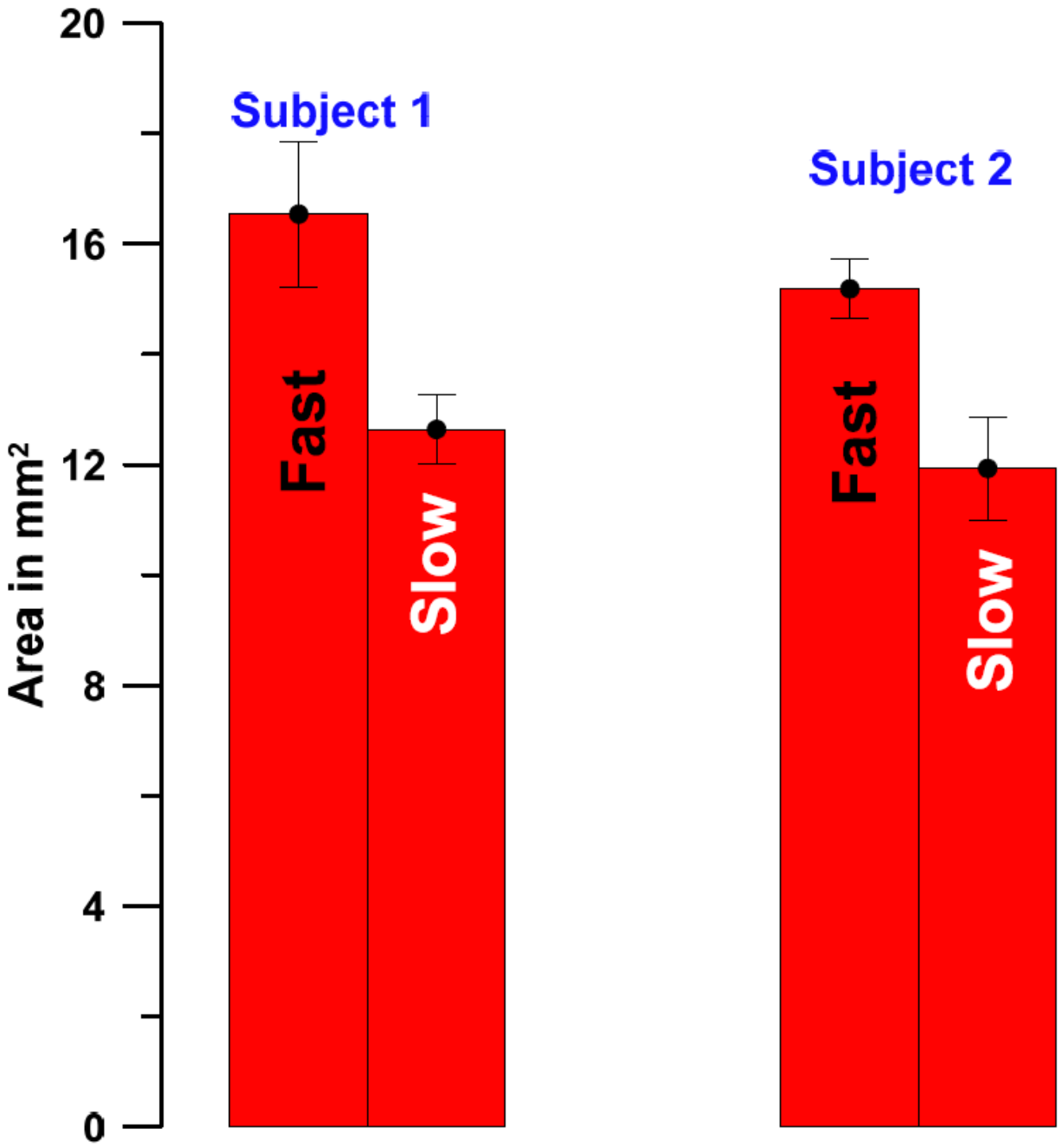

Figure F-S1. Area of a 3 µL blood spot dispensed at two different speeds within normal limits.
Spot area determined by ImageJ (https://imagej.nih.gov/ij/)

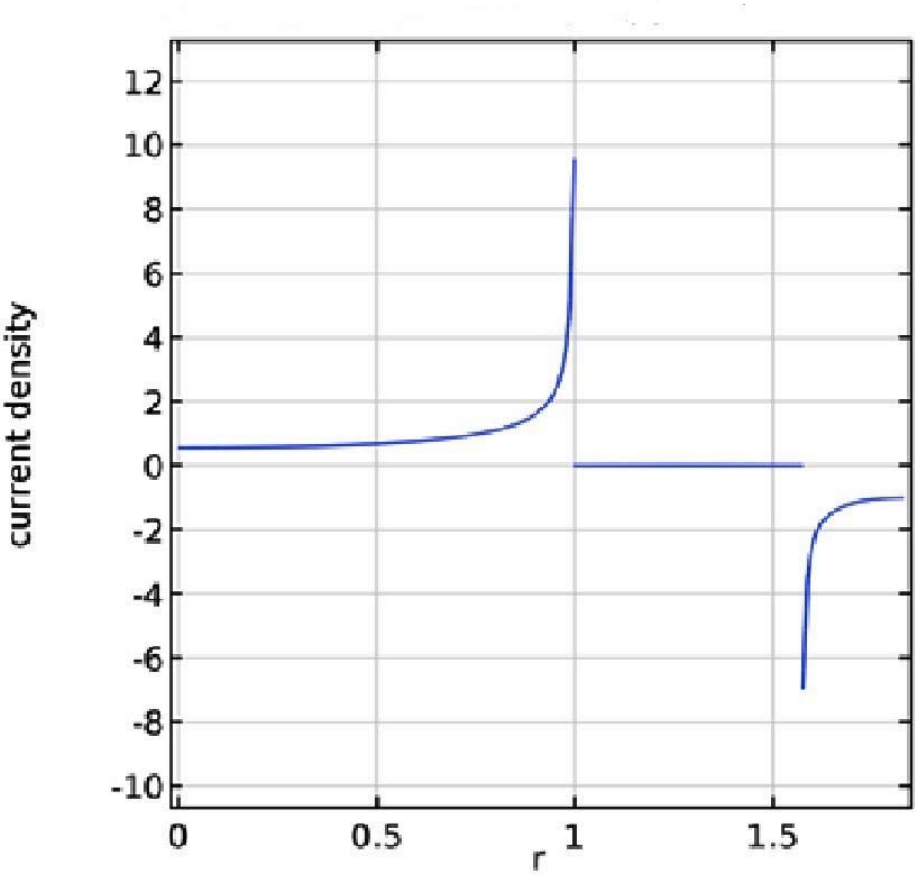

Figure F-S2. Normalized current density vs. the dimensionless radial position for probe C. See Figure 2 for the field distribution.

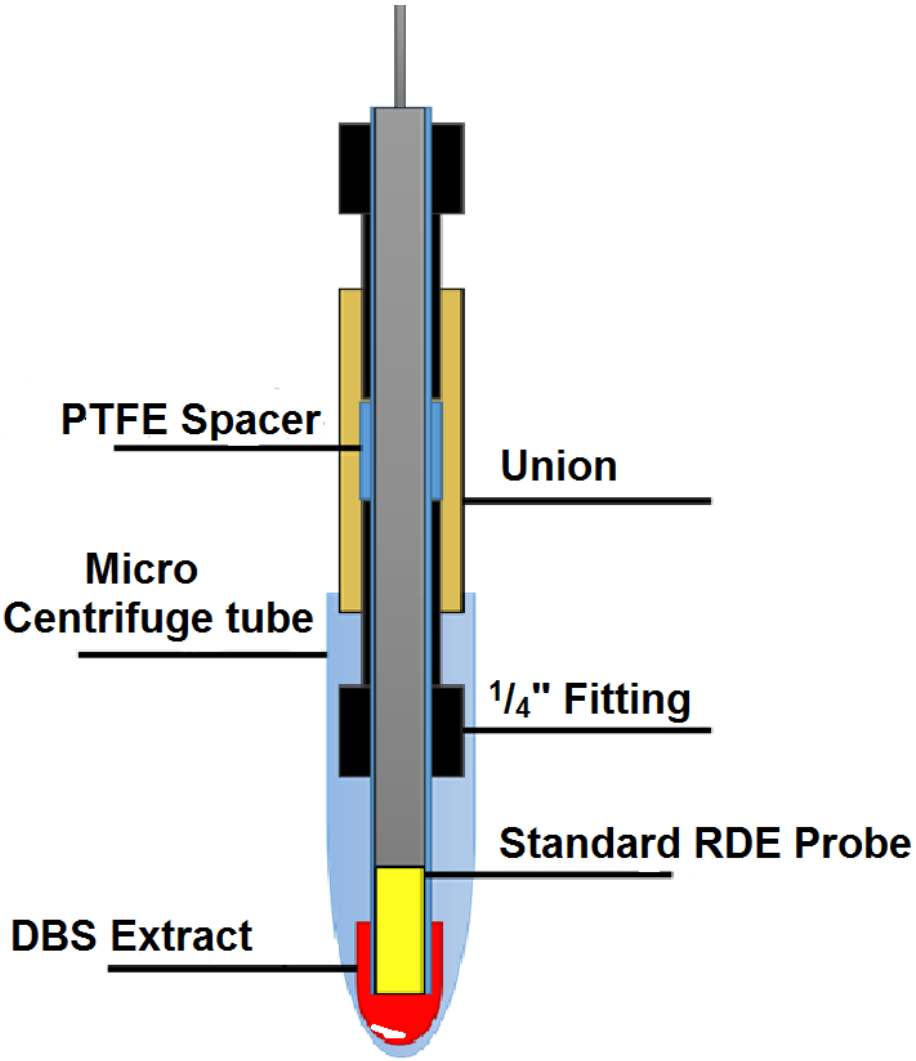

Figure F-S3. Construction of probe A to maintain constant blood immersion depth.

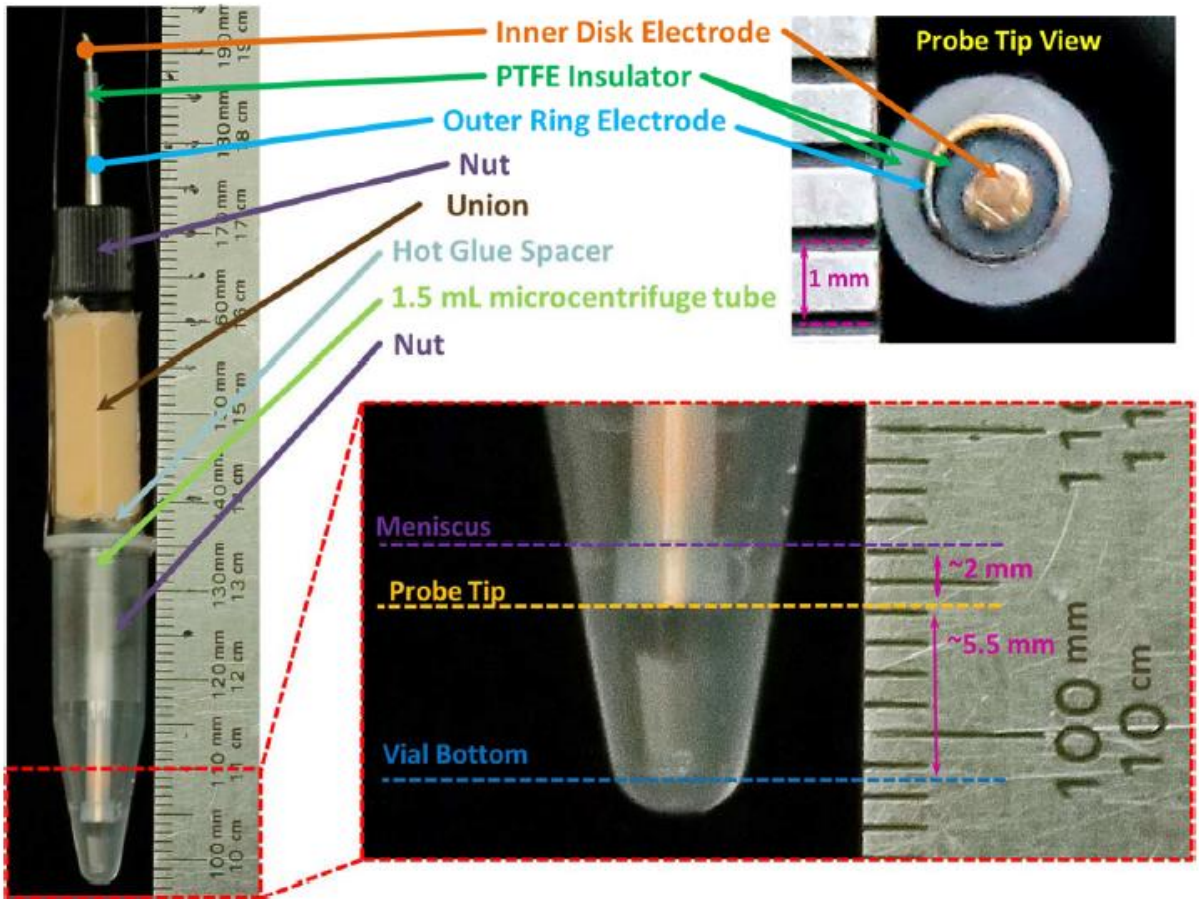

Figure F-S4. Photographs of the standard probe being dipped in 100 µL of water (left image).
A blown up image of the tip is shown in the lower right photo. The tip extends approximately 2 mm below the meniscus of the water. The tip lies about 5.5-6 mm above the microcentrifuge bottom. An end-on view is provided in the upper right corner where the disk and ring electrodes as well as PTFE insulators can be clearly seen.

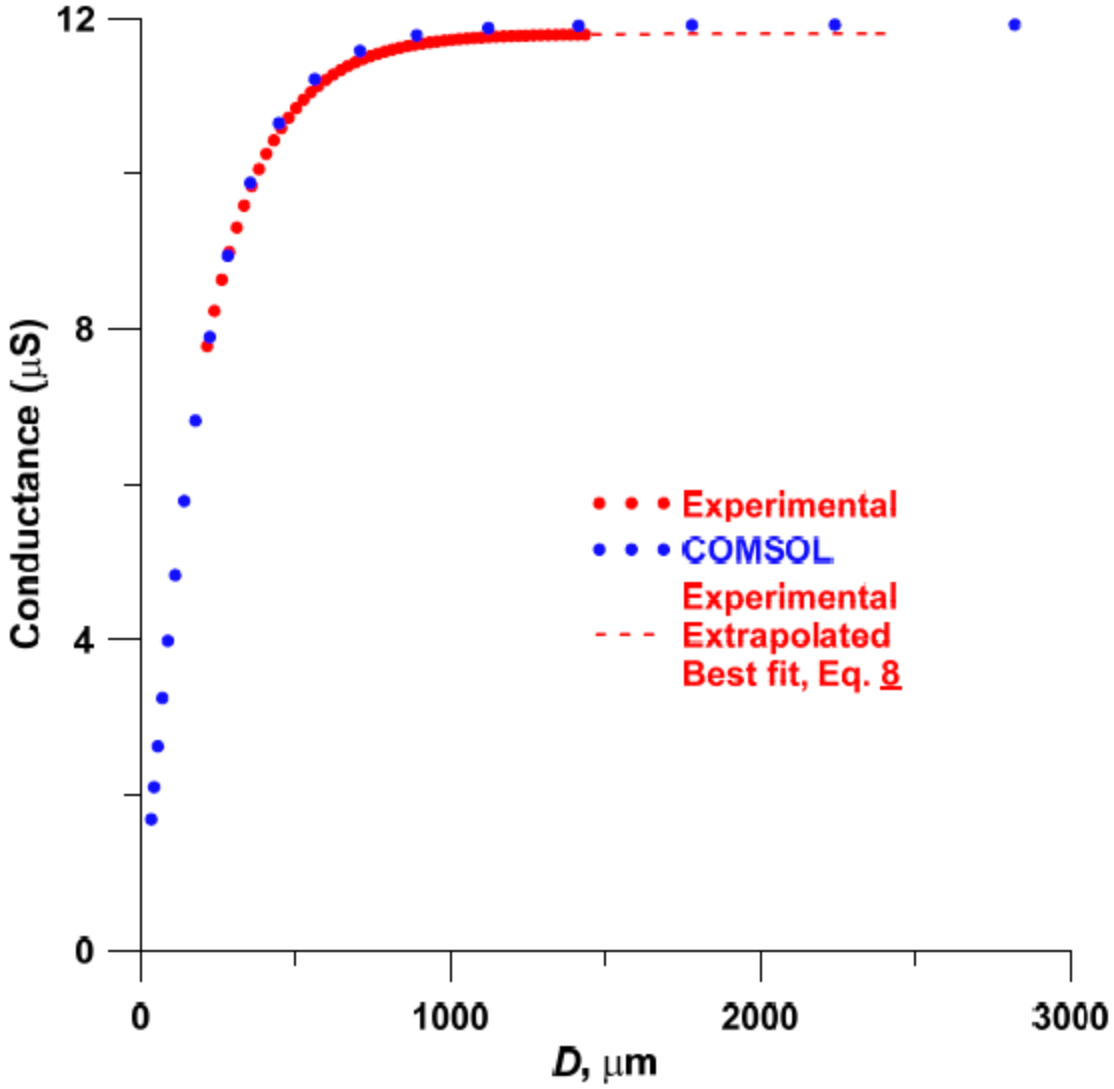

Figure F-S5. Comparison of experimental and simulation results for conductance measured by probe B versus sample depth.

$\log(r_2/r_1)$						D_{99}/r_1					
-1	0.5472	0.6277	0.7422	0.8826	1.0483	1.2644	1.4712	1.7062	1.8612	2.0434	2.0591
-0.8	0.6203	0.7043	0.8101	0.9657	1.1135	1.3188	1.5467	1.7963	2.0066	2.1444	2.1143
-0.6	0.7311	0.8074	0.9072	1.0391	1.2664	1.4108	1.6560	1.9090	2.1534	2.3096	2.3800
-0.4	0.8825	0.9479	1.0469	1.1667	1.3362	1.5344	1.7920	2.0744	2.3336	2.5317	2.6362
-0.2	1.0902	1.1506	1.2373	1.3619	1.5117	1.7293	1.9812	2.2842	2.5896	2.8233	2.9546
0	1.3763	1.4359	1.5118	1.6299	1.7873	1.9922	2.2581	2.5823	2.9112	3.2124	3.4030
0.2	1.7865	1.8395	1.9111	2.0254	2.1775	2.3695	2.6490	2.9733	3.3620	3.7208	3.9814
0.4	2.3668	2.4080	2.4910	2.6018	2.7416	2.9301	3.1965	3.5496	3.9665	4.4118	4.7711
0.6	3.1915	3.2584	3.3250	3.4185	3.5434	3.7229	3.9774	4.3581	4.7848	5.2784	5.7659
0.8	4.4194	4.4544	4.5366	4.6024	4.7351	4.9156	5.2391	5.5202	6.0062	6.6087	7.1572
1	6.1500	6.2340	6.3077	6.3892	6.4778	6.5542	6.8734	7.1429	7.5905	8.2788	8.8092
$\log(r_3/r_1)$	-1	-0.8	-0.6	-0.4	-0.2	0	0.2	0.4	0.6	0.8	1

Table F-S1. D_{99} as a function of r_2 and r_3.

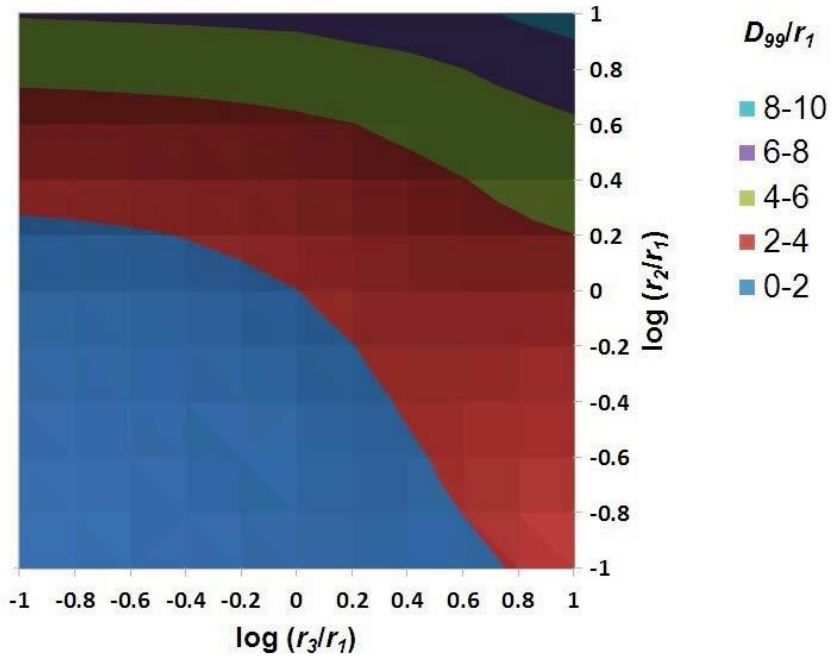

Figure C-S6a. Contour plot of D_{99} as a function of r_2 and r_3.

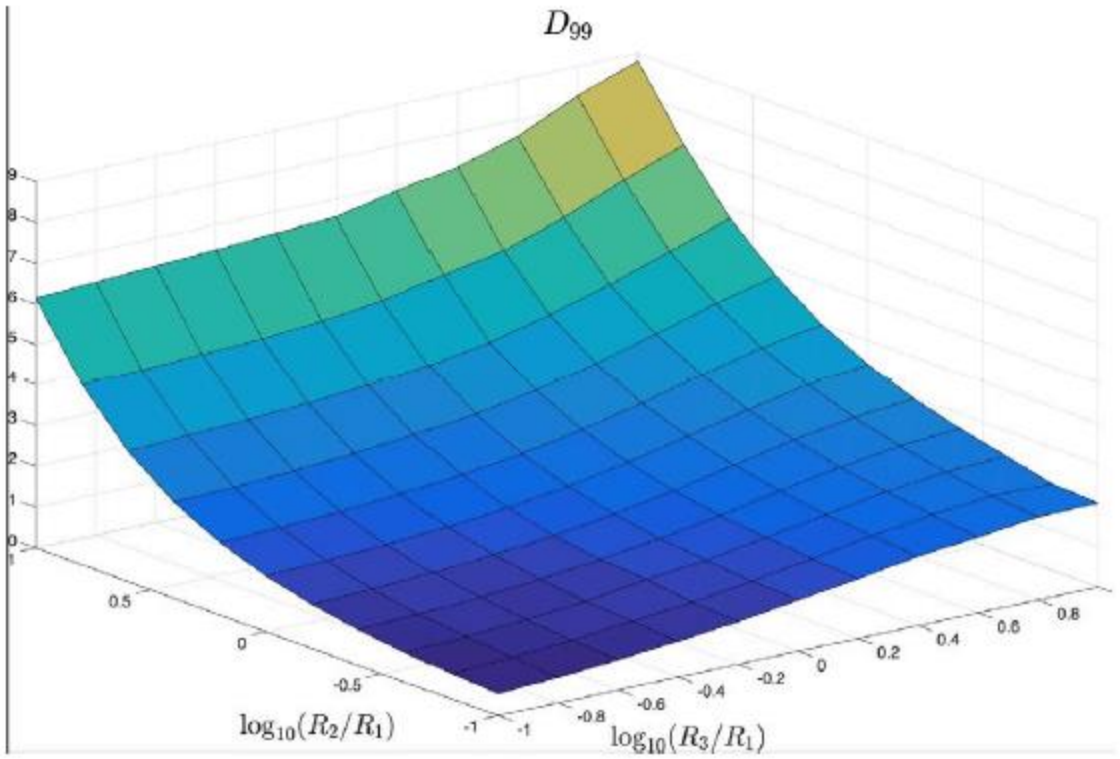

Figure F-S6b. Figure S6a. 3D plot of D_{99} as a function of r_2 and r_3

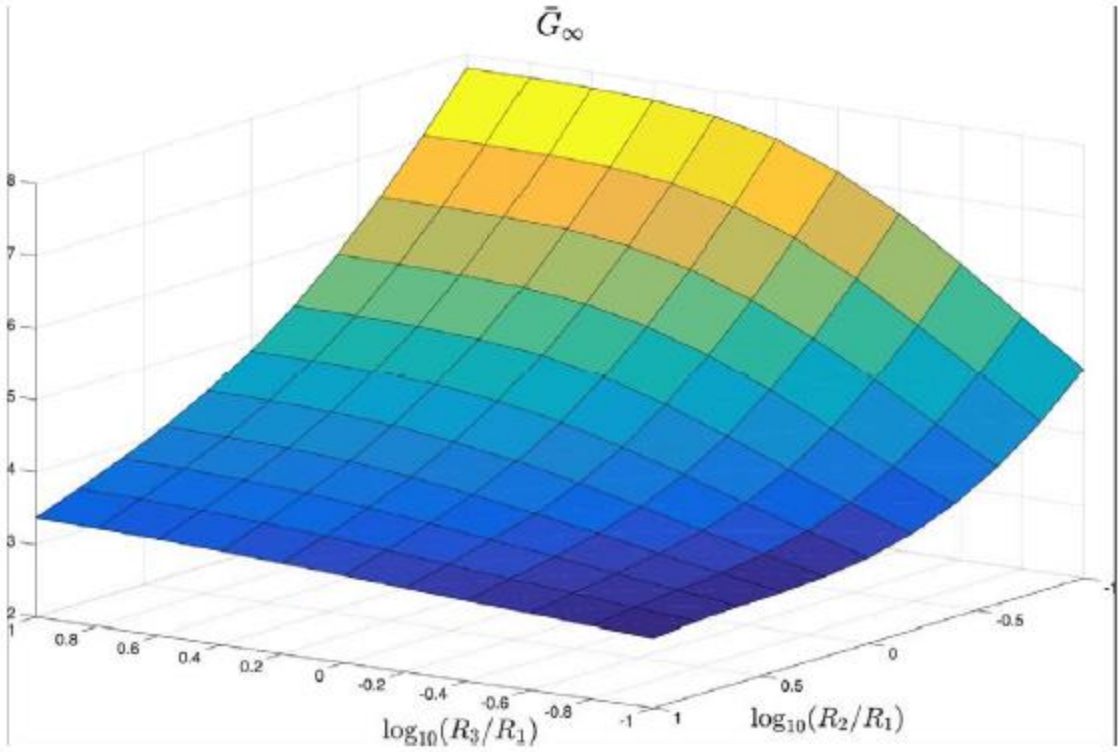

Figure F-S7a. G_∞ as a function of r_2 and r_3.

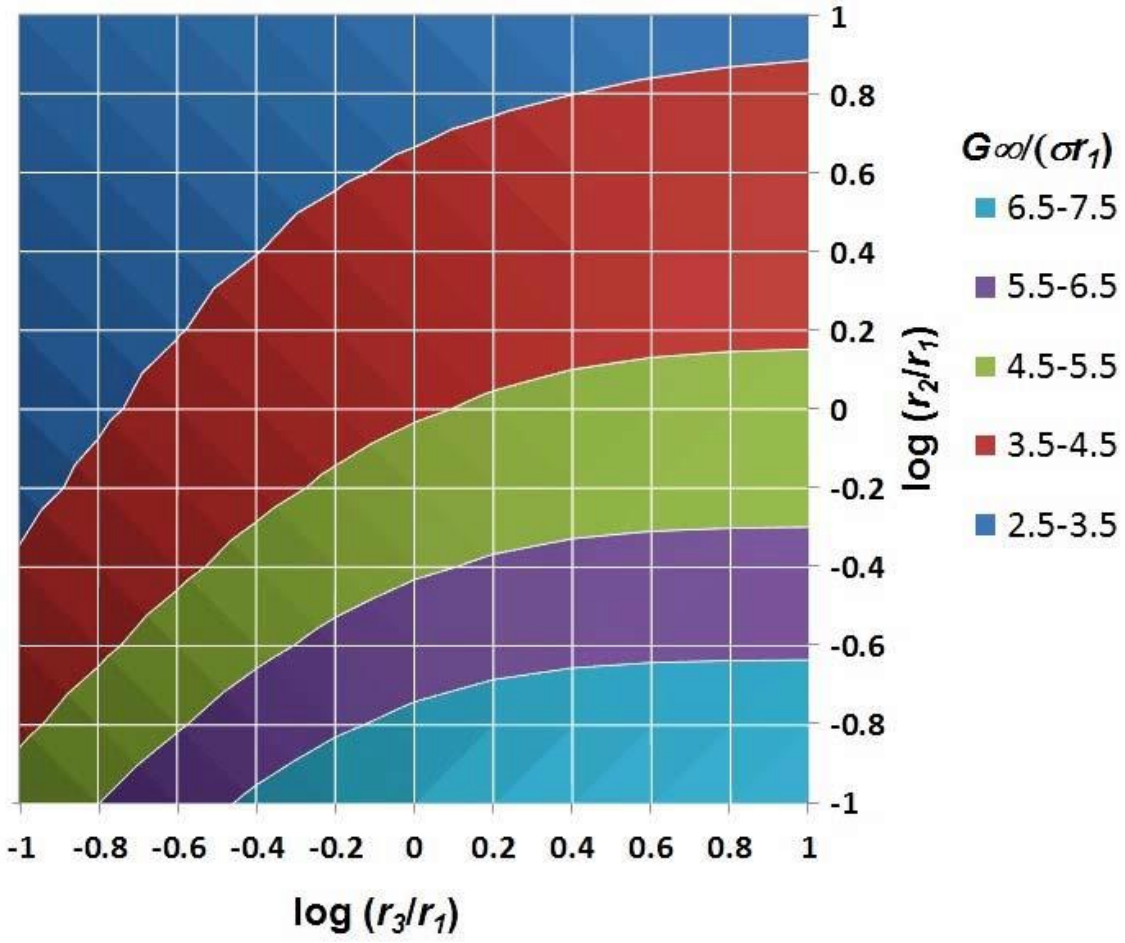

Figure F-S8. Contour plot of G_∞ as a function of r_2 and r_3.

$\log(r_2/r_1)$	$G_\infty/(\sigma r_1)$										
-1	4.8861	5.4946	6.1065	6.6677	7.1233	7.4519	7.6418	7.7405	7.7816	7.8021	7.8038
-0.8	4.3417	4.8821	5.4347	5.9597	6.3865	6.7013	6.8954	6.9960	7.0399	7.0565	7.0620
-0.6	3.9020	4.3641	4.8474	5.3128	5.7142	6.0153	6.2073	6.3100	6.3563	6.3743	6.3804
-0.4	3.5651	3.9489	4.3572	4.7606	5.1203	5.4014	5.5887	5.6936	5.7430	5.7627	5.7697
-0.2	3.3263	3.6361	3.9692	4.3054	4.6155	4.8689	5.0475	5.1537	5.2066	5.2290	5.2372
0	3.1748	3.4184	3.6806	3.9495	4.2050	4.4240	4.5882	4.6933	4.7499	4.7755	4.7855
0.2	3.0930	3.2788	3.4783	3.6844	3.8853	4.0652	4.2092	4.3091	4.3681	4.3975	4.4099
0.4	3.0557	3.1931	3.3394	3.4911	3.6417	3.7819	3.9010	3.9908	4.0495	4.0821	4.0974
0.6	3.0414	3.1384	3.2420	3.3492	3.4572	3.5604	3.6532	3.7287	3.7833	3.8173	3.8353
0.8	3.0147	3.0804	3.1504	3.2234	3.2974	3.3703	3.4380	3.4971	3.5436	3.5762	3.5957
1	2.9635	3.0077	3.0530	3.1003	3.1479	3.1955	3.2427	3.2853	3.3220	3.3500	3.3697
$\log(r_3/r_1)$	-1	-0.8	-0.6	-0.4	-0.2	0	0.2	0.4	0.6	0.8	1

Table F-S2. G_∞ as a function of r_2 and r_3.

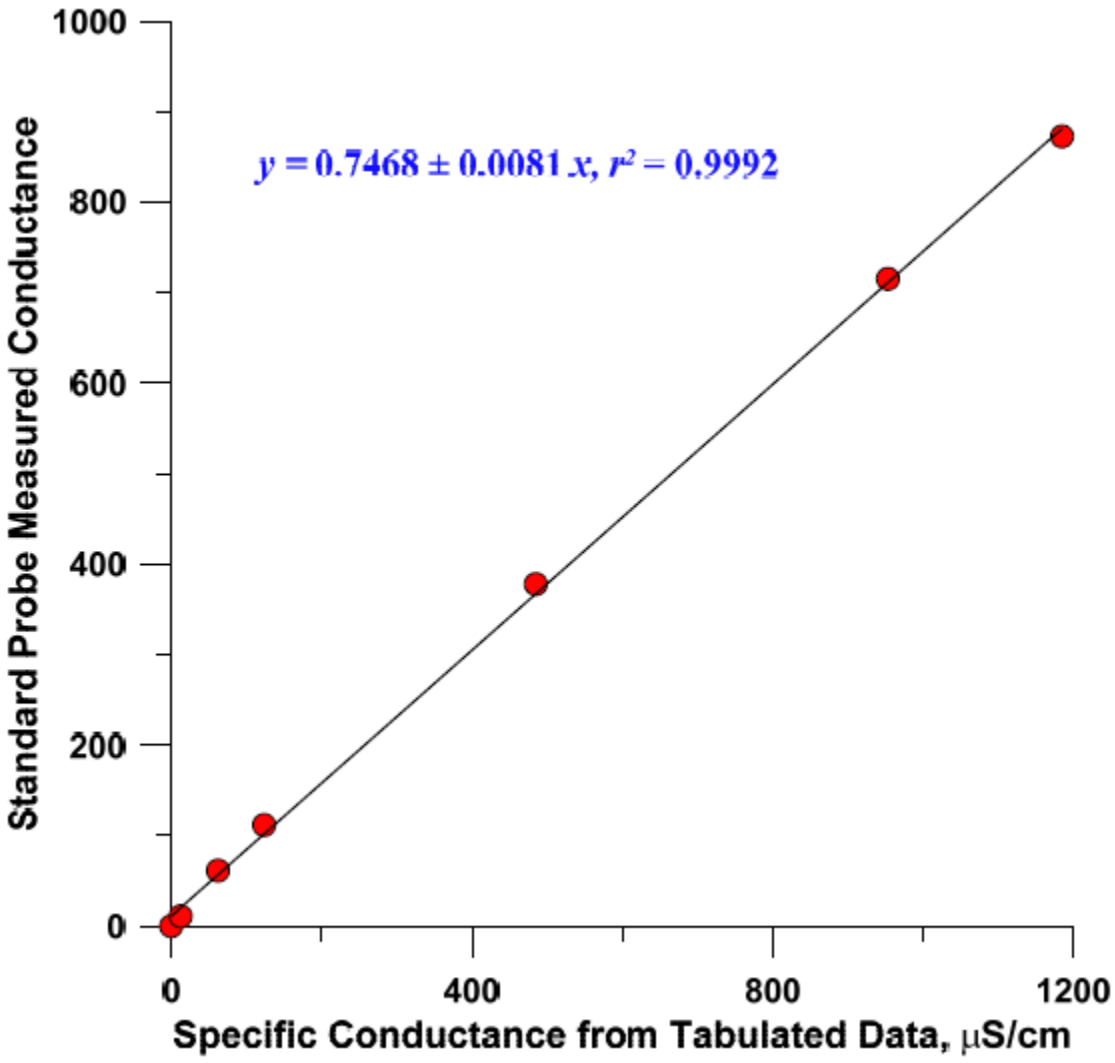

Figure F-S9. Probe A response to 0, 0.1, 0.5, 1.0, 4.0, 8.0 and 10.0 mM NaCl vs. tabulated data on specific conductance at these concentrations.
The values for 0.1, 4.0 and 8.0 mM NaCl were interpolated from extant data, see Figure S5.

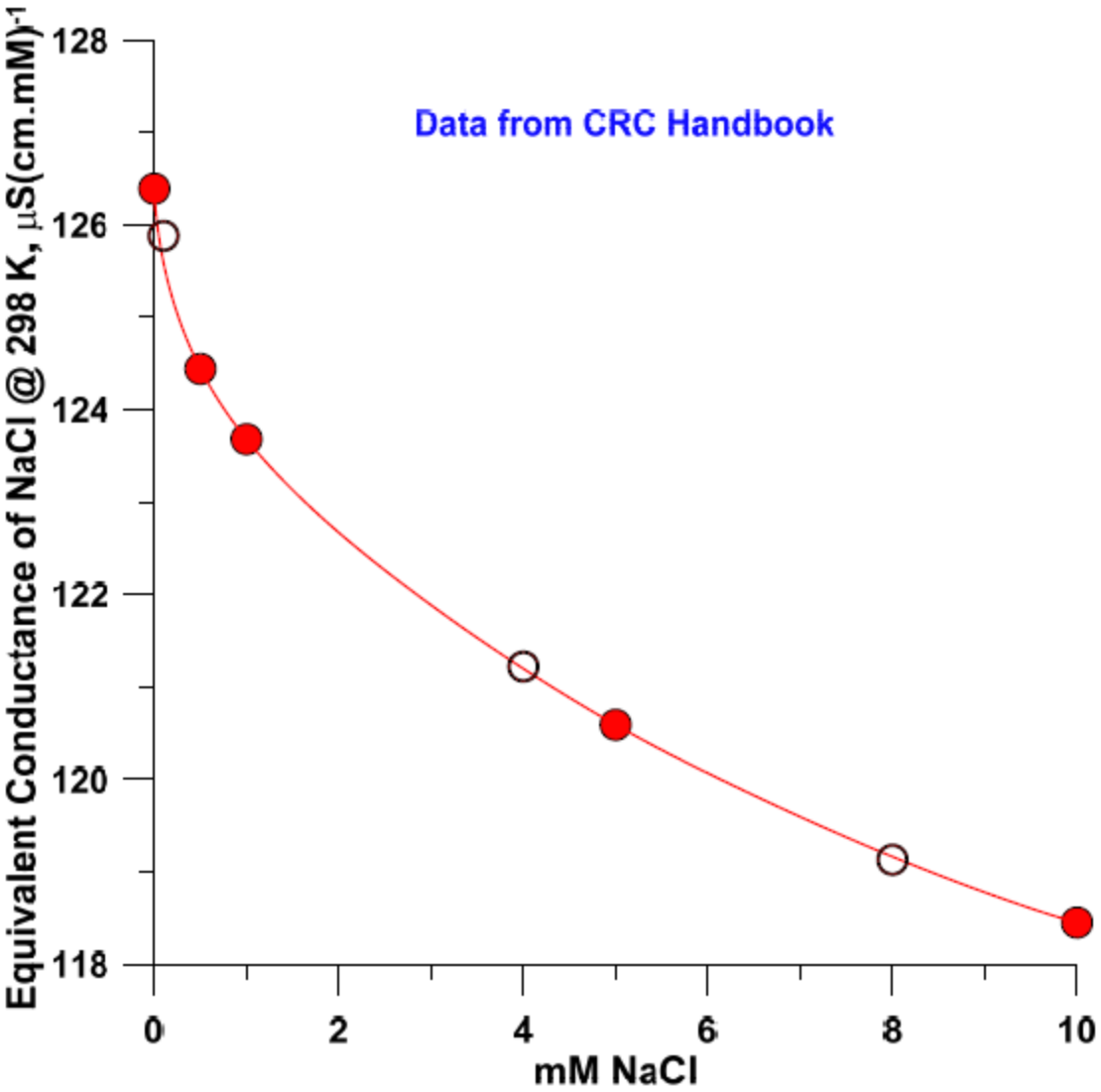

Figure F-S10. The solid circles are from tabulated data, the line drawn is a spline fit and the open circles are interpolated values at 0.1, 4.0 and 8.0 mM NaCl.
For a web-based source of the tabulated data, see

http://sites.chem.colostate.edu/diverdi/all_courses/CRC%20reference%20data/equivalent%20conductivity%20of%20electrolytes.pdf

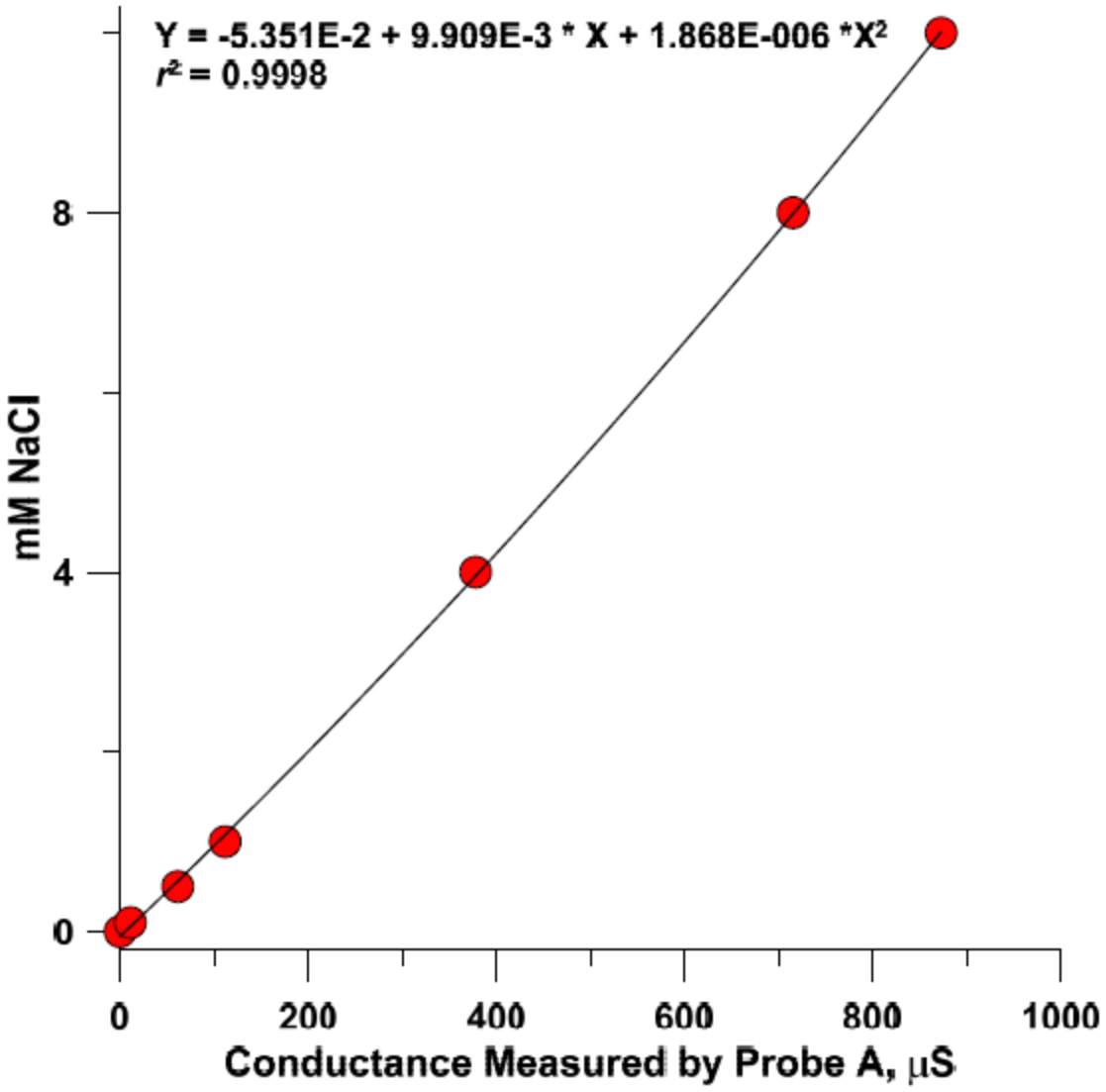

Figure F-S11. The best quadratic fit for the relationship between the conductance measured by probe A and the NaCl concentration.
Traditional x-y roles are reversed to permit facile calculation of the NaCl concentration.

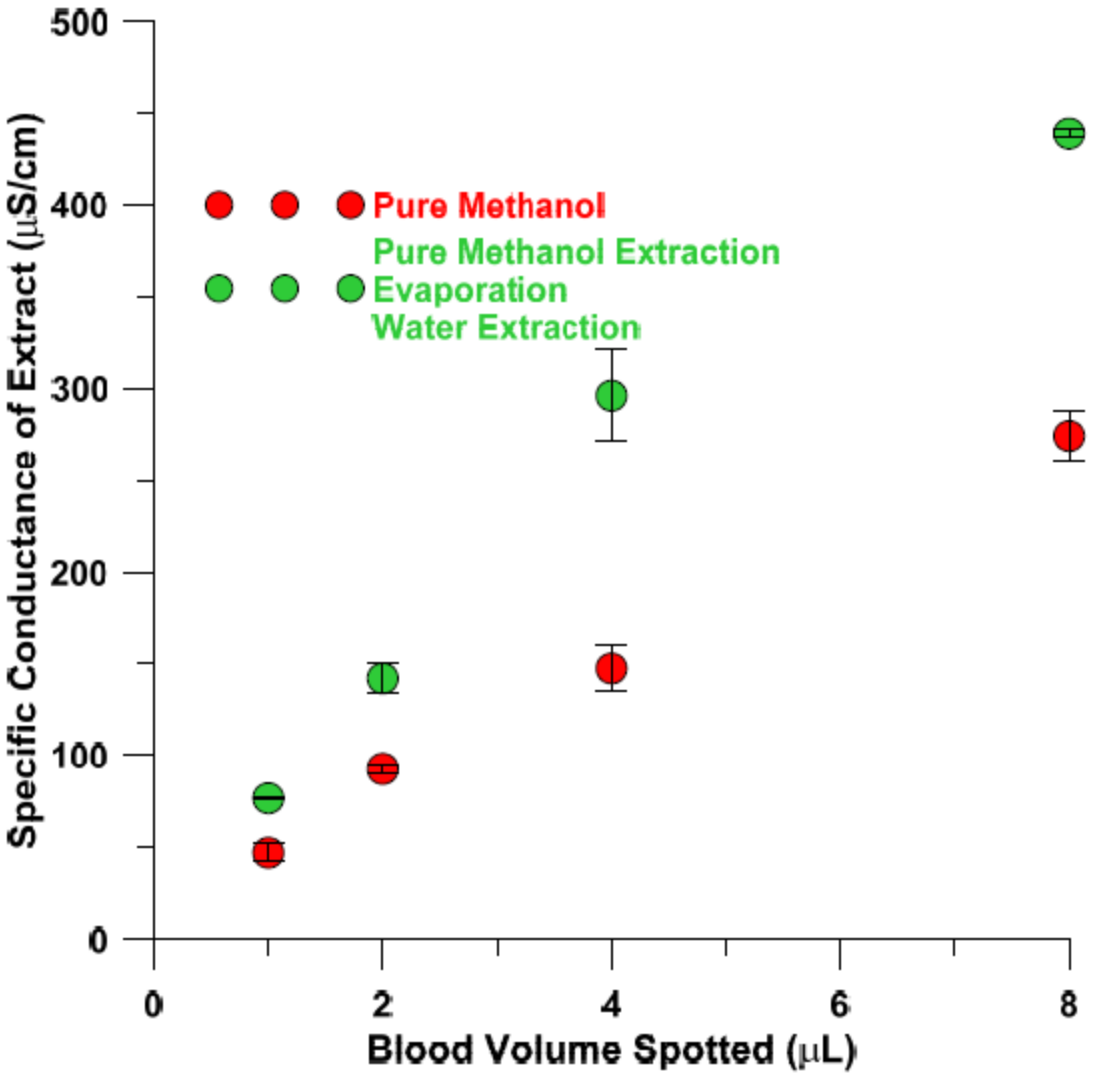

Figure F-S12. Specific conductance measured for different volumes of blood extracted on a 6.3 mm ϕ filter disk
into (a) 100 µL methanol: red symbols, and (b) the same extract as in a, then evaporated in a slow stream of N_2 and re-extracted in 100 µL water : green symbols (the latter procedure practiced in ref. 6).

References

[1] Small, H; Stevens, T; Bauman, W. C., Novel Ion Exchange Chromatographic Method Using Conductimetric Detection. Journal of Analytical Chemistry 1975, 47, 1801-1809.

[2] Small, H., Ion Chromatography: An Account of Its Conception and Early Development. Journal of Chemical Education 2004, 81 (9), 1277-1284.

[3] Huang, X., Improved end-column conductivity detector for capillary zone electrophoresis. Journal of Analytical Chemistry 1991, 63 (19), 2193-2196

[4] Kar, S.; Dasgupta, P. K.; Liu, H.; Hwang, H., Computer-Interfaced Bipolar Pulse Conductivity Detector for Capillary Systems. Journal of Analytical Chemistry 1994, 66, 2537- 2543.

[5] Avdalovic, N.; Pohl, C. A.; Rocklin, R. D.; Stillian, J. R., Determination of Cations and Anions by Capillary Electrophoresis Combined with Suppressed Conductivity Detection. Journal of Analytical Chemistry 1993, 65, 1470-1475.

[6] Pungor, E.; Townshend, A., Oscillometry and Conductometry, Pergamon Press, Oxford, 1965.

[7] Zemann, A. J.; Schnell, E.; Volgger, D.; Bonn, G. K., Contactless Conductivity Detection for Capillary Electrophoresis. Journal of Analytical Chemistry 1998, 70, 563-567.

[8] Fracassi da Silva, J. A.; do Lago, C. L., An Oscillometric Detector for Capillary Electrophoresis. Journal of Analytical Chemistry 1998, 70, 4339-4343.

[9] Kuban, P.; Muri, M. A.; Hauser, P. C., Application of a Contactless Conductivity Detector to the Determination of Inorganic ions in Ion Chromatography. The Analyst 2004, 129, 1-10.

[10] Kuban, P.; Hauser, P. C., A Review of the Recent Achievements in Capacitively Coupled Contactless Conductivity Detection. Analytical Chimica Acta 2008, 607, 15-29.

[11] Kuban, P.; Hauser, P. C., Fundamental aspects of contactless conductivity detection for capillary electrophoresis. Part I: Frequency behavior and cell geometry. Electrophoresis 2004, 25 (20), 3387-3397.

[12] Kuban, P.; Hauser, P. C., Fundamental aspects of contactless conductivity detection for capillary electrophoresis. Part II: Signal-to-noise ratio and stray capacitance. Electrophoresis 2004, 25 (20), 3398-3405.

[13] E. H. Sargent & Co.Sargent Model V Chemical Oscillometer Anal. Chem. **1952**, 24, 19A

[14] Pungor, E. Oscillometry and Conductometry; Pergamon Press: London, **1965**

[15] Gaš, B.; Demjaněnko, M.; Vacik, J. J. Chromatogr. A **1980**, 192, 253– 257

[16] Vacík, J.; Zuska, J.; Muselasová, I. J. Chromatogr. A **1985**, 320, 233– 240

[17] Pungor, E.; Pál, F.; Tóth, K. Anal. Chem. **1983**, 55, 1728– 1731

[18] Zemann, A. J.; Schnell, E.; Volgger, D.; Bonn, G. K. Anal. Chem. **1998**, 70, 563– 567

[19] Fracassi da Silva, J. A.; do Lago, C. L. Anal. Chem. **1998**, 70, 4339– 4343

[20] Mayrhofer, K.; Zemann, A. J.; Schnell, E.; Bonn, G. K. Anal. Chem. **1999**, 71, 3828– 3833

[21] Tůma, P.; Opekar, F.; Jelínek, I. Electroanalysis **2001**, 13, 989– 992

[22] Tanyanyiwa, J.; Galliker, B.; Schwarz, M. A.; Hauser, P. C. Analyst **2002**, 127, 214– 218

[23] Baltussen, E.; Guijt, R. M.; van der Steen, G.; Laugere, F.; Baltussen, S.; Van Dedem, G. W. Electrophoresis **2002**, 23, 2888– 2893

[24] Gaš, B.; Zuska, J.; Coufal, P.; van de Goor, T. Electrophoresis **2002**, 23, 3520– 3527

[25] Macka, M.; Hutchinson, J.; Zemann, A.; Shusheng, Z.; Haddad, P. R. Electrophoresis **2003**, 24, 2144– 2149

[26] Coltro, W. K. T.; Lima, R. S.; Segato, T. P.; Carrilho, E.; de Jesus, D. P.; do Lago, C. L.; da Silva, J. A. F. Anal. Methods **2012**, 4, 25– 33

[27] Elbashir, A. A.; Aboul-Enein, H. Y. Biomed. Chromatogr. **2012**, 26, 990– 1000

[28] Elbashir, A. A.; Aboul-Enein, H. Y. Biomed. Chromatogr. **2014**, 28, DOI: , DOI: 10.1002/bmc.3230

[29] Kubáň, P.; Hauser, P. C. Anal. Chim. Acta **2008**, 607, 15– 29

[30] Kubáň, P.; Hauser, P. C. Electrophoresis **2009**, 30, 176– 188

[31] Kubáň, P.; Hauser, P. C. Electrophoresis **2011**, 32, 30– 42

[32] Kubáň, P.; Hauser, P. C. Electrophoresis **2013**, 34, 55– 69

[33] Tůma, P.; Opekar, F.; Štulík, K. Electrophoresis **2002**, 23, 3718– 3724

[34] Tůma, P.; Samcová, E.; Štulík, K. Electroanalysis **2009**, 21, 590– 594

[35] Kubáň, P.; Hauser, P. C. Electrophoresis **2004**, 25, 3387– 3397

[36] Kubáň, P.; Hauser, P. C. Electrophoresis **2004**, 25, 3398– 3405

[37] Brito-Neto, J. G. A.; da Silva, J. A. F.; Blanes, L.; do Lago, C. L. Electroanalysis **2005**, 17, 1198– 1206

[38] Brito-Neto, J. G. A.; da Silva, J. A. F.; Blanes, L.; do Lago, C. L. Electroanalysis **2005**, 17, 1207– 1214

[39] Johnston, S. E.; Fadgen, K. E.; Tolley, L. T.; Jorgenson, J. W. J. Chromatogr. A **2005**, 1094, 148– 157

[40] Tůma, P.; Opekar, F.; Samcová, E.; Štulík, K. Electroanalysis **2008**, 20, 477– 484

[41] Kang, Q.; Zhang, Q.; Li, Y. L.; Li, D. D.; Shen, D. Z. Chin. Chem. Lett. **2012**, 23, 831–834

[42] Opekar, F.; Tůma, P.; Štulík, K. Sensors **2013**, 13, 2786– 2801

[43] Pencharee, S.; Faber, P. A.; Ellis, P. S.; Cook, P.; Intaraprasert, J.; Grudpan, K.; McKelvie, I. D. Anal. Methods **2012**, 4, 1278– 1283

[44] Kubáň, P.; Dasgupta, P. K.; Pohl, C. A. Anal. Chem. **2007**, 79, 5462– 5467

[45] Huang, X.; Dasgupta, P. K. Anal. Chim. Acta **2011**, 689, 155– 159

[46] Huang, X.; Foss, F. W., Jr.; Dasgupta, P. K. Anal. Chim. Acta **2011**, 707, 210– 217

[47] Zhang, M.; Yang, B. C.; Dasgupta, P. K. Anal. Chem. **2013**, 85, 7994– 8000

[48] Dasgupta, P. K.; Bao, L. Anal. Chem. **1993**, 65, 1003– 1011

[49] Tůma, P.; Samcová, E.; Štulík, K. Electroanalysis **2011**, 23, 1870– 1874

[50] Zhang, Z.; Li, Y.; Xu, Z.; Zhu, X.; Kang, Q.; Shen, D. Int. J. Electrochem. Sci. **2013**, 8, 3357– 3370

[51] Opekar, F.; Tůma, P.; Štulík, K. Sensors **2013**, 13, 2786– 2801

[52] Nürtemann, K.; Hilland, J.; Kaatze, U. J. Phys. Chem. A **1997**, 101, 6864– 6869

[53] Zhang, M.; Stamos, B. N.; Dasgupta, P. K. Anal. Chem., in press (DOI: , DOI: 10.1021/ac503247g)

[54] Bard, A. J.; Faulkner, L. R. Electrochemical Methods: Fundamentals and Applications, 2nd Edition; Wiley: New York, **2001**

[55] Tan, F.; Yang, B.; Guan, Y. Anal. Sci. **2005**, 21, 583– 585

[56] Stranahan, J. D. Phys. Rev. **1935**, 48, 538– 544

[57] Guijt, R. M.; Evenhuis, C. J.; Macka, M.; Haddad, P. R. Electrophoresis **2004**, 25, 4032–4057

[58] Kubáň, P.; Müri, M. A.; Hauser, P. C. Analyst **2004**, 129, 82– 86

[59] Shen, D.; Li, Y.; Zhang, Z.; Zhang, P.; Kang, Q. Talanta **2013**, 104, 39– 43

[60] Francisco, K. J. M.; do Lago, C. L. Electrophoresis **2009**, 30, 3458– 3464

[61] Daniel, V. V. Dielectric Relaxation; Academic Press: London, **1967**; Chapters 1 and 2, pp 1– 31

[62] Chen, Y.; Or, D. Water Resour. Res. **2006**, 42, Article No. W06424

[63] Drevinskas, T.; Kaljurand, M.; Marůska, A. Electrophoresis **2014**, 35, 2401– 2407

[64] Analog Devices. 24-Bit Capacitance-to-Digital Converter with Temperature Sensor. Datasheet AD 7745/7746, Figure 14, p 9

[65] Janasek, D.; Franzke, J.; Manz, A. *Nature* **2006**, *442*, 374-380.

[66] Lauer, H.; Rozing, G. P. *High Performance Capillary Electrophoresis*. Agilent Technologies, Germany: **2010**.

[67] Jorgenson, J. W.; Lukacs, K. D. *Anal. Chem.* **1981**, *53*, 1298-1302.

[68] Kennedy, R. T.; Jorgenson, J. W. *Anal. Chem.* **1989**, *61*, 1128-1135.

[69] Knox, J. H.; Gilbert, M. T. *J. Chromatogr. A* **1979**, *186*, 405-418.

[70] Zhang, M.; Yang, B.; Dasgupta, P. K. *Anal. Chem.* **2013**, *85*, 7994-8000.

[71] Zhang, M.; Yang, B.; Kanyanee, T.; Dasgupta, P. K. *Anal. Chem.* (following paper in this issue).

[72] Wang, X.; Cheng, C.; Wang, S.; Zhao, M.; Dasgupta, P. K.; Liu, S. *Anal. Chem.* **2009**, *81*, 7428-7435.

[73] Wang, X.; Veerappan, V.; Cheng, C.; Jiang, X.; Allen, R. D.; Dasgupta, P. K.; Liu, S. *J.*

Am. Chem. Soc. **2010,** *132,* 40-41.

[74]Manz A.; Simon W. *J. Chromatogr. Sci.* **1983,** *21,* 326-330.

[75] Knecht, L. A.; Guthrie, E. J.; Jorgenson, J. W. *Anal. Chem.* **1984,** *56,* 479-482.

[76] Manz, A.; Simon, W. *Anal. Chem.* **1987,** *59,* 74-79.

[77] Fracassi da Silva, J. A.; do Lago, C. L. *Anal. Chem.* **1998**, *70*, 4339-4343.

[78] Zemann, A. J.; Schnell, E.; Volgger, D.; Bonn, G. K. *Anal. Chem.* **1998**, *70*, 563-567.

[79] Tanyanyiwa, J.; Hauser, P. C. *Anal. Chem.* **2002**, *74*, 6378-6382.

[80] Tanyanyiwa, J.; Galliker, B.; Schwarz, M. A.; Hauser, P. C. *Analyst* **2002**, *127*, 214-218.

[81] Kubáň, P.; Hauser, P. C. *Anal. Chim. Acta* **2008**, *607*, 15-29.

[82] Kubáň, P.; Hauser, P. C. *Electrophoresis* **2013**, *34*, 55-69.

[83] Huang, X.; Dasgupta, P. K. *Anal. Chim. Acta* **2011**, *689*, 155-159.

[84] Huang, X.; Foss Jr, F. W., Dasgupta, P. K. *Anal. Chim. Acta* **2011**, *707*, 210-217.

[85] Dasgupta, P. K.; Bao, L. *Anal. Chem.* **1993**, *65*, 1003-1011.

[86] Wouters, S.; Wouters, B.; Jespers, S.; Desmet, G.; Eghbali, H.; Ruggink, C.; Eeltink, S. *J. Chromatogr. A* **2014,** *1355*, 253–260.

[87] Zhang, M.; Stamos, B. N.; Amornthammarong, N.; Dasgupta, P. K. *Anal. Chem.*

[88] Gaš, B.; Zuska, J.; Coufal, P.; van de Goor, T. *Electrophoresis* **2002,** *23*, 3520-3527.

[89] Mai, T. D.; Pham, T. T. T.; Pham, H. V.; Sáiz, J.; Ruiz, C. G.; Hauser, P. C. *Anal. Chem.* **2013,** *85*, 2333-2339.

[90] Ding, W.; Thornton, M. J.; Fritz, J. S. *Electrophoresis* **1998,** *19*, 2133-2139.

[91] Hu, W.; Haddad, P. R. *Trends Anal. Chem.* **1998,** *17*, 73-79.

[92] Kounaves, S. P.; Hecht, M. H.; West, S. J.; Morookian, J.-M.; Young, S. M.M.; Quinn, R.; Grunthaner, P.; Wen, X.; Weilert, M.; Cable, C. A. et al.. *J. Geophys. Res.* **2010,** *114,* E00A19.

[93] Hecht, M. H.; Kounaves, S. P.; Quinn, R. C.; West, R. C.; Young, S. M. M.; Ming, D. W.; Catling, D. C.; Clark, B. C.; Boynton, W. V.; Hoffman, J. et al.. Science **2009,** *325*, 64-67.

[94] Kounaves, S. P.; Hecht, M. H.; Kapit, J.; Gospodinova, K.; DeFlores, L.; Quinn, R. C.; Boynton, W. V.; Clark, B. C.; Catling, D. C.; Hredzak, P. et al.. *J. Geophys. Res.* **2010,** *115*, E00E10.

[95] Biemann, K.; Oro, J.; Toulmin III, P.;, Orgel, L. E.; Nier, A. O.; Anderson, D. M.; Simmonds, P. G.; Flory D; Diaz, A. V.; Rushneck, D. R. et al.. *Science* **1976,** *194,* 72–76.

[96]Biemann, K.; Oro, J.; Toulmin III, P.;, Orgel, L. E.; Nier, A. O.; Anderson, D. M.; Simmonds, P. G.; Flory D; Diaz, A. V.; Rushneck, D. R. et al.. *J. Geophys. Res.* **1977,** *82,*4641–4658.

[97]Ming, D. W.; Lauer Jr., H. V.; Archer Jr., P. D.; Sutter, B.; Golden, D. C.; Morris, R. V.; Niles, P. B.; Boynton, W. V. **2009**, 40th Lunar and Planetary Science Conference, Woodlands, TX.

[98] Navarro-González, R.; Vargas, E.; de la Rosa, J.;. Raga, A. C.; McKay, C. P. *J. Geophys. Res.* **2010,** *115,* E12010.

[99] Glavin, D.; Freissinet, C.; Eigenbrode, J.; Miller, K.; Martin, M.; Summons, R.; Steele, A.; Franz, H.; Archer, D.; Brinckerhoff, W. et al.. 45th Lunar and Planetary Science Conference, **2014,** Woodlands, TX.

[100] Davila, A. F.; Willson, D.; Coates, J. D.; McKay, C. P. *Int J Astrobio.* **2013**, *12,* 321-

325.

[101] Kirk, A. B.; Smith, E. E.; Tian, K.; Anderson, T. A.; Dasgupta, P. K. *Environ. Sci. Technol.* **2003**, 37, 4979-4981.

[102] Dasgupta, P. K.; Martinelango , K.; Jackson, W. A.; Anderson, T. A.; Tian K.; Tock, R. W.; Rajagopalan, S. *Environ. Sci. Technol.* **2005***, 39,* 1569-1575.

[103] Kirk, A. B.; Martinelango, P. K.; Tian, K.; Dutta, A.; Smith, E. E.; Dasgupta, P. K. *Environ. Sci. Technol.* **2005,** *39*, 2011-2017.

[104] Martinelango, P. K.; Tian, K.; Dasgupta, P. K. *Anal. Chim. Acta,* **2006,** *567,* 100-107.

[105] Dasgupta, P. K.; Dyke, J. V.; Kirk, A. B.; Jackson, W. A. *Environ. Sci. Technol.* **2006,** *40*, 6608-6614**.**

[106] Dyke, J. V.; Ito, K., Obitsu, T.: Hisamatsu, Y.: Dasgupta, P. K.; Blount, B. C. *Environ. Sci. Technol.* **2007,** *41*, 88-92.

[107] Kirk, A. B.; Dyke, J. V.; Martin, C. F.; Dasgupta, P. K. *Environ. Hlth. Persp.* **2007,** *115,* 182- 186.

[108] Kang, N.; Jackson, W. A.; Dasgupta, P. K.; Anderson, T. A. *Sci. Tot. Environ.* **2008,** 405, 301-309.

[109] Dasgupta, P. K; Kirk, A. B.: Dyke, J. V.; Ohira, S.-I. *Environ. Sci. Technol.* **2008,** *42,* 8115-8121.

[110] Ohira, S.I.; Kirk, A. B.; Dyke, J. V.; Dasgupta, P. K. *Environ. Sci. Technol.* **2008,** *42,* 9419–9423.

[111] Dasgupta, P. K. *Environ. Chem.* **2009,** *6*, 7–9.

[112] Kirk, A. B., Kroll, M.; Dyke, J. V.; Ohira, S.-I. Dias, R. A.; Dasgupta, P. K. *Sci. Tot. Environ.* **2012,** *420,* 73-78.

[113] Shelor, C. P.; Kirk, A. B.; Dasgupta, P. K.; Kroll, M.; Campbell, C. A., Choudhary, P. K. *Environ. Sci. Technol.* **2012,** *46,* 5151-5159.

[114] Kirk, A. B.; Dasgupta, P. K., Dyke, J. V.; Ohira, S.-I. *Sci. Tot. Environ.* **2012,** *443,* 939-943.

[115] Tian, K.; Dasgupta, P. K.; Anderson, T. A. Anal. Chem. 2003, 75, 701-706.

[116] Tian, K.; Cañas, J. E.; Dasgupta, P. K.; Anderson, T. A. *Talanta* **2005**, *65*, 750-755.

[117] Martinelango, P. K.; Anderson, J. L.; Dasgupta, P. K.; Armstrong, D. W.; Al-Horr, R. S.; Slingsby, R. W. Anal. Chem. **2005,** 77, 4829 - 4835.

[118] Dyke, J. V.; Kirk, A. B.; Martinelango, P. K.; Dasgupta, P. K. *Anal. Chim. Acta*, **2006,** *567,* 73-78.

[119] Martinelango, P. K.; Gümüs, G.; Dasgupta, P. K. *Anal. Chim. Acta,* **2006,** *567,* 79-86.

[120] Martinelango, P. K.; Dasgupta, P. K. *Anal. Chem.* **2007***, 79,* 7198-7201.

[121] Mai, T. D.; Pham, T. T. T.; Pham, H. V.; Sáiz, J.; Ruiz, C. G.; Hauser, P. C. *Anal. Chem.* **2013***, 85,* 2333-2339.

[122] Dasgupta, P. K.; Bao, L. *Anal*. *Chem*. **1993,** *65*, 1003-1011.

[123] Dasgupta, P. K.; Kar, S. *Anal. Chem.* **1995,** *67***,** 3853-3860.

[124] Kar, S.; Dasgupta, P. K. *J. Microcol. Sep.* **1996,** *8,* 561-568.

[125] Dasgupta, P. K.; Kar, S. *Anal. Chim. Acta* **1999,** *394,* 1-12.

[126] Zhang, M.; Stamos, B. N.; Dasgupta, P. K. Preceding paper in this issue

[127] Kuban, P.; Dasgupta, P. K. *Journal of Separation Science* **2004,** *27,* 1441-1457.

[128] Yang, B. C.; Zhang, F.; Liang, X. *Central Eur. J. Chem.* **2012,** *10,* 472-479.

[129] Cheong, W. J.; Ali, F.; Kim, Y. S.; Lee, J. W. *J. Chromatogr. A* **2013,** *1308,* 1-24.

[130] Pyo, D.; Dasgupta, P. K.; Yengoyan, L. S. *Anal. Sci.* **1997,** 13 (Suppl), 185-190.

[131] Breadmore, M. C.; Macka, M.; Avdalovic, N.; Haddad, P. R. *Analyst*, **2000,** *125,* 1235-1241.

[132] Zhang, S.; Macka, M.; Haddad, P. R. *Electrophoresis,* **2006,** *27*, 1069-1077.

[133] Hutchinson, J. P.; Hilder, E. F.; Macka, M.; Avdalovic, N.; Haddad, P. R. *J. Chromatogr. A* **2006,** 10-18.

[134] Zhang, M.; Yang, B. C.; Dasgupta, P. K. *Anal. Chem.* **2013,** *85,* 7994-8000.

[135] Zhang, M.; Stamos, B. N.; Amornthammarong, N.; Dasgupta, P. K. *Anal. Chem.*

[136] Christian, G. D.; Dasgupta, P. K.; Schug, K. A. *Analytical Chemistry*, 7th Ed. Wiley, 2013. pp 676-679.

[137] Walsh, S.; Diamond D. *Talanta* **1995**, *42*. 561-572.

[138] Dasgupta, P. K. *J. Chromatogr. A* **2008**, *1213*. 50-55.

[139] Caceci, M. S. *Anal. Chem.* **1989,** *61*, 2324-2327.

[140] Brumbaugh, E. E.; Ackers G. K. *J. Biol. Chem.* **1968,** *243*, 6315-6324.

[141] Gelderloos, G.D; Rowlen, K. L.; Birks, J. W. *Anal. Chem.* **1986,** *58,* 900-903.

[142] Rowlen, K. L.; Duell, K. A.; Avery, J. P.; Birks, J. W. *Anal. Chem.* **1989,** *61,* 2624-2630.

[143] Wu, X. Z.; Huang, T.; Liu, Z.; Pawliszyn, J. *TrAC: Trends Anal. Chem.* **2005,** *24,* 369-382.

[144]Convergent Bioscience, iCE280, http://www.proteinsimple.com/documents/iCE280_brochure_revC.pdf

[145] Xi, X.; Yeung, E. S. *Anal. Chem*. **1990**, *62*, 1580–1585.

[146] Kadjo, A. F.; Dasgupta, P. K. *Anal. Chim. Acta* **2013,** *773,* 1-8.

[147] Lin, S.-H.; Yu, T.; Sheu, A. Yang, D.-J.; Pai, S. C. *J. Chromatogr. A* **2008**, *1201,* 128–

131.

[148] Carlson, C. F. US Patent 2,297,691, 1942. Electrophotography.

[149] Zhang, M.; Stamos, B. N.; Amornthammarong, N.; Dasgupta, P. K. *Anal. Chem.* **2014,** *86,* 11538-11546.

[150] Zhang, M.; Stamos, B. N.; Dasgupta, P. K. *Anal. Chem.* **2014,** *86,* 11547-11553.

[151] Yang, B.; Zhang, M.; Kanyanee, T.; Stamos, B. N.; Dasgupta, P. K. *Anal. Chem.* **2014,** *86,* 11554-11561.

[152] Small, H. *Some Electrochemical Properties of an Ion Exchanger.* MSc. Thesis, Queens University, Belfast, Ireland. 1953.

[153] Zemann, A. J., Schnell, E., Volgger, D., Bonn, G. K. *Anal. Chem*. **1998**, *70*, 563–567.

[154] Fracassi da Silva, J. A., do Lago, C. L., *Anal. Chem*. **1998**, *70*, 4339–4343.

[155] Unterholzner, V.; Macka, M.; Haddad, P. R.; Zemann, A. *Analyst,* **2002,** *127,* 715-718.

[156] Macka, M.; Hutchinson, J.; Zemann, A.; Shusheng, Z.; Haddad, P. R. *Electrophoresis,* **2003,** *24,* 2144-2149.

[157] Gillespie, E.; Connolly, D.; Macka, M; Nesterenko, P. N.; Paull B. *Analyst,* **2007,** *132,* 1238-1245.

[158] Gillespie, E.; Connolly, D.; Macka, M.; Hauser, P.; Paull B. *Analyst,* **2008,** *133,* 1104-1110.

[159] Huang, W.; Seetasang, S.; Azizi, M.; Dasgupta, P. K. *Anal. Chem*. **DOI:** 10.1021/acs.analchem.6b03669

[160] Wahab, M. F.; Dasgupta, P. K.; Kadjo, A. F.; Armstrong, D. W. *Anal. Chim. Acta*. **2016,** *907,* 31-44.

[161] Connolly, D.; Floris, P.; Nesterenko, P.; Paull, B. *Trends in Anal. Chem.***2010,** *29,* 870-

884.

[162] Tallarek, U.; Bayer, E.; Guiochon, G. *J. Am. Chem. Soc.* **1998,** *120,* 1494-1505.

[163] Tallarek, U.; Baumeister, E.; Albert, K.; Bayer, E.; Guiochon, G. *J. Chromatogr. A,* **1995,** *696,* 1-8.

[164] Baumeister, E.; Klose, U.; Albert, K.; Bayer, E.; Guiochon, G. *J. Chromatogr. A,* **1995,** *694,* 321-331.

[165] Dasgupta, P. K. *J. Chromatogr. A* **2008,** *1213,* 50-55.

[166] Nikitas, P.; Pappa-Louisi, A.; Papageorgiou, A. *J. Chromatogr.* **2001,** *912*, 13-29.

[167] Hecht, M.H., et al., *Detection of Perchlorate and the Soluble Chemistry of Martian Soil at the Phoenix Lander Site.* Science, 2009. **325**(5936): p. 64-67.

[168] Glavin, D.P., et al., Evidence for perchlorates and the origin of chlorinated hydrocarbons detected by SAM at the Rocknest aeolian deposit in Gale Crater. Journal of Geophysical Research-Planets, 2013. 118(10): p. 1955-1973.

[169] Davila AF and Schulze-Makuch D (2016) The Last Possible Outposts for Life on Mars. *Astrobiology* 16.2: 159-168.

[170] McKay CP et al. (2003) Temperature and moisture conditions for life in the extreme arid region of the Atacama Desert: four years of observations including the El Niño of 1997-1998.*Astrobiology* 3.2: 393-406.

[171] Catling, D. C.; Claire, M. W.; Zahnle, R. C.; Quinn, R. C.; Clark, B. C.; Hecht, M. H.; Kounaves, S. *J. of Geophys. R.* , **2010**, *115*, 1-15.

[172] Tsitouridou, R; Puxbaum, H *Int. J. of Env. Anal. Chem.* **1987,** *31,* 11-22.

[173] Kappes, T.; Schnierle, P; Hauser, P. C. *Anal. Chem. Acta,* **1999**, *393*, 77-82.

[174] Kiplagat, I. K.; Kuban, P. Pelcova, P; Kuban, V. *J. Chromatogr. A.*, **2010**, *1217*, 5116-5123.

[175] Yang, B.; Zhang, M; Kanyanee, T.; Stamos, B. N.; Dasgupta, P. K. *Anal. Chem.*, **2014**, *86*, 11554-11561.

[176] Zhang, M.; Stamos, B. N.; Dasgupta, P. K. *Anal. Chem.*, **2014**, *86*, 11547-11553.

[177] Peters KE, Walters CC, and Moldowan JM (2005) The biomarker guide, volume

[178] Eigenbrode JL (2008) Fossil lipids for life-detection: a case study from the early Earth record. Strategies of Life Detection. Springer US: 161-185.

[179] Summons RE et al.. (2011) Preservation of martian organic and environmental records: final report of the Mars Biosignature Working Group. Astrobiology 11.2: 157-181.

[180] Skopintsev BA (1981) Decomposition of Organic Matter of Plankton, Humification and Hydrolysis. Elsevier Oceanography Series 31: 125-177.

[181] Henrichs SM and Doyle A) (1986) Decomposition of 14C-labeled organic substances in marine sediments. Limnol. Oceanogr 31.4: 765-778.

[182] Petsch ST, Eglinton TI, and Edwards KJ (2001) 14C-dead living biomass: evidence for

microbial assimilation of ancient organic carbon during shale weathering. Science, 292(5519): 1127-1131.

[183] Lehmann MF et al.. (2002) Preservation of organic matter and alteration of its carbon and nitrogen isotope composition during simulated and in situ early sedimentary diagenesis. Geochimica et Cosmochimica Acta 66.20: 3573-3584.

[184] Kuzyakov Y (2010) Priming effects: interactions between living and dead organic matter. Soil Biology and Biochemistry 42.9: 1363-1371.

[185] Holser WT, Schidlowski M, Mackenzie FT, Maynard JB (1988) Geochemical cycles of carbon and sulfur. In Gregor CB, Garrels RM, Mackenzie FT and Maynard JB (eds) Chemical Cycles in the Evolution of the Earth. John Wiley & Sons, New York: p 105-173.

[186] Hedges JI (1992) Global biogeochemical cycles: progress and problems. Marine chemistry 39.1: 67-93.

[187] Brocks JJ and Summons RE (2004) Sedimentary hydrocarbons, biomarkers for early life. In Biogeochemistry: Treatise on Geochemistry, Volume 8, ed W.H. Schle- singer, Elsevier Pergamon, Oxford, pp. 63–115.

[188] Des Marais DJ (2001) Isotopic evolution of the biogeochemical carbon cycle during the Precambrian. In: Stable Isotope Geochemistry, Rev. Mineral. 43, eds JW Valley and DR Cole, pp. 555-578.

[189] Van Veen JA and Kuikman PJ (1990) Soil structural aspects of decomposition of organic matter by micro-organisms. Biogeochemistry 11.3: 213-233.

[190] Farmer JD and Des Marais DJ (1999) Exploring for a record of ancient Martian life. Journal of Geophysical Research: Planets 104.E11: 26977-26995.

[191] Herrmann B and Henke W (1999) DNA preservation: a microsatellite-DNA study on ancient skeletal remains. Electrophoresis, 20, 1722-1728.

[192] Rethemeyer J et al.. (2010) Distribution of polar membrane lipids in permafrost soils and sediments of a small high Arctic catchment. Organic Geochemistry,41(10): 1130-1145.

[193] Geomorphology of Desert Environments; Parsons AJ, Abrahams AD, Eds.; Springer Netherlands: Dordrecht, 2009.

[194] Pyenson ND, et al.. (2014) Repeated mass strandings of Miocene marine mammals from Atacama Region of Chile point to sudden death at sea. Proceedings of the Royal Society of London B: Biological Sciences 281.1781: 20133316.

[195] Tuena de Gómez-Puyou and Gómez-Puyou, 1998

[196] Grant WD (2004) Life at low water activity. Philosophical Transactions of the Royal Society of London B: Biological Sciences, 359(1448): 1249-1267.

[197] Clarke JDA (2006) Antiquity of aridity in the Chilean Atacama Desert. Geomorphology 73: 101–114.

[198] McKay CP et al.. (2003) Temperature and moisture conditions for life in the extreme arid region of the Atacama Desert: four years of observations including the El Niño of 1997-1998. Astrobiology 3.2: 393-406.

[199] Davila AF and Schulze-Makuch D (2016) The Last Possible Outposts for Life on Mars.

Astrobiology 16.2: 159-168.

[200] Connon SA, Lester ED, Shafaat HS, Obenhuber DC, and Ponce A (2007) Bacterial diversity in hyperarid Atacama Desert soils. Journal of Geophysical Research: Biogeosciences, 112(G4).

[201] Amundson R (2001) The carbon budget in soils. Annual Review of Earth and Planetary Sciences, 29(1): 535-562.

[202] Lester ED, Satomi M, and Ponce A (2007) Microflora of extreme arid Atacama Desert soils. Soil Biology and Biochemistry, 39(2): 704-708.

[203] Warren-Rhodes KA et al.. (2006) Hypolithic cyanobacteria, dry limit of photosynthesis, and microbial ecology in the hyperarid Atacama Desert. Microbial Ecology 52.3: 389-398.

[204] Hartley AJ and Chong G (2002) Late Pliocene age for the Atacama Desert: implications for the desertification of western South America. Geology, 30(1): 43-46.

[205] Hartley AJ, Chong G, Houston J, and Mather AE (2005) 150 million years of climatic stability: evidence from the Atacama Desert, northern Chile. Journal of the Geological Society, 162(3): 421-424.

[206] Amundson R et al.. (2012) Geomorphologic evidence for the late Pliocene onset of hyperaridity in the Atacama Desert. Geological Society of America Bulletin 124.7-8: 1048-1070.

[207] Ewing SA et al.. (2006) A threshold in soil formation at Earth's arid–hyperarid transition." Geochimica et Cosmochimica Acta 70.21: 5293-5322.

[208] Sutter B, Dalton JB, Ewing SA, Amundson R, and McKay CP (2007). Terrestrial analogs for interpretation of infrared spectra from the Martian surface and subsurface:

Sulfate, nitrate, carbonate, and phyllosilicate-bearing Atacama Desert soils. Journal of Geophysical Research: Biogeosciences,112(G4).

[209] Ewing SA, Macalady JL, Warren-Rhodes K, McKay CP, and Amundson R (2008) Changes in the soil C cycle at the arid-hyperarid transition in the Atacama Desert. Journal of Geophysical Research: Biogeosciences, 113(G2).

[210] Ichihara KI, Shibahara A, Yamamoto K, and Nakayama T (1996) An improved method for rapid analysis of the fatty acids of glycerolipids. Lipids, 31(5): 535-539.

[211] Volkman JK (2006) Lipid markers for marine organic matter." Marine Organic Matter: Biomarkers, Isotopes and DNA. Springer Berlin Heidelberg: pp. 27-70.

[212] Simoneit BR, Summons RE, and Jahnke LL (1998) Biomarkers as tracers for life on early Earth and Mars. Origins of Life and Evolution of the Biosphere, 28(4-6): 475-483.

[213] Sun MY, Wakeham SG, and Lee C (1997) Rates and mechanisms of fatty acid degradation in oxic and anoxic coastal marine sediments of Long Island Sound, New York, USA. Geochimica et Cosmochimica Acta, 61(2): 341-355.

[214] Bordenave ML (1993). The sedimentation of organic matter. Applied Petroleum Geochemistry, Editions Technip, Paris: 15-76.

[215] Azua-Bustos A, Caro-Lara L, and Vicuña R (2015) Discovery and microbial content of the driest site of the hyperarid Atacama Desert, Chile. Environmental microbiology reports, 7(3): 388-394.

[216] Navarro-González R et al.. (2003) Mars-like soils in the Atacama Desert, Chile, and the dry limit of microbial life. Science, 302(5647): 1018-1021.

[217] Crits-Christoph A et al.. (2013) Colonization patterns of soil microbial communities in

the Atacama Desert. Microbiome, 1(28): 10-1186.

[218] Skelley AM et al.. (2007) Organic amine biomarker detection in the Yungay region of the Atacama Desert with the Urey instrument. Journal of Geophysical Research: Biogeosciences, 112(G4).

[219] Andersson RE (1980) Microbial lipolysis at low temperatures. Applied and environmental microbiology, 39(1): 36-40.

[220] Wang XS, Poinar HN, Poinar Jr GO, and Bada JL (1995) Amino acids in the amber matrix and in entombed insects. In: Amber, resinite and fossil resin, ed. Anderson K and Crelling JC: pp. 255-262.

[221] Bada JL, Wang XS, and Hamilton H (1999) Preservation of key biomolecules in the fossil record: current knowledge and future challenges.Philosophical Transactions of the Royal Society of London B: Biological Sciences, 354(1379): 77-87.

[222] Schweitzer MH (2004) Molecular paleontology: some current advances and problems. In Annales de paléontologie Vol. 90, No. 2: pp. 81-102.

[223] Georgiou CD (2015) Evidence for photochemical production of reactive oxygen species in desert soils. Nat Commun, 6, doi:10.1038/ncomms8100.

[224] Melendez I, Grice K, and Schwark L (2013) Exceptional preservation of Palaeozoic steroids in a diagenetic continuum. Scientific reports, 3.

[225] Williams AJ, Sumner DY, Alpers CN, Karunatillake S, and Hofmann BA (2015) Preserved Filamentous Microbial Biosignatures in the Brick Flat Gossan, Iron Mountain, California. Astrobiology, 15(8): 637-668.

[226] Maus JE and Ingham SC (2003) Employment of stressful conditions during culture production to enhance subsequent cold-and acid-tolerance of bifidobacteria. Journal of Applied Microbiology, 95(1): 146-154.

[227] Morgan CA, Herman N, White PA, and Vesey G (2006) Preservation of micro-organisms by drying; a review. Journal of microbiological methods,66(2): 183-193.

[228] Summons RE and Lincoln SA (2012) Biomarkers: Informative Molecules for Studies in Geobiology. In: Fundamentals of Geobiology, First Edition. Eds Knoll AH, Canfield DE and Konhauser KO, Blackwell Publishing Ltd: pp. 269-296.

[229] Rashby SE, Sessions AL, Summons RE, and Newman DK (2007) Biosynthesis of 2-methylbacteriohopanepolyols by an anoxygenic phototroph. Proc Natl Acad Sci USA 104: 15099–15104.

[230] Welander PV, Coleman ML, Sessions AL, Summons RE, and Newman DK (2010) Identification of a methylase required for 2-methylhopanoid production and implications for the interpretation of sedimentary hopanes. Proceedings of the National Academy of Sciences,107(19): 8537-8542.

[231] White DC, Meadows P, Eglinton G, and Coleman ML (1993) In situ measurement of microbial biomass, community structure, and nutritional status. Philos Trans Phys Sci Eng 344:59–67.

[232] Vestal RD and White DC (1989) Lipid analysis in microbial ecology. Quantitative approaches to the study of microbial communities. Bioscience 39:535–541.

[233] Volkman JK et al.. (1998). Microalgal biomarkers: a review of recent research developments. Organic Geochemistry, 29(5): 1163-1179.

[234] Kaneda TOSHI (1991) Iso-and anteiso-fatty acids in bacteria: biosynthesis, function, and taxonomic significance. Microbiological reviews,55(2): 288-302.

[235] Elias VO, Simoneit BR, and Cardoso JN (1997) Even n-alkane predominances on the

Amazon shelf and a Northeast Pacific hydrothermal system. Naturwissenschaften, 84(9): 415-420.

[236] Wakeham SG (1999) Monocarboxylic, dicarboxylic and hydroxy acids released by sequential treatments of suspended particles and sediments of the Black Sea. Organic Geochemistry, 30(9): 1059-1074.

[237] Volkman JK, Johns RB, Gillan FT, Perry GJ, and Bavor HJ (1980) Microbial lipids of

an intertidal sediment—I. Fatty acids and hydrocarbons.Geochimica et Cosmochimica Acta, 44(8): 1133-1143.

[238] Cranwell PA (1981) Diagenesis of free and bound lipids in terrestrial detritus deposited in a lacustrine sediment. Organic Geochemistry, 3(3): 79-89.

[239] Pearson A, Ingalls AE (2013) Assessing the Use of Archaeal Lipids as Marine Environmental Proxies. Annu. Rev. Earth Planet. Sci. 41, 359–384.

[240] Schouten S, Hopmans EC, Damsté JSS (2013) The organic geochemistry of glycerol dialkyl glycerol tetraether lipids: A review. Organic Geochemistry 54: 19–61.

[241] Weijers JW et al.. (2006) Membrane lipids of mesophilic anaerobic bacteria thriving in

peats have typical archaeal traits. Environmental Microbiology, 8(4): 648-657.

[242] Kates M (1978) The phytanyl ether-linked polar lipids and isoprenoid neutral lipids of extremely halophilic bacteria. Progress in Chemistry: Fats and Other Lipids 15(4): 301–342.

[243] Koga Y, Morii H (2005) Recent advances in structural research on ether lipids from Archaea including comparative and physiological aspects. Bioscience, Biotechnology, and Biochemistry 69 (11): 2019–2034.

[244] Jahnke LL et al.. (2008) Lipid biomarker and phylogenetic analyses to reveal archaeal biodiversity and distribution in hypersaline microbial mat and underlying sediment. Geobiology 6: 394–410.

[245] Birgel D et al.. (2014) Hypersaline conditions during deposition of the Calcare di Base revealed from archaeal di-and tetraether inventories. Organic Geochemistry. 77: 11–21.

[246] Wang F, Michalski G, Seo JH, Granger DE, Lifton N, and Caffee M (2015) Beryllium-10 concentrations in the hyper-arid soils in the Atacama Desert, Chile: Implications for arid soil formation rates and El Niño driven changes in Pliocene precipitation. Geochimica et Cosmochimica Acta, 160: 227-242.

[247] Jordan TE, Kirk-Lawlor NE, Blanco NP, Rech JA, and Cosentino NJ (2014) Landscape

modification in response to repeated onset of hyperarid paleoclimate states since 14 Ma, Atacama Desert, Chile. Geological Society of America Bulletin, 126(7-8): 1016-1046.

[248] Meadow JF et al.. (2015) Humans differ in their personal microbial cloud. PeerJ, 3, e1258.

[249] Bligh EG and Dyer WJ (1959) A rapid method of total lipid extraction and purification. Canadian journal of biochemistry and physiology, 37(8): 911-917.

[250] Jahnke LL, Stan-Lotter H, Kato K, and Hochstein LI (1992) Presence of methyl sterol and bacteriohopanepolyol in an outer-membrane preparation from Methylococcus capsulatus (bath). J Gen Microbiol 138:1759–1766.

[251] Kates M (1986) Techniques of lipidology. 2. rev.

[252] Bell CM & Padian K (1995) Pterosaur fossils from the Cretaceous of Chile: evidence for a pterosaur colony on an inland desert plain. Geological Magazine, 132(01): 31-38.

[253] Salgado L, et al.. (2008) First Late Jurassic dinosaur bones from Chile. Journal of Vertebrate Paleontology, 28(2): 529-534.

[254] Guthrie, R.; Susi, A. *Pediatrics*. **1963**, *32,* 338-343.

[255] Zytkovicz, T. H. Fitzgerald, E. F. Marsden, D. Larson, C. a; Shih, V. E. Johnson, D. M. Strauss, W. Comeau, M. Eaton, R. B.; Grady, G. F. *Clin. Chem*. **2001**, *47*, 1945-55.

[256] Therrell, B. L. Hannon, W. H. Pass, K. A.; Lorey, F. Brokopp, C. Eckman, J. Glass, M. Heidenreich, R. Kinney, S. Kling, S. Landenburger, G. Meaney, F. J. McCabe, E. R. Panny, S. Schwartz, M.; Shapira, E. *Biochem. Mol. Med*. **1996**, *57*, 116-24.

[257] Sherman, G. G.; Stevens, G.; Jones, S. A.; Horsfield, P. M. T; Stevens, Wendy, S. M. *J. AIDS* **2005**, *38*, 615-617.

[258] Allanson, A. L.; Cotton, M.M. Tettey, J. N. A.; Boytera, A.C. *J. Pharm. Biomed. Anal.*

2007, *44*, 963-969.

[259] Otero-santos, S. M.; Delinsky, A. D.; Valentin-Blasini, L.; Schiffer, J.; Blount, B. C. *Anal. Chem.* **2009,** *81,* 1931-1936.

[260] Spooner, N. Lad, R.; Barfield, M. *Anal. Chem*. **2009**, *81*, 1557-63.

[261] Barfield, M.; Spooner, N.; Lad, R. Parry, S.; Fowles, S. *J. Chromatogr. B,* **2008**, *870*, 32-37.

[262] McCabe, E. R. *Genome Res*. **1991**, *1*, 99-106.

[263] Edelbroek, P. M.: van der Heijden, J.; Stolk, L. M. L. Dried Blood Spot Methods in Therapeutic Drug Monitoring: Methods, Assays, and Pitfalls. *Therap. Drug Monit*. **2009**, *31*, 327-336.

[264] Li, W.; Tse, F. L. S. *Biomed. Chromatogr*. **2010**, *24*, 49-65.

[265] Rashed, M. S.; Bucknall, M. P.; Little, D.; Awad, A.; Jacob, M.; Alamoudi, M.; Alwattar, M.; Ozand, P. T. *Clin. Chem*. **1997**, *43*, 1129-1141.

[266] Chace, D. H.; Kalas, T. A.; Naylor, E. W. *Clin. Chem*. **2003**, *49*, 1797-1817.

[267] Chace, D. H. Hillman, S. L. Millington, D. S. Kahler, S. G. Adam, B. W.; Levy, H. L. *Clin. Chem*. **1996**, *42*, 349-55.

[268] Chace, D. H. Lim, T. Hansen, C. R. Adam, B. W.; Hannon, W. H. *Clin. Chim. Acta* **2009**, *402*, 14-18.

[269] Dintenfass, L. *Angiology* **1962**, *13*, 333-344.

[270] Adam, B. W.; Alexander, J. R.; Smith, S. J.; Chace, D. H.; Loeber, J. G.; Elvers, L. H.; Hannon, W. H. *Clin. Chem.* **2000,** *46,* 126-128.

[271] Hilder, E. F. *Aust. J. Chem.* **2011**, *64*, 843.

[272] Hilder, E. F.; Hon, W. B. U. S. Pat. App. Publication US 20140127669 A1, May 8, 2014.

[273] Erhardt, J. G.; Craft, N. E.; Heinrich, F.; Biesalski, H. K. *J. Nutr.* **2002,** *132,* 318-321.

[274] Bremmer, R. H.; de Bruin, K. G.; van Gemert, M. J. C.; Leeuwen, T. G.; Aalders, M. C. G.; *Forensic Sci. Int.*, **2012**, *216*, 1-11.

[275] Strasser, S.; Zink, A.; Kada, G.; Hinterdorfer, P.; Peschel, O.; Heckl, W. M.; Nerlich, A.G.; Thalhammer, S.; *Forensic Sci. Int*, **2006**, *170*, 8-14.

[276] Atlas, S. A. *J. Manage. Care Pharm.* **2007**, *13*, S9-S20.

[277] Howanitz, J. H.; Howanitz, P. J. *Am. J. Clin. Path*. **2007**, *127*, 56-59.

[278] Rao, D. A.; Tao, L.; Bhusan, V. First Aid for US Mle. **2008.** McGraw Hill Medical, New York.

[279] Reference range list from Uppsala University Hospital. *Laborationslista*. Article No. 40284 Sj74a. April 22, 2008

[280] de Rosny, G.; Chanzy, A.; Parde´, M.; Gaudu, J.-C.; Frangi, J.-P.; Laurent, J.-P. *J. Soil Soc. Am.* **2001,** *65,* 13-18.

[281] Bolvin, H.; Chambarel, A.; Chanzy, A. *J. Soil Soc. Am.* **2004,** *68,* 440-446.

[282] Dasgupta, P. K.; Surowiec, K. *Analytical chemistry*. **1996**, *68*, 1164-1168.

[283] Dasgupta, P. K.; Surowiec, K. *Anal. Chem*. **1996**, *68*, 4291-4299.

[284] Park, S. R.; Swerdlow, H. *Electroanalysis*. **2007**, *19*, 2294-2300.

[285] Voloudakis, K.; Vrahliotis, P.; Kastrinakis, E. G.; Nychas, S. G. *Meas. Sci. Technol.* **1999,** *10,* 100-105.

[286] Haber, C.; Jones, W. R.; Soglia, J.; Surve, M. A.; McGlynn, M.; Caplan, A.; Reineck, J. R.; Krstanovic, C. *J. Cap. Electrophoresis* 1996, 3(1), 1-11.

[287] Kim, C. Y. *Prog. Electromagnetics Res. B*, **2008,** *8,* 179-194.

[288] Olthuis, W.; Streekstra, W.; Bergveld, P. *Sensors Actuators B,* **1995,** *24,* 252-256.

[289] Crowley, J. M. *J. Electrostatics.* **1987**, *19*, 137–149.

[290] Crow, T. T. *Am J. Phys.* **1987***, 55,* 817–823.

[291] Hart, F. X. *Am. J. Phys.* **1989***, 57,* 1027–1034.

[292] Cheng, A. H.-D.; Cheng, D. T. *Eng. Anal. Bound. Elem.* **2005,** *29,* 268–302.

[293] Fachiroh, J.; Prasetyanti, P. R.; Paramita, D. K.; Prasetyawati, A. T.; Anggrahini, D. W.; Haryana, S. M.; Middeldorp, S. M. *J. Clin. Microbiol.* **2008,** *46,* 1374-1380.